Plasticité cristalline en présence de grandes déformations et d'endommagement

Andrei Musienko

To cite this version:

Andrei Musienko. Plasticité cristalline en présence de grandes déformations et d'endommagement. Mechanics [physics.med-ph]. École Nationale Supérieure des Mines de Paris, 2005. English. NNT : . tel-00159409

HAL Id: tel-00159409
https://pastel.hal.science/tel-00159409

Submitted on 3 Jul 2007

HAL is a multi-disciplinary open access archive for the deposit and dissemination of scientific research documents, whether they are published or not. The documents may come from teaching and research institutions in France or abroad, or from public or private research centers.

L'archive ouverte pluridisciplinaire **HAL**, est destinée au dépôt et à la diffusion de documents scientifiques de niveau recherche, publiés ou non, émanant des établissements d'enseignement et de recherche français ou étrangers, des laboratoires publics ou privés.

ECOLE DES MINES
DE PARIS

Collège doctoral

N° attribué par la bibliothèque
/_/_/_/_/_/_/_/_/_/_/_/

THESE

pour obtenir le grade de
Docteur de l'Ecole Nationale Supérieure des Mines de Paris
Spécialité Sciences et Génie des Matériaux

présentée et soutenue publiquement par

Andrey MUSIENKO

le 17 Mars 2005

Plasticité cristalline en présence de grandes déformations et d'endommagement

Directeur de thèse* : *Georges CAILLETAUD

Jury

M. Albrecht BERTRAM	Université de Magdeburg	
M. René BILLARDON	Université Paris VI	rapporteur
M. Esteban BUSSO	Imperial College, Londres	
M. Boris MELNIKOV	Univ. Tech. de St.Petersbourg	
M. Jean-Marc OLIVE	Université Bordeaux 1	
M. Gilles ROUSSELIER	EDF R&D	rapporteur
M. Georges CAILLETAUD	Ecole des Mines de Paris	directeur de thèse

Centre des Matériaux P.M. FOURT de l'Ecole des Mines de Paris,
B.P. 87, 91003 EVRY Cedex

Résumé

Ce travail s'inscrit dans le cadre de la plasticité cristalline. Sa première motivation est le développement d'une approche couplée, capable de prendre en compte l'interaction entre la plasticité et l'environnement dans les tubes de zircaloy des centrales nucléaires. La première étude sur la plasticité du zircaloy, influencée par l'environnement, a été menée par (O.Diard, G.Cailletaud, ENSMP). Les conditions d'interaction y sont bien caractérisées, et un premier modèle représentant l'endommagement des joints de grains suite à l'interaction avec l'iode y est proposé. Il restait à améliorer l'intégration numérique, et à utiliser le modèle pour des structures plus réalistes. Par ailleurs, il s'agit désormais de représenter l'endommagement intergranulaire, suivi de l'écrouissage transgranulaire, observé expérimentalement.

Afin d'atteindre ces objectifs, plusieurs points ont du être abordés. Une modélisation plus pertinente est ici utilisée pour les joints de grains, et une formulation du modèle en transformations finies est proposée. L'objectif initial a donc été élargi. En dehors des calculs d'agrégats endommagés du zircaloy, on trouvera les calculs d'une éprouvette de cuivre, maillée en 3d. C'est une étape indispensable pour tester la méthode numérique dans le cas de déformations modérées. Quelques résultats concernant la méthode numérique sont également présentés.

Le manuscrit est organisé en trois parties. Tout d'abord, la partie A est consacrée à la description des modèles. Les outils numériques sont ensuite expliqués dans la partie B. Enfin, la partie C présente les resultats numériques.

Dans la première partie, la formulation initiale d'un modèle du monocristal (section 1) est tout d'abord exposée ; puis vient le nouveau modèle DOS (Damage, Opening and Sliding) proposé pour une description de joints de grains (section 2) ; enfin la dernière section est consacrée aux algorithmes en transformations finies (section 3). L'élasticité, la plasticité J_2, la plasticité cristalline, et finalement le modèle DOS, sont successivement examinés. Le schéma implicite est utilisé pour l'intégration numérique.

Dans la Partie B, une méthode de génération de maillages particuliers, comportant une représentation explicite des joints de grains, avec de véritables éléments finis, est exposée. Cette procédure est développée de façon systématique, dans le cas 2d et 3d (section 4). Puis, le principe de calculs avec couplage est expliqué (section 5).

Les modèles du matériau et les outils numériques sont appliqués aux calculs d'aggrégats de zircaloy dans la section 7 de la partie C : une simulation de l'effet de corrosion sous contraintes des tubes du zircaloy dans l'environement de l'iode est proposée. Afin de montrer les possibilités de notre algorithme et d'avoir une comparaison avec l'expérience, la section 6 montre les résultats de calcul de l'état contrainte-déformation d'une éprouvette de cuivre, testée à l'Université de Leoben (O.Kolednik, et al.).

Abstract

This work addresses several problems in the framework of crystal plasticity. Its main motivation is the development of a coupled approach able to account for the interaction between environment, inelastic deformation and damage in a zircaloy alloy used for the cladding tubes in nuclear power plants. A first study was previously made by O.Diard on the same subject, and a preliminary numerical procedure was developed for performing the simulation.

Our purpose was to improve this first attempt, and to reach a quantitative agreement with the experimental data. The main modification to the initial model is a new geometrical representation of the "grain boundary". In fact, instead of having a special material for the grain boundary, we introduce a specific zone in each grain near the grain boundary. In this area, we still have the normal slip systems, corresponding to the grain it belongs to, but also specific systems to allow the boundary to slip and open. The resulting model (DOS) successfully represents damage, opening and sliding, and can be calibrated using experimental information on tubes submitted to complex load histories. A finite strain formulation is also provided. Finally, a model describing cleavage is in competition with intergranular damage, so that we are able to predict the transition from intergranular to transgranular cracking. These new features are implemented using a robust integration algorithm in the finite element code Zebulon.

A simulation of stress corrosion cracking of Zircaloy tubes in iodine environment (which appears as a result of pellet-cladding interaction in the core of nuclear pressurized-water reactors) is proposed. The predictions of the model are in good agreement with the experimental data describing the crack propagation rate.

The following points are obtained as sub-products of the study:

- Elasticity, J_2 plasticity, crystal plasticity, and the DOS model are successively studied, in the framework of small perturbation and large strain. The implicit Euler scheme is applied to the numerical integration of the single crystal under large strains. A special attention is payed to the problem of slip system activation.

- A method is proposed for generating specific finite element meshes, introducing an explicit representation of the grain boundaries with real elements. This procedure is systematically developed, in 2D and 3D cases.

A series of computations have also been performed on copper specimens, previously tested at the University of Leoben, Austria. The interesting point of the experimental study is that a true 3D microstructure is available, after successive polishing operation of the specimen (six slices are available, and the 3D mesh respects the real geometry). Various meshes are considered. This allows us to demonstrate that a really large number of elements are necessary to have a good representation of the local stress and strain fields. The comparison with the experiment is made on several levels: macroscopic curve, intragranular strain fields, slip system activity.

Remerciements

Ce travail a été realisé au Centre des Matériaux de l'Ecole des Mines de Paris entre 2000 et 2005. Je tiens donc à remercier Monsieur Jean-Pierre Trottier, Directeur du Centre, pour m'avoir accueilli dans ce laboratoire magnifique (sans oublier Liliane Locicero, Veronique Diamantino, Cindy Olivier qui ont effectué le coté pratique de cet accueil).

Je suis reconnaissant à Messieurs Albrecht BERTRAM, René BILLARDON, Esteban BUSSO, Boris MELNIKOV, Jean-Marc OLIVE, Gilles ROUSSELIER qui m'ont fait l'honneur de participer au jury de ma thèse, pour leurs corrections très importantes, pour leurs esprit critique, mais bienveillant.

Je vais essayer de ne pas oublier tous les thésards (et post-docs) du Centre, anciens comme actuels, sans lesquels le travail de thèse ne serait jamais finis. Je remercie infiniment Fabrice Barbe, Olivier Diard, Toufik Kanit, Sylvain Flouriot, Franck Alexandre, Bruno Barlas, Julia Chikina, Mihai Radu, Nikolay Osipov, Thomas Dick, Asmahana Zeghadi, Kamel Madi, Samira El-Mallouki, Céline Gérard pour leur soutien amical et leurs contributions scientifiques.

Je remercie les excellents spécialistes, regroupé autour du code ZéBuLoN, qui étaient toujours prêts a répondre à mes questions (parfois très dilettantes), pour leur patience et compréhension. Je tiens donc à remercier Stéphane Quilici, Farida Azzouz, Valéry Mounoury, Gregory Sainte-Luce, Laurent Jean-Faivre, Jacques Besson, Samuel Forest – pour le Centre des Matériaux, Frédéric Feyel – pour l'ONERA, Ronald Foerch – pour NW Numerics (USA).

Je remercie Mademoiselle Anna Vidineeva pour m'avoir supporté pendant les dernières années de thèse, pour avoir supporté mes visites trop courtes et désordonnées, auxquelles – je l'espère – on mettra bien de l'ordre un jour.

Mais le **GRAND MERCI**, – pour la confiance, pour la liberté, pour le soutien, pour le courage qui m'a manqué parfois, pour sa façon positive de réfléchir – le grand merci, je veux l'adresser à mon directeur de thèse, Monsieur Georges Cailletaud.

Contents

Résumé **i**

Abstract **iii**

Remerciements **v**

Introduction **xvii**

Part A Material models **1**

I Basic crystal plasticity model **3**
I.1 Known experimental results 3
I.2 Model formulation 4
I.3 Model extension for the cleavage representation 5

II Intergranular model **7**
II.1 Damage, Opening and Sliding model 19
II.2 A new strategy for grain boundary modeling 24

III Finite strains **27**
III.1 Notations 28
III.2 Elasticity 32
III.2.1 Models 32
III.2.2 Consistent tangent matrix 32
III.2.3 Results 33
III.3 J_2 plasticity 33
III.3.1 Model 34
III.3.2 Stress update algorithm 35
III.3.3 Consistent tangent matrix 36
III.3.4 Preparation for single crystal 36
III.3.5 Uniaxial tension test 39
III.3.6 Billet upsetting test 39
III.4 Crystal plasticity 43
III.4.1 Model 43
III.4.2 Numerical implementation problems 44
III.4.3 Stress update algorithm 45
III.4.4 Consistent tangent matrix 46
III.4.5 Single crystal tension test 47
III.4.6 Polycrystal compression test 48
III.5 Damage, Opening and Sliding 51

III.5.1 Model 51
III.5.2 Stress update algorithm 52
III.5.3 Note on damaged body kinematics under finite strains 52
III.6 Conclusion and Perspectives 52

Part B Numerical tools 55

IV Finite element meshes 57
IV.1 Introduction 57
IV.1.1 Grain boundaries - how to mesh them ? 58
IV.2 Voronoi tessellation to represent grains 58
IV.3 What is done ? 59
IV.3.1 2D 59
IV.3.2 3D 59
IV.4 Perspectives 60

V Coupled computation principle 69

Part C Applications 71

VI FE simulation of multicrystals at large strains 73
VI.1 Experiments 74
VI.2 Finite element meshes 74
VI.3 Material Parameter identification 75
VI.4 Note on the grain orientations 78
VI.5 Boundary conditions 79
VI.6 Results 79
VI.7 Discussion and Perspectives 81

VII Zircaloy computations 89
VII.1 Introduction 89
VII.2 Damaged grain boundaries versus perfect interface 90
VII.2.1 Crystal parameters and texture 90
VII.2.2 GB material parameters 90
VII.2.3 Boundary conditions 94
VII.2.4 Results and discussion 94
VII.2.5 Local fields 96
VII.2.6 Conclusion 96
VII.3 Uncoupled intergranular fracture 97
VII.4 Iodine influenced intergranular fracture 98
VII.4.1 Diffusion-damage coupling parameters 98
VII.4.2 Quasi-2D computational results 99
VII.4.3 3D computational results 100
VII.4.4 Crack propagation rate 100
VII.5 Iodine-influenced inter-transgranular fracture 100
VII.6 Conclusions 101

VIII Conclusions and perspectives 119
VIII.1 Perspectives 120

A Pre-existing algorithm of ZéBuLoN for single crystal model 121
A.1 Stress update algorithm . . . 121
  A.1.1 Possible numerical methods . . . 121
  A.1.2 Implicit integration for the single crystal model . . . 122
A.2 Algorithmic elasto-plastic moduli . . . 122
A.3 Check the nature of matrix $\mathcal{D}$ . . . 125

B Examples of the source code for integration procedures of material behavior models 127
B.1 Elasticity . . . 127
B.2 J2 plasticity . . . 128
B.3 Crystal plasticity . . . 130
References . . . 132

List of Figures

.1 Fuel assembly . . . xviii
.2 (a) - fuel rods, (b) - fuel pellets . . . xviii

I.1 Experimental evidence of Schmid law (Jillson, 1950) . . . 4
I.2 Experimental evidence of lateral hardening (Franciosi et al., 1980) . . . 5
I.3 Transgranular crack micrographs (Kubo et al., 1985) . . . 6

II.1 Experimental observations of polycrystalline materials . . . 7
II.2 (a) - Experimental evidence of grain boundary sliding; (b) - fracture surface of Zircaloy-4 in iodine environment (Fregonese, 1997) . . . 8
II.3 (a) - Experimental results of crack number and crack length increase with plastic deformation, Zircaloy-2 in iodine (Kubo et al., 1985); (b) - Experimental evidence of grain boundary sliding in Zirconium (Jacques, 1994) . . . 10
II.4 Fracture surface of Zircaloy-4 in aggressive environment : (a) - Intergranular, transgranular, ductile (Farina et al., 2003), (b) - Transgranular, intergranular, ductile (Knorr and Pelloux, 1982), (c) - Schematic view of influence of applied stress level on cracking morphology for semi-hard DHP-Cu (Mori et al., 2005) . . . 11
II.5 TG crack photos (Kubo et al., 1985) : (a) - Crack initiation, (b)- Crack propagation . . . 12
II.6 (a) - Transgranular zone fragment, F - Fluting region, PB - Basal cleavage planes (Farina et al., 2003), (b) - TG crack initiation scheme (Kubo et al., 1985) . . . 12
II.7 (a) - Intergranular stress corrosion cracking, Zircaloy-2 in iodine (Kubo et al., 1985); (b) - Intergranular creep fracture in alpha iron-tin alloy at 973 K (Watanabe, 1983) . . . 13
II.8 (a) - Tension curves of Zircaloy-4 (Geyer, 1999); (b) - Scheme of vacancies redistribution at the crack tip (Jones, 1985) . . . 13
II.9 Mechanism of transgranular crack propagation (a), and corresponding example of Cu-Al alloy fracture surface (b) –(Flanagan et al., 1991)– . . . 14
II.10 (a) - Intercrystalline fracture surfaces produced in Al-Zn-Mg bicrystals (Lynch, 1988); (b) - Scheme of ductile cracking, (c) - Scheme of SCC . . . 14
II.11 (a) - Discontinuous cleavage for 316 steel in $MgCl_2$ solution (Magnin et al., 1990); (b)(c) - Schema . . . 15
II.12 Schema of thin layer between two infinite half-spaces. Illustration of the asymptotic approach (Suquet, 1987) . . . 17
II.13 Illustration for the jump in the solution (Chaboche et al., 2001) . . . 18
II.14 DOS model response - tension only . . . 21
II.15 DOS model response - tension and shear . . . 21
II.16 DOS model response - shear in 2 directions . . . 21

II.17 DOS model response - parameters used for aggregate computations, iodine is absent . . . 22
II.18 DOS model response - parameters used for aggregate computations, iodine is present . . . 22
II.19 DOS model response - parameter which give an ”unwanted” result in aggregate computations . . . 23
II.20 Two visions of the grain boundary : (a) - the grain boundary is a layer of special properties between two grains ; (b) - each grain has its core and its grain boundary region . . . 25
II.21 Scheme with grain core and bicrystals at grain boundary (Evers et al., 2002) 25

III.1 Elastic tension test. Force-elongation curves. . . . 34
III.2 J_2 plasticity tension test. Stress strain curve. . . . 39
III.3 J_2 plasticity tension test. Force curve. . . . 40
III.4 J_2 plasticity billet upsetting. FE meshes (mesh1 and mesh2). . . . 40
III.5 J_2 plasticity billet upsetting - mesh1. Von Mises stress at 30% and 60% deflection. . . . 41
III.6 J_2 plasticity billet upsetting - mesh2 . Von Mises stress at 30% and 60% deflection. . . . 41
III.7 J_2 plasticity billet upsetting. Deformed shape from (Kudo and Matsubara, 1979) . . . 41
III.8 J_2 plasticity billet upsetting. Deformed shape from (Simo and Hughes, 1997) . . . 42
III.9 J_2 plasticity billet upsetting. Deformed shape from (Weber and Anand, 1990) . . . 42
III.10 Crystal 1 element tension stress-strain curve . . . 49
III.11 Finite element meshes used for crystal plasticity tests under finite strains: (a) 343-grain aggregate with cube-shaped 1 element grains; (b) 20-grain aggregate with realistic shaped grains (10326 tetrahedric elements) . . . 50
III.12 Cumulated plastic shear at finite strains after 50% compression: (a) 343-grain aggregate , (b) 20-grain aggregate . . . 50
III.13 Force-displacement curves for compression of a 343-grain aggregate. Pre-existing small strain, explicit finite strain and newly developed implicit finite strain are compared. . . . 51
III.14 Possible schemes of damaged body kinematics . . . 53

IV.1 Typical image of Voronoi polyhedra . . . 61
IV.2 Typical result of 2D mesh generation procedure after step 2 . . . 61
IV.3 Typical result of 2D mesh generation procedure after step 3 . . . 62
IV.4 Typical final result of 2D mesh generation procedure . . . 62
IV.5 Definition of grain boundary as a set of finite elements . . . 63
IV.6 2d extended mesh of 100 grains, used for computations . . . 63
IV.7 Grain boundaries for 100 grain mesh . . . 64
IV.8 Grain boundaries, two elements by width . . . 64
IV.9 3D finite element mesh without grain boundaries, (a) - elsets view, (b) - one nset example . . . 65
IV.10 3D finite element mesh with grain boundaries, (a) - outside view of the 20-grain aggregate, (b) - GB only for the same aggregate . . . 65
IV.11 3D finite element mesh with grain boundaries, (a) - outside view of the 100-grain aggregate, (b) - GB only for the same aggregate . . . 66

IV.12 Remeshing for two close multiple points 66
IV.13 (a) - Four GB planes with a multiple point, (b) - Two multiple points connected with a triple line 66
IV.14 (a) - Remeshing near a multiple point, (b) - multiple point and triple lines FE structure with a grain 67
IV.15 Two element per width grain boundaries for 3D case 67

V.1 Schema, illustrating the coupled computation principle 70

VI.1 Macroscopic strain-stress curve 75
VI.2 SEM micrographs at 0% and 10% macrostrains 75
VI.3 Strains in tensile and transverse directions at 5% macrostrain (exp.) . . . 76
VI.4 Inversed pole figure maps for the tensile and normal directions at 5% macrostrain 76
VI.5 "Small" and "big" finite element meshes 76
VI.6 "Modified small" and "extended small" finite element meshes 77
VI.7 Surface views (a,b,c) and cut at 100 μm (d,e,f); comparisons between the 2D extended mesh (no change between a and d), the EBSD microsgraph (real structure in b and e) and the 3D mesh (mesh update in agreement with experiment, in c and f) 77
VI.8 Euler angles rotation 79
VI.9 Grain orientation references for experiment and simulation 80
VI.10 Displacement field –Ux component– experiment and computation 80
VI.11 SEM image (fragment) at 0% and 10% macrostrain, with profiles to plot local behavior (Tatschl, 2000) 82
VI.12 Total average $\epsilon_{11} - \sigma_{11}$ curves 82
VI.13 Local strains for Profile1 83
VI.14 Comparison for ϵ_{11} at 5% macrostrain ("small" mesh and experiment) . . 84
VI.15 Comparison for ϵ_{22} at 5% macrostrain ("small" mesh and experiment) . . 85
VI.16 Comparison for ϵ_{11} at 5% macrostrain ("2D extended small" and "3D small" mesh) 86
VI.17 Comparison for ϵ_{22} at 5% macrostrain ("2D extended small" and "3D small" mesh) 87

VII.1 Stress–strain curve for optimized J_2 theory parameters 93
VII.2 Mesh coordinate systems to illustrate boundary conditions: (a) 100gr2dext; (b) 20gr3d 94
VII.3 Global average stress-strain curves 102
VII.4 Average normal stress in GB versus GB angle to tension direction. Relatively small plastic strains 103
VII.5 Average normal stress in GB versus GB angle to tension direction. Developed plastic strains 104
VII.6 sig22 dependence on Y coordinate for Y=0 line 105
VII.7 Von Mises stress fields at 2% macrostrain 106
VII.8 Cumulated plastic strain fields at 2% macrostrain 107
VII.9 Von Mises stress and damage fields evolution for non-coupled test 108
VII.10 Von Mises stress and damage fields evolution for non-coupled test - end . 109
VII.11 Two parameter sets - wanted and unwanted damage and inelastic opening strain (δ) distributions 110
VII.12 Von Mises stress and damage fields evolution for coupled test 111
VII.13 Two parameter sets - wanted and unwanted iodine profile and damage field 112

VII.14 Von Mises stress and damage fields evolution for coupled test - 3d 113
VII.15 Damage fields on grain boundary structure - 3d 114
VII.16 Inter-transgranular fracture transition 115
VII.17 Aggregate fragment, iodine coupled intergranular and uncoupled transgranular material behavior. One can see iodine coupled intergranular crack - on the left (IG), and transgranular crack initiation near the grain boundary, which then enters a neighboor grain - on the right (TG) . . . 116
VII.18 Aggregate fragment, iodine-coupled intergranular and transgranular material behavior. One can see intergranular (IG) crack, followed by transgranular (TG) one 116
VII.19 Transgranular crack initiation, qualitative comparison of typical computation result and known literature image; computation field of cumulated prismatic+basal slip versus experimental micrograph from (Kubo et al., 1985). Here : 1 - grain, preferably oriented for prismatic or basal slip, gr59 in the computation ; 2 - grain with less prismatic+basal, but more pyramidal slip, gr53 in the computation; 3 - transgranular crack initiation 117
VII.20 Average slips for 2 grains near transgranular crack initiation 117
VII.21 Crack projection length as a function of time for iodine coupled intergranular fracture. 118

List of Tables

III.1 Material parameters for J_2 plasticity tension test 39
III.2 Material parameters for J_2 plasticity billet upsetting test 40
III.3 Material parameters for single crystal tension test 47
III.4 Material parameters for polycrystal compression test 48

IV.1 List of actual FE meshes, used in the computations 68

VII.1 Material parameters for Zircaloy 91
VII.2 List of FE computations 95
VII.3 Damage parameters for DOS only test 97
VII.4 Damage parameters for DOS only test –alternative set– 97
VII.5 Damage parameters for coupled IG test 99
VII.6 Damage parameters for coupled IG test - alternative set 99

Introduction

This work addresses several problems in the framework of crystal plasticity. Its first motivation is the development of a coupled approach able to account for the interaction between environment and plasticity in zircaloy tubes of a nuclear power plant. Assemblies of such a tubes – examples can be seen in fig. .1 – is a core of a nuclear reactor. Each tube contain a number of fuel pellets (see fig. .2-b), that forms a fuel rod (see fig. .2-a). A first study on the environmentally influenced plasticity of zircaloy had been made (Diard, 2001). The conditions of the interactions were then well characterized, and a first model has been proposed to represent the damage of grain boundaries, due to iodine interaction. After this initial attempt, it was still necessary to improve the quality of the numerical integration, and to use the model with more realistic microstructures. On the other hand, the new challenge was to represent the sequence of intergranular damage followed by transgranular hardening, as observed in the experiments.

In order to achieve these goals, a series of problems have been revisited. In the present work, a more careful modeling of the grain boundary area is used, a finite strain formulation of the model is proposed. As a result, the initial objective has been enlarged. Beside the computation of damaged zircaloy aggregates, the reader will find some computations of a copper specimen which has been fully meshed in 3D. This was a critical step to test the numerical method in the case of moderate strain. We will also show several results concerning the numerical method.

The manuscript is organized in three parts. Part A is devoted to the description of the models. Numerical tools are explained in part B. Part C contains the simulation results.

Part A starts with the formulation of the initial single crystal model (section 1), followed by the new Damage, Opening and Sliding (DOS) model proposed for the description of the grain boundaries (section 2). Section 3 is devoted to algorithms for finite transformation. We will successively examine elasticity, J_2 plasticity, crystal plasticity, and finally the DOS model. The implicit Euler scheme is applied to the numerical integration of the single crystal under large strains.

In part B, we show a method for generating specific meshes introducing an explicit representation of the grain boundaries with real elements. This procedure is systematically developed, in 2D and 3D case (section 4). Then, a coupled computation principle is explained (section 5).

Both material models and numerical tool will be applied for the computation of our zircaloy aggregates in section 7 of part C : a simulation of stress corrosion cracking of Zircaloy tubes in iodine environment (which appears as a result of pellet-cladding interaction in the core of nuclear pressurized-water reactors) is proposed. In order to demonstrate the capabilities of our algorithms and to have a comparison with experiment, section 6 shows the results of the computation of the stress-strain state of OFHC copper specimens tested at

University of Leoben (Tatschl and Kolednik, 2002a).

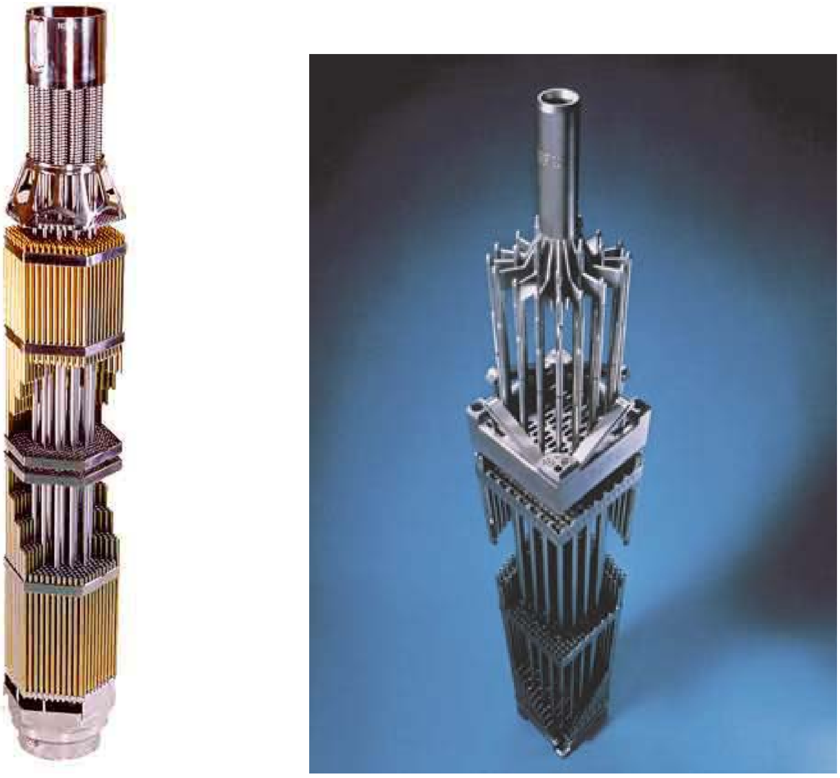

(a) Russia

(b) France

Figure .1 : Fuel assembly

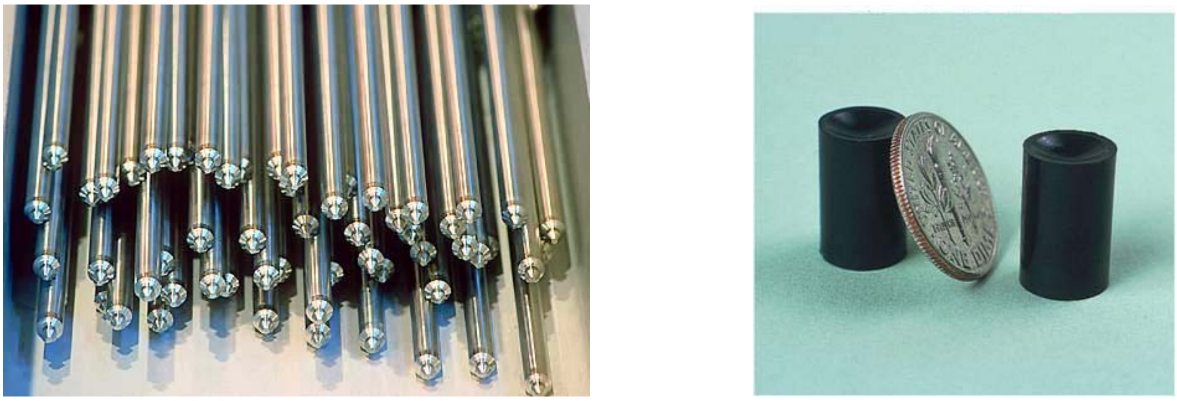

(a)

(b)

Figure .2 : (a) - fuel rods, (b) - fuel pellets

Part A

Material models

Chapter -I-

Basic crystal plasticity model

Contents

I.1 Known experimental results **3**
I.2 Model formulation **4**
I.3 Model extension for the cleavage representation **5**

I.1 Known experimental results

Very complex theories have been developed in the framework of crystal plasticity (Budiansky and Wu, 1962)(Hutchinson, 1964)(Asaro, 1983)(Asaro and Needleman, 1985)(Jordan and Walker, 1985) They are designed to take into account several microscales, the presence of heterogeneities, the various population of dislocations, *etc...*

The purpose of the model considered here is to capture the specificities related to the main mechanisms. It will then consider:

1. Slip planes and directions. Plastic deformation of single crystals happens by shear of one part of crystal on another one. This shear occurs in specific planes (called slip planes), and directions (slip directions). Slip planes and directions are defined by the crystallography of the given crystal.

There are several types of crystallographic structures. In the present work, only FCC (face centered cubic) and HCP (hexagonal close-packed) were used, respectively for copper and zircaloy.

These results are usually first referenced to (Schmid and Boas, 1935). Now they are classical and one can find slip planes and directions in (Kocks, 1970)(FCC) and (Tome and Kocks, 1985)(HCP) for instance.

2. Schmid law. Tension tests on single crystals show, that differently oriented single crystals of a given metal start slipping when different stresses are applied to the cross section, but that *the stresses resolved on the slip plane and in the slip direction are always the same.* It was first found by Schmid (Schmid and Boas, 1935), and later verified by (Jillson, 1950). Results of (Jillson, 1950) – on Zinc – are presented in fig.I.1. One can see that critical stress depend on crystal orientation in such a manner, that $\sigma \sin\chi \cos\lambda = const.$

3. Latent hardening. Experiments on the secondary specimens, cut from the primary loaded parent crystal, have shown that these secondary specimens represent higher yield limit, than the primary ones. Classical results for Aluminium and Copper can be found in (Kocks and Brown, 1966) and (Franciosi et al., 1980) –see fig.I.2–. These results are usually interpreted as a presence of *latent hardening*, i.e. the effect of hardening of nonactive slip systems due to plastic slip on others active slip systems.

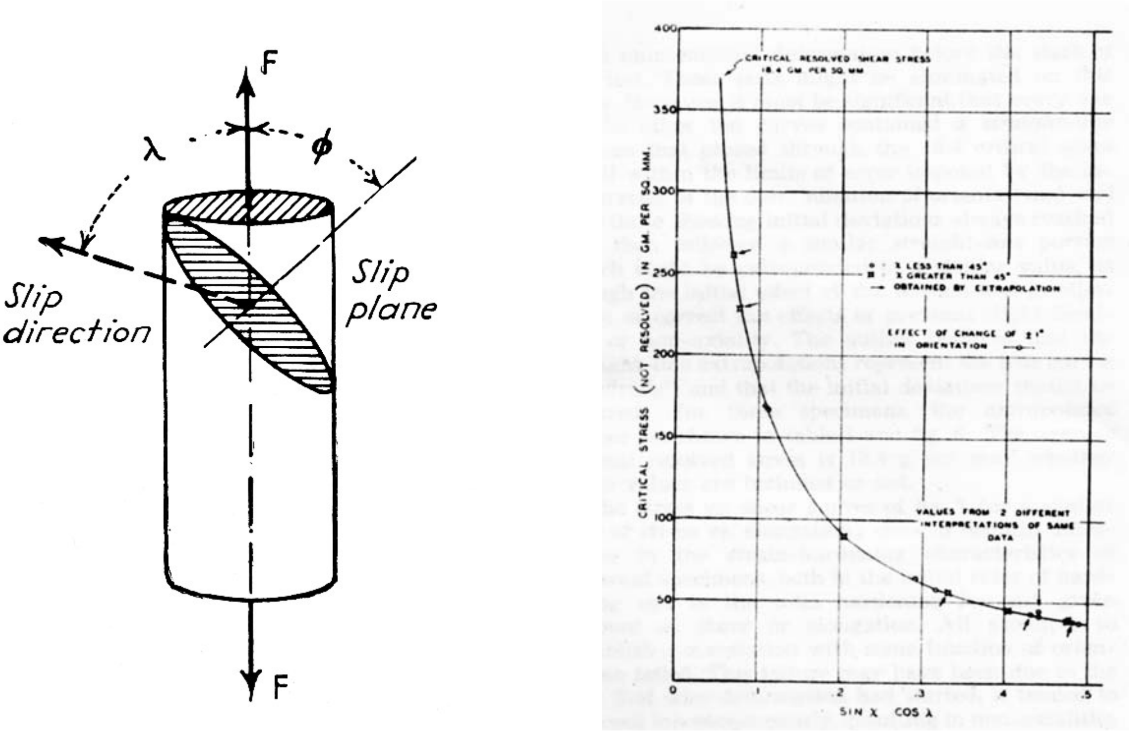

(a) specimen orientation (b) critical stress

Figure I.1 : Experimental evidence of Schmid law (Jillson, 1950)

I.2 Model formulation

The model is formulated here as proposed in (Cailletaud, 1991) and (Meric et al., 1991), following the small strains assumption. Additive decomposition of a strain rate into an elastic and a plastic part is used –eq. I.1–. The plastic deformation rate is calculated as a sum of elementary slips on all the crystalline slip systems –eq. I.4–. Slip systems are geometrically defined by means of $\underset{\sim}{\mathbf{m}}_{\mathrm{s}}$ tensors –eq. I.2–. Here $\underline{\mathbf{n}}_{\mathrm{s}}$ is the normal to the slip plane, and $\underline{\mathbf{l}}_{\mathrm{s}}$ is the slip direction. Following the Schmid law, each elementary slip rate , $\dot{\gamma}_{\mathrm{s}}$, depends on the resolved shear stress, τ_{s}. A fully phenomenological Norton-like viscoplastic relation is proposed –eq. I.5–. Isotropic and kinematic hardening (in a classical Ishlinsky-Prager manner) are taken into account by means of the internal variables r_{s} and x_{s} –eq. I.3–. In order to represent the effect of latent hardening, the resulting isotropic hardenings for different slip systems are interconnected by means of an interaction matrix h_{sr} .

$$\dot{\underset{\sim}{\varepsilon}} = \dot{\underset{\sim}{\varepsilon}}^{e} + \dot{\underset{\sim}{\varepsilon}}^{\mathrm{p}} \tag{I.1}$$

$$\tau_{\mathrm{s}} = \underset{\sim}{\sigma} : \underset{\sim}{\mathbf{m}}_{\mathrm{s}} = \frac{1}{2}\,\underset{\sim}{\sigma} : (\underline{\mathbf{n}}_{\mathrm{s}} \otimes \underline{\mathbf{l}}_{\mathrm{s}} + \underline{\mathbf{l}}_{\mathrm{s}} \otimes \underline{\mathbf{n}}_{\mathrm{s}}) \tag{I.2}$$

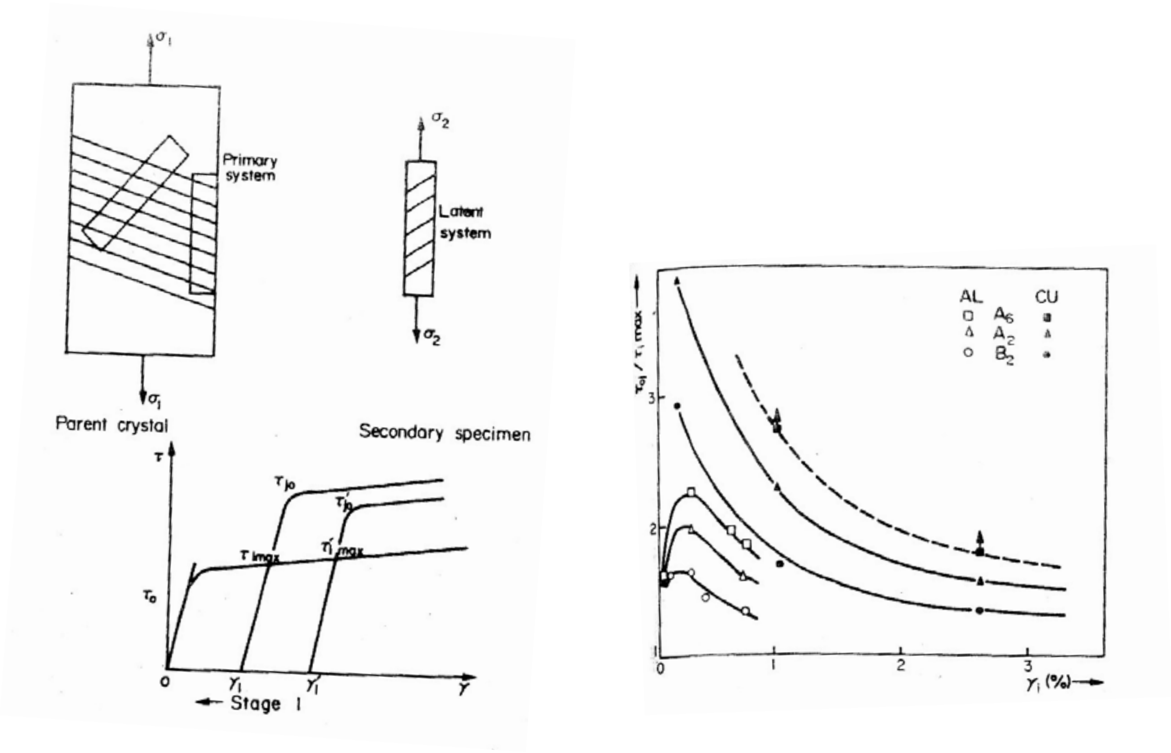

(a) specimens

(b) results

Figure I.2 : Experimental evidence of lateral hardening (Franciosi et al., 1980)

$$x_{\rm s} = c\ \alpha_{\rm s} \quad ; \quad r_{\rm s} = R_0 + bQ \sum_r h_{sr} q_{\rm r} = R_0 + Q \sum_r h_{sr} \left\{ 1 - e^{-bv_{\rm r}} \right\} \tag{I.3}$$

$$\dot{\gamma}_{\rm s} = \dot{v}_{\rm s} sign\left(\tau_{\rm s} - x_{\rm s}\right) \quad ; \quad \underset{\sim}{\dot{\varepsilon}}^{\rm p} = \sum_s \underset{\sim}{\mathbf{m}}_{\rm s} \dot{\gamma}_{\rm s} \tag{I.4}$$

$$\dot{v}_{\rm s} = \left\langle \frac{|\tau_{\rm s} - x_{\rm s}| - r_{\rm s}}{K} \right\rangle^n \quad \text{with } \langle x \rangle = Max(x, 0) \quad \text{and} \quad v_{\rm s}(t=0) = 0 \tag{I.5}$$

$$f_s = |\tau_{\rm s} - x_{\rm s}| - r_{\rm s} \tag{I.6}$$

$$\dot{\alpha}_{\rm s} = \dot{\gamma}_{\rm s} - d\ \alpha_{\rm s} \dot{v}_{\rm s} \quad \text{with} \quad \alpha_{\rm s}(t=0) = 0 \quad ; \quad \dot{q}_{\rm s} = (1 - b\, q_{\rm s}) \dot{v}_{\rm s} \tag{I.7}$$

After its initial implementation (Meric et al., 1991) in the Finite Element code ZSeT/ZéBuLoN, it has been used in a series of computations, for industrial applications, like turbine blades (Cailletaud et al., 2003a), or polycrystalline aggregates –see, for instance, (Barbe et al., 2001a)–.

I.3 Model extension for the cleavage representation

Cleavage of crystallized substances is the result of a splitting readily in one or more definite directions, in which the cohesive attraction is a minimum, affording more or less smooth surfaces; the direction of the dividing plane is the cleavage plane. This type of fracture happens as a separation of a single crystal into two parts following some crystallographic plane, because external loading exceeds interatomic forces. For the case of Zircaloy in iodine environment, studied in present work, the plane of transgranular fracture is the basal plane $\{0001\}$ – see Fig.II.5–.

Cleavage modeling can be seen as an extension of the single crystal model. Let $\underline{\mathbf{n}}$ to be a normal vector to the cleavage plane (basal plane in our case). Assuming that the critical variable for cleavage supposed is the normal stress $\sigma_{cleav} = \underline{\mathbf{n}} \cdot \underset{\sim}{\sigma} \cdot \underline{\mathbf{n}}$ and R_{cleav} the cleavage limit, the crystal behavior will be purely plastic provided $\sigma_{cleav} < R_{cleav}$.

The cleavage failure will take place when the stress will reach R_{cleav}. In the present work, instead of a pure time independent formalism, a time dependence is introduced, in order to regularize the solution, so that the stress will decrease progressively. This is computationally more convenient, and can be adapted by changing the values of K and n. A cleavage related inelastic strain is used :

$$\underset{\sim}{\dot{\varepsilon}}^{cleav} = \dot{\delta}^{cleav} \underline{\mathbf{n}} \otimes \underline{\mathbf{n}}$$

$$\dot{\delta}^{cleav} = \left\langle \frac{\sigma_{cleav} - R_{cleav} - Q(1 - exp(-b\delta^{cleav}))}{K} \right\rangle^{n}$$

Parameter Q should be chosen less then zero, in order to have softening behavior.

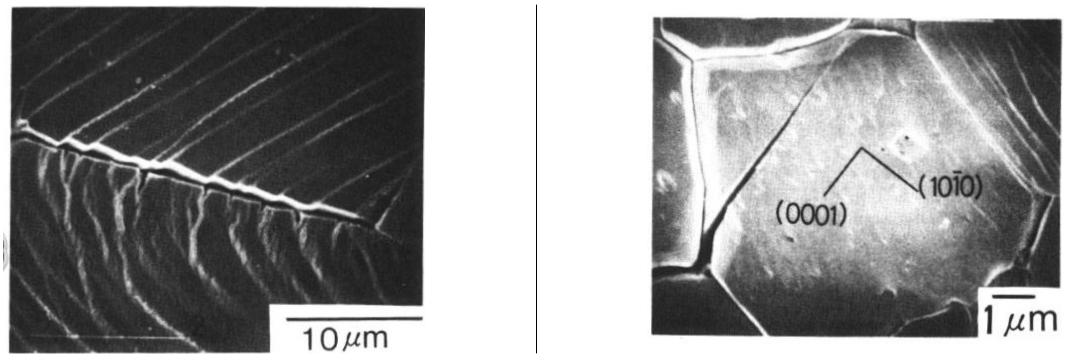

Figure I.3 : Transgranular crack micrographs (Kubo et al., 1985)

Chapter -II-

Intergranular model

Contents

II.1 Damage, Opening and Sliding model 19
II.2 A new strategy for grain boundary modeling 24

When a solid forms from the liquid, small randomly oriented crystallites nucleate and grow. The crystals grow until they meet each other, and, in general, they will not be of exactly the same orientation. The boundary where they meet becomes a surface, and the mismatch in their orientation is accommodated by distortion and gaps in atomic arrangements. Grain boundaries can be seen on the polished surface of metal, by means of optical or electronic microscope. Examples for the materials studied in this work – oxygen free high conductivity (OFHC) copper and Zircaloy-4 – are presented in fig.II.1.

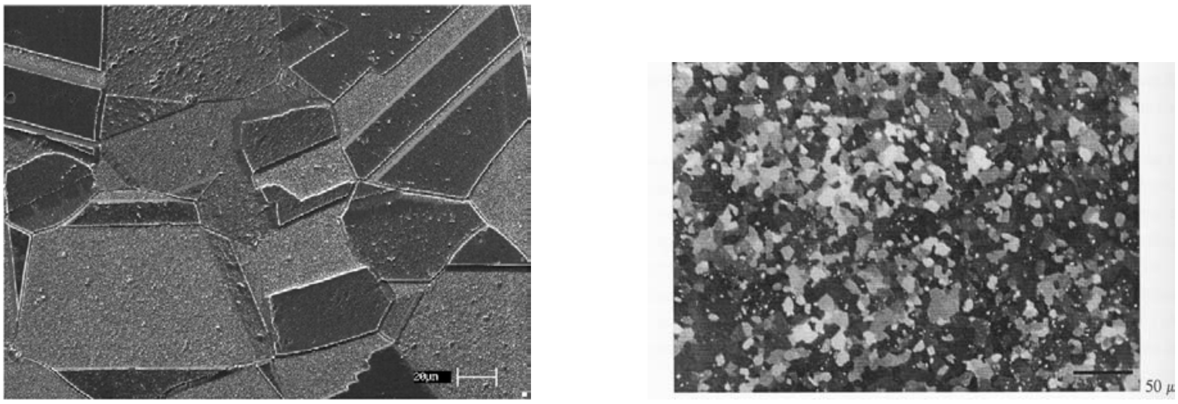

(a) OFHC copper (Tatschl, 2000)

(b) Zircaloy-4 (Fregonese, 1997)

Figure II.1 : Experimental observations of polycrystalline materials

Grain boundary is believed now to be a two-dimensional defect of crystalline cell (Flewitt and R.K.Wild, 2001), with the thickness of 2-3 atom size. The value of 8Å is reported for the grain boundary thickness in (Budai et al., 1979), as a result of X-ray diffraction experiments on gold.

Grain boundary sliding. The previous observations were made on pure metals, at very small strains. The conclusions are not the same on real alloys, submitted to realistic loadings. Due to the high level of incompatibility of the deformation field, grain boundaries are highly perturbated areas. Unexpected slip systems (secondary slip) happens in this location, so that a non negligeable zone can affect a specific behavior. On the other hand, slip can happen at grain interfaces (*grain boundary sliding*). This effect has been observed experimentally (see for instance (Miura et al., 2000; Parker and Wilshire, 1977; Yoshida et al., 2004). In fig. II.2, one can see a particle of B_2O_3 liquid at the grain boundary of a copper bi-crystal after the deformation. This particle was of circular shape before the deformation, and in the figure one can see a result of the two half-spheres relative motion.

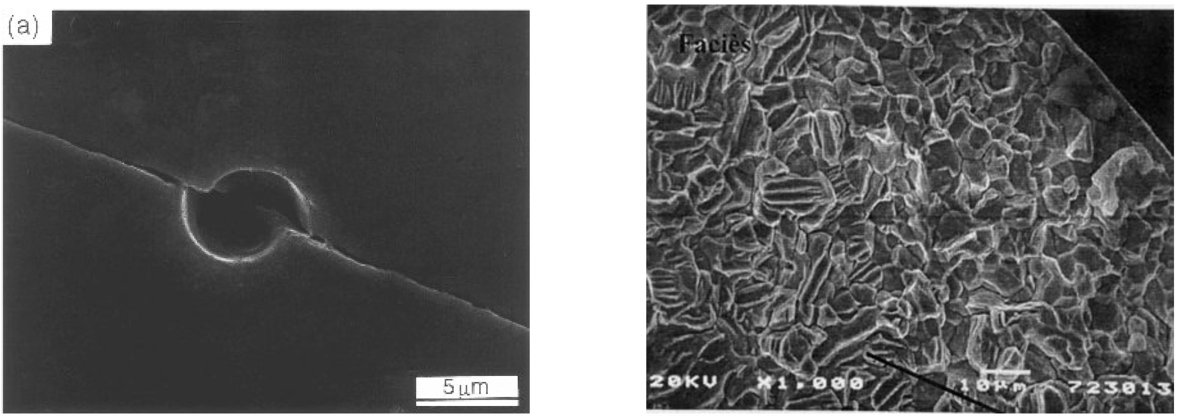

(a) copper GB (Miura et al., 2000)

(b) Zircaloy-4 (Fregonese, 1997)

Figure II.2 : (a) - Experimental evidence of grain boundary sliding; (b) - fracture surface of Zircaloy-4 in iodine environment (Fregonese, 1997)

Grain boundary fracture, stress corrosion cracking(SCC) of Zircaloy

A bibliographical study on the subject of damage of Zircaloy cladding, and the methods to model this damage, was done in (Diard, 2001). The present work in based on the conclusions of this bibliography. We will repeat here the most important facts, necessary for the understanding of the model choice.

1. Iodine and Cesium were found in cracked claddings. They were also found necessary for the fracture. Review on the subject can be found in (Cox, 1990). Recent review on iodine chemistry for the cracking of Zircaloy reactor cladding can be found in (Sidky, 1998). Stress corrosion cracking by iodine or metal vapour embrittlement by cesium/cadmium vapours is believed to happen(Cox et al.,).

2. There is an oxide layer inside the Zircaloy tube, which protects Zircaloy from the stress corrosion. But failure occurs at 0.5 % strain. This is the reason why it is not taken into account in the present study.

3. Iodine influences the fracture process as a gas, even if rigid compounds of iodine and Zircaloy can appear, due to chemical reactions.

4. Typical rupture surface of Zircaloy in iodine environment represent two zones : intergranular and transgranular. This basic result was obtained experimentally by (Fregonese, 1997) for instance, as shown in fig. II.2. Depending on the loading

conditions, either intergranular fracture happens first, and then transgranular, or the other way round –see fig. II.4–. (*i*) for (Fregonese, 1997),(Farina et al., 2003),(Kubo et al., 1985), the tests are performed under prescribed strain rate, in an aggressive environment. As a consequence, the first stage of cracking happens for relatively small stress levels, without plastic strain, and it is intergranular. As the crack goes on, the effective cross section of the specimen decreases, and the stress level goes up. After some critical stress (or plastic strain) value, the fracture type changes into transgranular. (*ii*) On the other hand, in (Knorr and Pelloux, 1982), the experiment was made on DCB (double cantilever beam) specimen, which was *first* loaded (by inserting a wedge into the machined notch) and then put into aggressive atmosphere. In that case, maximal loading takes place at the beginning of the test. This fact produces transgranular fracture as a first stage, then intergranular failure, followed by a crack arrest. (*iii*) Fracture can be purely transgranular if the load is high and permanent (Woo Seog Ryu et al., 1988), or in the case of single crystal (Haddad and Dorado, 1994). (*iv*) Fracture also can be purely intergranular, if the specimen is first kept in iodine environment: a one-millimeter rod was kept for 40 hours, and then loaded (Duffo and Farina, 2005).

All these experimental facts are in accordance with the schematic process proposed in (Mori et al., 2005) for Copper –see figII.4-c –.

5. Intergranular. Number and depth of intergranular cracks increase with the deformation. It was observed in imposed strain test on Zircaloy-2 in iodine environment by (Kubo et al., 1985) –see fig. II.3.a–. The conditions were: constant strain rate $4.4 \cdot 10^{-5} s^{-1}$, temperature 350°C, iodine concentration $1.3 \cdot 10^{3}$ Pa. Stress–strain tension curves for Zircaloy-4 without iodine at 350°C under different strain rates are presented in fig. II.8-a.

6. Intergranular. In a tension test for Zirconium Z1 in Argon (i.e. inert atmosphere) at 350°C(imposed strain rate between $3.3 \cdot 10^{-4} s^{-1}$ and $5.0 \cdot 10^{-6} s^{-1}$), grain boundary slip was observed (Jacques, 1994) – see fig. II.3-b –.

   Creep fracture of alpha-iron tin alloy at 973 K is reported to happen by grain boundary sliding and fracture (Watanabe, 1983). One can note intergranular character of both creep fracture and stress corrosion cracking of Zircaloy – see fig.II.7–.

7. Intergranular. A texture effect exists. It is not introduced in our study, nevertheless there is no difficulty to account for it in the framework of the proposed methodology.

8. Transgranular

   It was shown that transgranular cracks initiate near the grain boundary –see Fig.II.5.a–. The upper grain (1), which is oriented favorably for prismatic slip to occur, shows large plastic deformation, while grain (2) which is oriented unfavorably does not. The initiation sites of the transgranular cracks generally coincide with the intersections of coarse slip bands and the grain boundary. Cracks always extend into the neighboring grain, which is oriented unfavorably for prismatic slip operation. The scheme of a transgranular crack initiation, proposed in (Kubo et al., 1985), is presented in Fig. II.6.b–. As reported in (Kubo et al., 1985), transgranular microcracks initiated preferentially at intersections of coarse slip bands and grain boundaries. They extended along basal planes into grains which are oriented less favorably for prismatic slip. Once initiated, the crack propagates in the basal plane {0001} –see Fig.II.5.b–.

   More detailed studies (Fregonese, 1997)(Farina et al., 2003) show, that the transgranular crack propagation is rather the result of a competition between quasi-cleavage (brittle fracture) and fluting in the prismatic planes (ductile fracture). It can be seen in Fig.II.6-a. In the present study, only cleavage in basal planes will be considered.

9. Explanations of SCC mechanism. (Jones, 1985) Transgranular SCC is explained as divacancies appearance and redistribution, followed by cleavage.
10. Explanations of SCC mechanism. (Flanagan et al., 1991) Transgranular SCC cracking in FCC is studied. Dog-leg crack is explained. We do not study it.
11. Explanations of SCC mechanism. (Lynch, 1988)(Lynch, 1989) Transgranular and intergranular SCC are not distinguished. TEM observations for different materials show small dimples on fracture surface under SCC conditions, while relatively large, deep dimples with small dimples within and between then appear for ductile fracture. Example for Al-Zn-Mg bicrystals is shown in fig. II.10-a. An adsorbtion-induced localized slip mechanism of fracture is then proposed. It is illustrated in fig.II.10-b,c.
12. Explanations of SCC mechanism. (Magnin et al., 1990) The model was initially proposed to explain SCC of 316 steel in $MgCl_2$ –see fig. II.11-a–.

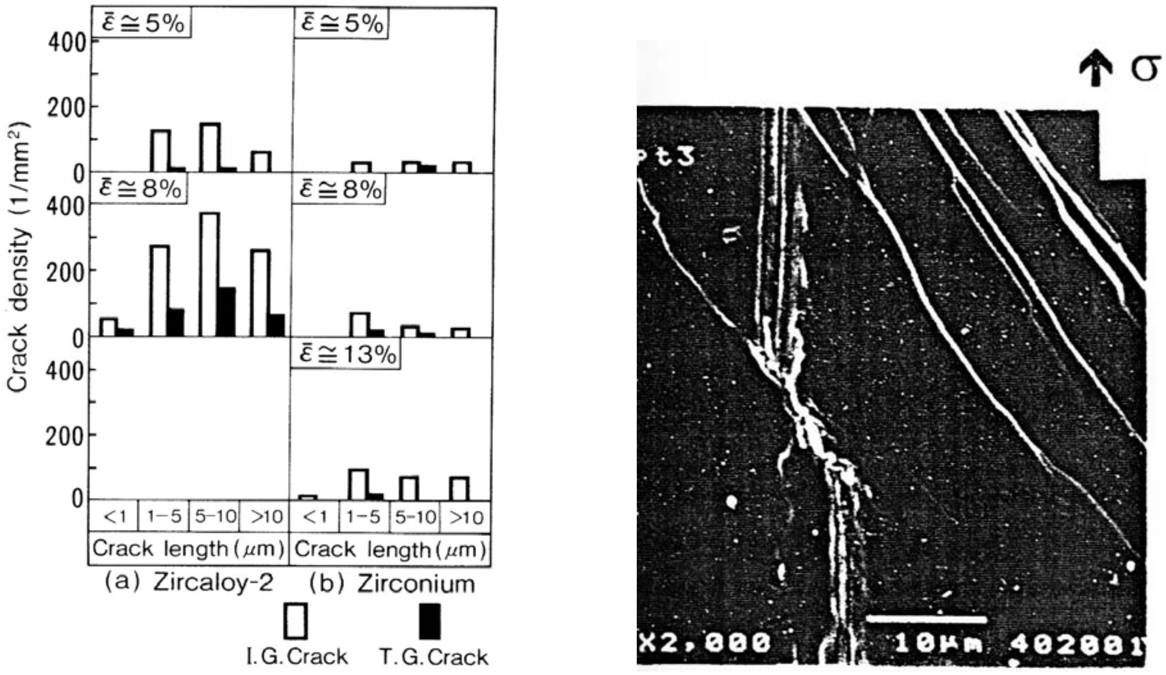

(a) (b)

Figure II.3 : (a) - Experimental results of crack number and crack length increase with plastic deformation, Zircaloy-2 in iodine (Kubo et al., 1985); (b) - Experimental evidence of grain boundary sliding in Zirconium (Jacques, 1994)

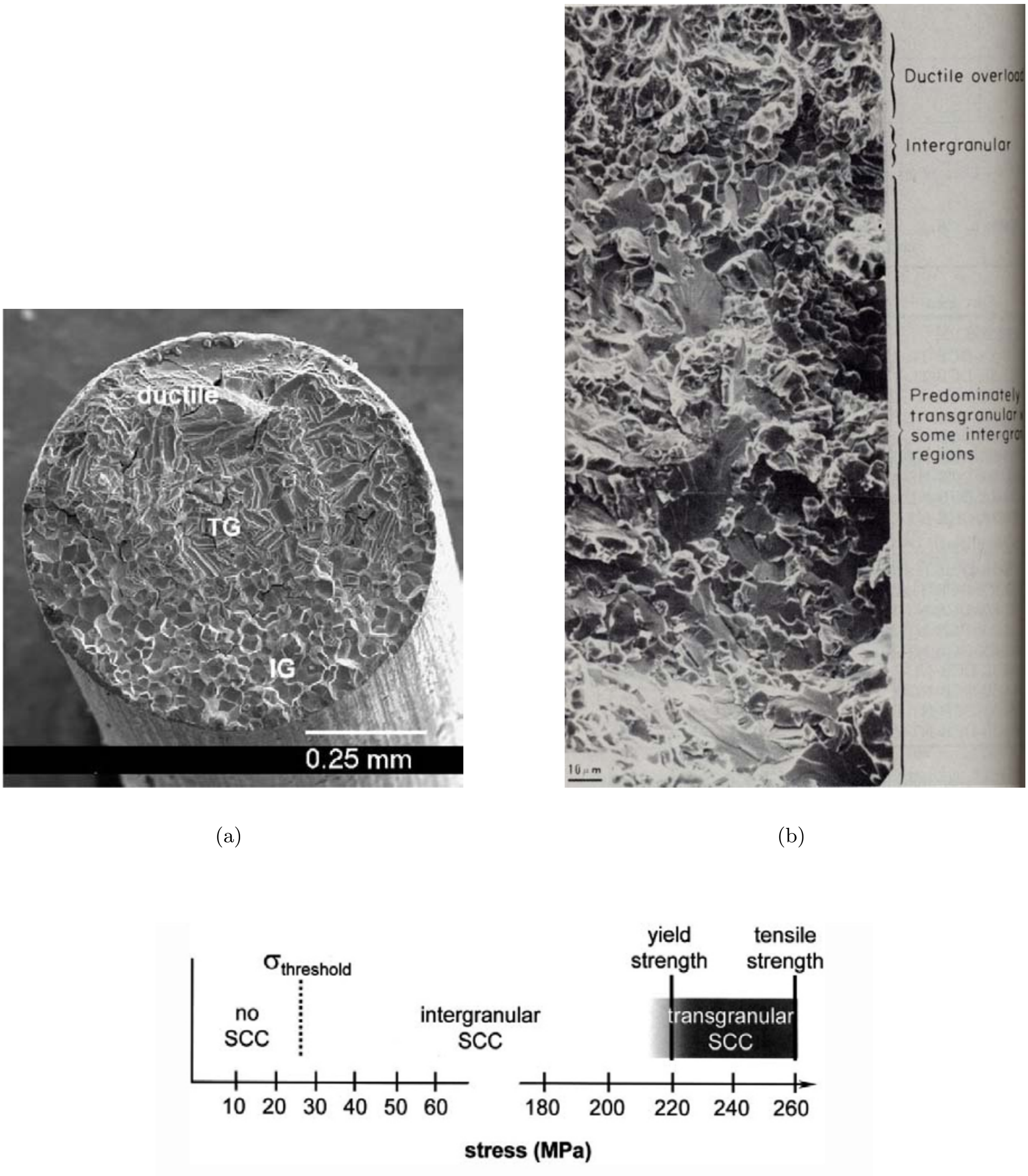
ductile
TG
IG
0.25 mm
Ductile overloa
Intergranular
Predominately
transgranular
some intergra
regions
10 µm
σ_threshold
no
SCC
intergranular
SCC
yield
strength
tensile
strength
transgranular
SCC
10
20
30
40
50
60
180
200
220
240
260
stress (MPa)

(a)

(b)

(c)

Figure II.4 : Fracture surface of Zircaloy-4 in aggressive environment : (a) - Intergranular, transgranular, ductile (Farina et al., 2003), (b) - Transgranular, intergranular, ductile (Knorr and Pelloux, 1982), (c) - Schematic view of influence of applied stress level on cracking morphology for semi-hard DHP-Cu (Mori et al., 2005)

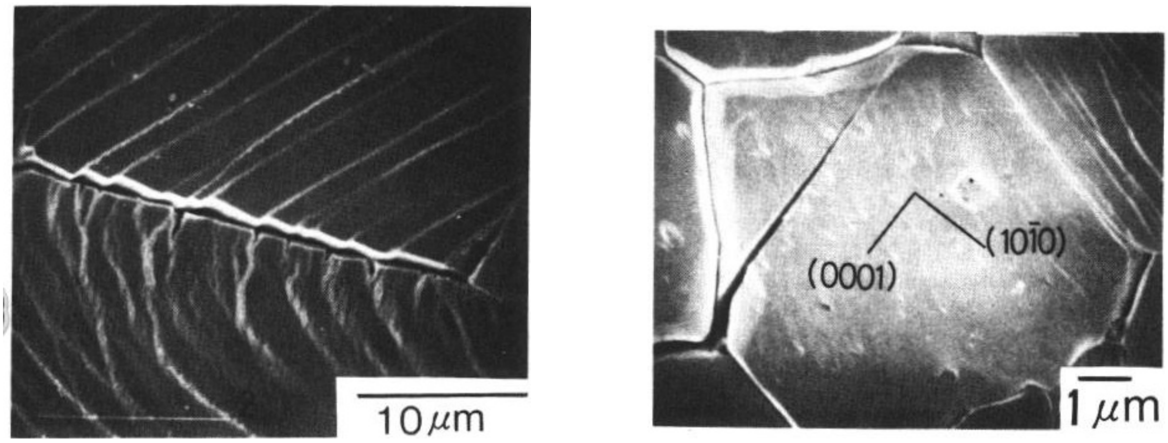
10 μm
(0001)
(10$\bar{1}$0)
1 μm

(a) (b)

Figure II.5 : TG crack photos (Kubo et al., 1985) : (a) - Crack initiation, (b)- Crack propagation

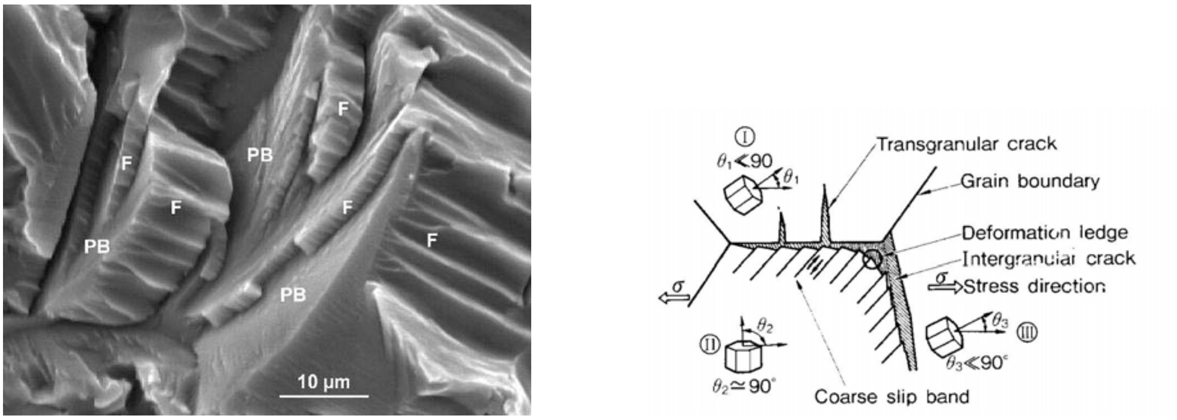
F
PB
F
F
PB
F
PB
F
10 μm
①
$\theta_1 < 90$
θ_1
Transgranular crack
Grain boundary
Deformation ledge
Intergranular crack
σ Stress direction
σ
②
θ_2
$\theta_2 \simeq 90^\circ$
θ_3
③
$\theta_3 \ll 90^\circ$
Coarse slip band

(a) (b)

Figure II.6 : (a) - Transgranular zone fragment, F - Fluting region, PB - Basal cleavage planes (Farina et al., 2003), (b) - TG crack initiation scheme (Kubo et al., 1985)

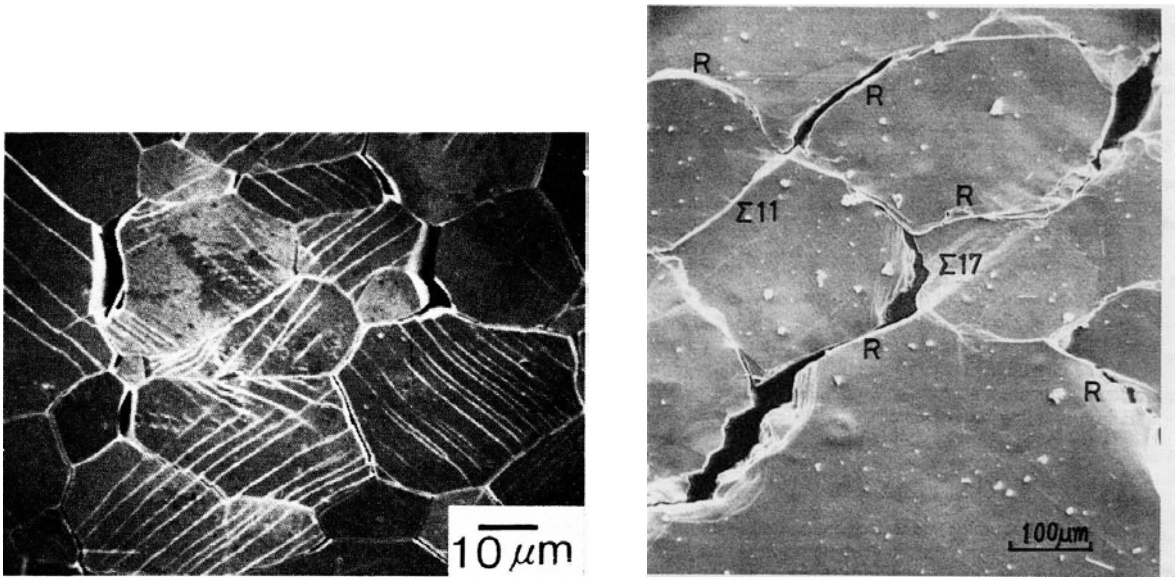

(a) (b)

Figure II.7 : (a) - Intergranular stress corrosion cracking, Zircaloy-2 in iodine (Kubo et al., 1985); (b) - Intergranular creep fracture in alpha iron-tin alloy at 973 K (Watanabe, 1983)

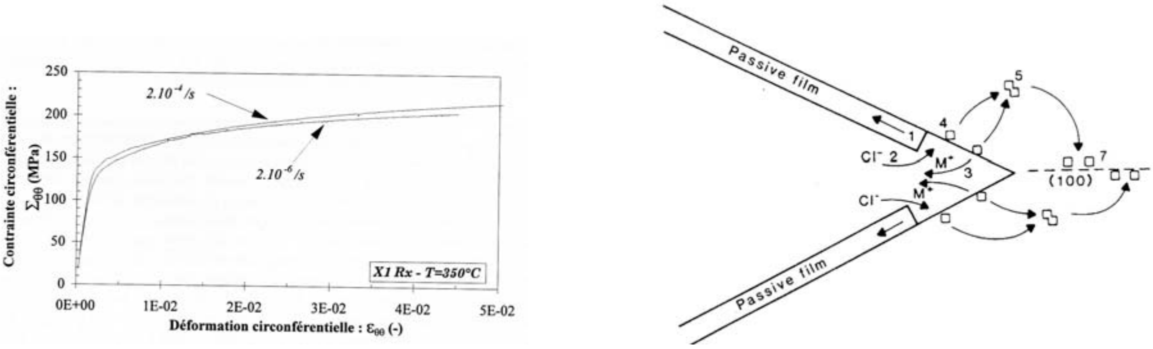

(a) (b)

Figure II.8 : (a) - Tension curves of Zircaloy-4 (Geyer, 1999); (b) - Scheme of vacancies redistribution at the crack tip (Jones, 1985)

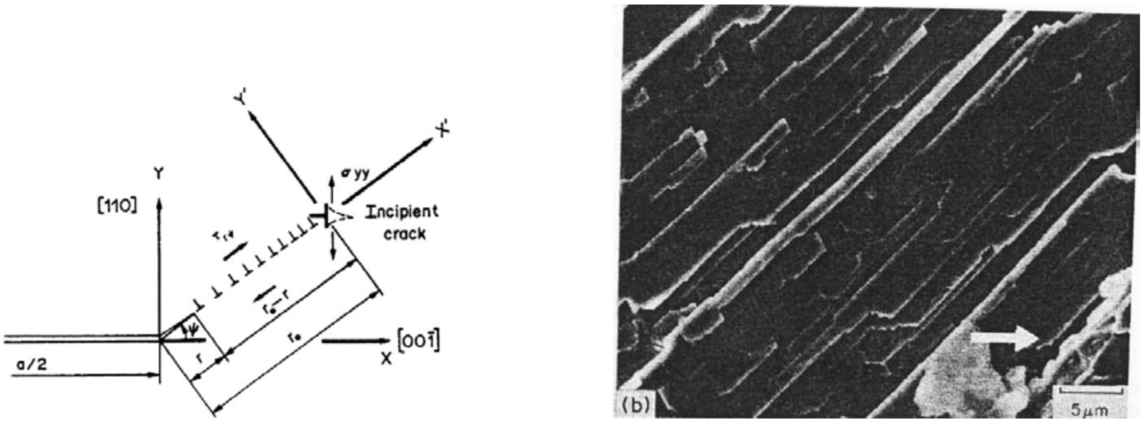
Y'
X'
σ yy
Y
[110]
Incipient
crack
τ
ψ
r₀−r
a/2
r
r₀
[001̄]
X
(b)
5 μm

(a)

(b)

Figure II.9 : Mechanism of transgranular crack propagation (a), and corresponding example of Cu-Al alloy fracture surface (b) –(Flanagan et al., 1991)–

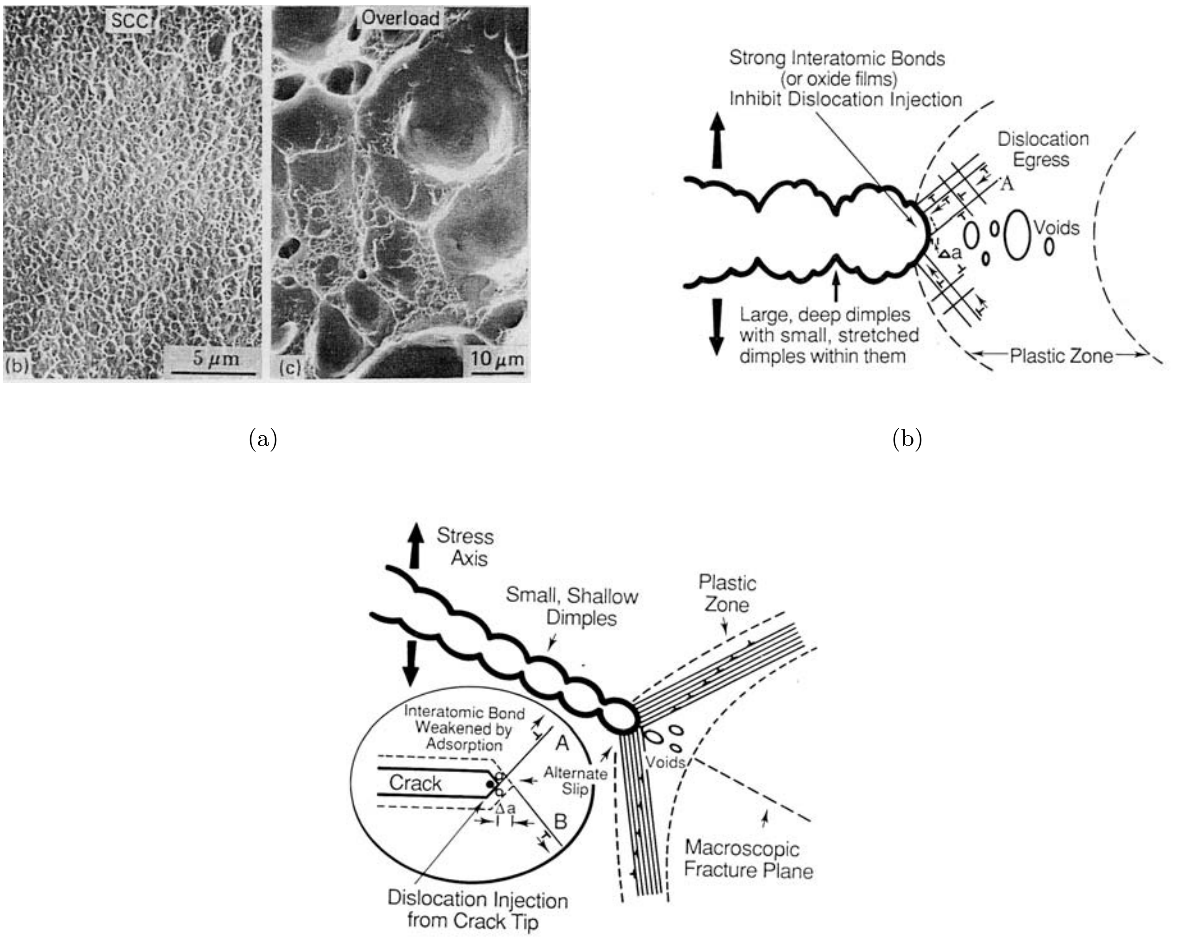
SCC
(b)
5 μm
Overload
(c)
10 μm
Strong Interatomic Bonds
(or oxide films)
Inhibit Dislocation Injection
Dislocation
Egress
A
Δa
Voids
Large, deep dimples
with small, stretched
dimples within them
Plastic Zone
Stress
Axis
Small, Shallow
Dimples
Plastic
Zone
Interatomic Bond
Weakened by
Adsorption
A
Alternate
Slip
Crack
Δa
B
Voids
Macroscopic
Fracture Plane
Dislocation Injection
from Crack Tip

(a)

(b)

(c)

Figure II.10 : (a) - Intercrystalline fracture surfaces produced in Al-Zn-Mg bicrystals (Lynch, 1988); (b) - Scheme of ductile cracking, (c) - Scheme of SCC

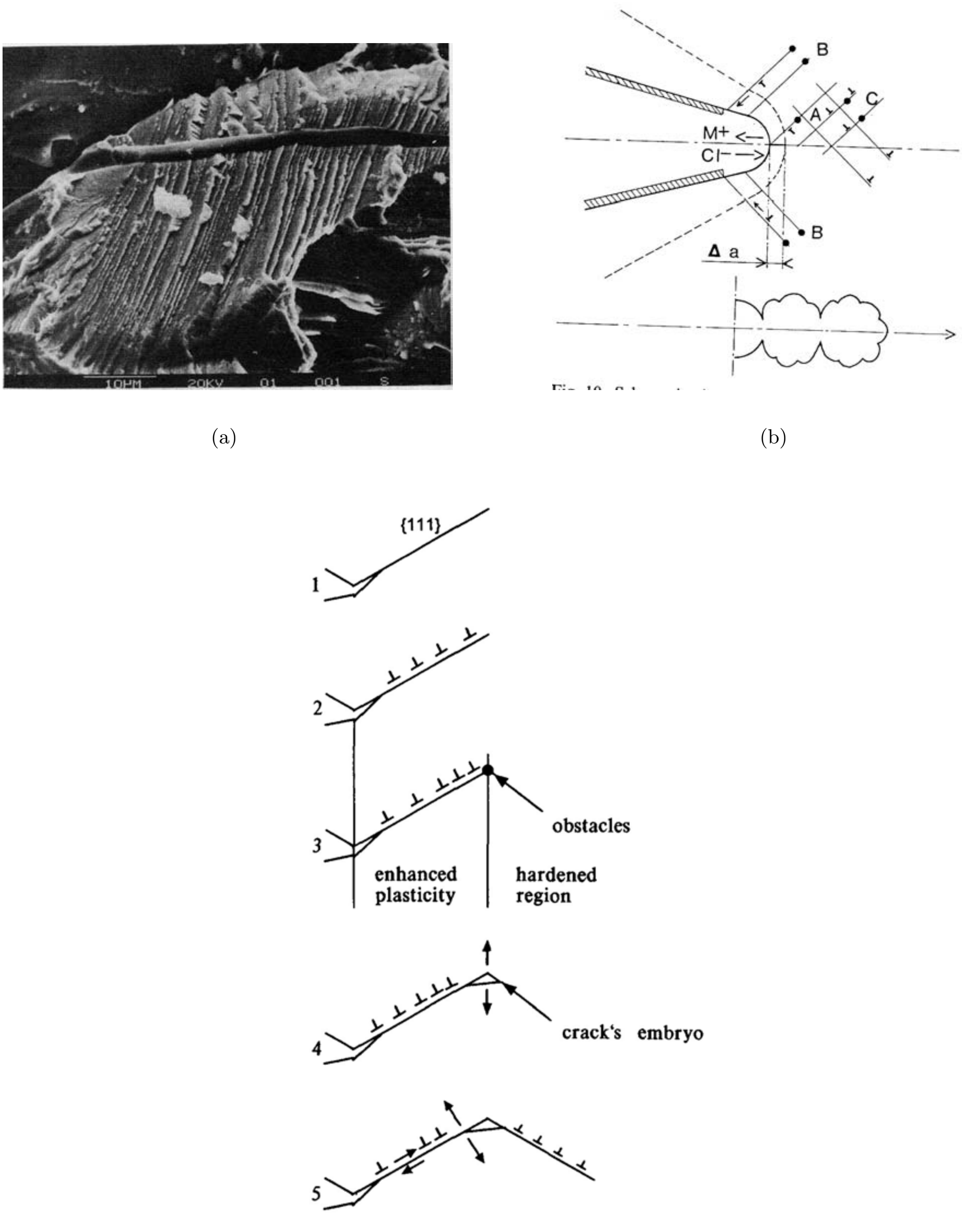
10µm 20KV 01 001 S
B
C
A
M+
Cl−
B
Δ a
a
{111}
1
2
3
obstacles
enhanced plasticity
hardened region
4
crack's embryo
5

(a) (b)

(c)

Figure II.11 : (a) - Discontinuous cleavage for 316 steel in $MgCl_2$ solution (Magnin et al., 1990); (b)(c) - Schema

Intergranular (interface) modeling

A lot of papers dealing with intergranular damage can be found in the literature. They can be divided into the following groups :

1. Asymptotic analysis of the thin layer between two materials. This approach is applied in (Suquet, 1987)(Michel et al., 1994) (Lebon et al., 2004) (Mishuris and Ochsner, 2004). These authors study a plane strain state of two infinite elastic bodies, separated by a thin elasto-visco-plastic layer (of depth δ) –see fig. II.12–.

   The stress-strain state of this structure is studied by an asymptotic method. The basic idea of this method is a presentation of the solution as a series of a small parameter. (layer width in our case). Then some first coefficients of the series have to be found. Usually it is more simple, then to find a whole solution. Keeping only the members of δ^1, it was found that :

   - The stress can be considered as constant in the layer
   - The stress is linearly connected with a displacement jump. The coefficient is defined by the layer material properties. In particular, for elastic-plastic Hencky type material, the following equations were obtained (Mishuris and Ochsner, 2004):

     $$[U_x] = \frac{2\delta}{\tilde{\mu}}\sigma_{xy} \quad [U_y] = \frac{2\delta}{\tilde{\lambda}+2\tilde{\mu}}\sigma_y$$

     Here $\tilde{\mu}$ and $\tilde{\lambda}$ - generalized Lamé coefficients. A similar type of equations was obtained for elasto-viscous material in (Lebon et al., 2004) :

     $$\underset{\sim}{\sigma} \cdot \underline{\mathbf{n}} = \frac{K_L}{\delta}[U] + \frac{K_\theta}{\delta}[\dot{U}]$$

     $$K_L = \begin{pmatrix} \mu & 0 \\ 0 & \lambda + 2\mu \end{pmatrix} \quad K_\theta = \begin{pmatrix} \mu\theta_\mu & 0 \\ 0 & \lambda\theta_\lambda + 2\mu\theta_\mu \end{pmatrix}$$

     where θ_λ and θ_μ are characteristic times.

   A generalized material model is used by (Suquet, 1987) as

   $$\underset{\sim}{\sigma} = k_\delta |\underset{\sim}{\varepsilon}|^{p-2}\underset{\sim}{\varepsilon} = k_\delta \varphi'(\underset{\sim}{\varepsilon})$$

   $$k_\delta = K\delta^\alpha \quad \varphi(\underset{\sim}{\mathbf{e}}) = \frac{|\underset{\sim}{\mathbf{e}}|^p}{p}$$

   This author demonstrates that the solution ($\underset{\sim}{\sigma}^\delta$,$\underline{\mathbf{u}}^\delta$) converges toward ($\underset{\sim}{\sigma}^0$,$\underline{\mathbf{u}}^0$), with

   $$\underset{\sim}{\sigma}^0 = \underset{\approx}{\mathbf{a}} : \underset{\sim}{\varepsilon}(\underline{\mathbf{u}}^0) \quad \text{in} \quad \Omega_+ \cup \Omega_-$$

   $$\nabla \cdot \underset{\sim}{\sigma}^0 + \underline{\mathbf{f}} = 0 \quad \text{in} \quad \Omega$$

   $$\underset{\sim}{\sigma}^0 \cdot \underline{\mathbf{n}} = 0 \quad \text{on S if} \quad \alpha > p - 1$$

   $$\underset{\sim}{\sigma}^0 \cdot \underline{\mathbf{n}} = Kj'([\![\underline{\mathbf{u}}^0]\!]) \quad \text{on S if} \quad \alpha = p - 1$$

   Here the potential $j(\underline{\lambda})$ is defined on S as :

   $$j(\underline{\lambda}) = \varphi({}^{\{}\underline{\lambda} \otimes \underline{\mathbf{n}}^{\}})$$

   $$j'(\underline{\lambda}) = \frac{1}{2}|{}^{\{}\underline{\lambda} \otimes \underline{\mathbf{n}}^{\}}|^{p-2}(\underline{\lambda} + \underline{\lambda} \cdot \underline{\mathbf{nn}})$$

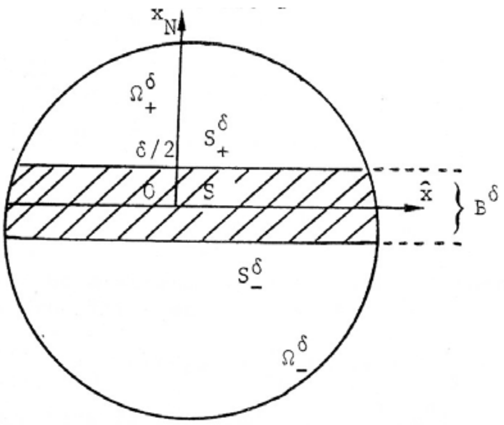

Figure II.12 : Schema of thin layer between two infinite half-spaces. Illustration of the asymptotic approach (Suquet, 1987)

2. Zero-width grain boundary interface. In (Onck and van der Giessen, 1997), the grain boundary is seen as a fictitious layer of linear elastic springs against opening and sliding:

   $$\dot{\sigma}_n = k_n(\dot{\delta} - \dot{\delta}_c)$$

   $$\dot{\tau}_n = k_s(\dot{\gamma} - \dot{\gamma}_s)$$

   Here k_n and k_s - are the elastic stiffnesses of the normal and shearing spring layers, respectively. δ_c is an average grain separation due to cavity growth.

   $$\delta_c = \frac{V}{\pi b^2} \qquad \dot{\delta}_c = \frac{\dot{V}}{\pi b^2} - \frac{2V}{\pi b^2}\frac{\dot{b}}{b}$$

   Grain boundary sliding can be seen as a viscous process :

   $$\dot{\gamma}_s = w\frac{\tau}{\eta}$$

   with w - grain boundary width, and η - viscosity coefficient. Sliding was neglected in (Onck and van der Giessen, 1997).

   In (Needleman, 1987), a nonlinear cohesive law is proposed. The idea comes from classical fracture mechanics works due to Dugdale and Barenblatt. Let $\underline{\mathbf{T}}$ be a force per unit surface on the interface, with

   $$T_n = \underline{\mathbf{n}} \cdot \underline{\mathbf{T}}$$

   $$T_t = \underline{\mathbf{t}} \cdot \underline{\mathbf{T}}$$

   $$T_b = \underline{\mathbf{b}} \cdot \underline{\mathbf{T}}$$

   Let A and B be two points initially on the opposite sides of the interface, and

   $$u_n = \underline{\mathbf{n}} \cdot \Delta\underline{\mathbf{u}}_{AB}$$

   $$u_t = \underline{\mathbf{t}} \cdot \Delta\underline{\mathbf{u}}_{AB}$$

   $$u_b = \underline{\mathbf{b}} \cdot \Delta\underline{\mathbf{u}}_{AB}$$

   The connection between $\underline{\mathbf{T}}$ and $\underline{\mathbf{u}}_{AB}$ are then specified using a potential Φ:

   $$T_n = \frac{\partial\phi}{\partial u_n} \quad T_t = \frac{\partial\phi}{\partial u_t} \quad T_b = \frac{\partial\phi}{\partial u_b}$$

$$\phi(u_n\, u_t\, u_b) = \frac{27}{4}\sigma_{max}\delta \left\{ \frac{1}{2}\left(\frac{u_n}{\delta}\right)^2 \left[1 - \frac{4}{3}\left(\frac{u_n}{\delta}\right) + \frac{1}{2}\left(\frac{u_n}{\delta}\right)^2\right] \right.$$
$$+ \frac{1}{2}\alpha\left(\frac{u_t}{\delta}\right)^2 \left[1 - \frac{u_n}{\delta}\right]^2$$
$$\left. + \frac{1}{2}\alpha\left(\frac{u_b}{\delta}\right)^2 \left[1 - \frac{u_n}{\delta}\right]^2 \right\}$$

3. Viscous regularization.

   As pointed out in (Chaboche et al., 2001), a problem of a jump in the solution can occur while using a rate independent cohesion law. Let us consider a simple 2D example with one interface element and one elastic plate element. Let us consider the total displacement control at the position of BB'. The total displacement U is a sum of the interface separation u and the elastic elongation of a plate element :

   $$U = u + \frac{L}{U_0}T$$

   Here T denotes the applied stress, E_0 – Young's modulus, L the length of the elastic part. The behavior of the interface is described as

   $$T = E \cdot F(u/\delta) \cdot u/\delta$$

   If the stiffness $k = E_0/L$ is high enough, one can expect the solution jump from u_a to u_b –see fig. II.13–.

   One of the possibilities to avoid this problem is to use a rate-dependent interface model. This introduces a so-called viscous regularization, which is used in different branches of mathematical analysis –see for instance (Attouch, 1996) for a review-. In particular, a creep damage equation was used in (Chaboche et al., 1997) to simulate the interface behavior. The corresponding interface model can be written as follows:

   $$\dot{T} = E(1-d)\frac{u}{\delta}$$

   $$\dot{d} = \frac{1}{\tau_0}\left(\frac{T}{A}\right)^r (1-d)^{-s}$$

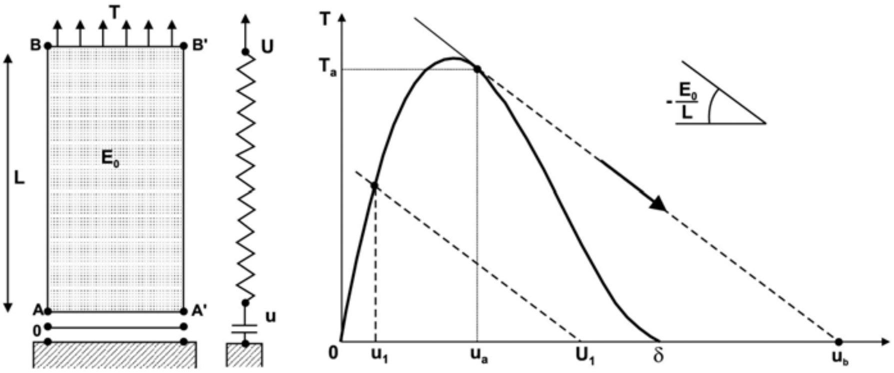

Figure II.13 : Illustration for the jump in the solution (Chaboche et al., 2001)

The choice made in the present study, consists in accepting the continuous formalism of damage mechanics (Lemaitre, 1996), written in terms of stress and strain, keeping in mind that the grain boundary is a highly anisotropic area. It will be modeled in a finite element (FE) mesh by classical elements, with a specific local behavior.

II.1 Damage, Opening and Sliding model

1. Model formulation. The grain boundary (GB) is supposed to be a regular surface. The constitutive equations of the GB will be expressed in a local framework, with the axis x_1 normal to the plane, and axes x_2 and x_3 in the plane of the GB. The constitutive equations should take into account the anisotropy, namely, the GB material should resist to a normal stress, applied in 1 direction, but not in 2 or 3. In the initial implementation, we considered that the material must be very stiff in the normal direction, so that the grains remain pasted in absence of damage. Following the same idea, the moduli must be low in the transverse direction, so that the boundaries do not carry any load and do not perturb the grain equilibrium. As well, GB should accept in-plane shear (12 and 13), but not the 23 shear. These ideas are actually consistent with the "springs" of (Onck and van der Giessen, 1997). Such an anisotropy leads to the special elastic tensor form:

$$\underset{\approx}{\mathbf{\Lambda}} = diag(\mathrm{E}, \eta, \eta, \mu, \eta, \mu) \tag{II.1}$$

where the terms η remain small. Their effect will be neglected in the following, to let the GB just follow the grain behavior for 22, 33 and 23 stress components. Having this anisotropy in mind, the scheme of damage mechanics must be adapted. Introducing only one variable D figuring scalar damage, the classical approach (Lemaitre, 1985)(Lemaitre, 1996) proposes a modification of the elasticity related part of the free energy, so that:

$$\rho\psi_e = \frac{1}{2}(1-D)\underset{\sim}{\varepsilon}_e : \underset{\approx}{\mathbf{\Lambda}} : \underset{\sim}{\varepsilon}_e \tag{II.2}$$

The variable Y energetically conjugated with D is obtained by taking the opposite of the partial derivative of $\rho\psi_e$ with respect to D. Using the previously defined elastic tensor, and preserving only the three predominant terms, it comes:

$$\begin{aligned} Y = -\frac{\partial \rho\psi_e}{\partial D} &= \frac{1}{2}\underset{\sim}{\varepsilon}_e : \underset{\approx}{\mathbf{\Lambda}} : \underset{\sim}{\varepsilon}_e = \frac{1}{2(1-D)^2}\underset{\sim}{\sigma} : \underset{\approx}{\mathbf{\Lambda}}^{-1} : \underset{\sim}{\sigma} \\ &= \frac{1}{2(1-D)^2}\left(\frac{\sigma_{11}^2}{E} + \frac{\sigma_{12}^2+\sigma_{13}^2}{\mu}\right) = \frac{1}{2(1-D)^2}\left(\frac{\sigma_n^2}{E} + \frac{\tau^2}{\mu}\right) \end{aligned}$$

As expected, GB opening δ and GB sliding γ will respectively correspond to σ_n and τ, and D will correspond to Y. In the following, a new variable σ_d will be considered instead of Y:

$$\sigma_d = \sqrt{\sigma_n^2 + \beta\tau^2} = (1-D)\sqrt{2EY} \tag{II.3}$$

In this variable, which is derived from Y, the coefficient β characterizes the ratio E/μ. For a zero value of β, damage will be driven by the normal stress only.

The evolution equations for D, δ and γ are defined in the framework of a viscoplastic multipotential approach, since all the phenomena are rate-dependent. To get correct constitutive equations, respecting the second principle of thermodynamics, it is enough to chose convex potentials for all three variables. These potentials should be dependent on the associated stresses. Norton-like viscous potentials with a threshold are chosen. The potential driving the normal flow depends on the positive part of σ_n, and shear depends on the absolute value of τ:

$$F_n = \frac{K_n}{n_n+1}\left\langle \frac{f_n}{K_n}\right\rangle^{n_n+1} \quad \text{with: } f_n = \frac{<\sigma_n>}{1-D} - R_n \tag{II.4}$$

$$F_t = \frac{K_t}{n_t+1}\left\langle \frac{f_t}{K_t}\right\rangle^{n_t+1} \quad \text{with: } f_t = \frac{|\tau|}{1-D} - R_t \tag{II.5}$$

$$F_d = \frac{K_d}{n_d+1}\left\langle \frac{f_d}{K_d}\right\rangle^{n_d+1} \quad \text{with: } f_d = Y - R_d \tag{II.6}$$

Derivation with respect to the conjugate stresses will immediately give us the flow rules:

$$\underset{\sim}{\dot{\varepsilon}}_n = \frac{\partial F_n}{\partial \underset{\sim}{\sigma}} = \left\langle \frac{< \sigma_n > /(1-D) - R_n}{K_n} \right\rangle^{n_n} (1-D)^{-1} \underline{\mathbf{n}} \otimes \underline{\mathbf{n}} = \dot{\delta} \underset{\sim}{\mathbf{N}} \tag{II.7}$$

$$\underset{\sim}{\dot{\varepsilon}}_t = \frac{\partial F_t}{\partial \underset{\sim}{\sigma}} = \left\langle \frac{|\tau|/(1-D) - R_t}{K_t} \right\rangle^{n_t} (1-D)^{-1} \{\underline{\mathbf{n}} \otimes \underline{\mathbf{t}}\} = \dot{\gamma} \underset{\sim}{\mathbf{T}} \tag{II.8}$$

$$\dot{d} = \frac{\partial F_d}{\partial Y} = \left\langle \frac{Y - R_d}{K_d} \right\rangle^{n_d} \tag{II.9}$$

The internal variable d can be seen as equal to damage D. We will suppose, more generally,

$$\dot{d} = (1-D)^{k-r} \dot{D} \tag{II.10}$$

One can mention, that with $R_d \equiv 0$, $2n_d \equiv r$, $K_d\sqrt{2E} \equiv A$, using D instead of d and σ_d instead of Y, the equation II.9 becomes the classical Kachanov-Rabotnov law for creep damage :

$$\dot{D} = \left(\frac{\sigma_d}{A}\right)^r (1-D)^{-k} \tag{II.11}$$

In the described model, inelastic flow can start without any damage, provided the corresponding stress becomes higher than the threshold. Opening and shear are not coupled as long as no damage exists. On the other hand, either a positive normal stress or a shear stress can develop damage, and have an influence on the sliding and opening rate.

2. Typical stress-strain response of the model. A few results for the stress-strain response of DOS-model are presented here, in order to illustrate the capabilities of the model.

First, typical results of the tension and shear stress components contribution are shown. Strain was imposed, with a few unloadings. In fig. II.14, the loading is an axial strain perpendicular to the grain boundary. As expected, the stress level decreases as damage increases. One can also see from the three unloadings, that the elastic modulus decreases during the tension. In fig. II.15, the previous result is compared with a combined tension-shear loading case. One can see, that the addition of shear makes damage accumulation faster. This is normal, since damage in the model is driven by σ_d , which is a combination of normal and shear stress. Fig. II.16 demonstrates that the roles of σ_{12} and σ_{13} in the model are equivalent. One has now a pure shear test, the first period being with σ_{12} shear, and the second one with σ_{13} shear. The memory of the first loading period is kept during the second period.

3. Evaluation of the energy dissipation. In order to check the relative importance of opening, sliding and damage contribution into the failure mechanism, this section shows the evolution of the energy dissipated by opening during a tension perpendicular to the grain boundary. The energy is computed as $\int(\sigma_n\dot{\delta} + \tau\dot{\gamma})dt$.

Figure II.17 shows the response for a set of material parameters (A = 100000.; r = 4.; k = 3; $R_n = 900$; $K_n = 200$; n = 8) which suppress damage. The energy starts growing when the applied stress reaches R_n . The stress reaches the higher level then $R_n = 900$, because of the viscosity effect. With the parameter set used in the computations of Chapter VII (A = 1000.; r = 4.; k = 3; $R_n = 900$; $K_n = 200$; n = 8) damage starts early, so that the energy associated with opening remains low – see Fig.II.18 – . On the other hand, for the alternative set (A = 5000.; r = 2.; k = 3; $R_n = 10$; $K_n = 750$; n = 8) the energy starts growing at low values of damage –see fig.II.19– The model is then quite sensitive to the physics of the deformation phenomenon. It could be then calibrated by means of experimental data dealing with interface energy.

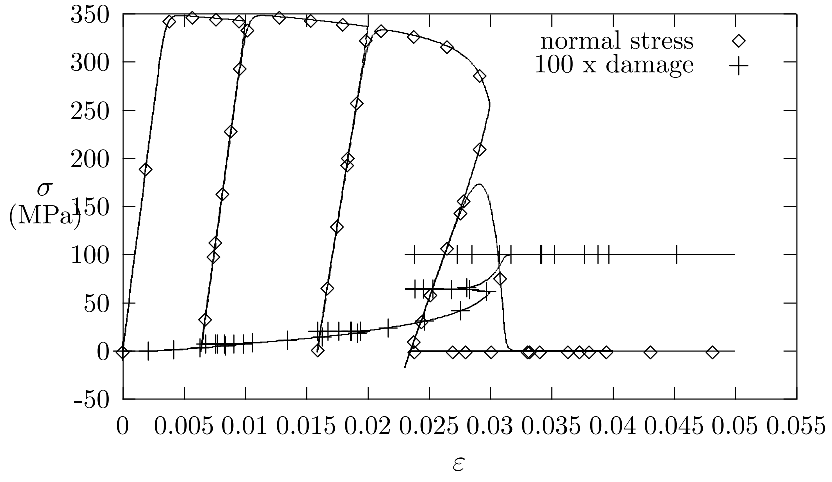

Figure II.14 : DOS model response - tension only

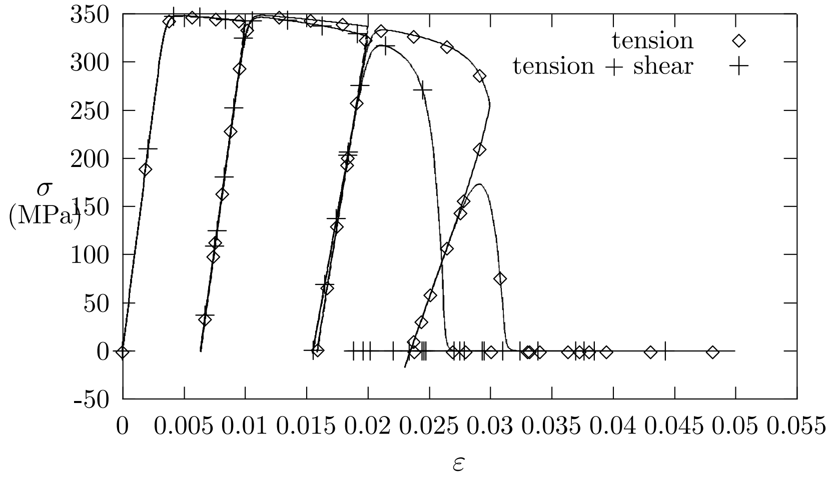

Figure II.15 : DOS model response - tension and shear

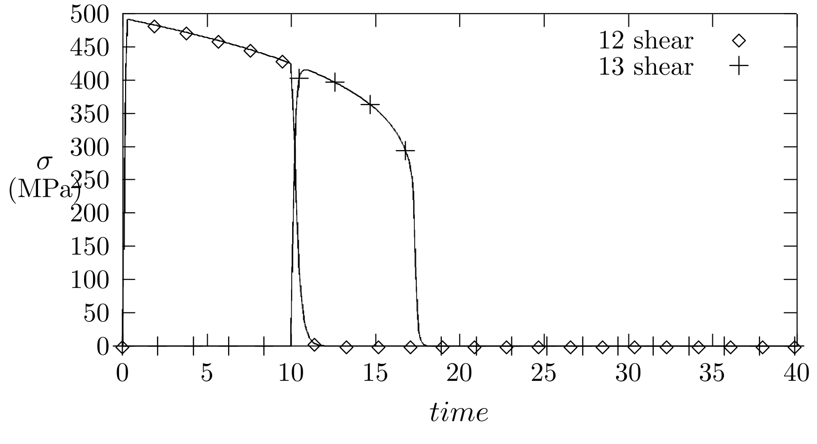

Figure II.16 : DOS model response - shear in 2 directions

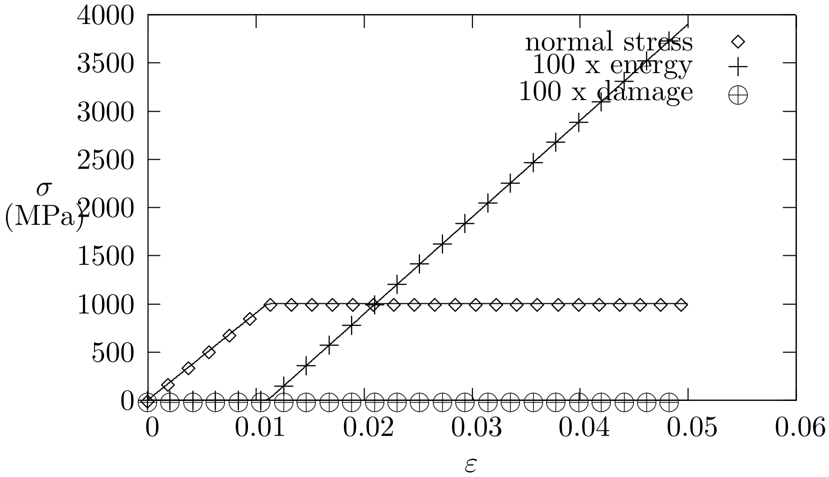

Figure II.17 : DOS model response - parameters used for aggregate computations, iodine is absent

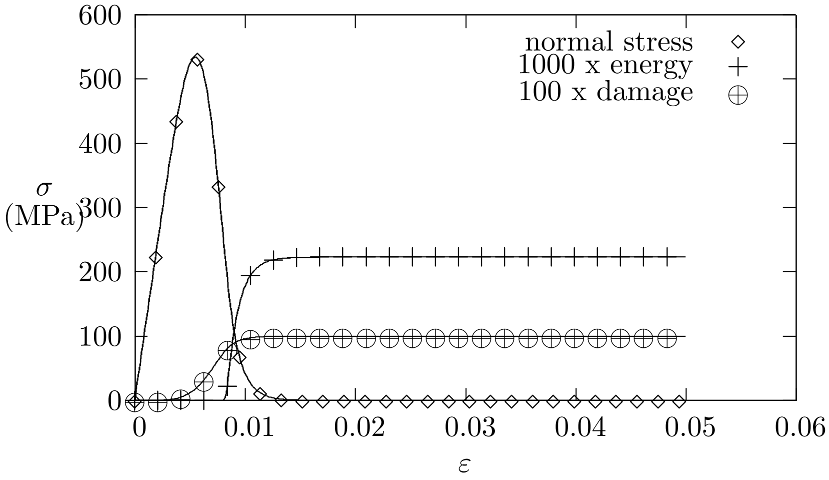

Figure II.18 : DOS model response - parameters used for aggregate computations, iodine is present

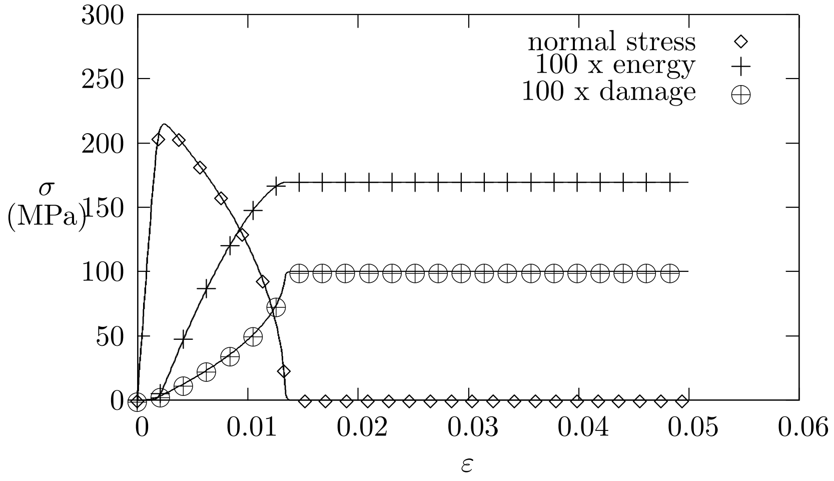

Figure II.19 : DOS model response - parameter which give an "unwanted" result in aggregate computations

II.2 A new strategy for grain boundary modeling

For all the approaches listed in the preceding section, the authors have considered the grain boundary as an interface with distinct material properties. Giving a certain thickness to the grain boundary, as made in (Diard, 2001), offers a possibility for introducing specific mechanisms. Nevertheless, the question of the mechanical properties –even the elastic ones– remains an open problem. A series of difficulties can arise if quantitative data are to be produced by the model. This is why the present work wants to explore a new way of modeling this critical area. The grain boundary will be considered as *two layers*, one in each grain. Figure II.20 illustrates the important difference originating from this concept. Each grain has now its core region, and its grain boundary region. This idea can be found in (Evers et al., 2002) – see fig.II.21 – . In the work of (Evers et al., 2002), the idea is used for a polycrystal type of model. Intoducing of the idea into the direct finite element modelling with real-shaped grains seem to be the priority of the present work. This is a first step toward a more complete modeling, in which the grain could be represented by an "onion-type" mesh, allowing it to present a series of disturbed areas near the boundaries. Having such long and ill-conditioned elements can of course be a problem. Nevertheless, the problem will be reduced when finer and finer meshes are possible. On the other hand, from a numerical point of view, the present strategy offers the opportunity to have several Gauss points not far from the critical area, which is not the case for a cohesive zone model. In the grain boundary element, the behavior is obtained by superposition of several deformation mechanisms. Each half grain boundary has the attributes of the grain it belongs to, plus the DOS model. Two important consequences of this choice will be that :

- non-damaged grain boundaries will naturally give the same results as the classical approach with ideal grain interfaces;
- since the grains are not "equal" with respect to damage, the model will be able to make a difference between damage developing on the one or the other side of the grain boundary.

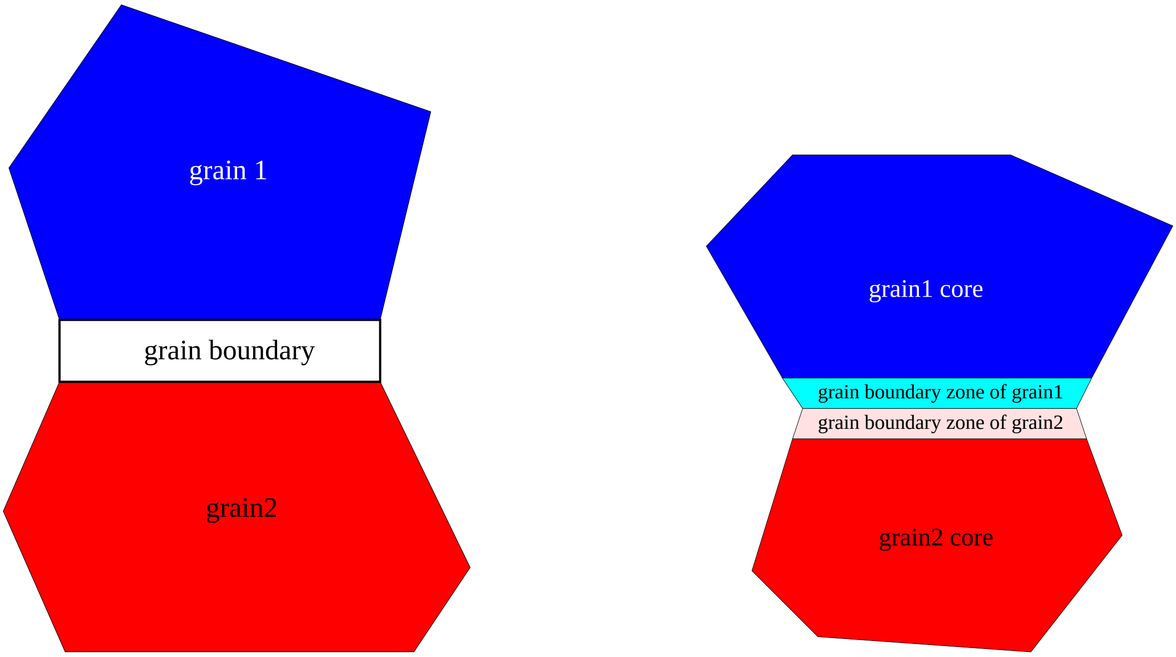
grain 1
grain boundary
grain2
grain1 core
grain boundary zone of grain1
grain boundary zone of grain2
grain2 core

(a) (b)

Figure II.20 : Two visions of the grain boundary : (a) - the grain boundary is a layer of special properties between two grains ; (b) - each grain has its core and its grain boundary region

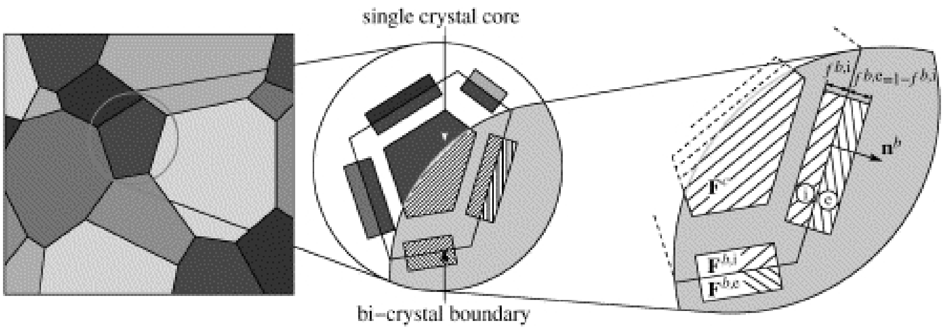
single crystal core
bi−crystal boundary
f^{b,i}
f^{b,e}=1−f^{b,i}
n^b
F^c
i
e
F^{b,i}
F^{b,e}

Figure II.21 : Scheme with grain core and bicrystals at grain boundary (Evers et al., 2002)

Chapter -III-

Finite strains

Contents

III.1 Notations 28
III.2 Elasticity 32
  III.2.1 Models 32
  III.2.2 Consistent tangent matrix 32
  III.2.3 Results 33
III.3 J_2 plasticity 33
  III.3.1 Model 34
  III.3.2 Stress update algorithm 35
  III.3.3 Consistent tangent matrix 36
  III.3.4 Preparation for single crystal 36
  III.3.5 Uniaxial tension test 39
  III.3.6 Billet upsetting test 39
III.4 Crystal plasticity 43
  III.4.1 Model 43
  III.4.2 Numerical implementation problems 44
  III.4.3 Stress update algorithm 45
  III.4.4 Consistent tangent matrix 46
  III.4.5 Single crystal tension test 47
  III.4.6 Polycrystal compression test 48
III.5 Damage, Opening and Sliding 51
  III.5.1 Model 51
  III.5.2 Stress update algorithm 52
  III.5.3 Note on damaged body kinematics under finite strains 52
III.6 Conclusion and Perspectives 52

Since large deformations are present, at least locally, during the failure of the aggregate, it is now necessary to revisit the numerical strategies used in our code. It is then well known that, according to the formalism, curious behaviors can be obtained, as shown for instance in a recent study by (Semenov et al., 2003). A comprehensive description is shown, starting from elasticity and J_2 plasticity. An implicit scheme was successfully applied to this last case; the algorithm is detailed here as well as some computational examples. A crystal plasticity model is then considered. The application of the implicit scheme is detailed. Typical computation results are shown. The final purpose is to apply the chosen formalism –the implicit Euler scheme– to the single crystal model including DOS capabilities.

Notations used under large strains are first defined.

III.1 Notations

- Identity tensor of 2nd order : $\underset{\sim}{\mathbf{I}}$ such that $I_{ij} = \delta_{ij}$
- Identity tensor of 4th order : $\underset{\approx}{\mathbf{I}}$ such that $I_{ijkl} = \frac{1}{2}(\delta_{ik}\delta_{jl} + \delta_{il}\delta_{jk})$

Kinematics :

- Initial coordinates : $\underline{\mathbf{X}}$
- Actual coordinates : $\underline{\mathbf{x}}$
- Deformation gradient tensor : $\underset{\sim}{\mathbf{F}} = \frac{\partial \underline{\mathbf{x}}}{\partial \underline{\mathbf{X}}}$
- Inversed tensor, transposed tensor, inversed and transposed tensor : $\underset{\sim}{\mathbf{F}}^{-1} \quad \underset{\sim}{\mathbf{F}}^{T} \quad \underset{\sim}{\mathbf{F}}^{-T}$
- Volume change factor : $\mathcal{J} = det\underset{\sim}{\mathbf{F}} = \rho_o/\rho$
- Right Cauchy–Green tensor : $\underset{\sim}{\mathbf{C}} = \underset{\sim}{\mathbf{F}}^{T}\underset{\sim}{\mathbf{F}}$ (with $d\underline{\mathbf{x}}_1 \cdot d\underline{\mathbf{x}}_2 = d\underline{\mathbf{X}}_1 \cdot \underset{\sim}{\mathbf{C}} \cdot d\underline{\mathbf{X}}_2$)
- Left Cauchy–Green tensor : $\underset{\sim}{\mathbf{b}} = \underset{\sim}{\mathbf{F}}\underset{\sim}{\mathbf{F}}^{T}$
- Velocity gradient tensor : $\underset{\sim}{\mathbf{L}} = \underset{\sim}{\mathbf{grad}}\,\underline{\mathbf{v}} = \dot{\underset{\sim}{\mathbf{F}}}\underset{\sim}{\mathbf{F}}^{-1}$ (with $d\dot{\underline{\mathbf{x}}} = \underset{\sim}{\mathbf{L}}d\underline{\mathbf{x}} = \dot{\underset{\sim}{\mathbf{F}}}\underset{\sim}{\mathbf{F}}^{-1}d\underline{\mathbf{x}} = \dot{\underset{\sim}{\mathbf{F}}}d\underline{\mathbf{X}}$)
- Strain rate tensor : $\underset{\sim}{\mathbf{D}} = {}^{\{}\underset{\sim}{\mathbf{L}}^{\}}$ (with $\frac{d}{dt}(d\underline{\mathbf{x}}_1.d\underline{\mathbf{x}}_2) = 2d\underline{\mathbf{x}}_1.\underset{\sim}{\mathbf{D}}.d\underline{\mathbf{x}}_2 = d\underline{\mathbf{X}}_1.\dot{\underset{\sim}{\mathbf{C}}}.d\underline{\mathbf{X}}_2$)
- Spin tensor : $\underset{\sim}{\mathbf{\Omega}} = {}^{\}}\underset{\sim}{\mathbf{L}}^{\{}$
- Polar decomposition : $\underset{\sim}{\mathbf{F}} = \underset{\sim}{\mathbf{R}}\underset{\sim}{\mathbf{U}}$ ($\underset{\sim}{\mathbf{R}}$ - rotation, $\underset{\sim}{\mathbf{U}}$ - stretch tensor; one has $\underset{\sim}{\mathbf{C}} = \underset{\sim}{\mathbf{U}}^{T}\underset{\sim}{\mathbf{U}}$)

Strains :

- Green–Lagrange : $\underset{\sim}{\mathbf{E}} = \frac{1}{2}(\underset{\sim}{\mathbf{C}} - \underset{\sim}{\mathbf{I}})$
- Logarithmic : $\underset{\sim}{\mathbf{E}}_o = \log \underset{\sim}{\mathbf{U}}$
- In the case of plasticity, the multiplicative decomposition of the deformation gradient :

$$\underset{\sim}{\mathbf{F}} = \underset{\sim}{\mathbf{F}}^{e}\underset{\sim}{\mathbf{F}}^{p}$$

The derivative of the deformation gradient tensor can be represented as follows :

$$\begin{aligned}
\dot{\underset{\sim}{\mathbf{F}}} =& \dot{\underset{\sim}{\mathbf{F}}}^{e}\underset{\sim}{\mathbf{F}}^{p} + \underset{\sim}{\mathbf{F}}^{e}\dot{\underset{\sim}{\mathbf{F}}}^{p} \\
\underset{\sim}{\mathbf{L}} =& \dot{\underset{\sim}{\mathbf{F}}}\underset{\sim}{\mathbf{F}}^{-1} = \dot{\underset{\sim}{\mathbf{F}}}^{e}\underset{\sim}{\mathbf{F}}^{p}\underset{\sim}{\mathbf{F}}^{p-1}\underset{\sim}{\mathbf{F}}^{e-1} + \underset{\sim}{\mathbf{F}}^{e}\dot{\underset{\sim}{\mathbf{F}}}^{p}\underset{\sim}{\mathbf{F}}^{p-1}\underset{\sim}{\mathbf{F}}^{e-1} \\
\underset{\sim}{\mathbf{L}} =& \dot{\underset{\sim}{\mathbf{F}}}^{e}\underset{\sim}{\mathbf{F}}^{e-1} + \underset{\sim}{\mathbf{F}}^{e}\dot{\underset{\sim}{\mathbf{F}}}^{p}\underset{\sim}{\mathbf{F}}^{p-1}\underset{\sim}{\mathbf{F}}^{e-1}
\end{aligned}$$

- one can keep the following definition for velocity gradient in plasticity : $\underset{\sim}{\mathbf{L}}^{p} = \dot{\underset{\sim}{\mathbf{F}}}^{p}\underset{\sim}{\mathbf{F}}^{p-1}$

Stresses :

- Stress tensor of Cauchy : $\underset{\sim}{\sigma}$
- Stress tensor of Piola–Kirchhoff PK2 : $\underset{\sim}{\mathbf{S}} = \mathcal{J}\underset{\sim}{\mathbf{F}}^{-1}\underset{\sim}{\sigma}\underset{\sim}{\mathbf{F}}^{-T}$
- Stress tensor of Piola–Kirchhoff PK1 : $\underset{\sim}{\mathbf{\Pi}} = \mathcal{J}\underset{\sim}{\sigma}\underset{\sim}{\mathbf{F}}^{-T}$
- Stress tensor of Hencky : $\underset{\sim}{\mathbf{T}} = \mathcal{J}\underset{\sim}{\mathbf{R}}^{T}\underset{\sim}{\sigma}\underset{\sim}{\mathbf{R}}$

The power by mass unit can be written as

$$\frac{1}{\rho}\underset{\sim}{\sigma} : \underset{\sim}{\mathbf{D}} = \frac{1}{\rho_o}\underset{\sim}{\mathbf{S}} : \dot{\underset{\sim}{\mathbf{E}}} = \frac{1}{\rho_o}\underset{\sim}{\mathbf{\Pi}} : \dot{\underset{\sim}{\mathbf{F}}} = \frac{1}{\rho}\underset{\sim}{\mathbf{T}} : \dot{\underset{\sim}{\mathbf{E}}}_{\mathbf{o}}$$

Stress rates :

- Jauman rate: $\underset{\sim}{\mathbf{T}}^{J} = \dot{\underset{\sim}{\mathbf{T}}} + \underset{\sim}{\mathbf{T}}\underset{\sim}{\mathbf{\Omega}} - \underset{\sim}{\mathbf{\Omega}}\underset{\sim}{\mathbf{T}}$

- Truesdell rate: $\underset{\sim}{\mathbf{T}}^{\nabla} = \dot{\underset{\sim}{\mathbf{T}}} - \underset{\sim}{\mathbf{L}}\underset{\sim}{\mathbf{T}} - \underset{\sim}{\mathbf{T}}\underset{\sim}{\mathbf{L}}^{T} + \underset{\sim}{\mathbf{T}}\,\mathrm{Tr}\,\underset{\sim}{\mathbf{L}}$

The matrices $[M_L]$ et $[M_R]$ are introduced, to perform left and right multiplication, so that:

$$\{\underset{\sim}{\mathbf{a}}.\underset{\sim}{\mathbf{b}}\} = \left[M_L(\underset{\sim}{\mathbf{a}})\right].\{\underset{\sim}{\mathbf{b}}\} \tag{III.1}$$

$$\{\underset{\sim}{\mathbf{b}}.\underset{\sim}{\mathbf{a}}\} = \left[M_R(\underset{\sim}{\mathbf{a}})\right].\{\underset{\sim}{\mathbf{b}}\} \tag{III.2}$$

Here $\underset{\sim}{\mathbf{a}}$ and $\underset{\sim}{\mathbf{b}}$ – the arbitrary 2nd order tensors. The matrices $[M_L]$ and $[M_R]$ are linear with respect to tensor $\underset{\sim}{\mathbf{a}}$. The matrix $[M_L]$ (resp. $[M_L]$) is such that the result of the multiplication by the tensor $\underset{\sim}{\mathbf{b}}$ in Voigt notation, provides the tensor $\underset{\sim}{\mathbf{a}}.\underset{\sim}{\mathbf{b}}$ (resp. $\underset{\sim}{\mathbf{b}}.\underset{\sim}{\mathbf{a}}$) in Voigt notation. One has the following relations:

$$(1) \qquad \left[M_L(\underset{\sim}{\mathbf{a}}^T)\right]^T = \left[M_L(\underset{\sim}{\mathbf{a}})\right] \tag{III.3}$$

$$(2) \qquad \left[M_R(\underset{\sim}{\mathbf{a}}^T)\right]^T = \left[M_R(\underset{\sim}{\mathbf{a}})\right] \tag{III.4}$$

$$(3) \qquad [T]^T = [T] \tag{III.5}$$

$$(4) \qquad \text{if } \underset{\sim}{\mathbf{a}} = \underset{\sim}{\mathbf{a}}^T \text{ then } \left[M_L(\underset{\sim}{\mathbf{a}})\right]^T = \left[M_L(\underset{\sim}{\mathbf{a}})\right] \tag{III.6}$$

$$(5) \qquad \text{if } \underset{\sim}{\mathbf{a}} = \underset{\sim}{\mathbf{a}}^T \text{ then } \left[M_R(\underset{\sim}{\mathbf{a}})\right]^T = \left[M_R(\underset{\sim}{\mathbf{a}})\right] \tag{III.7}$$

Virtual power principle : In the absolute (Galilean) space at any time for any system, the virtual power of all the loads (internal and external) is equal to zero for any virtual displacement.

It can be written in different terms and for different configurations of the deformed body, in particular:

$$-\int_{\Omega} \underset{\sim}{\sigma} : \underset{\sim}{\mathbf{D}} d\Omega + \int_{\Omega} \underline{\mathbf{f}} \cdot \underline{\mathbf{V}} d\Omega + \int_{\partial\Omega} \underline{\mathbf{T}} \cdot \underline{\mathbf{V}} dS = 0$$

$$-\int_{\Omega_0} \underset{\sim}{\mathbf{\Pi}} : \dot{\underset{\sim}{\mathbf{F}}} d\Omega_0 + \int_{\Omega_0} \underline{\mathbf{f}}_0 \cdot \underline{\mathbf{V}} d\Omega_0 + \int_{\partial\Omega_0} \underline{\mathbf{T}}_0 \cdot \underline{\mathbf{V}} dS_0 = 0$$

$$-\int_{\Omega_0} \underset{\sim}{\mathbf{S}} : \dot{\underset{\sim}{\mathbf{E}}} d\Omega_0 + \int_{\Omega_0} \underline{\mathbf{f}}_0 \cdot \underline{\mathbf{V}} d\Omega_0 + \int_{\partial\Omega_0} \underline{\mathbf{T}}_0 \cdot \underline{\mathbf{V}} dS_0 = 0$$

$$-\int_{\Omega_t} \underset{\sim}{\mathbf{S}}_t^{t+\Delta t} : \dot{\underset{\sim}{\mathbf{E}}}_t^{t+\Delta t} d\Omega_t + \int_{\Omega_t} \underline{\mathbf{f}}_t \cdot \underline{\mathbf{V}} d\Omega_t + \int_{\partial\Omega_t} \underline{\mathbf{T}}_t \cdot \underline{\mathbf{V}} dS_t = 0$$

Depending on the reference used for the material behavior, the correspondent finite element formulation differs (Bathe, 1996). The formulation is called *total lagrangian*, if the initial reference is used. On the other hand, if the reference at the beginning of the current intergration step is used, the formulation is called *updated lagrangian*.

First principle of thermodynamics or the law of energy conservation.

$$\dot{E} + \dot{K} = P^e + Q$$

Here E - internal energy, K - kinetic energy, Q - rate of incoming heat, P^e - power of external forces (surface or volumetric).

$$K = \frac{1}{2}\int_{\Omega} \underline{\mathbf{V}} \cdot \underline{\mathbf{V}} d\Omega$$

$$E = \int_{\Omega} \rho e d\Omega = \int_{\Omega_0} \rho_0 e d\Omega_0$$

$$Q = \int_{\Omega} \rho r d\Omega - \int_{\partial\Omega} \underline{\mathbf{q}} \cdot \underline{\mathbf{n}} dS$$

Finally, using the result of the virtual power principle, one has :

$$\rho\dot{e} = \underset{\sim}{\sigma} : \underset{\sim}{\mathbf{D}} + \rho r - \nabla \cdot \underline{\mathbf{q}}$$

Second principle of thermodynamics : the rate of change of the internal entropy is not less than the rate of entropy supplied by external heat sources.

$$\dot{S} \geq \int \frac{\rho r}{T} d\Omega - \int \frac{\underline{\mathbf{q}} \cdot \underline{\mathbf{n}}}{T} dS$$

The local form of this Clausius-Duhem inequality is

$$\rho\dot{s} \geq \frac{r}{T} - \frac{1}{T}\nabla \cdot \underline{\mathbf{q}}$$

Combination of the first and second laws of thermodynamics gives :

$$-\rho(\dot{e} - T\dot{s}) - \frac{\underline{\mathbf{q}}}{T} \cdot \nabla T + \underset{\sim}{\sigma} : \underset{\sim}{\mathbf{D}} \geq 0$$

Let us introduce the *free energy*, by $\Psi = e - Ts$. The inequality can be rewritten as :

$$-\rho(\dot{\Psi} + s\dot{T}) + \underset{\sim}{\sigma} : \underset{\sim}{\mathbf{D}} - \frac{\underline{\mathbf{q}}}{T} \cdot \nabla T \geq 0$$

The following combination is called *internal dissipation* :

$$\Phi = \underset{\sim}{\sigma} : \underset{\sim}{\mathbf{D}} - \rho(\dot{\Psi} + s\dot{T})$$

Let us suppose now, $\Psi = \Psi(\underset{\sim}{\mathbf{E}}^*_e;\alpha_i;T)$ with $\underset{\sim}{\mathbf{E}}^*_e$ - any elastic strain measure, α_i - internal variables. It comes,

$$\underset{\sim}{\sigma} : \underset{\sim}{\mathbf{D}} - \rho\frac{\partial\Psi}{\partial\underset{\sim}{\mathbf{E}}^*}\dot{\underset{\sim}{\mathbf{E}}}^* - \rho(s + \frac{\partial\Psi}{\partial T})\dot{T} - \rho\frac{\partial\Psi}{\partial\alpha_i}\dot{\alpha}_i - \frac{\underline{\mathbf{q}}}{T} \cdot \nabla T \geq 0$$

Let us see two particular choices of strain measure : Green-Lagrange strain ($\underset{\sim}{\mathbf{E}} = \frac{1}{2}(\underset{\sim}{\mathbf{F}}^T\underset{\sim}{\mathbf{F}} - \underset{\sim}{\mathbf{I}}$) and logarithmic Hencky strain ($\underset{\sim}{\mathbf{H}} = ln\underset{\sim}{\mathbf{U}}$).

1. Green-Lagrange strain. The development is rather well-known – see for instance (Besson et al., 2001) –

   Let us introduce $\underset{\sim}{\mathbf{S}}^e = \mathcal{J}\underset{\sim}{\mathbf{F}}_e^{-1}\underset{\sim}{\sigma}\underset{\sim}{\mathbf{F}}_e^{-T}$. Let us also suppose the multiplicative strain decomposition $\underset{\sim}{\mathbf{F}} = \underset{\sim}{\mathbf{F}}^e\underset{\sim}{\mathbf{F}}^p$. The stress energy can be written as :

   $$\frac{1}{\rho}\underset{\sim}{\sigma} : \underset{\sim}{\mathbf{D}} = \frac{1}{\rho_0}(\underset{\sim}{\mathbf{S}}^e : \dot{\underset{\sim}{\mathbf{E}}}_e + (\underset{\sim}{\mathbf{F}}_e^T\underset{\sim}{\mathbf{F}}_e\underset{\sim}{\mathbf{S}}^e) : (\dot{\underset{\sim}{\mathbf{F}}}_p\underset{\sim}{\mathbf{F}}_p^{-1}))$$

   Let us introduce the free energy as $\Psi = \Psi(\underset{\sim}{\mathbf{E}}_e;\alpha_i;T)$. The Clausius-Duhem inequality can be rewritten as :

   $$\rho(\frac{\underset{\sim}{\mathbf{S}}^e}{\rho_0} - \frac{\partial\Psi}{\partial\underset{\sim}{\mathbf{E}}_e}) : \dot{\underset{\sim}{\mathbf{E}}}_e - \rho(s + \frac{\partial\Psi}{\partial T})\dot{T} - -\rho\frac{\partial\Psi}{\partial\alpha_i}\dot{\alpha}_i + \rho(\underset{\sim}{\mathbf{F}}_e^T\underset{\sim}{\mathbf{F}}_e\frac{\underset{\sim}{\mathbf{S}}^e}{\rho_0}) : (\dot{\underset{\sim}{\mathbf{F}}}_p\underset{\sim}{\mathbf{F}}_p^{-1}) - \frac{\underline{\mathbf{q}}}{T} \cdot \nabla T \geq 0$$

   It follows :

   $$\frac{\underset{\sim}{\mathbf{S}}^e}{\rho_0} - \frac{\partial\Psi}{\partial\underset{\sim}{\mathbf{E}}_e} = 0$$

   $$s + \frac{\partial\Psi}{\partial T} = 0$$

$$\underset{\sim}{\mathbf{\Sigma}} : (\dot{\underset{\sim}{\mathbf{F}}}_p \underset{\sim}{\mathbf{F}}_p^{-1}) + X_i \cdot \dot{\alpha}_i \geq 0$$

Here $\underset{\sim}{\mathbf{\Sigma}} = \frac{1}{i\rho_0}(\underset{\sim}{\mathbf{F}}_e^T \underset{\sim}{\mathbf{F}}_e \underset{\sim}{\mathbf{S}}^e)$ - is the Mandel stress tensor. The last inequality is automatically met, if there exists a potential $\Omega(\underset{\sim}{\mathbf{\Sigma}};X_i)$, such that

$$\dot{\underset{\sim}{\mathbf{F}}}_p \underset{\sim}{\mathbf{F}}_p^{-1} = \frac{\partial \Omega}{\partial \underset{\sim}{\mathbf{\Sigma}}}$$

$$\dot{\alpha}_i = \frac{\partial \Omega}{\partial X_i}$$

2. Logarithmic strain. One can suppose that

$$\dot{\underset{\sim}{\mathbf{H}}} = \underset{\approx}{\mathbf{P}} : \dot{\underset{\sim}{\mathbf{F}}} \qquad \underset{\sim}{\mathbf{T}} = \underset{\sim}{\mathbf{\Pi}} : \underset{\approx}{\mathbf{P}}^{-1}$$

Under such a condition, the stress energy can be rewritten :

$$\underset{\sim}{\sigma} : \underset{\sim}{\mathbf{D}} = \underset{\sim}{\mathbf{T}} : \dot{\underset{\sim}{\mathbf{H}}}$$

One can also suppose that

$$\underset{\sim}{\mathbf{H}}^e = \frac{1}{2} ln \underset{\sim}{\mathbf{C}} - \underset{\sim}{\mathbf{H}}^p$$

$$\Psi = \Psi(\underset{\sim}{\mathbf{H}}^e;\alpha_i;T)$$

Under these assumptions one can proceed in a similar manner as in the Green-Lagrange strain case, in order to obtain a thermodynamically consistent fully anisotropic elasto-plasticity theory.

Two points should be mentioned :

- The logarithmic decomposition[1] is – generally speaking – not the same, as the multiplicative decomposition $\underset{\sim}{\mathbf{F}} = \underset{\sim}{\mathbf{F}}^e \underset{\sim}{\mathbf{F}}^p$. Nevertheless, for the special case of coaxial total and plastic deformations (i.e. $\underset{\sim}{\mathbf{R}}^e = 0$; such a model is seen below, in section III.3) the multiplicative and logarithmic additive decompositions are equivalent. In this sense logarithmic ansatz can be seen as "close" to the multiplicative one.
- The representation of the stress $\underset{\sim}{\mathbf{T}}$, conjugate to the logarithmic strain measure, is quite complex. But it is already done in (Hoger, 1987) or (Miehe and Lambrecht, 2001).

The logarithmic framework was successfully used for computations in (Papadopoulos and Lu, 1998)(Papadopoulos and Lu, 2001)(Miehe et al., 2002) The results have been found close to those obtained by the use of the multiplicative ansatz.

---

[1] let us also use the term "ansatz" instead – it can be found in (Miehe et al., 2002) for instance – Strictly speaking, "ansatz" is more general, then "decomposition", but it is more compact.

III.2 Elasticity

The theory of finite elastic deformations is quite well developed at the moment. There are a lot of models, even with the condition for each theory to become the classical Hooke's law under small strains. Theoretical frameworks will be found in monographs like (Lurie, 1990)(Truesdell, 1972)(Marsden and Hughes, 1983). Computational aspects are discussed for instance in (Bonet and Wood, 1997) (Belytschko et al., 2000). The purpose of the section is to check the validity of various implementation, and to tests them into ZéBuLoN. It can be seen as an exercise, known from the literature, but necessary for understanding the code possibilities and the way to use them. Note that all the models will use an hyperelastic formulation. The hypoelastic formulation using Jauman derivative in the corotational frame was already available in ZéBuLoN.

III.2.1 Models

Three models, rather well known from the literature, were taken: Neo–Hooke, Green–Lagrange, and Hencky (logarithmic) elasticity. They were chosen as simple, and known to be convenient for metals (Anand, 1979)(Anand, 1986). Green–Lagrange is classically used for single crystal, and Hencky is more popular for polycrystals.

- Neo-Hooke compressible law

  The following formulations can be found –see for instance (Bonet and Wood, 1997)(Belytschko et al., 2000):

$$\underset{\sim}{\mathbf{S}} = \mu(\underset{\sim}{\mathbf{I}} - \underset{\sim}{\mathbf{C}}^{-1}) + \lambda ln\mathcal{J}\underset{\sim}{\mathbf{C}}^{-1}$$

$$\underset{\sim}{\sigma} = \frac{\mu}{\mathcal{J}}(\underset{\sim}{\mathbf{b}} - \underset{\sim}{\mathbf{I}}) + \frac{\lambda}{\mathcal{J}} ln\mathcal{J}\underset{\sim}{\mathbf{I}}$$

  Different examples are given in (Simo and Hughes, 1997):

$$\underset{\sim}{\mathbf{S}} = \mu(\underset{\sim}{\mathbf{I}} - \underset{\sim}{\mathbf{C}}^{-1}) + \lambda\frac{\mathcal{J}^2 - 1}{2}\underset{\sim}{\mathbf{C}}^{-1}$$

$$\underset{\sim}{\tau} = \mu(\underset{\sim}{\mathbf{b}} - \underset{\sim}{\mathbf{I}}) + \lambda\frac{\mathcal{J}^2 - 1}{2}\underset{\sim}{\mathbf{I}}$$

- Green-Lagrange

$$\underset{\sim}{\mathbf{S}} = \underset{\approx}{\mathbf{L}} : \underset{\sim}{\mathbf{E}}$$

- Logarithmic (Hencky)

$$\underset{\sim}{\sigma} = \frac{1}{\mathcal{J}}\underset{\approx}{\mathbf{L}} : log\underset{\sim}{\mathbf{V}}$$

III.2.2 Consistent tangent matrix

As mentioned in (Belytschko et al., 2000), for updated Lagrangian formulation the material tangent stiffness is nothing but the Truesdell tangent, $\underset{\approx}{\mathbf{C}}_{Tru}$, connecting Truesdell stress rate and strain rate tensors:

$$\underset{\sim}{\tau}^{\nabla} = \underset{\approx}{\mathbf{C}}_{Tru} : \underset{\sim}{\mathbf{D}}$$

For total Lagrangian formulation, the same role is played by $\underset{\approx}{\mathbf{C}}_{SE}$,

$$\dot{\underset{\sim}{\mathbf{S}}} = \underset{\approx}{\mathbf{C}}_{SE} : \dot{\underset{\sim}{\mathbf{E}}}$$

One can mention the relation between them (Belytschko et al., 2000)

$$\underset{\approx}{\mathbf{C}}_{Tru} = \frac{1}{\mathcal{J}} F_{im} F_{jn} F_{kp} F_{lq} C^{SE}_{mnpq}$$

It is then enough to know just one of them, to easily develop both updated and total Lagrangian integration schemes.

For the three just mentioned laws the tangent modulus formulae can be found in literature ((Bonet and Wood, 1997)(Simo and Hughes, 1997)). They are as follows:

$$\underset{\approx}{\mathbf{C}}_{Tru} = \frac{\lambda}{\mathcal{J}} \underset{\sim}{\mathbf{I}} \otimes \underset{\sim}{\mathbf{I}} + \frac{2}{\mathcal{J}} (\mu - \lambda ln\mathcal{J}) \underset{\approx}{\mathbf{I}}$$

$$\underset{\approx}{\mathbf{C}}_{Tru} = \frac{\lambda}{\mathcal{J}} \underset{\sim}{\mathbf{I}} \otimes \underset{\sim}{\mathbf{I}} + \frac{1}{\mathcal{J}} (2\mu + \lambda(1 - \mathcal{J}^2)) \underset{\approx}{\mathbf{I}}$$

$$\underset{\approx}{\mathbf{C}}_{SE} = \underset{\approx}{\mathbf{L}}$$

$$\underset{\approx}{\mathbf{C}}_{Tru} = \frac{1}{\mathcal{J}} \underset{\approx}{\mathbf{L}} : \frac{\partial ln \underset{\sim}{\mathbf{V}}}{\partial \underset{\sim}{\mathbf{b}}} : \frac{\partial \underset{\sim}{\mathbf{b}}}{\partial \underset{\sim}{\mathbf{D}}} - \underset{\approx}{\mathbf{M}}_L(\underset{\sim}{\sigma}) - \underset{\approx}{\mathbf{M}}_R(\underset{\sim}{\sigma})$$

III.2.3 Results

The present model have been implemented as plugins of the ZéBuLoN code. The source code is self explanatory; it is shown in Appendix B . Force displacement curves of tension test till 100% for isotropic material (E=200000 MPa, $\nu = 0.33$) are presented in fig. III.1. The computations can be done in quite a few steps (10 steps, or even 1). Typical convergence was as follows:

```
seq:  1 incr:  1 dt:10       t:10
 iter:  1 | R |/| Fext |= 2.452e-02  | Fext |=11125.345426
 iter:  2 | R |/| Fext |= 3.512e-06  | Fext |=11273.790976
 iter:  3 | R |/| Fext |= 7.494e-14  | Fext |=11273.768911
```

The ratio of global residual to external loading (| R |/| Fext |) is seen to converge to zero with a quadratic rate of convergence[2].

III.3 J$_2$ plasticity

The theories of elasto-(visco)-plasticity in finite strains are still being in discussion, as seen for example in (Idesman, 2003)(Nedjar, 2002a)(Nedjar, 2002b)(Xiao et al., 2000). On the other hand, effective numerical algorithms for some particular theories are already available since (Weber and Anand, 1990),(Moran et al., 1990) and (Eterovic and Bathe, 1990). The purpose of this section is –just as in the previous exercise with elasticity– to implement up-to-date solution methods in large strain elasto-plastic modelling. For that purpose, a particular model of J$_2$-plasticity and the appropriate numerical approach were taken from (Weber and Anand, 1990) and implemented into finite element code ZéBuLoN. A series of numerical tests, taken from the literature, are performed to show the formulation effectiveness.

---

[2] Variable x_i is said to have convergence of order p to the limit x , if there is c, 0<c<1, such as

$$||x_{i+1} - x|| \leq c||x_k - x||^p \quad k = 0, 1, ..i$$

If $p = 1$, convergence is linear, for $p = 2$ – quadratic

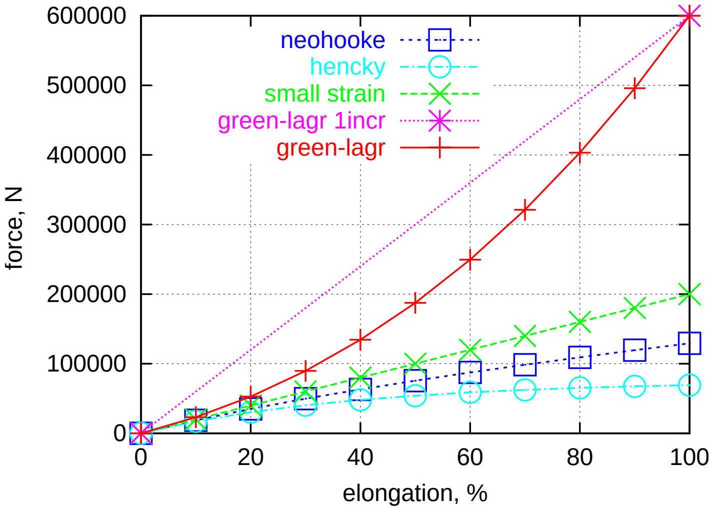

Figure III.1 : Elastic tension test. Force-elongation curves.

III.3.1 Model

The multiplicative decomposition of strain gradient is used,

$$\underset{\sim}{\mathbf{F}} = \underset{\sim}{\mathbf{F}}_e \underset{\sim}{\mathbf{F}}_p$$

For elastic part, the elastic strain is calculated

$$\underset{\sim}{\mathbf{F}}_e = \underset{\sim}{\mathbf{R}}_e \underset{\sim}{\mathbf{U}}_e$$

$$\underset{\sim}{\mathbf{E}}_e = ln \underset{\sim}{\mathbf{U}}_e$$

The elastic strain is connected to the energetically conjugated stress $\underset{\sim}{\mathbf{T}}$ by Hook's law:

$$\underset{\sim}{\mathbf{T}} = \underset{\approx}{\mathbf{L}} : \underset{\sim}{\mathbf{E}}_e$$

$$\underset{\sim}{\mathbf{T}} = \mathcal{J} \underset{\sim}{\mathbf{R}}^T \underset{\sim}{\sigma} \underset{\sim}{\mathbf{R}}$$

Once the yield criterion

$$f(\underset{\sim}{\mathbf{T}}) = \mathcal{J}(\underset{\sim}{\mathbf{T}}) - R(p)$$

is satisfied, the plastic part appears

$$\underset{\sim}{\mathbf{L}}_p = \dot{\underset{\sim}{\mathbf{F}}}_p \underset{\sim}{\mathbf{F}}_p^{-1}$$

Only the symmetric part is preserved, which is as follows :

$$\underset{\sim}{\mathbf{D}}_p = \dot{p} \underset{\sim}{\mathbf{N}}$$

$$\underset{\sim}{\mathbf{N}} = \frac{3}{2} \frac{dev \underset{\sim}{\mathbf{T}}}{\sigma} = \frac{\partial \mathcal{J}}{\partial \underset{\sim}{\mathbf{T}}}$$

$$\mathcal{J}^2 = \frac{3}{2} dev \underset{\sim}{\mathbf{T}} : dev \underset{\sim}{\mathbf{T}}$$

III.3.2 Stress update algorithm

According to the expression of $\dot{\underset{\sim}{\mathbf{F}}}_p = \underset{\sim}{\mathbf{L}}_p \underset{\sim}{\mathbf{F}}_p$, the result of the integration is

$$\underset{\sim}{\mathbf{F}}_p = exp(\Delta t \underset{\sim}{\mathbf{L}}_p) \underset{\sim}{\mathbf{F}}_p(t)$$

We state :

$$\underset{\sim}{\mathbf{F}}_{tr} = \underset{\sim}{\mathbf{F}} \underset{\sim}{\mathbf{F}}_p^{-1}(t)$$

The elastic part of gradient transformation is then :

$$\underset{\sim}{\mathbf{F}}_e = \underset{\sim}{\mathbf{F}} \underset{\sim}{\mathbf{F}}_p^{-1} = \underset{\sim}{\mathbf{F}}_{tr} exp(-\Delta t \underset{\sim}{\mathbf{D}}_p)$$

The polar decomposition of $\underset{\sim}{\mathbf{F}}_{tr}$ gives :

$$\underset{\sim}{\mathbf{F}}_{tr} = \underset{\sim}{\mathbf{R}}_{tr} \underset{\sim}{\mathbf{U}}_{tr}$$

On the other hand,

$$\underset{\sim}{\mathbf{F}}_{tr} = \underset{\sim}{\mathbf{F}}_e exp(\Delta t \underset{\sim}{\mathbf{D}}_p) = \underset{\sim}{\mathbf{R}}_e \underset{\sim}{\mathbf{U}}_e exp(\Delta t \underset{\sim}{\mathbf{D}}_p)$$

The comparison of the last two equations provides then

$$\underset{\sim}{\mathbf{R}}_e = \underset{\sim}{\mathbf{R}}_{tr}$$

and

$$\underset{\sim}{\mathbf{U}}_{tr} = \underset{\sim}{\mathbf{U}}_e exp(\Delta t \underset{\sim}{\mathbf{D}}_p)$$

Taking the logarithm from both sides, one gets

$$\underset{\sim}{\mathbf{E}}_{tr} = \underset{\sim}{\mathbf{E}}_e + \Delta t \underset{\sim}{\mathbf{D}}_p$$

or the following equivalent expression:

$$\underset{\sim}{\mathbf{E}}_{tr} = \underset{\sim}{\mathbf{E}}_e + \Delta p \underset{\sim}{\mathbf{N}}$$

Such a formulation can be found for instance in (Weber and Anand, 1990). The originality of our approach is that we use a unique iterative process to solve the system formed by the two nonlinear equations, the unknowns of which are $\underset{\sim}{\mathbf{E}}_e$ and Δp. A Newton method is used, so the Jacobian matrix has to be calculated. The residuals are:

$$\begin{aligned}\mathcal{F}_e &= \underset{\sim}{\mathbf{E}}_e + \Delta p \underset{\sim}{\mathbf{N}} - \underset{\sim}{\mathbf{E}}_{tr} \\ \mathcal{F}_p &= \mathcal{J}(\underset{\sim}{\sigma}) - R(p)\end{aligned}$$

Jacobian is as follows:

$$\begin{aligned}\frac{\partial \mathcal{F}_e}{\partial \Delta \underset{\sim}{\mathbf{E}}_e} &= \underset{\approx}{\mathbf{I}} + \Delta p \frac{\partial \underset{\sim}{\mathbf{N}}}{\partial \Delta \underset{\sim}{\mathbf{E}}_e} \\ \frac{\partial \mathcal{F}_e}{\partial \Delta p} &= \underset{\sim}{\mathbf{N}} \\ \frac{\partial \mathcal{F}_p}{\partial \Delta \underset{\sim}{\mathbf{E}}_e} &= \underset{\sim}{\mathbf{N}} : \underset{\approx}{\mathbf{L}} \\ \frac{\partial \mathcal{F}_p}{\partial \Delta p} &= -\frac{\partial R(p)}{\partial \Delta p}\end{aligned}$$

Here

$$\frac{\partial \underset{\sim}{\mathbf{N}}}{\partial \Delta \underset{\sim}{\mathbf{E}}_e} = \frac{3}{2\sigma} \underset{\approx}{\mathbf{J}} : \underset{\approx}{\mathbf{L}} - \frac{1}{\sigma} \underset{\sim}{\mathbf{N}} \otimes \underset{\sim}{\mathbf{N}} : \underset{\approx}{\mathbf{L}}$$

III.3.3 Consistent tangent matrix

As for the elastic case, the Truesdell elastoplastic modulus should be found:

$$\underset{\sim}{\sigma}^{\nabla} = \underset{\approx}{\mathbf{C}} : \underset{\sim}{\mathbf{D}}$$

One can note, that

$$\mathcal{J}\underset{\sim}{\sigma}^{\nabla} = \dot{\underset{\sim}{\tau}} - \underset{\sim}{\mathbf{L}} \cdot \underset{\sim}{\tau} - \underset{\sim}{\tau} \cdot \underset{\sim}{\mathbf{L}}^{T}$$

$$\dot{\underset{\sim}{\tau}} = \frac{\partial \underset{\sim}{\mathbf{R}}\underset{\sim}{\mathbf{T}}\underset{\sim}{\mathbf{R}}^{T}}{\partial t} = \dot{\underset{\sim}{\mathbf{R}}}\underset{\sim}{\mathbf{R}}^{T}\underset{\sim}{\tau} + \underset{\sim}{\tau}\underset{\sim}{\mathbf{R}}\dot{\underset{\sim}{\mathbf{R}}}^{T} + \underset{\sim}{\mathbf{R}}\dot{\underset{\sim}{\mathbf{T}}}\underset{\sim}{\mathbf{R}}^{T}$$

$$\mathcal{J}\underset{\sim}{\sigma}^{\nabla} = \underset{\sim}{\mathbf{R}}\dot{\underset{\sim}{\mathbf{T}}}\underset{\sim}{\mathbf{R}}^{T} - (\underset{\sim}{\mathbf{L}} - \dot{\underset{\sim}{\mathbf{R}}}\underset{\sim}{\mathbf{R}}^{T}) \cdot \underset{\sim}{\tau} - \underset{\sim}{\tau} \cdot (\underset{\sim}{\mathbf{L}}^{T} - \underset{\sim}{\mathbf{R}}\dot{\underset{\sim}{\mathbf{R}}}^{T})$$

Let us suppose that[3]

$$\underset{\sim}{\mathbf{D}} \approx \underset{\sim}{\mathbf{L}} - \dot{\underset{\sim}{\mathbf{R}}}\underset{\sim}{\mathbf{R}}^{T}$$

If so,

$$\sigma^{\nabla} = \frac{1}{\mathcal{J}}\underset{\sim}{\mathbf{R}}\dot{\underset{\sim}{\mathbf{T}}}\underset{\sim}{\mathbf{R}}^{T} - \underset{\sim}{\mathbf{D}} \cdot \underset{\sim}{\sigma} - \underset{\sim}{\sigma} \cdot \underset{\sim}{\mathbf{D}}$$

It is enough now to find

$$\dot{\underset{\sim}{\mathbf{T}}} = \hat{\underset{\approx}{\mathbf{C}}} : \bar{\underset{\sim}{\mathbf{D}}}$$

$$\bar{\underset{\sim}{\mathbf{D}}} = \underset{\sim}{\mathbf{R}}^{T}\underset{\sim}{\mathbf{D}}\underset{\sim}{\mathbf{R}}$$

$$\dot{\underset{\sim}{\mathbf{T}}} = \underset{\approx}{\mathbf{L}} : \dot{\underset{\sim}{\mathbf{E}}}_{e} = \underset{\approx}{\mathbf{L}} : \frac{\partial \dot{\underset{\sim}{\mathbf{E}}}_{e}}{\partial \dot{\underset{\sim}{\mathbf{E}}}_{tr}} : \frac{\partial \dot{\underset{\sim}{\mathbf{E}}}_{tr}}{\partial \bar{\underset{\sim}{\mathbf{D}}}} : \bar{\underset{\sim}{\mathbf{D}}}$$

Easy to see, that

$$\bar{\underset{\sim}{\mathbf{D}}} = {}^{\{}\Delta \underset{\sim}{\mathbf{U}}_{tr}\underset{\sim}{\mathbf{U}}_{tr}^{-1\}}$$

On the other hand,

$$\underset{\sim}{\mathbf{E}}_{tr} = log\underset{\sim}{\mathbf{U}}_{tr}$$

Let us suppose, that

$$\frac{\partial \Delta log\underset{\sim}{\mathbf{U}}_{tr}}{\partial \Delta \underset{\sim}{\mathbf{U}}_{tr}\underset{\sim}{\mathbf{U}}_{tr}^{-1}} \approx \underset{\approx}{\mathbf{I}}$$

Finally,

$$\sigma^{\nabla} = \left(\frac{1}{\mathcal{J}}\phi^{\underset{\sim}{\mathbf{R}}}_{fw}\left[\underset{\approx}{\mathbf{L}} : \left(\frac{\partial \mathcal{F}_{e}}{\partial \Delta \underset{\sim}{\mathbf{E}}_{e}}\right)^{-1}\right] - \underset{\approx}{\mathbf{M}}_{L}(\underset{\sim}{\sigma}) - \underset{\approx}{\mathbf{M}}_{R}(\underset{\sim}{\sigma})\right) : \underset{\sim}{\mathbf{D}}$$

III.3.4 Preparation for single crystal

Single crystal in large deformations is usually treated according to Mandel's $\underset{\sim}{\mathbf{F}} = \underset{\sim}{\mathbf{F}}_{e}\underset{\sim}{\mathbf{F}}_{p}$ decomposition, using the so called isoclinic configuration (Mandel, 1973). This implies naturally an other type of elasticity, as observed in (Anand and Kothari, 1996)(Miehe, 1996b). The Green strain measure is introduced

$$\underset{\sim}{\mathbf{E}} = \frac{1}{2}(\underset{\sim}{\mathbf{U}}^{2} - \underset{\sim}{\mathbf{I}})$$

Due to exponential integration, one can write:

$$\underset{\sim}{\mathbf{F}}_{p} = exp(\Delta t\underset{\sim}{\mathbf{L}}_{p})\underset{\sim}{\mathbf{F}}_{p}(t)$$

---

[3] It is exactly true for the case $\underset{\sim}{\mathbf{R}} = \underset{\sim}{\mathbf{I}}$, but not correct in general. We will, nevertheless, keep this idea, as it simplifies the formula, and leads to acceptable numerical convergence.

We state:

$$\underset{\sim}{\mathbf{F}}_{tr} = \underset{\sim}{\mathbf{F}}\underset{\sim}{\mathbf{F}}_p^{-1}(t)$$

If so,

$$\underset{\sim}{\mathbf{F}}_{tr} = \underset{\sim}{\mathbf{F}}_e exp(\Delta t \underset{\sim}{\mathbf{L}}_p) \approx \underset{\sim}{\mathbf{F}}_e(\underset{\sim}{\mathbf{I}} + \Delta t \underset{\sim}{\mathbf{L}}_p)$$

Having in mind the type of chosen elastic strain, we construct

$$\underset{\sim}{\mathbf{F}}_{tr}^T \underset{\sim}{\mathbf{F}}_{tr} = (\underset{\sim}{\mathbf{I}} + \Delta t \underset{\sim}{\mathbf{L}}_p)^T \underset{\sim}{\mathbf{F}}_e^T \underset{\sim}{\mathbf{F}}_e (\underset{\sim}{\mathbf{I}} + \Delta t \underset{\sim}{\mathbf{L}}_p)$$

First order development gives:

$$\underset{\sim}{\mathbf{C}}_{tr} = \underset{\sim}{\mathbf{C}}_e + 2\Delta t^{\{} \underset{\sim}{\mathbf{L}}_p \underset{\sim}{\mathbf{C}}_e{}^{\}}$$

Or, in terms of Lagrangian strains,

$$\underset{\sim}{\mathbf{E}}_{tr} = \underset{\sim}{\mathbf{E}}_e + \Delta t^{\{} \underset{\sim}{\mathbf{L}}_p \underset{\sim}{\mathbf{C}}_e{}^{\}}$$

Note that, with the same precision, one can write

$$\underset{\sim}{\mathbf{E}}_{tr} = \underset{\sim}{\mathbf{E}}_e + \Delta t^{\{} \underset{\sim}{\mathbf{L}}_p \underset{\sim}{\mathbf{C}}_{tr}{}^{\}}$$

The nonlinear system obtained with log measures can be effectively resolved by Newton method. One can have mathematically the same system here. It is enough to suppose:

$$\underset{\sim}{\mathbf{L}}_p \underset{\sim}{\mathbf{C}}_e = \dot{p}\frac{3}{2\sigma} dev \underset{\sim}{\mathbf{S}}_e$$

$$\sigma^2 = \frac{3}{2} dev \underset{\sim}{\mathbf{S}}_e : dev \underset{\sim}{\mathbf{S}}_e$$

with $\underset{\sim}{\mathbf{S}}_e = \underset{\approx}{\mathbf{L}} : \underset{\sim}{\mathbf{E}}_e$.

The problem of this approach is that it may not preserve plastic incompressibility, i.e. $det \underset{\sim}{\mathbf{F}}_p \neq 1$ after such an algorithm.

Different types of corrections are then proposed by the authors (Anand and Kothari, 1996)(Miehe, 1996b). On the other hand, in (Miehe, 1996a) an exponential map is applied (which automatically preserve $det \underset{\sim}{\mathbf{F}}_p = 1$).

Here, the correction of (Miehe, 1996b) was implemented on the just explained simple model. The resulting stress update algorithm is listed below. The name of each item corresponds to the module in ZéBuLoN code. `@Prestep` is applied before the iteration process, `@CalcGradF` is the section that is called during the Newton iterations, `@StrainPart` is computed after the convergence of the Newton method.

1. (@PreStep) Normalize $\underset{\sim}{\mathbf{F}}$ as

$$\hat{\underset{\sim}{\mathbf{F}}} = \mathcal{J}^{-1/3} \underset{\sim}{\mathbf{F}}$$

2. (@PreStep) Compute trial state as

$$\underset{\sim}{\mathbf{F}}_{tr} = \hat{\underset{\sim}{\mathbf{F}}} \underset{\sim}{\mathbf{F}}_p^{-1}(t)$$

$$\underset{\sim}{\mathbf{F}}_{tr} = \underset{\sim}{\mathbf{R}}_{tr} \underset{\sim}{\mathbf{U}}_{tr}$$

$$\underset{\sim}{\mathbf{E}}_{tr} = \frac{1}{2}(\underset{\sim}{\mathbf{U}}_{tr}^2 - \underset{\sim}{\mathbf{I}})$$

3. (@CalcGradF) Calculate the residuals and Jacobian matrix as follows.

$$\left\{\begin{array}{lcl} \mathcal{F}_e & = & \underset{\sim}{\mathbf{E}}_e + \Delta p \underset{\sim}{\mathbf{N}} - \underset{\sim}{\mathbf{E}}_{tr} \\ \mathcal{F}_p & = & \sigma - R(p) \end{array}\right. \tag{III.8}$$

$$\frac{\partial \mathcal{F}_e}{\partial \Delta \underset{\sim}{\mathbf{E}}_e} = \underset{\approx}{\mathbf{I}} + \Delta p \frac{\partial \underset{\sim}{\mathbf{N}}}{\partial \Delta \underset{\sim}{\mathbf{E}}_e} \tag{III.9}$$

$$\frac{\partial \mathcal{F}_e}{\partial \Delta p} = \underset{\sim}{\mathbf{N}} \tag{III.10}$$

$$\frac{\partial \mathcal{F}_p}{\partial \Delta \underset{\sim}{\mathbf{E}}_e} = \underset{\sim}{\mathbf{N}} : \underset{\approx}{\mathbf{L}} \tag{III.11}$$

$$\frac{\partial \mathcal{F}_p}{\partial \Delta p} = -\frac{\partial R(p)}{\partial \Delta p} \tag{III.12}$$

4. (@CalcGradF) Find new estimation for $\underset{\sim}{\mathbf{E}}_e$ and p variables and restart CalcGradF.

5. (@StrainPart) Find

$$\underset{\sim}{\mathbf{C}}_e = 2\underset{\sim}{\mathbf{E}}_e + \underset{\sim}{\mathbf{I}}$$

6. (@StrainPart) Consider, that $dev\underset{\sim}{\mathbf{C}}_e$ is good. Correct the trace of $\underset{\sim}{\mathbf{C}}_e$ so that

$$det(dev\underset{\sim}{\mathbf{C}}_e + f\underset{\sim}{\mathbf{I}}) = 1$$

For that purpose solve the scalar equation

$$f^3 - J_2(dev\underset{\sim}{\mathbf{C}}_e) \cdot f - (1 - det(dev\underset{\sim}{\mathbf{C}}_e)) = 0$$

7. (@StrainPart) Compute $\underset{\sim}{\mathbf{F}}_e$ as

$$\hat{\underset{\sim}{\mathbf{F}}}_e = \underset{\sim}{\mathbf{R}}_{tr}\underset{\sim}{\mathbf{U}}_e^{corr}$$

$$\underset{\sim}{\mathbf{F}}_p = \hat{\underset{\sim}{\mathbf{F}}}_e^{-1}\hat{\underset{\sim}{\mathbf{F}}}$$

$$\underset{\sim}{\mathbf{F}}_e = \underset{\sim}{\mathbf{F}}\underset{\sim}{\mathbf{F}}_p^{-1}$$

8. (@StrainPart) Compute Cauchy stress:

$$\underset{\sim}{\mathbf{E}}_e^{corr} = \frac{1}{2}(\underset{\sim}{\mathbf{F}}_e^T\underset{\sim}{\mathbf{F}}_e - \underset{\sim}{\mathbf{I}})$$

$$\bar{\underset{\sim}{\mathbf{T}}} = \underset{\approx}{\mathbf{L}} : \underset{\sim}{\mathbf{E}}_e^{corr}$$

$$\underset{\sim}{\sigma} = \frac{1}{\mathcal{J}}\underset{\sim}{\mathbf{F}}_e\bar{\underset{\sim}{\mathbf{T}}}\underset{\sim}{\mathbf{F}}_e^T$$

After such a correction, the following tangent was found convenient for the computations.

$$\sigma^{\nabla} = \left(\frac{1}{J}\phi^{\underset{\sim}{\mathbf{F}}_e}_{fw}\left[\underset{\approx}{\mathbf{L}} : \left(\frac{\partial \mathcal{F}_e}{\partial \Delta \underset{\sim}{\mathbf{E}}_e}\right)^{-1}\right] - \underset{\approx}{\mathbf{M}}_L(\underset{\sim}{\sigma}) - \underset{\approx}{\mathbf{M}}_R(\underset{\sim}{\sigma})\right) : \underset{\sim}{\mathbf{D}}$$

E	200000 MPa
ν	0.3
R_0	100 MPa
H	200 MPa

Table III.1 : Material parameters for J_2 plasticity tension test

III.3.5 Uniaxial tension test

A tension test till 200% for one 3D eight-node finite element is presented here. The material parameters are shown in tab.III.1.

The resulting stress-strain curve is presented in fig.III.2. This is a typical almost bilinear response of a elastoplastic model with linear isotropic hardening. On the other hand, the force-time curve is shown in fig.III.3. A softening behavior is observed, due to geometrical effect of large strain formalism application. The computation was done with 10 integration steps, and only two local iterations were necessary for each increment.

It is interesting to note that, for this test, the terms of $\underset{\approx}{\mathbf{M}}_L(\underset{\sim}{\sigma})$ and $\underset{\approx}{\mathbf{M}}_R(\underset{\sim}{\sigma})$ in material tangent were of several orders smaller, compared to the rest. They were, so far, not significant. But, for more complex stress states (as in the billet upsetting example) they become important.

The volume change factor, J, is quite important for convergence. Forgetting J in material tangent may lead to poor global convergence even in tension test.

Correction of plastic incompressibility - as in section III.3.4 - is important for the convergence. Formally the same material tangent gives much worse convergence without such a correction.

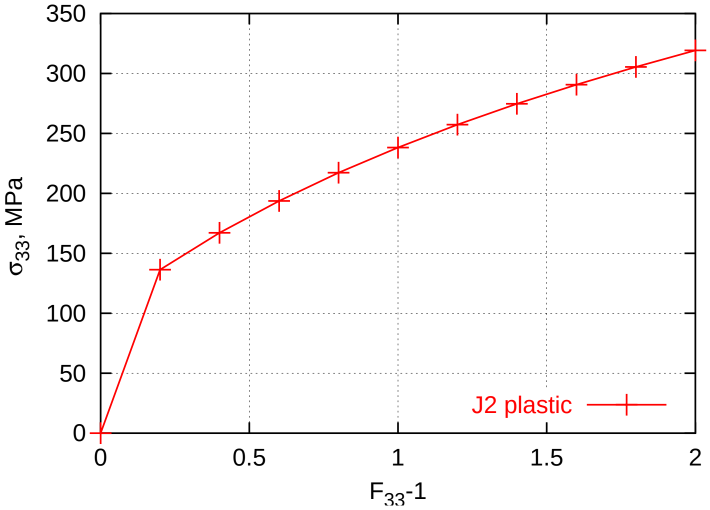

Figure III.2 : J_2 plasticity tension test. Stress strain curve.

III.3.6 Billet upsetting test

This test is a classical severe test for large strain elastoplasticity numerical procedure. It is used, for instance, in (Taylor and Becker, 1983)(Weber and Anand, 1990).

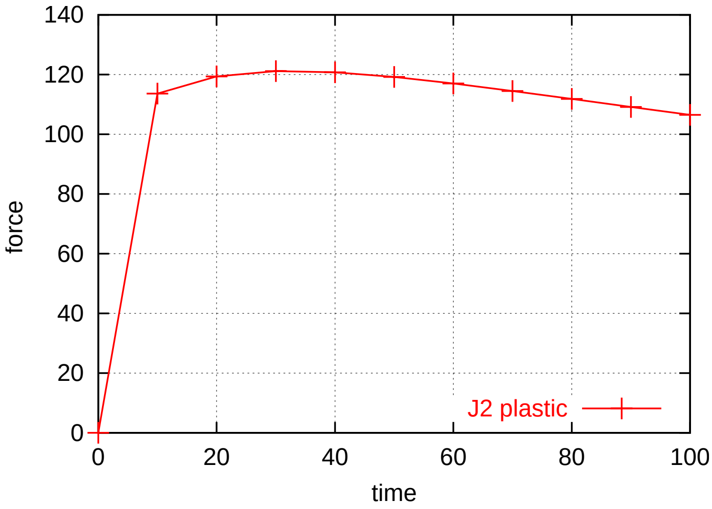

Figure III.3 : J_2 plasticity tension test. Force curve.

A cylindrical billet of 10 mm radius and 30 mm hight is compressed by 2 rigid planes till 60% of height reduction.

E	200000 MPa
ν	0.3
R_0	100 MPa
H	300 MPa

Table III.2 : Material parameters for J_2 plasticity billet upsetting test

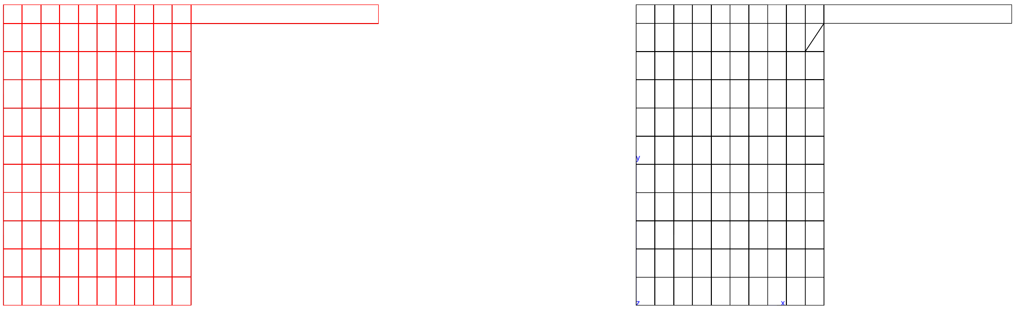

Figure III.4 : J_2 plasticity billet upsetting. FE meshes (mesh1 and mesh2).

Material parameters are presented in table III.2 . Two finite element meshes are shown in fig III.4 (due to the symmetry, only a quarter of the specimen is meshed)

Von Mises stress maps at 30 and 60% of compression can be seen in fig. III.5,III.6. One can note the similar deformed shape with those, known from the literature (see fig. III.7,III.8, III.9).

The computation was done in 35 steps. The convergence is quadratic, as shown by the following sequence

```
seq:  1 incr: 34 dt:0.02299  t:0.9989
 iter:  1 | R |/| Fext |= 1.370e-01  | Fext |=712992.217769
```

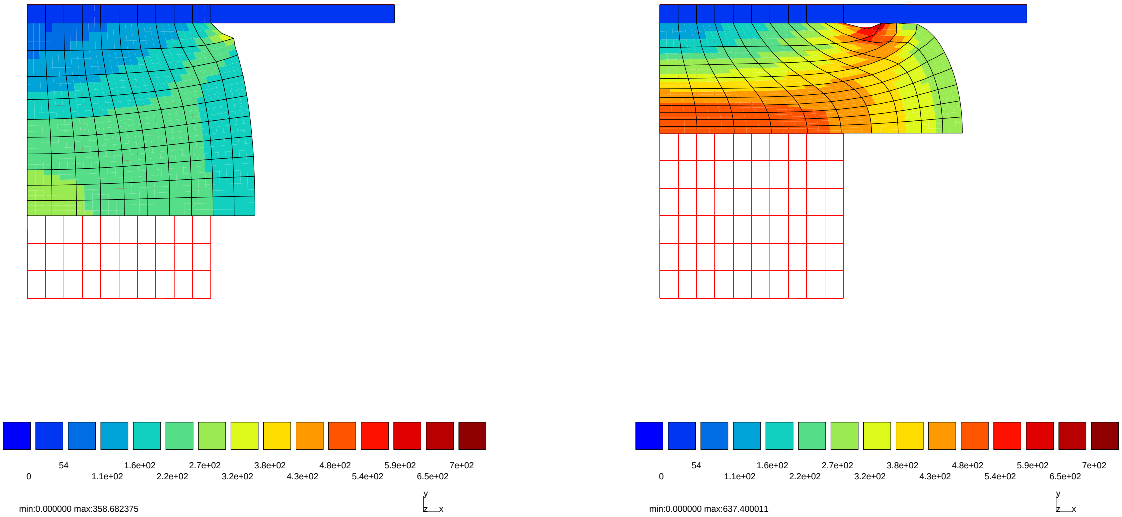
0
54
1.1e+02
1.6e+02
2.2e+02
2.7e+02
3.2e+02
3.8e+02
4.3e+02
4.8e+02
5.4e+02
5.9e+02
6.5e+02
7e+02
min:0.000000 max:358.682375
y
z x
min:0.000000 max:637.400011

Figure III.5 : J_2 plasticity billet upsetting - mesh1. Von Mises stress at 30% and 60% deflection.

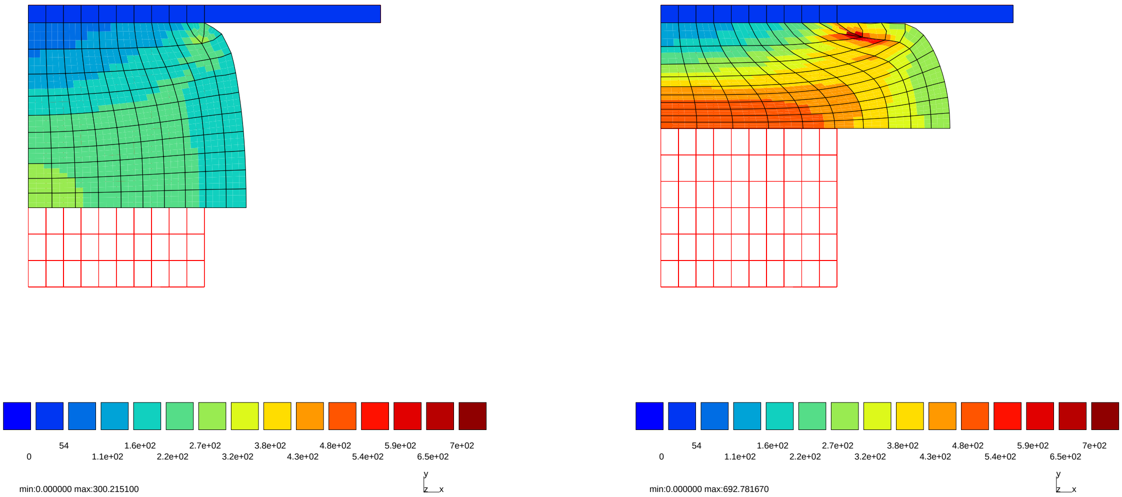
0
54
1.1e+02
1.6e+02
2.2e+02
2.7e+02
3.2e+02
3.8e+02
4.3e+02
4.8e+02
5.4e+02
5.9e+02
6.5e+02
7e+02
min:0.000000 max:300.215100
y
z x
min:0.000000 max:692.781670

Figure III.6 : J_2 plasticity billet upsetting - mesh2 . Von Mises stress at 30% and 60% deflection.

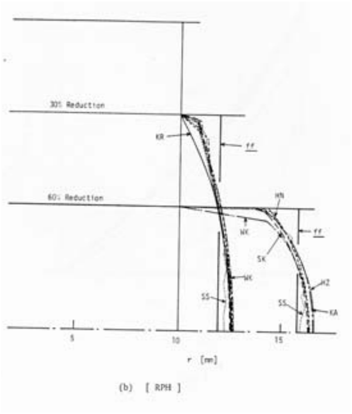

Figure III.7 : J_2 plasticity billet upsetting. Deformed shape from (Kudo and Matsubara, 1979)

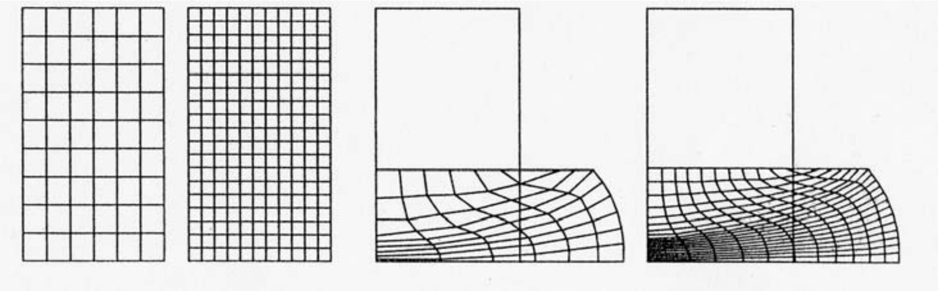

Figure III.8 : J_2 plasticity billet upsetting. Deformed shape from (Simo and Hughes, 1997)

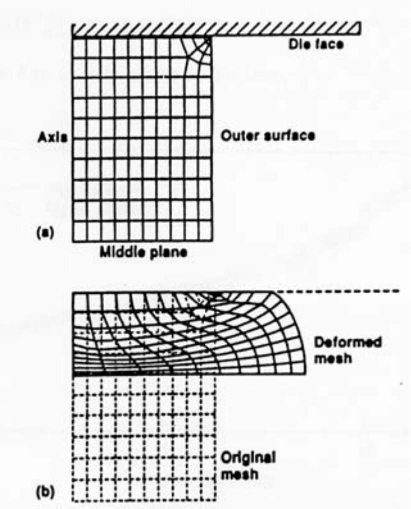
Die face
Axis
Outer surface
(a)
Middle plane
Deformed mesh
Original mesh
(b)

Figure III.9 : J_2 plasticity billet upsetting. Deformed shape from (Weber and Anand, 1990)

```
iter:  2 | R |/| Fext |= 5.729e-02  | Fext |=705010.017456
iter:  3 | R |/| Fext |= 1.690e-04  | Fext |=706224.783687
iter:  4 | R |/| Fext |= 2.972e-07  | Fext |=706255.898038
iter:  5 | R |/| Fext |= 1.025e-10  | Fext |=706255.839341
```

III.4 Crystal plasticity

III.4.1 Model

The finite strain formalism of the basic crystalline model presented in section I is taken from (Cailletaud et al., 2003b). A multiplicative decomposition of the strain gradient is used, as

$$\underset{\sim}{\mathbf{F}} = \underset{\sim}{\mathbf{F}}_e \underset{\sim}{\mathbf{F}}_p$$

For the elastic part, the elastic strain is calculated

$$\underset{\sim}{\mathbf{C}}_e = \underset{\sim}{\mathbf{F}}_e^T \underset{\sim}{\mathbf{F}}_e$$

$$\underset{\sim}{\mathbf{E}}_e = \frac{1}{2}(\underset{\sim}{\mathbf{C}}_e - \underset{\sim}{\mathbf{I}})$$

The second Piola-Kirchhoff stress is obtained

$$\underset{\sim}{\mathbf{S}}_e = J \underset{\sim}{\mathbf{F}}_e^{-1} \underset{\sim}{\sigma} \underset{\sim}{\mathbf{F}}_e^{-T}$$

$$\underset{\sim}{\mathbf{S}}_e = \underset{\approx}{\mathbf{L}} : \underset{\sim}{\mathbf{E}}_e$$

Plastic part is computed as a sum over all active slip systems:

$$\underset{\sim}{\mathbf{L}}_p = \dot{\underset{\sim}{\mathbf{F}}}_p \underset{\sim}{\mathbf{F}}_p^{-1} = \sum \dot{\gamma}_s \underset{\sim}{\mathbf{N}}_s^0$$

Here $\underset{\sim}{\mathbf{N}}_s^0$ is the tensor which describes the slip system geometry. Index '0' means the relaxed configuration. It is obtained from the slip direction $\underline{\mathbf{l}}_s$ and the normal to the slip plane $\underline{\mathbf{n}}_s$:

$$\underset{\sim}{\mathbf{N}}_s^0 = \underline{\mathbf{l}}_s^0 \otimes \underline{\mathbf{n}}_s^0$$

Is can be also written in current configuration,

$$\underline{\mathbf{l}}_s = \underset{\sim}{\mathbf{F}}_e \cdot \underline{\mathbf{l}}_s^0$$

$$\underline{\mathbf{n}}_s = \underset{\sim}{\mathbf{F}}_e^{-T} \cdot \underline{\mathbf{n}}_s^0$$

Slip rate for any system, $\dot{\gamma}_s$ is defined by a Norton-type law, similar to the small strain case of the chapter I.2:

$$\dot{\gamma}_s = \left\langle \frac{|\tau_s - x_s| - r_s}{K} \right\rangle^n sign(\tau_s - x_s)$$

For the present section, we neglect the kinematic hardening x_s, and simplify the isotropic hardening R_s as:

$$r_s = R_s = R_0 + Q \cdot v_s$$

The resolved shear stress, τ_s is

$$\tau_s = \underset{\sim}{\sigma} : \underset{\sim}{\mathbf{N}}_s = (\underset{\sim}{\mathbf{C}}_e \cdot \underset{\sim}{\mathbf{S}}_e) : \underset{\sim}{\mathbf{N}}_s^0 \approx \underset{\sim}{\mathbf{S}}_e : \underset{\sim}{\mathbf{N}}_s^0$$

III.4.2 Numerical implementation problems

To implement such a kind of model by means of implicit integration scheme, some points of difficulty should be discussed.

1. Rate dependent or rate-independent model ?
   The difficulty attached to the rate-independent model is known. Authors use to claim that this is due to the problem of the choice of the active slip systems. In fact, the choice of the set of active slip system does not relate exactly to the rate-independent or viscous character of the flow. It depends rather on the presence of elastic region. As a matter of fact, it is mandatory for a rate-independent model to have an elastic region, and, in the literature, viscoplastic models do not have any threshold.

2. Elastic region

   - $R_0 = 0$
     One can refuse to have an elastic region at all, as classically done in (Asaro, 1983),(Asaro and Needleman, 1985),(Kalidindi and Anand, 1994)(Anand, 2004), for instance.
     Advantage: all the slip systems are always active, there is not need to choose them. A time-independent behavior may be recovered with very high values of the viscosity exponent. Nevertheless, this introduces an artificial regularization near the corners of the yield surface, which can influence the direction of the inelastic flow.

   - $R_0 \neq 0$
     Problem: one needs to choose active slip systems. There are two solutions to this problem. The first type of solution comes from the physical analysis of the deformation process, the second one is an algorithmic solution. In the first type of approach, the references are the papers by Bishop and Hill (Bishop and Hill, 1951), and Chin and Mammel (Chin and Mammel, 1969), which propose a maximization of the plastic work. On the other hand, a series of algorithmic solutions are proposed (Simo and Hughes, 1997) (Miehe, 1996b) (Cuitino and Ortiz, 1992) (Anand and Kothari, 1996) (Schmidt-Baldassari, 2003).

3. Slip residual
   The system built for an implicit formulation of the problem contains first the tensorial relation between stresses and strains, and also a set of scalar equations for expressing the hardening on each slip system. This last type of equation can be expressed in terms of strain rate, or in terms of stresses:

   - $\Delta v_s = (\frac{|\tau_s| - \dots}{\dots})^n$
     Problem: for large steps, $(\tau_{trial})^n$ can be too big, that causes local divergence. In (Kalidindi and Anand, 1994) the condition $|\underset{\sim}{\mathbf{T}}| < \eta \cdot s_0$ must be verified to accept the Newton correction. The heuristic parameter η is usually chosen equal to $2/3$.

   - $\tau_s - R_s - (v_s)^{1/n} = 0$
     Advantage: if it converges, it converges in 2-3 iterations, as mentioned in (Cuitino and Ortiz, 1992).
     Problem: this residual can not be computed if $v_s < 0$. Something should be done to avoid that. This problem may disappear if a preliminary operation to determine the active slip system is applied.

4. Numerical decomposition
   The decomposition is unique under small strains. Under finite strains, two possibilities are known from the literature.

   - exponential map
     One can enlarge the approach of (Weber and Anand, 1990) on the crystal plasticity model. Such an example can be found in (Miehe, 1996a).
     Advantage : the algorithm automatically respects plastic incompressibility.
     Problem : the application of the approach is practically restricted to elastically isotropic materials – the Neo-Hooke law is used in (Miehe, 1996a) –
   - Green strain
     In this work we want to have an anisotropic elastic law. In such a case, a numerical scheme like (Kalidindi and Anand, 1994) is the most convenient.
     Problem: the numerical algorithm does not preserve plastic incompressibility, i.e. $det\underset{\sim}{\mathbf{F}}_p \neq 1$. A correction is then needed. Several correction techniques are found in the literature (Kalidindi and Anand, 1994), (Miehe, 1996b). One of them was tested in chap.III.3.4.

In this work, we have tested a series of new solutions for integrating crystal plasticity. These attempts will be shown below. On the other hand, we have pre-existing methods in ZéBuLoN :

- θ-method, which implements Simo's ideas (Simo and Hughes, 1997) for the small strain formalism (Foerch, 1996).
- Runge-Kutta technique, which can be efficient with viscoplastic model formulations

A brief description of these methods is given in Appendix A.

III.4.3 Stress update algorithm

One can try basically the same idea as for the J_2 plasticity case. Due to the exponential approximation one can write:

$$\underset{\sim}{\mathbf{F}}_p = exp(\Delta t\underset{\sim}{\mathbf{L}}_p)\underset{\sim}{\mathbf{F}}_p(t)$$

We state:

$$\underset{\sim}{\mathbf{F}}_{tr} = \underset{\sim}{\mathbf{F}}\underset{\sim}{\mathbf{F}}_p^{-1}(t)$$

If so,

$$\underset{\sim}{\mathbf{F}}_{tr} = \underset{\sim}{\mathbf{F}}_e exp(\Delta t\underset{\sim}{\mathbf{L}}_p) \approx \underset{\sim}{\mathbf{F}}_e(\underset{\sim}{\mathbf{I}} + \sum \Delta\gamma_s\underset{\sim}{\mathbf{N}}_s^0)$$

Having in mind the type of chosen elastic strain, we construct

$$\underset{\sim}{\mathbf{F}}_{tr}^T\underset{\sim}{\mathbf{F}}_{tr} = (\underset{\sim}{\mathbf{I}} + \sum \Delta\gamma_s\underset{\sim}{\mathbf{N}}_s^0)^T\underset{\sim}{\mathbf{F}}_e^T\underset{\sim}{\mathbf{F}}_e(\underset{\sim}{\mathbf{I}} + \sum \Delta\gamma_s\underset{\sim}{\mathbf{N}}_s^0)$$

A first order development gives:

$$\underset{\sim}{\mathbf{C}}_{tr} = \underset{\sim}{\mathbf{C}}_e + 2\sum \Delta\gamma_s{}^{\{}\underset{\sim}{\mathbf{N}}_s^0\underset{\sim}{\mathbf{C}}_e{}^{\}}$$

Or, in Lagrangian strains,

$$\underset{\sim}{\mathbf{E}}_{tr} = \underset{\sim}{\mathbf{E}}_e + \sum \Delta\gamma_s{}^{\{}\underset{\sim}{\mathbf{N}}_s^0\underset{\sim}{\mathbf{C}}_e{}^{\}}$$

We add then the equations for elementary slip rates, as

$$\Delta\gamma_s = \left\langle \frac{|\tau_s| - R_s}{K} \right\rangle^n sign(\tau_s)$$

Finally the residuals are:

$$\left\{\begin{array}{lll} \mathcal{F}_e & = & \underset{\sim}{\mathbf{E}}_e + \sum \Delta v_s sign(\tau_s)^{\{}\underset{\sim}{\mathbf{N}}_s^0 \underset{\sim}{\mathbf{C}}_e{}^{\}} - \underset{\sim}{\mathbf{E}}_{tr} \\ \mathcal{F}_v & = & \Delta v_s - \left\langle \frac{|\tau_s| - R_s}{K} \right\rangle^n \end{array}\right.$$

We solve this system for the unknowns $\underset{\sim}{\mathbf{E}}_e$ (or may be $\underset{\sim}{\mathbf{C}}_e$) and Δv_s by means of the Newton method. The Jacobian is then needed, which is as follows

$$\begin{aligned} \frac{\partial \mathcal{F}_e}{\partial \Delta \underset{\sim}{\mathbf{E}}_e} &= \underset{\approx}{\mathbf{I}} + \sum \Delta v_s sign(\tau_s) \left[\underset{\approx}{\mathbf{M}}_l(\underset{\sim}{\mathbf{N}}_s) + \underset{\approx}{\mathbf{M}}_r(\underset{\sim}{\mathbf{N}}_s^T) \right] \\ \frac{\partial \mathcal{F}_e}{\partial \Delta v_s} &= sign(\tau_s)^{\{}\underset{\sim}{\mathbf{N}}_s \underset{\sim}{\mathbf{C}}_e{}^{\}} \\ \frac{\partial \mathcal{F}_v}{\partial \Delta \underset{\sim}{\mathbf{E}}_e} &= -\frac{n}{K} \left\langle \frac{|\tau_s| - R_s}{K} \right\rangle^{n-1} sign(\tau_s) \underset{\sim}{\mathbf{N}}_s : \underset{\approx}{\mathbf{L}} \\ \frac{\partial \mathcal{F}_v}{\partial \Delta v_s} &= 1 + \frac{n}{K} \left\langle \frac{|\tau_s| - R_s}{K} \right\rangle^{n-1} Q \end{aligned}$$

There is, in fact, another possibility for the slip solution. One can invert the slip equation, in order to have:

$$\mathcal{F}_v = |\tau_s| - R_s - K \left(\frac{\Delta v_s}{\Delta t} \right)^{1/n}$$

In such a formulation $\eta \mathcal{F}_v$ with $\eta = 0.01..0.0001$ is used, to have a similar order of magnitude with $\mathcal{F}_e$.

The derivatives are

$$\frac{\partial \mathcal{F}_v}{\partial \Delta \underset{\sim}{\mathbf{E}}_e} = sign(\tau_s) \underset{\sim}{\mathbf{N}}_s : \underset{\approx}{\mathbf{L}}$$

$$\frac{\partial \mathcal{F}_v}{\partial \Delta v_s} = -\frac{\partial R_s}{\partial \Delta v_s} - \frac{K}{n \Delta t} \left(\frac{\Delta v_s}{\Delta t} \right)^{1/n-1}$$

Note, that it is not possible to calculate such a residual for $\Delta v_s < 0$. It can be avoided by means of a slight correction, as

$$\mathcal{F}_v = |\tau_s| - R_s - K \left(\left(\frac{\Delta v_s}{\Delta t} + 1 \right)^{1/n} - 1 \right)$$

III.4.4 Consistent tangent matrix

Some ideas for the tangent matrix are presented here. Truesdell's elastoplastic modulus should be found,

$$\underset{\sim}{\sigma}^{\nabla} = \underset{\approx}{\mathbf{C}} : \underset{\sim}{\mathbf{D}}$$

One can note, that

$$\mathcal{J} \underset{\sim}{\sigma}^{\nabla} = \dot{\underset{\sim}{\tau}} - \underset{\sim}{\mathbf{L}} \cdot \underset{\sim}{\tau} - \underset{\sim}{\tau} \cdot \underset{\sim}{\mathbf{L}}^T$$

$$\phi^e_{back}(\mathcal{J} \underset{\sim}{\sigma}^{\nabla}) = \dot{\underset{\sim}{\mathbf{S}}}_e - \underset{\sim}{\mathbf{L}}_p \cdot \underset{\sim}{\mathbf{S}}_e - \underset{\sim}{\mathbf{S}}_e \cdot \underset{\sim}{\mathbf{L}}_p^T$$

So, it is enough to find

$$\phi^e_{back}(\mathcal{J} \underset{\sim}{\sigma}^{\nabla}) = \bar{\underset{\approx}{\mathbf{C}}} : \bar{\underset{\sim}{\mathbf{D}}}$$

where

$$\bar{\underset{\sim}{\mathbf{D}}} = \phi^e_{back}(\underset{\sim}{\mathbf{D}}) = \underset{\sim}{\mathbf{F}}_e^T \underset{\sim}{\mathbf{D}} \underset{\sim}{\mathbf{F}}^e$$

and then

$$\underset{\approx}{\mathbf{C}} = \frac{1}{\mathcal{J}}\phi^{e}_{fw}(\underset{\approx}{\bar{\mathbf{C}}})$$

Let us calculate $\underset{\approx}{\bar{\mathbf{C}}}$. One can check that

$$\begin{gathered}
\underset{\approx}{\bar{\mathbf{C}}} = \underset{\approx}{\bar{\mathbf{C}}}_1 - \underset{\approx}{\bar{\mathbf{C}}}_2 \\
\underset{\sim}{\dot{\mathbf{S}}}_e = \underset{\approx}{\bar{\mathbf{C}}}_1 : \underset{\sim}{\bar{\mathbf{D}}} \\
\underset{\sim}{\mathbf{L}}_p \cdot \underset{\sim}{\mathbf{S}}_e + \underset{\sim}{\mathbf{S}}_e \cdot \underset{\sim}{\mathbf{L}}_p^T = \underset{\approx}{\bar{\mathbf{C}}}_2 : \underset{\sim}{\bar{\mathbf{D}}}
\end{gathered}$$

Then

$$\begin{gathered}
\underset{\sim}{\bar{\mathbf{D}}} = \underset{\sim}{\mathbf{F}}_e^{T}{}^{\{}\underset{\sim}{\dot{\mathbf{F}}}\underset{\sim}{\mathbf{F}}^{-1}{}^{\}}\underset{\sim}{\mathbf{F}}_e = \\
\underset{\sim}{\mathbf{F}}_e^{T}{}^{\{}\underset{\sim}{\dot{\mathbf{F}}}_e\underset{\sim}{\mathbf{F}}_e^{-1} + \underset{\sim}{\mathbf{F}}_e\underset{\sim}{\dot{\mathbf{F}}}_p\underset{\sim}{\mathbf{F}}_p^{-1}\underset{\sim}{\mathbf{F}}_e^{-1}{}^{\}}\underset{\sim}{\mathbf{F}}_e = \\
{}^{\{}\underset{\sim}{\mathbf{F}}_e^{T}\underset{\sim}{\dot{\mathbf{F}}}_e{}^{\}} + {}^{\{}\underset{\sim}{\mathbf{C}}_e\underset{\sim}{\mathbf{L}}_p{}^{\}} = \Delta\underset{\sim}{\mathbf{E}}_e + {}^{\{}\underset{\sim}{\mathbf{C}}_e\underset{\sim}{\mathbf{L}}_p{}^{\}} = \Delta\underset{\sim}{\mathbf{E}}_{tr}
\end{gathered}$$

if so,

$$\underset{\approx}{\bar{\mathbf{C}}}_1 = \frac{\partial\Delta\underset{\sim}{\mathbf{S}}_e}{\partial\Delta\underset{\sim}{\mathbf{E}}_{tr}} = \underset{\approx}{\mathbf{L}} : \frac{\partial\Delta\underset{\sim}{\mathbf{E}}_e}{\partial\Delta\underset{\sim}{\mathbf{E}}_{tr}} = \underset{\approx}{\mathbf{L}} : \left[\frac{\partial\mathcal{F}_e}{\partial\Delta\underset{\sim}{\mathbf{E}}_e}\right]^{-1}$$

it is then easy to see that

$$\underset{\sim}{\mathbf{L}}_p \cdot \underset{\sim}{\mathbf{S}}_e + \underset{\sim}{\mathbf{S}}_e \cdot \underset{\sim}{\mathbf{L}}_p^T = \sum_s \Delta v_s sign(\tau_s)(\underset{\sim}{\mathbf{N}}_s\underset{\sim}{\mathbf{S}}_e + \underset{\sim}{\mathbf{S}}_e\underset{\sim}{\mathbf{N}}_s^T) = 2\sum_s \Delta v_s sign(\tau_s){}^{\{}\underset{\sim}{\mathbf{N}}_s\underset{\sim}{\mathbf{S}}_e{}^{\}}$$

As

$$\Delta\underset{\sim}{\mathbf{E}}_{tr} = \Delta\underset{\sim}{\mathbf{E}}_e + \sum_s \Delta v_s sign(\tau_s){}^{\{}\underset{\sim}{\mathbf{N}}_s\underset{\sim}{\mathbf{C}}_e{}^{\}}$$

then

$$\frac{\partial(\bullet)}{\partial\Delta\underset{\sim}{\mathbf{E}}_{tr}} = \frac{\partial(\bullet)}{\partial\Delta\underset{\sim}{\mathbf{E}}_e}\frac{\partial\Delta\underset{\sim}{\mathbf{E}}_e}{\partial\Delta\underset{\sim}{\mathbf{E}}_{tr}} + \sum_s \frac{\partial(\bullet)}{\partial\Delta v_s}\frac{\partial\Delta v_s}{\partial\Delta\underset{\sim}{\mathbf{E}}_{tr}} = \frac{\partial(\bullet)}{\partial\Delta\underset{\sim}{\mathbf{E}}_e}\left[\frac{\partial\mathcal{F}_e}{\partial\Delta\underset{\sim}{\mathbf{E}}_e}\right]^{-1} + \sum_s \frac{\partial(\bullet)}{\partial\Delta v_s}\left[\frac{\partial\mathcal{F}_e}{\partial\Delta v_s}\right]^{-1}$$

Application of this rule finally gives

$$\underset{\approx}{\bar{\mathbf{C}}}_2 = 2\sum_s sign(\tau_s){}^{\{}\underset{\sim}{\mathbf{N}}_s\underset{\sim}{\mathbf{S}}_e{}^{\}}\left[\frac{\partial\mathcal{F}_e}{\partial\Delta v_s}\right]^{-1}$$

III.4.5 Single crystal tension test

A tension test till 200% for 1 finite element has been performed here. The material parameters are presented in table III.3. The stress strain curve is presented in fig. III.10 . One can see that the computation was done in a quite small (10) number of time steps. The tension axis was parallel to the [001] crystallographic direction, so that among twelve slip systems, four were non active, and eight were active with the same absolute slip value.

y1111	y1122	y1212	K	n	R0	Q	b
250000.0	200000.0	200000.0	10.0	10.0	100.	35.	7.

Table III.3 : Material parameters for single crystal tension test

III.4.6 Polycrystal compression test

A cube-shaped finite element mesh was taken first, with 343 elements. Each element was then associated with a grain of a given crystallographic orientation. Then, a 20-grain aggregate made of tetrahedral elements was taken. Both meshes are presented in fig.III.11

The material parameters are presented in tab. III.4. Compression was applied, by means of imposed displacements (Uz=0 for all the nodes with z=0; Uz = -0.5*meshsize for all the nodes with z=meshsize). The contour of the cumulated slip is shown on the deformed shape of the aggregates after 50% deformation in fig. III.12. Force - displacement curves for the compression test of 343-grain aggregate are shown in fig.III.13. Three numerical realizations are compared: pre-existing small strain and explicit finite strain, with newly developed implicit finite strain. One can see, that the finite strain curves differ significantly from the small strain one, due to geometrical effect. The results for both finite strain realizations – explicit and implicit– are similar. The implicit algorithm represent less time steps for this test (29 time steps compared to 48 steps of explicit realization till 25% global strain). This is because the higher rate of global convergence for the implicit scheme. Typical convergence for implicit method was as follows :

```
seq:  1 incr: 21 dt:1.786   t:18.86
 iter:  1 | R |/| Fext |= 3.192e-02  | Fext |=15722.905922
 iter:  2 | R |/| Fext |= 1.489e-03  | Fext |=15651.792045
 iter:  3 | R |/| Fext |= 4.857e-05  | Fext |=15649.551795
```

On the other hand, explicit method gives:

```
seq:  1 incr: 25 dt:1.447    t:18.76
 iter:  1 | R |/| Fext |= 5.418e-03  | Fext |=15948.628690
 iter:  2 | R |/| Fext |= 3.141e-03  | Fext |=15936.654610
 iter:  3 | R |/| Fext |= 2.205e-03  | Fext |=15935.853274
 iter:  4 | R |/| Fext |= 1.627e-03  | Fext |=15935.908450
 iter:  5 | R |/| Fext |= 1.235e-03  | Fext |=15936.028576
 iter:  6 | R |/| Fext |= 9.556e-04  | Fext |=15936.134151
```

One can note that convergence of the implicit scheme is better then linear.

y1111	y1122	y1212	K	n	R0	Q	b
250000.0	200000.0	200000.0	1000.0	5.0	100.	350.	7.

Table III.4 : Material parameters for polycrystal compression test

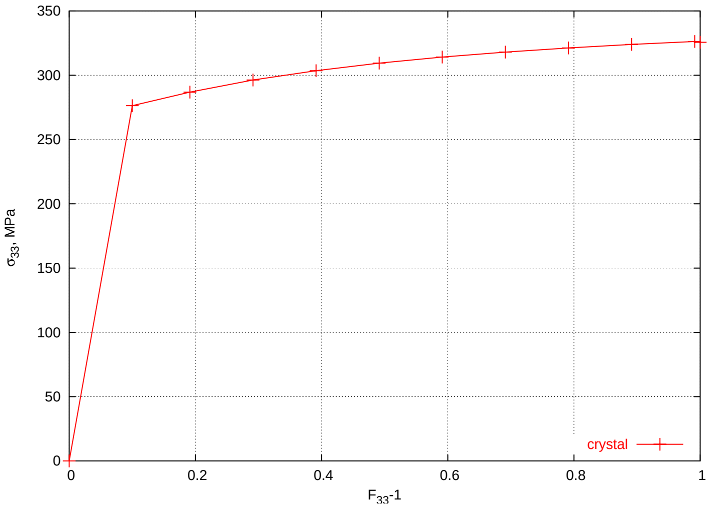

(a)

Figure III.10 : Crystal 1 element tension stress-strain curve

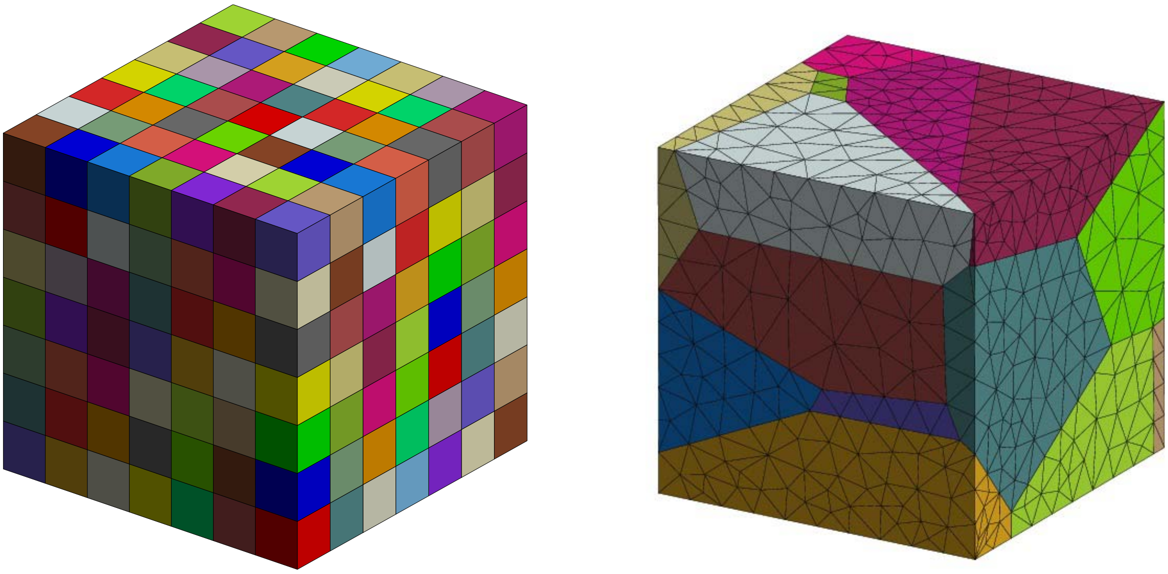

(a) (b)

Figure III.11 : Finite element meshes used for crystal plasticity tests under finite strains: (a) 343-grain aggregate with cube-shaped 1 element grains; (b) 20-grain aggregate with realistic shaped grains (10326 tetrahedric elements)

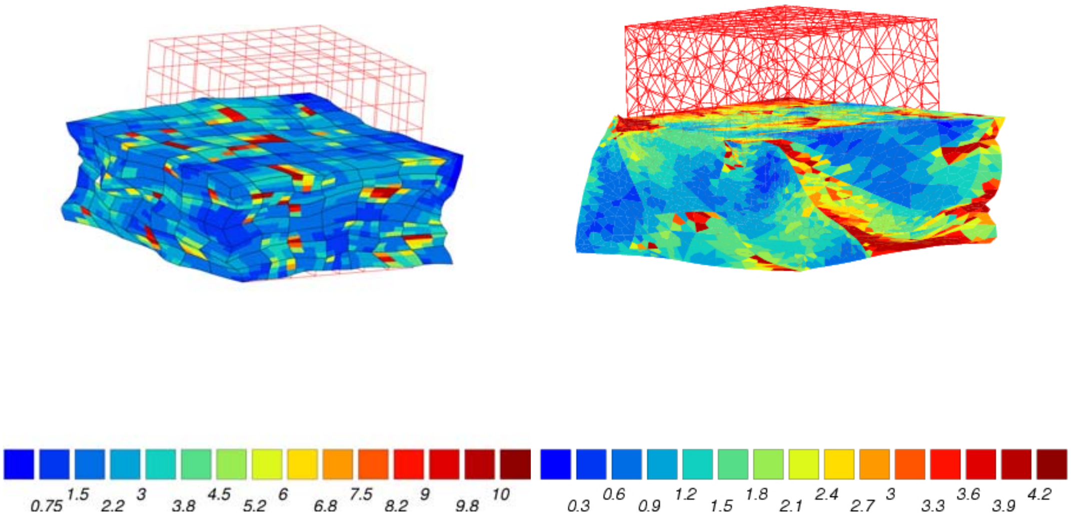
0.75 1.5 2.2 3 3.8 4.5 5.2 6 6.8 7.5 8.2 9 9.8 10
0.3 0.6 0.9 1.2 1.5 1.8 2.1 2.4 2.7 3 3.3 3.6 3.9 4.2

(a) (b)

Figure III.12 : Cumulated plastic shear at finite strains after 50% compression: (a) 343-grain aggregate , (b) 20-grain aggregate

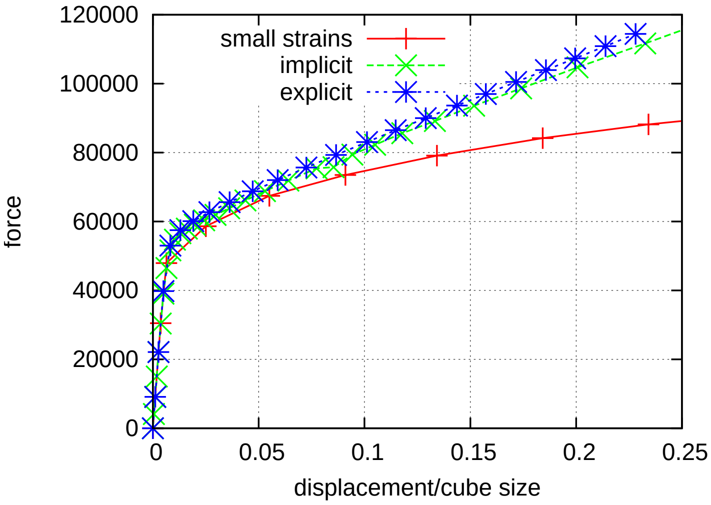

Figure III.13 : Force-displacement curves for compression of a 343-grain aggregate. Pre-existing small strain, explicit finite strain and newly developed implicit finite strain are compared.

III.5 Damage, Opening and Sliding

III.5.1 Model

The Clausius-Duhem inequality under finite strains for isothermal processes in the initial reference frame can be written as (Besson et al., 2001)

$$-\rho_0\dot{\Psi} + \underset{\sim}{\mathbf{S}} : \dot{\underset{\sim}{\mathbf{E}}} \geq 0$$

$$-\rho\dot{\Psi} + \underset{\sim}{\sigma} : \underset{\sim}{\mathbf{D}} \geq 0$$

Let us suppose that there is no direct coupling between damage and plasticity. In that case, at the elastically unloaded (isoclinic) configuration, one can write:

$$\rho_0\Psi = \rho_0\Psi^e(\underset{\sim}{\mathbf{E}}^e, D, T) + \rho_0\Psi^p(\delta, \gamma, T)$$

Formally following the classical approach of damage mechanics(Lemaitre, 1996), let us also suppose that

$$\rho_0\Psi^e(\underset{\sim}{\mathbf{E}}^e, D, T) = \frac{1}{2}(1-D)\underset{\sim}{\mathbf{E}}_e : \underset{\approx}{\mathbf{\Lambda}} : \underset{\sim}{\mathbf{E}}_e$$

With $\underset{\sim}{\mathbf{E}}^e$ the Green tensor, and $\underset{\sim}{\sigma}$ the Cauchy stress, and denoting $\underset{\sim}{\mathbf{S}} = \mathcal{J}\underset{\sim}{\mathbf{F}}^{e-1}\underset{\sim}{\sigma}\underset{\sim}{\mathbf{F}}^{e-T}$ and $\underset{\sim}{\mathbf{\Sigma}} = \mathcal{J}\underset{\sim}{\mathbf{F}}^{eT}\underset{\sim}{\sigma}\underset{\sim}{\mathbf{F}}^{e-T}$, the dissipation is

$$(\underset{\sim}{\mathbf{S}} - \rho_0\frac{\partial\Psi}{\partial\underset{\sim}{\mathbf{E}}^e})\dot{\underset{\sim}{\mathbf{E}}}^e + \rho_0\underset{\sim}{\mathbf{\Sigma}} : \underset{\sim}{\mathbf{L}}^p - \rho_0\frac{\partial\Psi}{\partial\delta}\dot{\delta} - \rho_0\frac{\partial\Psi}{\partial\gamma}\dot{\gamma} - \rho_0\frac{\partial\Psi}{\partial D}\dot{D} \geq 0$$

$$\underset{\sim}{\mathbf{L}}^p = (\text{usually } \dot{\underset{\sim}{\mathbf{F}}}^p\underset{\sim}{\mathbf{F}}^p) = \dot{\delta}\underset{\sim}{\mathbf{N}} + \dot{\gamma}\underset{\sim}{\mathbf{T}}$$

$$R_n = \rho_0\frac{\partial\Psi}{\partial\delta} \quad ; \quad R_t = \rho_0\frac{\partial\Psi}{\partial\gamma} \quad ; \quad Y = -\rho_0\frac{\partial\Psi}{\partial D}$$

$$\underset{\sim}{\mathbf{S}} = \rho_0\frac{\partial\Psi}{\partial\underset{\sim}{\mathbf{E}}^e}$$

$$\rho_0\left(\underset{\sim}{\mathbf{\Sigma}} : \underset{\sim}{\mathbf{N}} - R_n\right)\dot{\delta} + \rho_0\left(\underset{\sim}{\mathbf{\Sigma}} : \underset{\sim}{\mathbf{T}} - R_t\right)\dot{\gamma} + \rho_0 Y\dot{D} \geq 0$$

$\underset{\sim}{\mathbf{S}}$ classically associated to $\underset{\sim}{\mathbf{E}}^e$

$\underset{\sim}{\mathbf{\Sigma}}$ used to compute $\sigma_n = \underset{\sim}{\mathbf{\Sigma}} : \underset{\sim}{\mathbf{N}}$ and $\tau = \underset{\sim}{\mathbf{\Sigma}} : \underset{\sim}{\mathbf{T}}$ Choosing the same potentials, as in small deformation case, the equations for D, δ, γ can be kept.

III.5.2 Stress update algorithm

Following the J_2 plasticity example, an implicit numerical scheme can be formally rewritten.

$$\underset{\sim}{\mathbf{L}}^p = \dot{\underset{\sim}{\mathbf{F}}}^{\mathbf{p}} \underset{\sim}{\mathbf{F}}^p = \dot{\delta}\underset{\sim}{\mathbf{N}} + \dot{\gamma}\underset{\sim}{\mathbf{T}}$$

$$\dot{\underset{\sim}{\mathbf{F}}}^{\mathbf{p}} = (\dot{\delta}\underset{\sim}{\mathbf{N}} + \dot{\gamma}\underset{\sim}{\mathbf{T}})\underset{\sim}{\mathbf{F}}^{p-1}$$

$$\underset{\sim}{\mathbf{F}}^p_{n+1} = \underset{\sim}{\mathbf{F}}^p_n \exp(\Delta\delta\underset{\sim}{\mathbf{N}}_{n+1} + \Delta\gamma\underset{\sim}{\mathbf{T}}_{n+1})$$

$$\underset{\sim}{\mathbf{F}}^* = \underset{\sim}{\mathbf{F}}_{n+1}\underset{\sim}{\mathbf{F}}^{p\,-1}_n \qquad ; \qquad \underset{\sim}{\mathbf{F}}^e_{n+1} = \underset{\sim}{\mathbf{F}}_{n+1}\underset{\sim}{\mathbf{F}}^p_{n+1}{}^{-1}$$

$$\begin{aligned}
\underset{\sim}{\mathbf{F}}^* &= \underset{\sim}{\mathbf{F}}^e_{n+1} \exp(\Delta\delta\underset{\sim}{\mathbf{N}}_{n+1} + \Delta\gamma\underset{\sim}{\mathbf{T}}_{n+1}) \\
&\approx \underset{\sim}{\mathbf{F}}^e_{n+1}(\underset{\sim}{\mathbf{I}} + \Delta\delta\underset{\sim}{\mathbf{N}}_{n+1} + \Delta\gamma\underset{\sim}{\mathbf{T}}_{n+1})
\end{aligned}$$

$$\begin{aligned}
\underset{\sim}{\mathbf{F}}^{*T}\underset{\sim}{\mathbf{F}}^* &= (\underset{\sim}{\mathbf{I}} + \Delta\delta\underset{\sim}{\mathbf{N}}_{n+1} + \Delta\gamma\underset{\sim}{\mathbf{T}}_{n+1})^T \underset{\sim}{\mathbf{F}}^{eT}_{n+1}\underset{\sim}{\mathbf{F}}^e_{n+1}(\underset{\sim}{\mathbf{I}} + \Delta\delta\underset{\sim}{\mathbf{N}}_{n+1} + \Delta\gamma\underset{\sim}{\mathbf{T}}_{n+1}) \\
&= \underset{\sim}{\mathbf{F}}^{eT}_{n+1}\underset{\sim}{\mathbf{F}}^e_{n+1} + 2^{\{}(\Delta\delta\underset{\sim}{\mathbf{N}}_{n+1} + \Delta\gamma\underset{\sim}{\mathbf{T}}_{n+1})^T)\underset{\sim}{\mathbf{C}}^e_{n+1}{}^{\}}
\end{aligned}$$

The new $\mathcal{F}^e$ equation in the nonlinear system is:

$$\underset{\sim}{\mathbf{E}}^* = \underset{\sim}{\mathbf{E}}^e_{n+1} + {}^{\{}(\Delta\delta\underset{\sim}{\mathbf{N}}_{n+1} + \Delta\gamma\underset{\sim}{\mathbf{T}}_{n+1})^T)\underset{\sim}{\mathbf{C}}^e_{n+1}{}^{\}}$$

III.5.3 Note on damaged body kinematics under finite strains

Under small strains all body configurations: initial, deformed, damaged - are the same. For finite strains this is no longer true. Thus, one should be able to define damaged body configuration, compared to the initial and deformed ones. Different ways to see the damaged configuration can be found in the literature. For instance, a scheme with fictitious effective configuration is proposed in (Voyiadjis and Deliktas, 2000). A multiscale point of view, based on classical ideas of defects in elastic bodies (Eliseev, 1999), is proposed in (Clayton and McDowell, 2003)(Clayton and McDowell, 2004). DOS model formulation in finite strains, proposed above, is a correct formal extension of the small deformation formalism. It can be seen as using a fictitious undeformed but damaged configuration.

III.6 Conclusion and Perspectives

The final goal of this chapter was to create an efficient implicit integration scheme for a crystal model with damage under finite strains. To do so, it was found necessary to perform a systematical study of more simple models. A number of elastic and J2-plastic models were then implemented into ZéBuLoN. Resulting algorithms were proved to have quadratic convergence. These exercises gave the possibility to find an appropriate shape for the global consistent tangent matrix. It was also found, that even with a multiplicative finite strain formalism, numerical manipulations allow to recover an additive form for the elastic-plastic strain partition. The shape of this equation depends on the type of elasticity, which is used. Then, an implicit integration scheme was applied to the crystal plasticity model. First results for polycrystalline aggregates were obtained with reasonable computation time (about 1 day for the large mesh of fig. III.12-b). Global convergence of the method was then shown to be better, than for a pre-existing explicit integration scheme. Still it is believed to be possible to have better numerical convergence. Proper plastic volume correction, or a slip system choice are to be added to the numerical scheme.

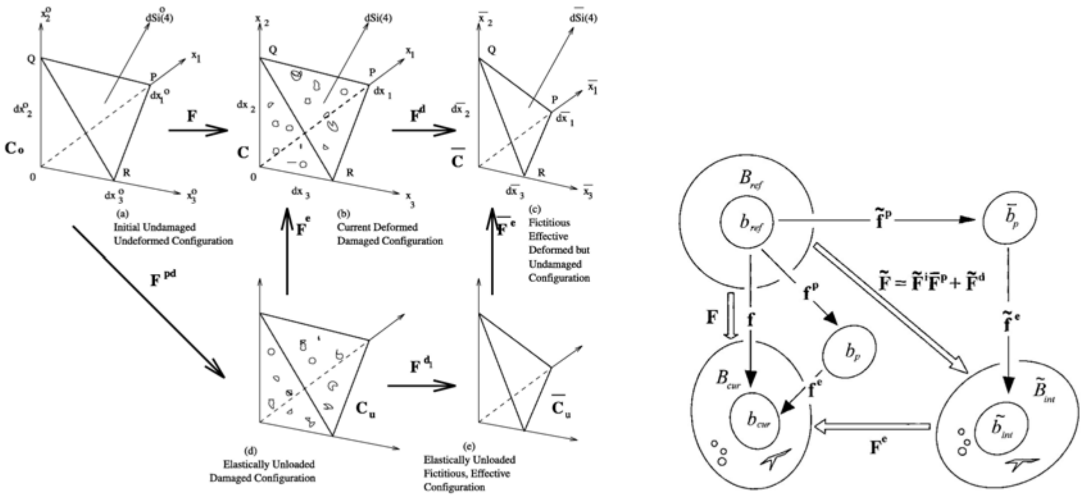
F
F^d
F^pd
F^e
F^d_1
C_o
C
C̄
C_u
C̄_u
Q
P
R
dSi(4)
(a)
Initial Undamaged
Undeformed Configuration
(b)
Current Deformed
Damaged Configuration
(c)
Fictitious
Effective
Deformed but
Undamaged
Configuration
(d)
Elastically Unloaded
Damaged Configuration
(e)
Elastically Unloaded
Fictitious, Effective
Configuration
B_ref
b_ref
b̃_p
f̃^p
F̃ = F̃^i F̃^p + F̃^d
f^p
f̃^e
F
f
b_p
f^e
B_cur
b_cur
B̃_int
b̃_int
F^e

(a) (Voyiadjis and Deliktas, 2000) (b) (Clayton and McDowell, 2003)

Figure III.14 : Possible schemes of damaged body kinematics

Part B

Numerical tools

Chapter -IV-

Finite element meshes

Contents

IV.1 Introduction . . . 57
IV.1.1 Grain boundaries - how to mesh them ? . . . 58
IV.2 Voronoi tessellation to represent grains . . . 58
IV.3 What is done ? . . . 59
IV.3.1 2D . . . 59
IV.3.2 3D . . . 59
IV.4 Perspectives . . . 60

This chapter describes the developments made to ”open grain boundaries” in realistic synthetic aggregates which are obtained by Voronoï tessellation. Both 2D and 3D cases are treated. The new elements are inserted by an automatic procedure as a thin layer between two grains in the finite element mesh. The triple points have a specific numerical treatment.

IV.1 Introduction

When creating a real like finite element mesh, three methods are known from the literature.

1. regular mesh, single phase elements
2. regular mesh, multiphase elements
3. free mesh

The idea of the first one is as follows. Finite element mesh is regular. Realistic grain image is then imposed, and grains represented as the sets of finite elements. It makes meshing problem quite simple, but provides stair-like grain interfaces. One can find examples in (Bhattacharyya et al., 2001) (Clayton and McDowell, 2004)

The second method can be seen as an extension of the previous one. The finite element mesh is still regular, but grains are now presented as sets of Gauss integration points. So that one finite element can be shared by several grains. Grain interfaces are more accurate, but still stair-like. This method was promoted in (Lippmann et al., 1997), an application for crystalline aggregates can be found in (Barbe et al., 2001a).

In the third method, grain regions are meshed directly, with any free mesh techniques. This approach needs an advanced FE meshing procedure, but seems the most natural. It represents exactly the grain interfaces. An example can be found in (Espinosa and Zavattieri, 2003a) (Espinosa and Zavattieri, 2003b).

Which of the three methods can be used to proceed with the grain boundaries ? Actually, the three solutions can be found in the literature. For the first one, (Clayton and McDowell, 2004) can be cited. Successful computations are shown there. One can note, however, some strange periodicity in the resulting cavitation process, which seems to be related to the FE mesh. As for the second one, (Roberts and Garboczi, 2001) can be cited. The paper deals with foam modeling, but one can easily use the same method for a polycrystal. The advantage of the method is that one can easily play with the (grain boundary/grain core) volume ratio.

We choose anyway the third one. An example of its application can be found in (Zhang et al., 2004).

IV.1.1 Grain boundaries - how to mesh them ?

Once we have chosen the free mesh method to construct an aggregate, another question comes : how to mesh grain boundaries ? Several approaches can be found in the literature:

1. zero-width GB,
2. one element width GB,
3. remeshing near GB,
4. no grain boundaries as special interface between grains, but each grain has its core and boundary layer.

The first approach is developed in works of (Tvergaard, 1984)(Tvergaard, 1990)(Needleman, 1987).

Examples of second approach can be found in (Diard et al., 2002).

For the third approach one can note a work of (Weyer et al., 2002). But in (Cizelj and Riesch-Oppermann, 2002) of the same authors, the remeshing is used only to get better precision near grain boundaries.

The idea of the fourth approach can be found in (Evers et al., 2002). A polycrystal model is proposed there, so there is no ”real” mesh for the grain boundaries. Nevertheless, in their model they suppose each grain to have its core region and its grain boundary layer.

In the present document, we will show a comparison between the second and the third solution, to chose the third approach for the computations.

IV.2 Voronoi tessellation to represent grains

Voronoi polyhedra approach is widely used in material science to represent real-like polycrystals –see for instance (Cizelj and Riesch-Oppermann, 2002)(Barbe et al., 2001a)(Barbe et al., 2001b)–.

The method of the aggregate creation is based on the space(plane) division by the Voronoi polyhedra. They were formally identified - for instance - by (Decker and Jeulin, 2000), by means of the *influence zones*. Let $D \subset R^2(R^3)$ to be a real domain, and $E = \{A_i\}$ - a number N of random points, so that $A_i \in D$. Let also $d(P_1, P_2)$ to be a euclidean distance between any points P_1 and P_2. If so, the influence zone of the center A_i can be defined as:

$$zi(A_i) = \{P \in D \mid d(P, A_i) < d(P, A_j) \forall j \neq i\}$$

The polyhedra centers can be distributed in the space, following any random law. In this work, the method using a repulsion distance (like in O.Diard's thesis) is used. This allows to control a minimum size of the grains and to obtain a regular grain size distribution.

IV.3 What is done ?

2D and 3D cases are distinguished. Basically, any aggregate mesh generation, 2D or 3D, consists of two stages. In the first stage, the aggregate itself is generated, without grain boundaries. And then, the grain interfaces are opened to insert the grain boundary finite elements.

The generation of aggregates is a pre-existing capability of the code ZéBuLoN. 2D generation is straightforward with the classical tools of the code. 3D generation respecting the grain boundary is a more difficult problem. Several procedures are under development at the present time. 20-grain and 100-grain 3D meshes were available (Mounoury, 2002)(Cailletaud et al., 2003b).

The generation of grain boundaries for 2D meshes was developed in the framework of O. Diard's thesis (Diard, 2001). Nevertheless, the procedure was reconstructed in the frame of this work, since the developments were no longer adapted to the current version of the code. On the other hand, a better modularity was necessary to produce either one or two interface finite elements in the width of grain boundary.

The procedure for adding one or two elements in 3D grain boundaries was completely developed in the framework of this study.

IV.3.1 2D

As already mentioned, the aggregate creation in 2D is based on the plane division by the Voronoi triangulation. A typical polyhedra structure is shown in Fig.IV.1. This structure is then meshed by quadratic or linear triangular elements. GB lines are respected exactly, a typical result is given in Fig. IV.2 .

A ZéBuLoN module was developed to add the grain boundary elements between the grains. It has to create the elements, and to generate the normal directions defining the grain boundary frame. A typical result is given in Fig.IV.3. Each grain boundary is represented now as a independent element set (elset) –see Fig.IV.5–.

The 2D procedure was also adopted to insert two elements in the GB width –see fig.IV.8– instead of one. It will allow us to use a GB material behavior, based on the relevant grain properties. It will also allow to check the FE mesh density effect.

As any grain –in reality– has 3D anisotropy, this should be taken into account. The 2D meshes are thus extended in the third direction, in order to use a full 3D crystal plasticity model without any additional restrictions on the type of slip system. For the tests of the present work, the mesh of 100 grains was created, with and without grain boundaries. The mesh size (39904 nodes, 7890 elements - with GB) was chosen to be able to perform easy computations on a single processor. This mesh is presented, without GB, in Fig.IV.6 and with the inserted GB structure, in the Fig.IV.7.

IV.3.2 3D

The aggregate creation in the 3D case is also based on the space division by the Voronoi polyhedra. These regions are then meshed with tetrahedral linear (or quadratic) finite elements. As mentioned above, only 20 grain (Fig.IV.9) and 100 grain (Fig.IV.11) meshes are available at the moment.

The automatic procedure was newly developed, to add grain boundary elements in (nearly) arbitrary 3D crystalline aggregate FE mesh. For the grain boundary introduction, in-between any 2 grains, prismatic elements are inserted, while prisms and tetrahedra are needed for the triple lines and quadruple points.

This procedure input is a crystalline aggregate finite element mesh (like in Fig.IV.9). From the geometrical point of view, there are some restrictions for the input.

1. It is quite clear that only 2 grains can have a common plane. But, already a line can be - in principle - sheared by 3 (at least), and also 4, 5 etc grains. This is the restriction of the tool: the input mesh should have only triple lines. In other words, 3 and only 3 grains can have one common line in the mesh.

2. Another important restriction: all the grains are supposed to be convex polyhedra.

3. As for the joints in the multiple points, the procedure is general. Geometrically, even with triple lines only, one can have 4 grains (at least) having one common point, but one can find also 6 grains, 8 grains, and, probably, more. Up to now, only 4, 6 and 8 cases were met in the examples. The proposed procedure can deal with any multiple point, of any topology.

The procedure consists of four basic stages. *First stage*: remesh to avoid too close points. The main idea of this stage, is to avoid multiple points of the grain structure to be in the same finite element. A typical situation before and after this remeshing can be seen in Fig.IV.12. *Second stage*: remesh to avoid too close points –continue–. The idea of this stage is to avoid multiple points to be in one finite element with an opposite triple line. It is quite similar, but not the same, as the first stage. It is probably a field for improvement to glue these 2 stages. *Third stage*: remesh multiple points. The program finds all the finite elements, touching a given multiple point - all these elements are thetrahedra. And then, the program cuts all these elements 2 times, with a radius h and $2h$. The parameter h has a given value. Typical result after remeshing can be seen in Fig.IV.14-a. So, each initial tetrahedron is now made of three finite elements: a small tetrahedron, and two prisms. Each multiple point is now surrounded by two spheres, of radius h and $2h$. *Fourth stage*: add GB lines and planes. This last procedure adds triple line prismatic elements, GB plane prismatic elements, and connects them with the multiple point spheres and initial grains. Line–point connection can be seen in the Fig.IV.13-b. Plane connection is shown in Fig.IV.13-a. The connection of the multipoint to the grain can be seen in Fig.IV.14-b. In principle, any number of grains can be modified by the procedure. Up to now, 20 grain and 100 grain aggregates were made. The CPU time for a 100-grain aggregate (38752 nodes, 127745 linear finite elements) modification is about 4 hours on 3 GHz PC processor. In fact, the CPU is mostly used to paste the various sets of nodes and elements. This procedure is needed to glue the duplicate nodes, which have the same coordinates. The standard ZéBuLoN procedure is used at this stage. It is not well adapted for a large number of elements and sets. This is totally independent from our procedure, and will be improved in the near future.

IV.4 Perspectives

Once the automatic grain boundary insertion procedure is developed, it can be easily modified for the different types of finite elements. Namely, the 3D case was done for linear finite elements only. One can adopt the procedure for the quadratic elements, or the semi-quadratic ones (the elements, which have linear interpolation in grain boundary width direction, but quadratic in grain boundary plane).

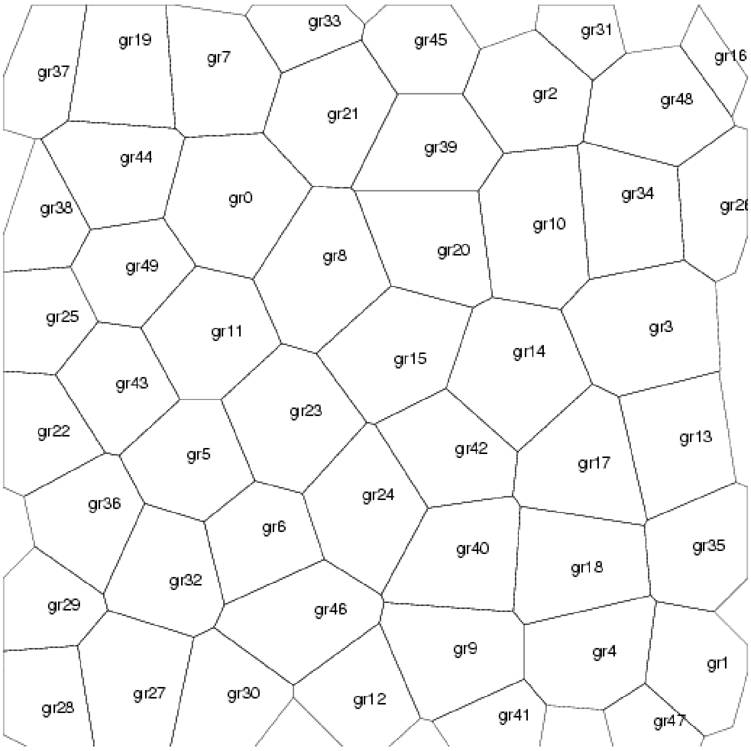
gr37
gr19
gr7
gr33
gr45
gr31
gr16
gr21
gr2
gr48
gr44
gr39
gr0
gr38
gr34
gr2
gr10
gr8
gr20
gr49
gr25
gr3
gr11
gr14
gr15
gr43
gr23
gr13
gr22
gr42
gr17
gr5
gr36
gr24
gr6
gr40
gr35
gr18
gr32
gr29
gr46
gr9
gr4
gr1
gr27
gr30
gr12
gr28
gr41
gr47

Figure IV.1 : Typical image of Voronoi polyhedra

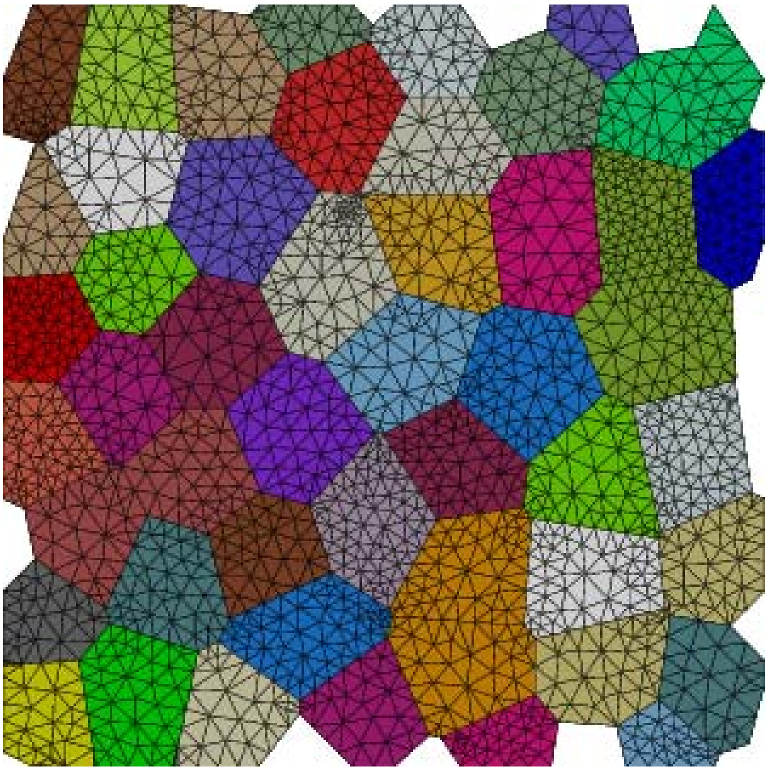

Figure IV.2 : Typical result of 2D mesh generation procedure after step 2

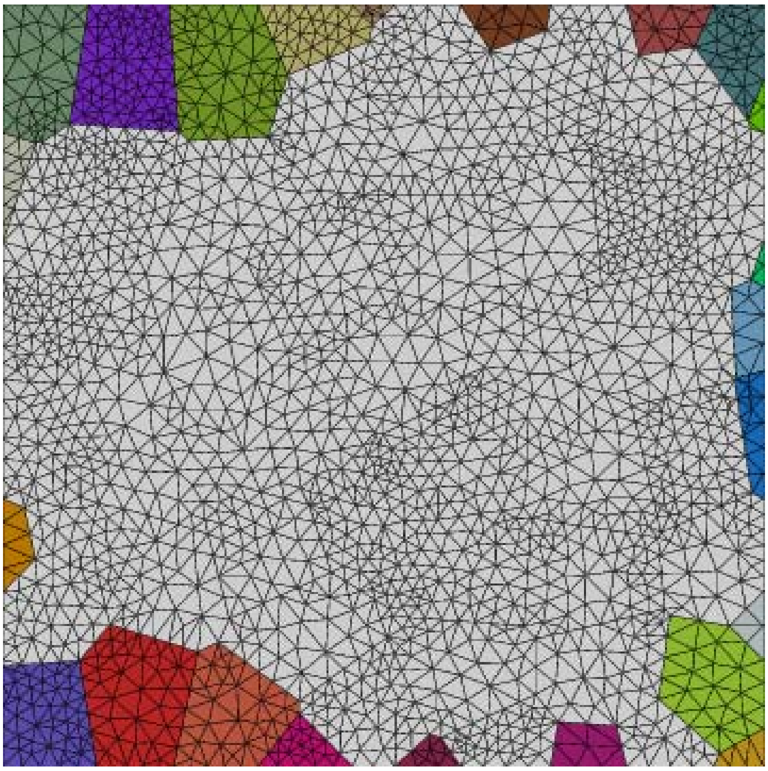

Figure IV.3 : Typical result of 2D mesh generation procedure after step 3

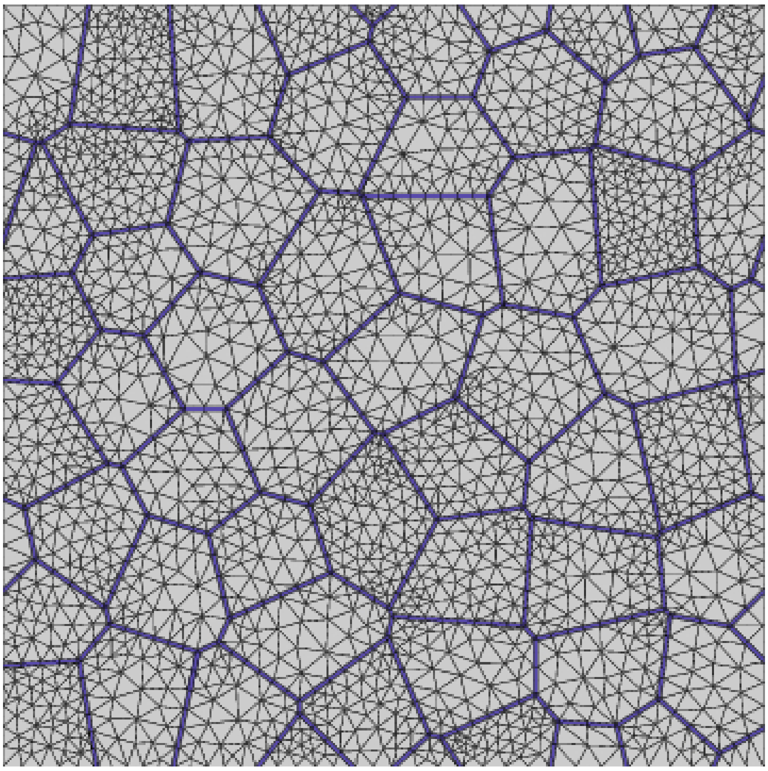

Figure IV.4 : Typical final result of 2D mesh generation procedure

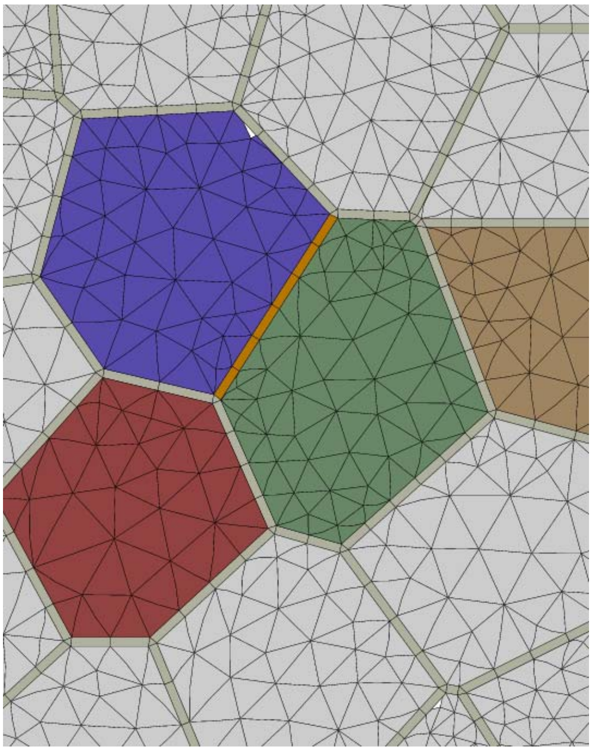

Figure IV.5 : Definition of grain boundary as a set of finite elements

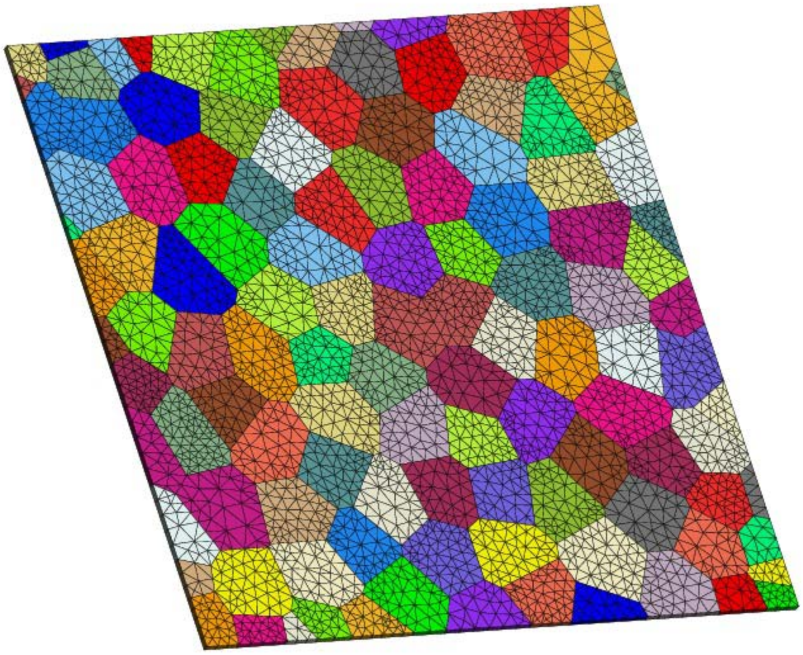

Figure IV.6 : 2d extended mesh of 100 grains, used for computations

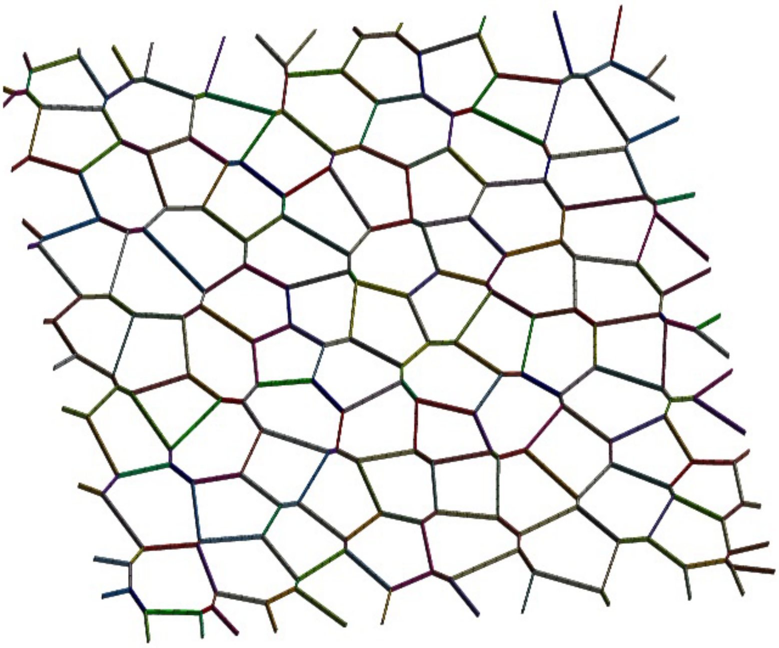

Figure IV.7 : Grain boundaries for 100 grain mesh

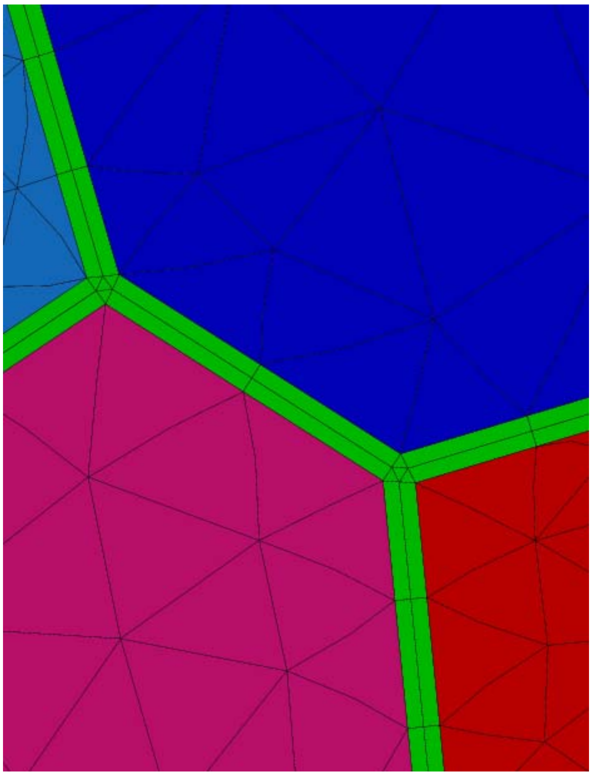

Figure IV.8 : Grain boundaries, two elements by width

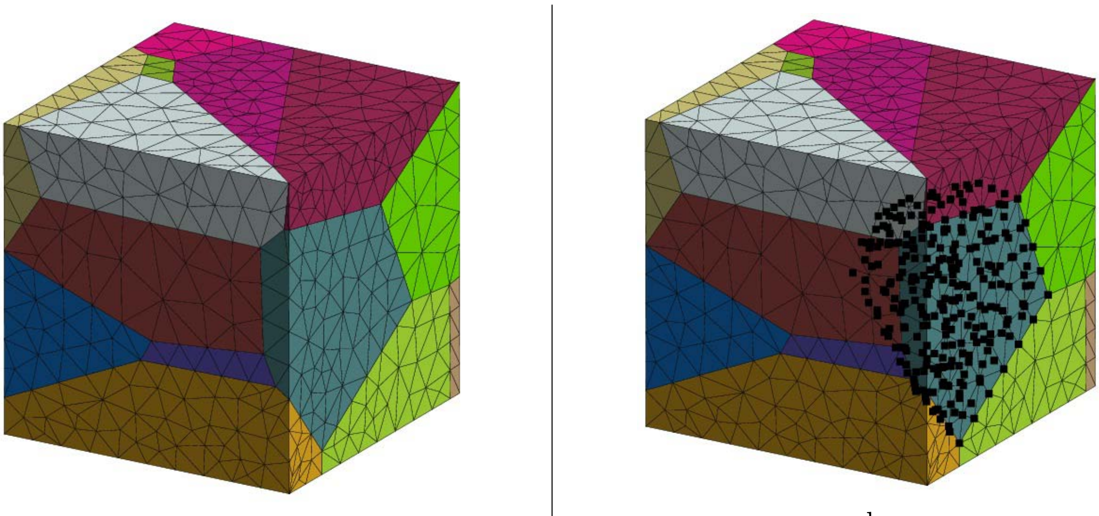

a b

Figure IV.9 : 3D finite element mesh without grain boundaries, (a) - elsets view, (b) - one nset example

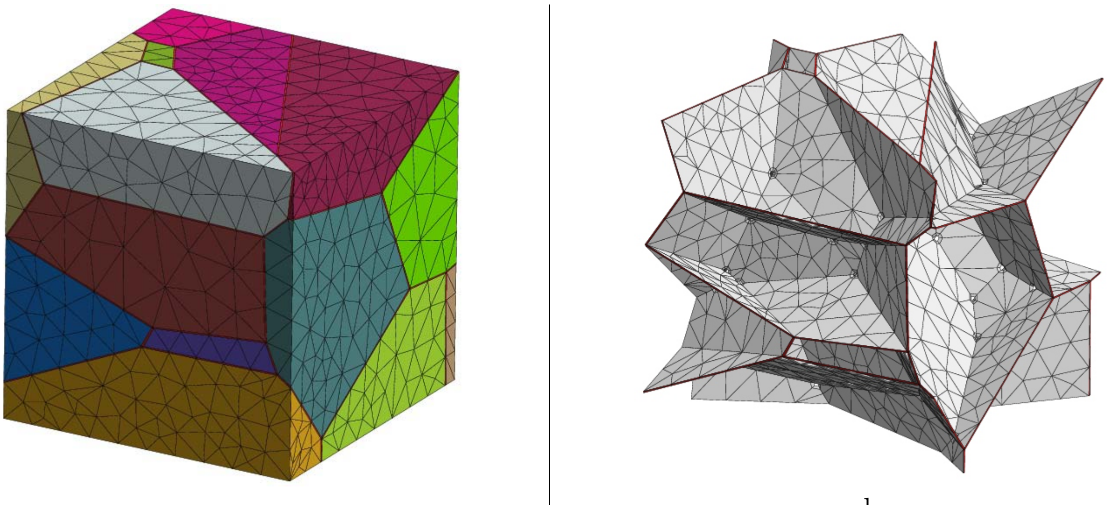

a b

Figure IV.10 : 3D finite element mesh with grain boundaries, (a) - outside view of the 20-grain aggregate, (b) - GB only for the same aggregate

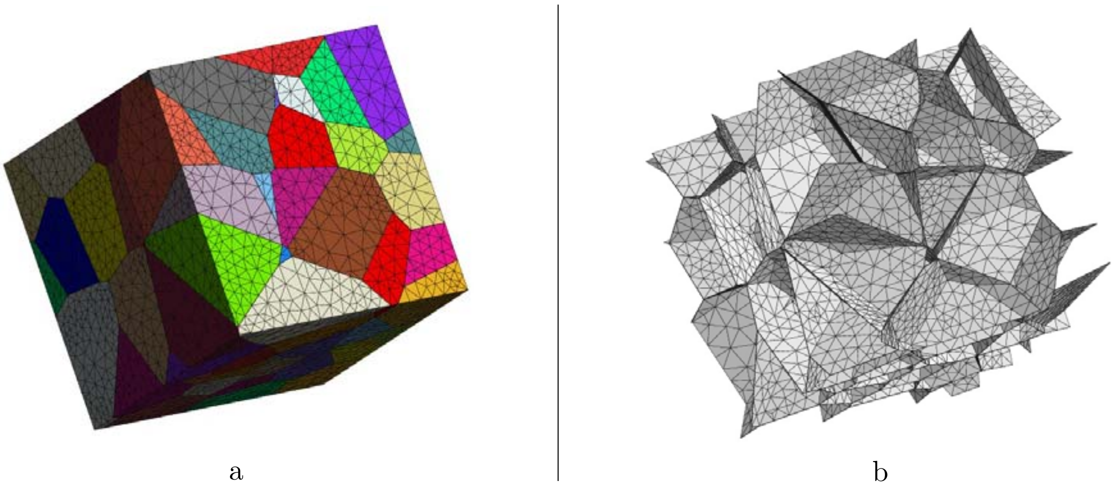

Figure IV.11 : 3D finite element mesh with grain boundaries, (a) - outside view of the 100-grain aggregate, (b) - GB only for the same aggregate

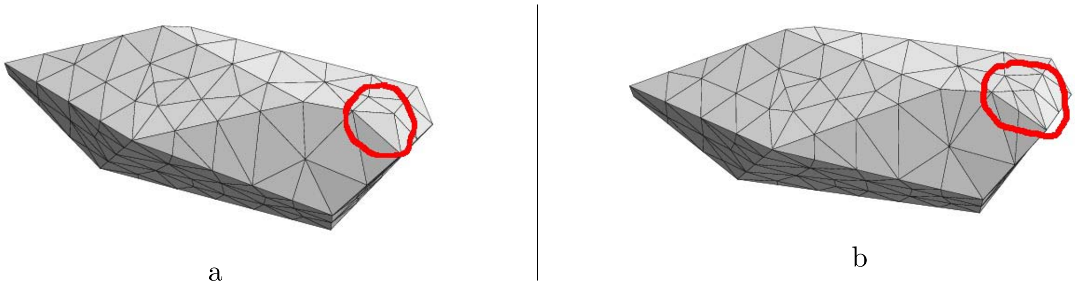

Figure IV.12 : Remeshing for two close multiple points

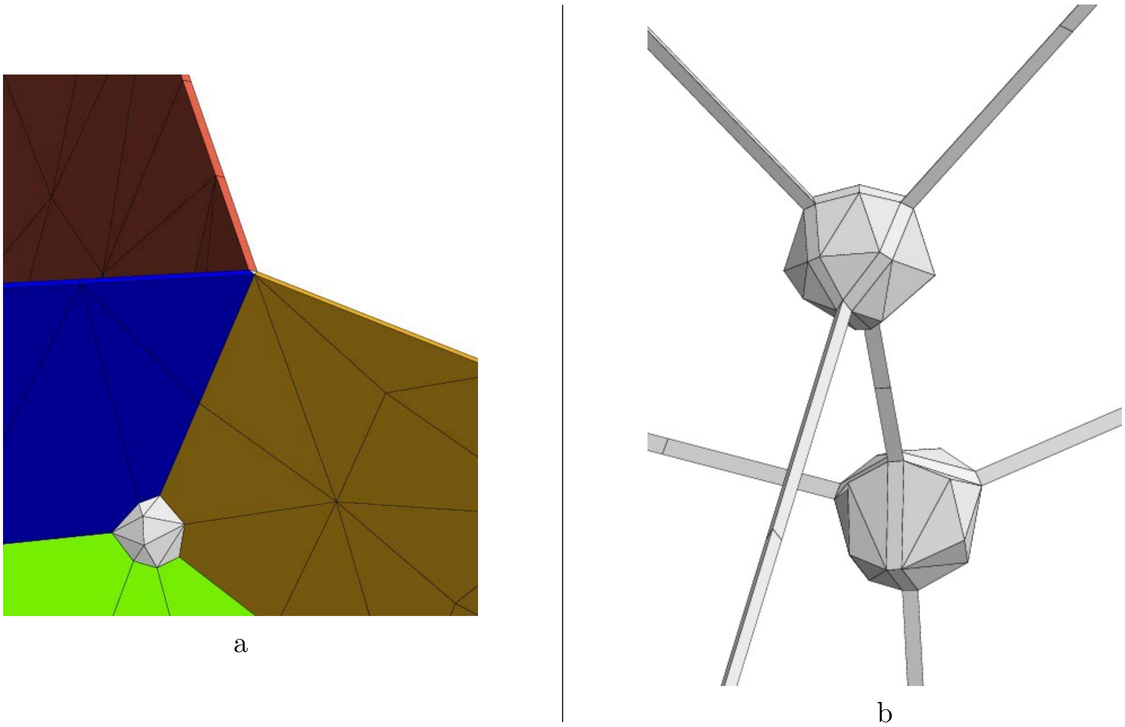

Figure IV.13 : (a) - Four GB planes with a multiple point, (b) - Two multiple points connected with a triple line

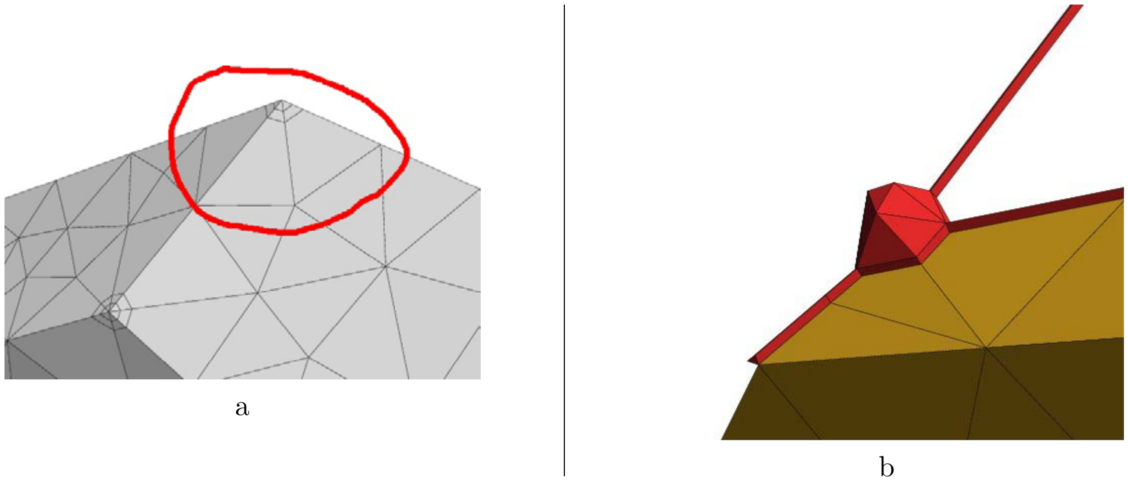

a

b

Figure IV.14 : (a) - Remeshing near a multiple point, (b) - multiple point and triple lines FE structure with a grain

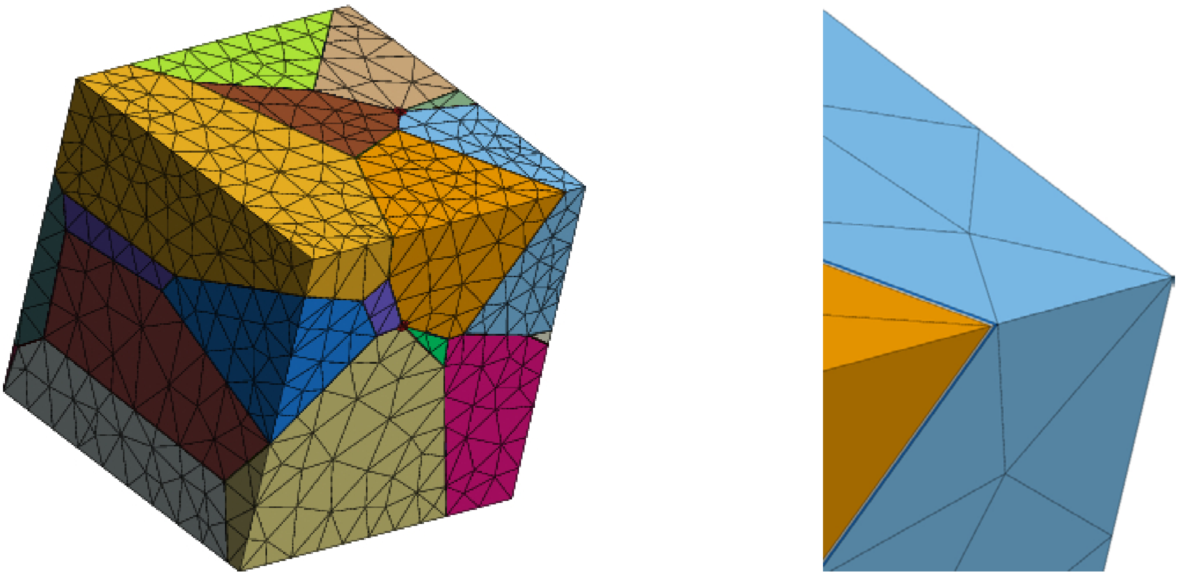

(a) all

(b) detail

Figure IV.15 : Two element per width grain boundaries for 3D case

Table IV.1 : List of actual FE meshes, used in the computations

Notation	Dimension	With/without GB	Quad/Lin	Grains	Nodes	Elements
100gr2dext	extended 2d[a]	no GB	quadratic	115	30551	6679
100gr2dextGB	extended 2d	GB[b]	quadratic	115	38693	7890
100gr2dextGBlin	extended 2d	GB	linear	115	9166	7890
100gr2dextGB2ele	extended 2d	GB: 2 FE/width[c]	quadratic	115	48473	9465
100gr2dextGB2eleLin	extended 2d	GB: 2 FE/width	linear	115	11818	9465
20gr3d	3d	no GB	linear	20	2129	10326
20gr3dGB	3d	GB	linear	20	4763	14934
20gr3dGB2ele	3d	GB	quadratic	20	36114	18081
100gr3d	3d	no GB	linear	100	15940	86751
100gr3dGB	3d	GB	linear	100	38752	127745

---

[a] 2d mesh, extended in the third direction for 1 element depth

[b] grain boundaries with 1 element per width

[c] grain boundaries with 2 elements per width

Chapter -V-

Coupled computation principle

The method of weak coupling was used to take into account the environmental effect. This method is a pre-existing tool of the code ZéBuLoN. The principle of the method is presented in the schema – see fig.V.1 – .

Iodine adsorption is simulated by the solution of a diffusional problem, based on classical Fick's laws:

$$\underline{\mathbf{J}} = \mathbf{D} \cdot \nabla C$$

$$\frac{\partial C}{\partial t} = \mathbf{D} \cdot \Delta C$$

Here C - concentration, $\mathbf{D}$ - diffusion coefficient, $\underline{\mathbf{J}}$ - material flux.

The diffusion coefficient strongly depends on damage. Consequently, iodine propagation follows damage front in the GB. From a numerical point of view, the coupling is obtained by running two simultaneous problems, which are coupled at each time step. For each integration step, the diffusion problem is solved first. Iodine concentration is then exported to the mechanical problem to compute concentration dependent parameters. With these newly obtained parameters, the mechanical problem is solved. It provides stress, strain and damage fields. Damage is then exported to the diffusion problem, to compute damage dependent parameters, and recompute the same time step. For each time step, a fixed point algorithm is then introduced. At least two loops are performed for each time step (diffusion-mechanics-diffusion-mechanics).

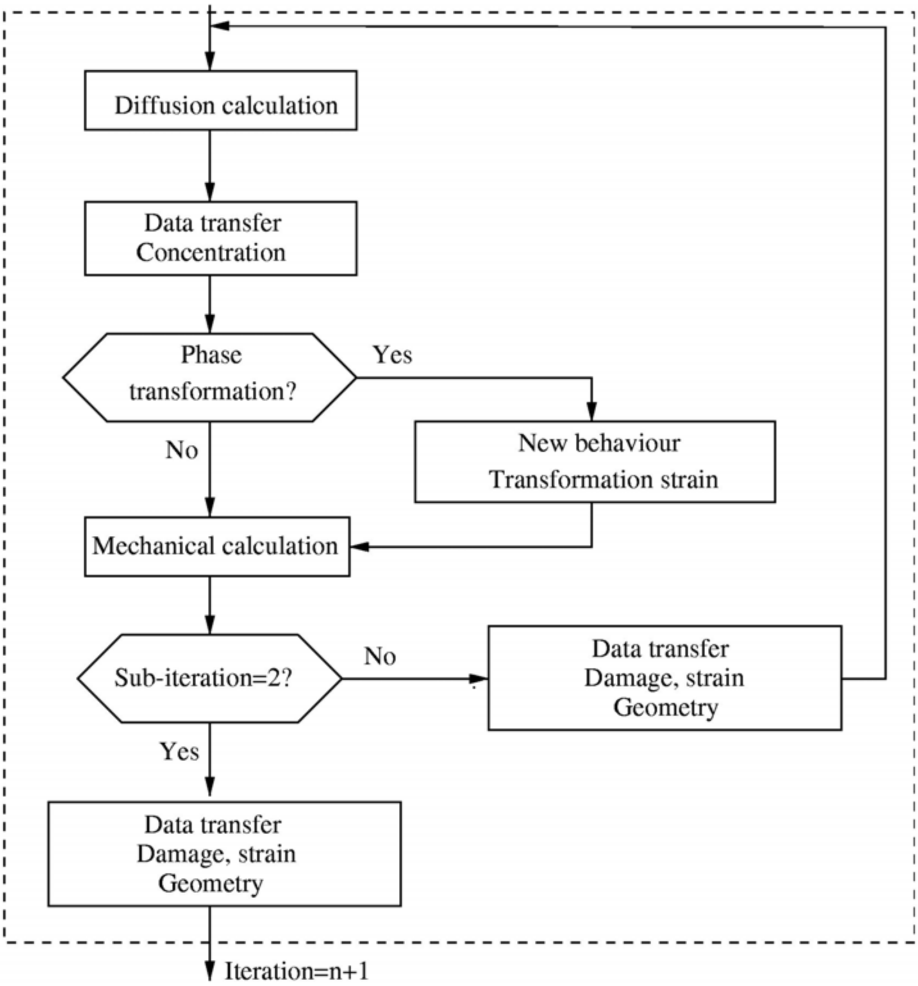
Diffusion calculation
Data transfer
Concentration
Phase
transformation?
Yes
No
New behaviour
Transformation strain
Mechanical calculation
Sub-iteration=2?
No
Data transfer
Damage, strain
Geometry
Yes
Data transfer
Damage, strain
Geometry
Iteration=n+1

Figure V.1 : Schema, illustrating the coupled computation principle

Part C

Applications

Chapter -VI-

FE simulation of multicrystals at large strains

Contents

VI.1 Experiments 74
VI.2 Finite element meshes 74
VI.3 Material Parameter identification 75
VI.4 Note on the grain orientations 78
VI.5 Boundary conditions 79
VI.6 Results 79
VI.7 Discussion and Perspectives 81

One of the interesting possibilities of crystal plasticity approach is to simulate real 3D microstructures, in order to check the validity of the model.

The earliest work of that type was done on brass in 1983 (Hashimoto and Margolin, 1983a)(Hashimoto and Margolin, 1983b). Since then, number of works were done on copper (Teodosiu et al., 1993) (Delaire et al., 2000), aluminum (Becker and Panchanadeeswaran, 1995)(Bhattacharyya et al., 2001) (Sachtleber et al., 2002) and IF steel (Erieau and Rey, 2004). Let us also mention the purely experimental works, which could serve as a basis for the computations (Schroeter and McDowell, 2003) (Zhang and Tong, 2004).

The single crystal model used in this work was shown to give good results when compared to tests on single crystal tension-compression specimens, and also on more complex configurations, like copper bicrystals (Meric et al., 1991)(Meric et al., 1994), or multicrystalline specimens with large grain size (Eberl, 2000).

The present study has two purposes:

- Check the single crystal model possibilities to predict the local behavior of real multicrystal with fully 3D grain morphology
- Check the influence of 3D grain morphology on the surface strain field predictions of the theory.

In what follows, experiments on OFHC (oxygen free high conductivity) polycrystalline copper are described first. Then the finite element mesh is treated, as well as the parameter identification procedure. Computational results are presented for surface strain fields and the average stress-strain curve.

VI.1 Experiments

The material testing procedure shown in the study was developed at the Erich Schmid Institute of Material Science in Leoben, Austria by O.Kolednik and co-authors (see for inst. (Tatschl and Kolednik, 2002a) (Tatschl and Kolednik, 2002b)). Tension tests on polycrystalline OFHC (oxygen-free high conductivity) copper polycrystalline specimens were made (Tatschl, 2000). Specimens with a cross section at 2x2 mm and a gauge length of 10 mm were used. In steps of about 1% SEM-micrographs were taken; the maximum global tensile strain was 10 %. An image comparison system is used to process the micrographs and compute the local strain fields. The key part of the system is a digital image analysis system to find homologue points on two micrographs taken at different loading stages, i.e. points in the images that belong to the same physical point on the specimen. The homologue points form a displacement field which is derived numerically to determine the local in-plane strain increments of the considered deformation step. The analyzed area was 250x350 μm. Orientation Image Microscopy (OIM) analyses were conducted to measure the local grain orientation before the loading, then at 5 and 10% strain. Since the real geometry of the grain is supposed to have a large influence on the observed results, a huge effort was made to characterize the 3D geometry of the grains (Schmidegg, 2000). After the test, six layers of material were successively removed by an electropolishing process, and an OIM-analysis was made after each removal. As a result, we get the local crystal orientation at the depth of 20, 35, 53, 64, 82, and 100 μm below the initial surface from which the three-dimensional (3D) grain structure of the near-surface region can be reconstructed.

The following experimental results were obtained:

- the macroscopic stress-strain curve for the whole specimen (Fig.VI.1)
- SEM-micrographs after different loading stages (typical images are presented in Fig.VI.2)
- surface strain fields (presented in Fig.VI.3), derived numerically from the displacement field. The last one, not presented here, was obtained by digital image analysis from SEM-micrographs.
- OIM analysis results, presented as an inverse pole figure maps (typical images presented in Fig.VI.4).

VI.2 Finite element meshes

Starting from the OIM-analyses of the different layers, two 3D finite element meshes were created (Schmidegg, 2000). Namely, one mesh with 30000 nodes (”small”) and a refined mesh with 130000 nodes (”big”). They are presented in Fig. VI.5. In total, the core region consists of about 100 grains.

In order to check the influence of 3D morphology, another mesh was added to this collection. It is built by means of a simple extrusion of the surface of the specimen. Its thickness is the same as the thickness of the normal aggregate. Since the geometry is much simpler (columnar grains), the size of the mesh is much smaller (14076 nodes). It will be called ”extended small” mesh –see fig. VI.6–. In figure VI.7, EBSD-micrographs, ”small” and ”extended small” meshes view are presented for the specimen outside surface and for the last cut with an EBSD measurement (about 100 μm far from the external surface). Both ”small” and ”extended small” meshes follow EBSD-micrograph on the specimen surface. In the depth, the ”small” mesh still follows EBSD-micrograph, which changes significantly. On the other hand, the view of ”extended small” mesh remains the same, as on the surface.

In order to check if a better result can be used by embedding the mesh in an other equivalent material to regularize the boundary conditions, an other type of mesh was generated. In this last case, both core region meshes (”small” and ”big”) were extended laterally and into the depth: each near-surface mesh was automatically embedded into a second mesh as shown in Fig.VI.6. Two combined meshes, the ”modified small” (54690 nodes) and the ”modified big” (185258 nodes) were so obtained.

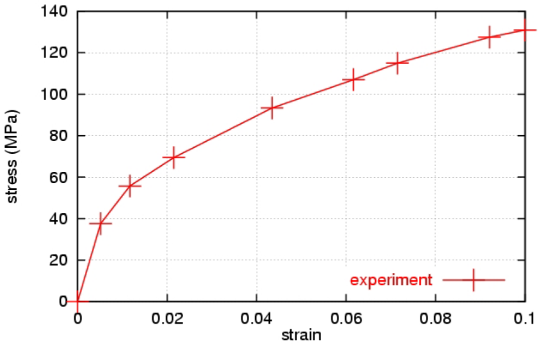

Figure VI.1 : Macroscopic strain-stress curve

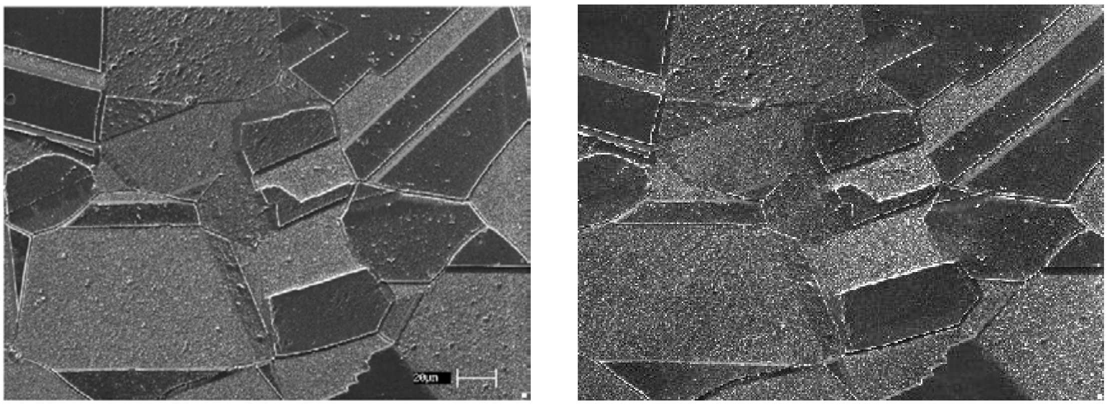

Figure VI.2 : SEM micrographs at 0% and 10% macrostrains

VI.3 Material Parameter identification

The single crystal model, explained in Chapter 1, was applied.

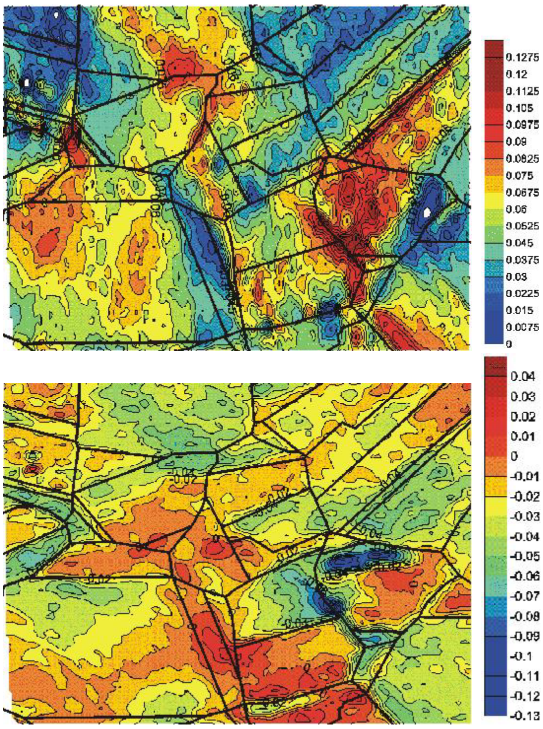

Figure VI.3 : Strains in tensile and transverse directions at 5% macrostrain (exp.)

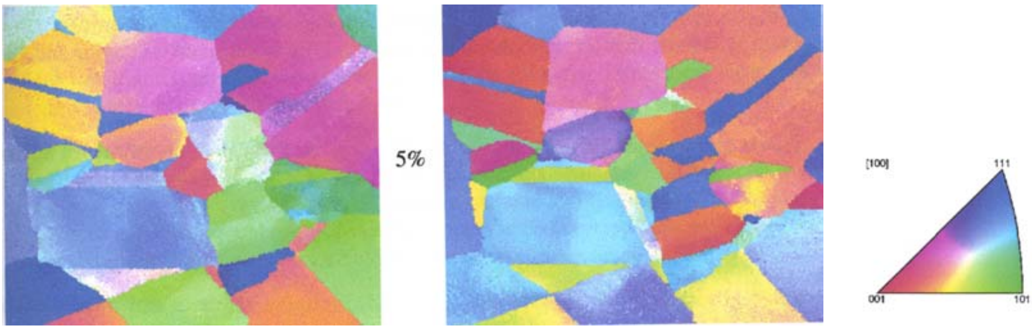

Figure VI.4 : Inversed pole figure maps for the tensile and normal directions at 5% macrostrain

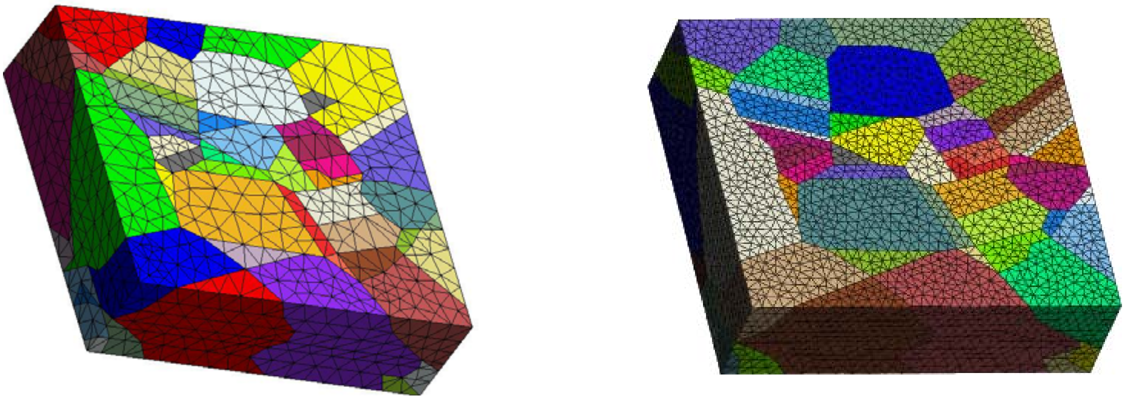

Figure VI.5 : "Small" and "big" finite element meshes

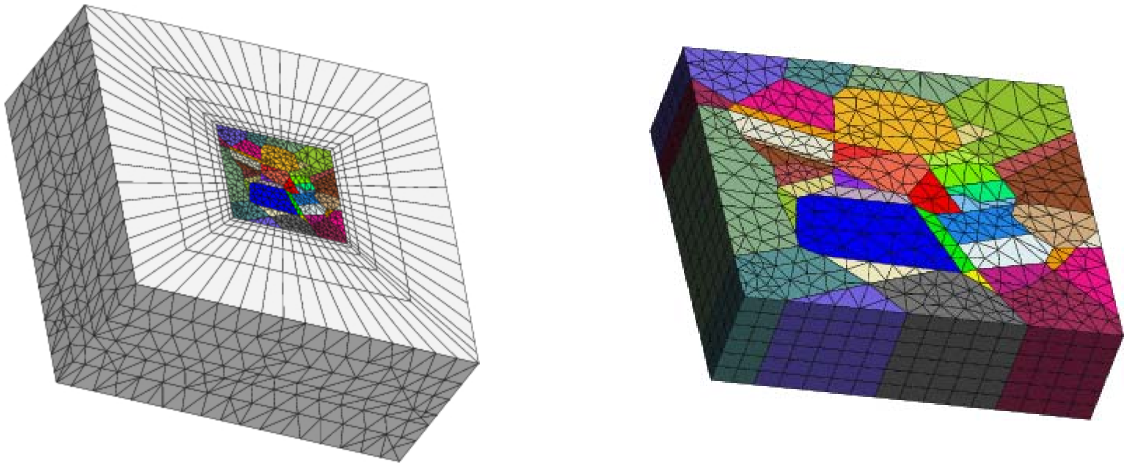

Figure VI.6 : ”Modified small” and ”extended small” finite element meshes

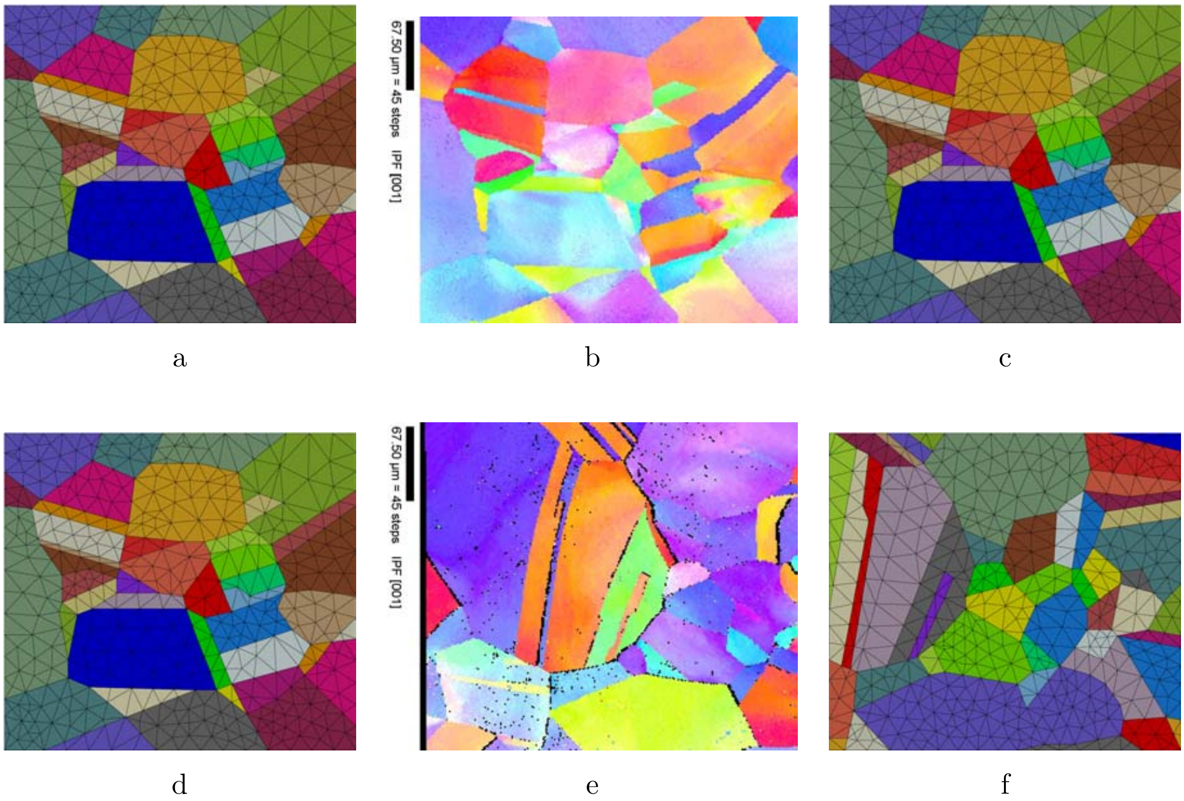
67.50 µm = 45 steps IPF [001]
67.50 µm = 45 steps IPF [001]

a b c

d e f

Figure VI.7 : Surface views (a,b,c) and cut at 100 μm (d,e,f); comparisons between the 2D extended mesh (no change between a and d), the EBSD microsgraph (real structure in b and e) and the 3D mesh (mesh update in agreement with experiment, in c and f)

Elastic material parameters for copper crystals were taken from the literature. Parameters from three literature sources (Shtremel, 1997) (Meric et al., 1994) (Kalidindi and Anand, 1994) were compared and they were found to be quite close to each other. The parameters from (Meric et al., 1994) were taken for our modeling, namely

$$L_{1111} = 159300 \text{ MPa} \qquad L_{1122} = 121900 \text{ MPa} \qquad L_{1212} = 80900 \text{ MPa}$$

The plasticity parameters were initially identified for a cyclic loading test of copper single crystals (Meric et al., 1994). The maximal strain in these tests was 0.1-0.5 %.

For the present tension test, the maximal strain is 10%. The material parameters were adapted to fit with this new range, specially those which define isotropic (Q,b) and kinematic (C,D) hardening (Schmidegg, 2000). The interaction matrix (h_{ij}) and viscosity parameters (K,n) were kept from (Meric et al., 1994). The final parameter set, used in computations is as follows.

$$\text{K=5MPa} \cdot s^{\frac{1}{n}} \quad \text{n} = 10 \quad \text{C=4500MPa} \quad \text{D=600.0}$$
$$R_0\text{=1.8MPa} \quad \text{Q=6MPa} \quad \text{b=15}$$

$$h_1 = 1.0 \qquad h_2 = 4.4 \qquad h_3 = 4.75 \qquad h_4 = 4.75 \qquad h_5 = 4.75 \qquad h_6 = 5.0$$

VI.4 Note on the grain orientations

Crystallographic orientation should be given for each grain to simulate its physical anisotropy. Numerical values of grain orientations are known from OIM-experimental results. But one has to take care about the correct application of these measurements in the simulations. One should verify the coincidence of the following terms between finite element simulation and EBSD measurements:

1. the Euler angle formalism,
2. the rotation applied from the specimen coordinates to the crystal coordinates,
3. the specimen coordinate system.

In the present case, both ZéBuLoN and EBSD follow the so-called Bunge type of Euler angles. It means, that the transformation happens by means of three sequential rotations, around Z axe first, than about new X, and then about new Z. The angles are named ϕ_1, ψ, ϕ_2 respectively. Appropriate rotations are shown in fig.VI.4 It was also found, that this rotation transforms vectors *from specimen coordinates to the crystal coordinates.*

It means, that to get actual vector $\underline{\mathbf{v}}_a$ one has to multiply the original vector $\underline{\mathbf{v}}_o$ by the rotation matrix $\underset{\sim}{\mathbf{R}}$.

$$\underline{\mathbf{v}}_a = \underset{\sim}{\mathbf{R}} \cdot \underline{\mathbf{v}}_o$$

The rotation matrix $\underset{\sim}{\mathbf{R}}$, also called Bunge matrix, is as follows:

$$\underset{\sim}{\mathbf{R}} = \left\{ \begin{array}{lll} c_1c_2 - s_1s_2c_g & s_1c_2 + c_1s_2c_g & s_2s_g \\ -c_1s_2 - s_1c_2c_g & -s_1s_2 + c_1c_2c_g & c_2s_g \\ s_1s_g & -c_1s_g & c_g \end{array} \right\} \tag{VI.1}$$

with $c_1 = cos\phi_1 \quad s_1 = sin\phi_1 \quad c_2 = cos\phi_2 \quad s_2 = sin\phi_2 \quad c_g = cos\psi \quad s_g = sin\psi$

On the other hand, the specimen coordinate system for EBSD measurements and finite element mesh is not the same. If fig. VI.9 the EBSD results and finite element mesh are presented as seen with appropriate software. One can note that to get EBSD reference from ZéBuLoN reference, one has to add a 180°rotation around Z-axis.

Finally, if $(\phi_1 \quad \psi \quad \phi_2)$ are the EBSD measured angles, one should take for ZéBuLoN computation $(\phi_1 + \pi \quad \psi \quad \phi_2)$ [1].

VI.5 Boundary conditions

The displacements were prescribed for all the surfaces except the top surface, which was free. The given displacements values were as follows.

$$\underline{\mathbf{u}} = \underset{\sim}{\epsilon} \cdot \underline{\mathbf{x}}$$

$$\underset{\sim}{\epsilon} = (0.10, -0.04933, -0.04933)$$

VI.6 Results

The average stress σ_{11} (sig11) *versus* average strain ε_{11} (eto11) curve for the whole structure can be obtained by means of a self-consistent approach, using the single crystal material parameters and a material without any texture. The result can then be compared with the experimental macroscopic curve. This is made in Fig.VI.12. One can mention than these two curves are in agreement. Interestingly, they coincide also with the results obtained with the FE aggregates: this demonstrates that the 100-grain sampling is not far from being a Representative Volume Element, and that the mesh is reasonably fine to accommodate the local strain gradients.

A qualitative comparison of the local strain components (ε_{11} and ε_{22}) is now made for the specimen surface. The strain fields are presented in figs.VI.14, VI.15. A good agreement is found for the positions of low (blue color) and high (red color) strain zones.

---

[1] This last artefact was finally exhibited and solved by Thomas Dick, who is gratefully acknowledged here

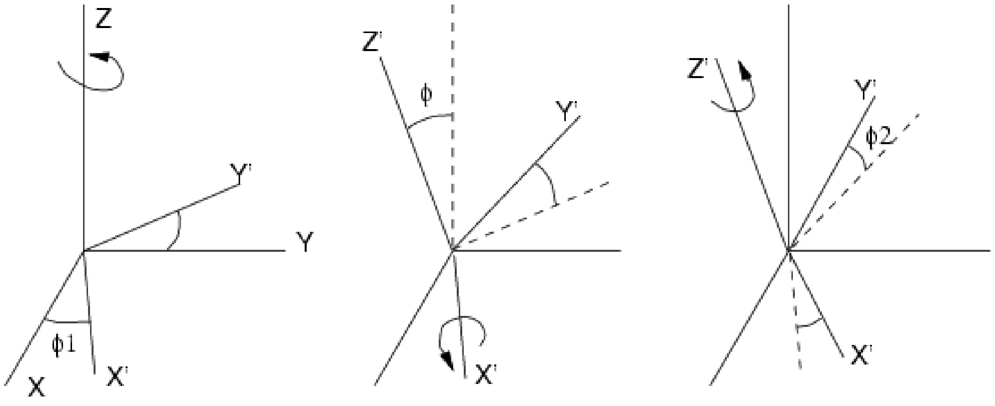

Figure VI.8 : Euler angles rotation

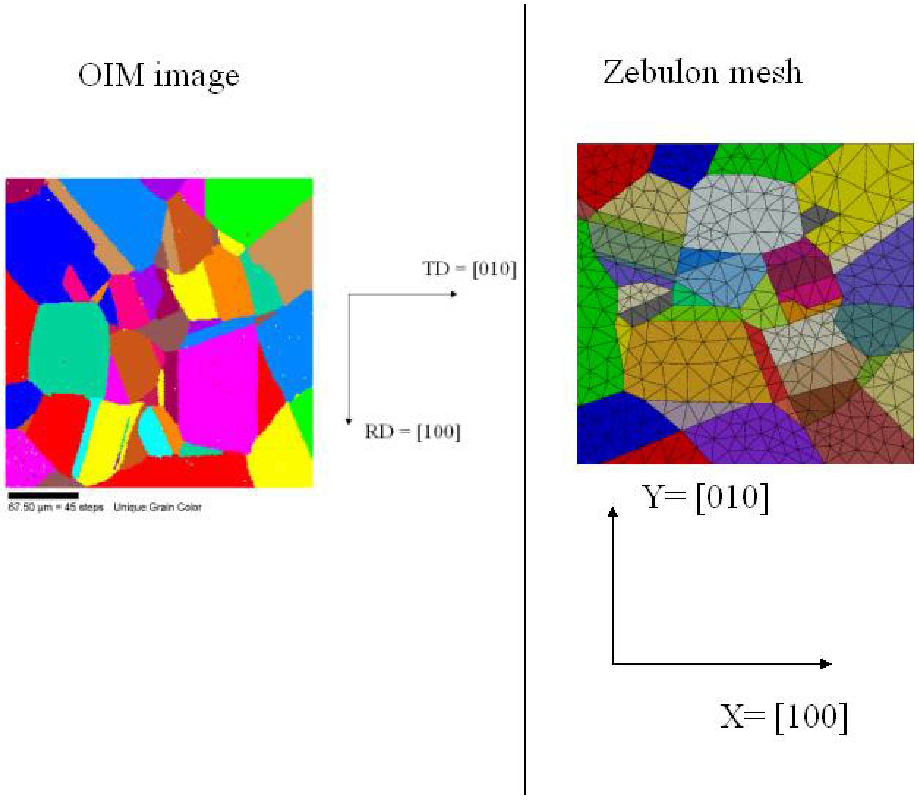
OIM image
TD = [010]
RD = [100]
67.50 µm = 45 steps Unique Grain Color
Zebulon mesh
Y= [010]
X= [100]

Figure VI.9 : Grain orientation references for experiment and simulation

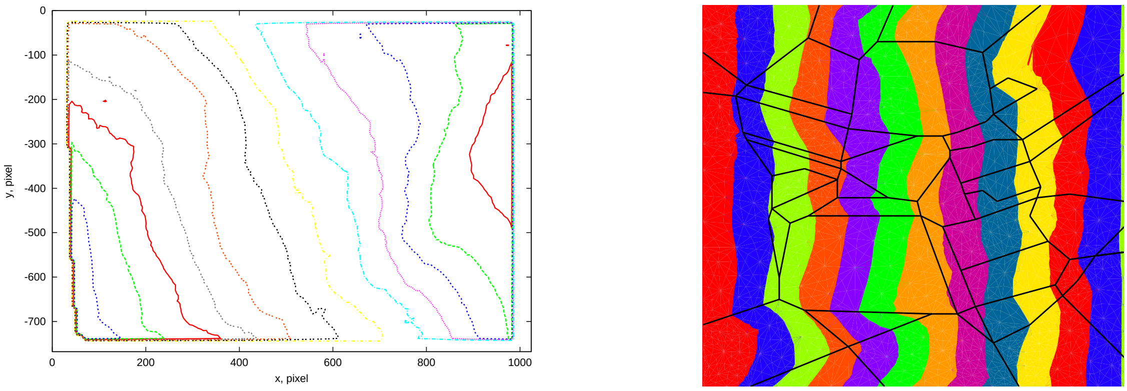

Figure VI.10 : Displacement field –Ux component– experiment and computation

A more quantitative comparison is made, by plotting a strain profile (Profile 1 in fig. VI.11) from both numerical simulation and experiment –see Fig. VI.13–. The results are then quite satisfactory.

If the "extended small" mesh is now used, one can observe important differences between this solution and the full 3D case –see fig.VI.16, VI.17–. A better agreement with experiment is found with the 3D mesh.

VI.7 Discussion and Perspectives

Let us list here assumptions made to achieve the just explained result:

- The finite element mesh used in the analysis remains coarse (30000 nodes for about 100 grains, i.e. 300 nodes/grain. As a reference, to reach 0.1% precision 114375 nodes for 52 grains, i.e. 2200 nodes/grain were taken in (Zeghadi et al., 2005); while changing a cubic mesh from 12x12x12 elements, 8000 nodes to 24x24x24 - 60000 nodes for 200 grains, 10 % of local field change reported in (Barbe et al., 2001a)). Some small grains were therefore neglected in the present computation.

- The material parameters set is probably not unique. Since the amount of experimental data is reduced, one could consider for instance other values for the interaction matrix. A still open discussion concerns the cross-hardening terms. They were taken around 1.4 in (Kalidindi and Anand, 1994). This is also the value proposed by Kocks on aluminium (Kocks and Brown, 1966) or Franciosi (Franciosi, 1985). After Méric, we have a value of about 5. Let us note first that these values are inputs of different expressions for describing latent hardening, so that the values cannot be compared directly. On the other hand, recent simulations by discrete dislocation dynamics tend to demonstrate that values smaller than 1 should be preferable – see for instance (Madec, 2001) – Anyway, it would be interesting to check the sensitivity of the results to this term.

- Boundary conditions are not absolutely realistic. Figure VI.10 shows a comparison of the displacement contours taken from computation and experiment. For the sake of simplicity, the imposed displacement was uniform on the left and right side of the mesh. Nevertheless, the experimental profile is rather diagonal. This can be interpreted as a presence of a local bending applied by the surrounding on the set of grains.

Despite all these approximations, the computational results of the full 3D mesh are in good agreement with experimental data. On the other hand, results for 2D extended mesh were found to be different from the 3D case, but still with some traces of experimental behavior.

Therefore, the following perspectives are open for this part of the study:

1. *Improvement of the obtained computational results*: use a refined finite element mesh, like the already existing "big" mesh; verify material parameters; apply measured displacements as boundary conditions;

2. *Improve comparison between experimental and computational results*: in order to find a tolerance of finite element predictions compared to experiment;

3. *Improve comparison between 3D, extended 2D computations and experimental data*: one should be able to judge, what is true and what is wrong in extended 2D computation compared to 3D;

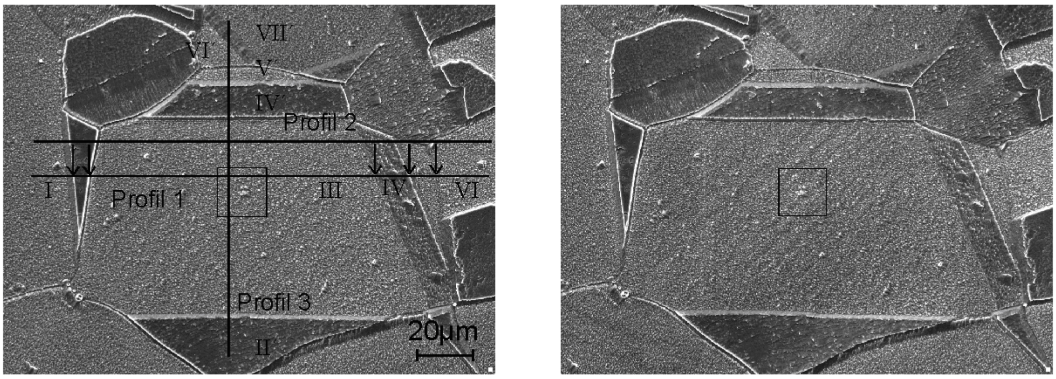

Figure VI.11 : SEM image (fragment) at 0% and 10% macrostrain, with profiles to plot local behavior (Tatschl, 2000)

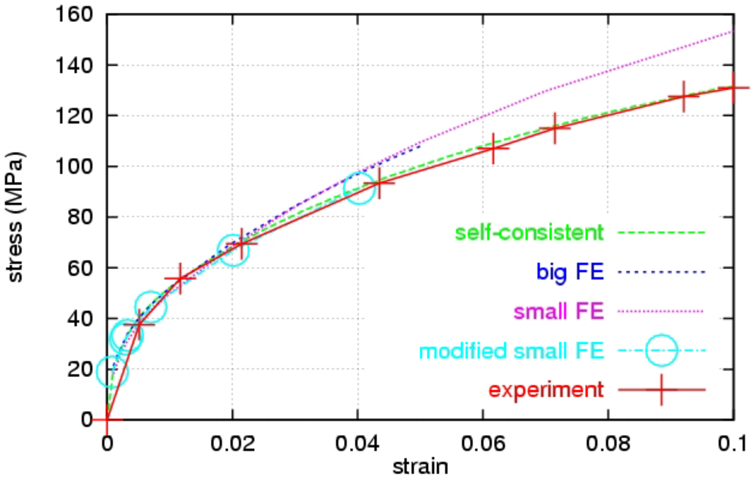

Figure VI.12 : Total average $\epsilon_{11} - \sigma_{11}$ curves

4. *Formulate relations* between surface measurements and 3D strain fields;

5. *Create a procedure of 3D morphology reconstruction*: starting from surface field measurements;

6. *Use the field information to identify the single crystal model parameters from the whole experimental data*: such a procedure is proposed for instance in (Hoc et al., 2003).

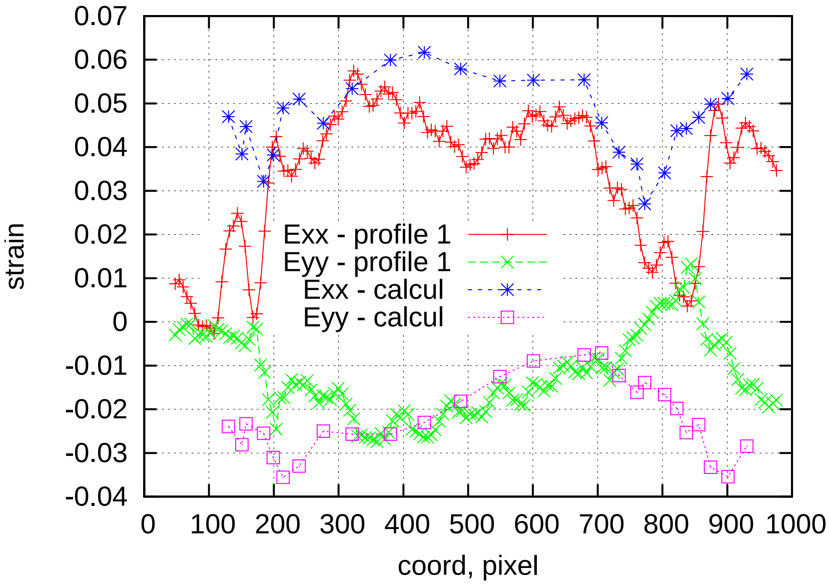

Figure VI.13 : Local strains for Profile1

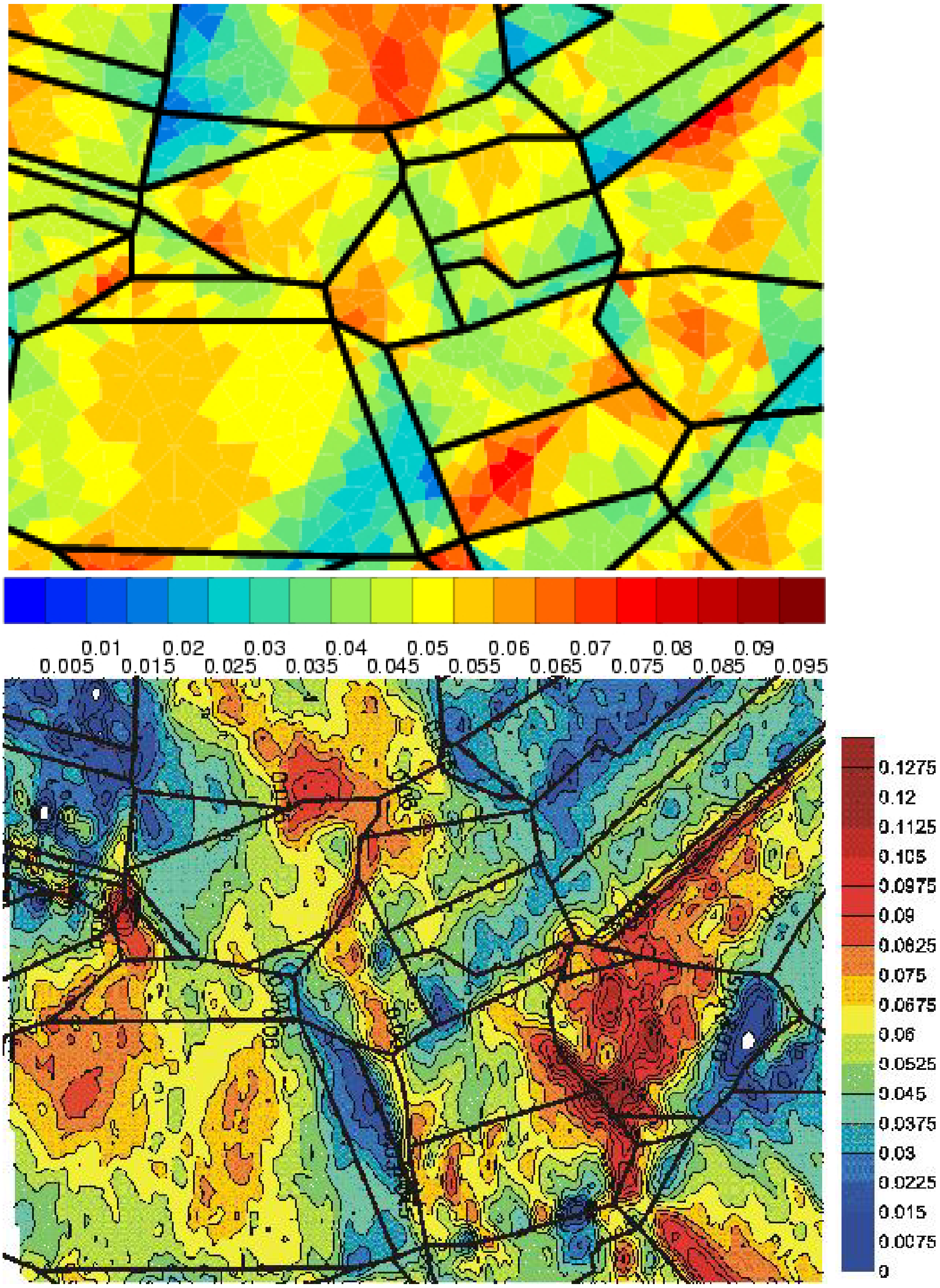

Figure VI.14 : Comparison for ϵ_{11} at 5% macrostrain ("small" mesh and experiment)

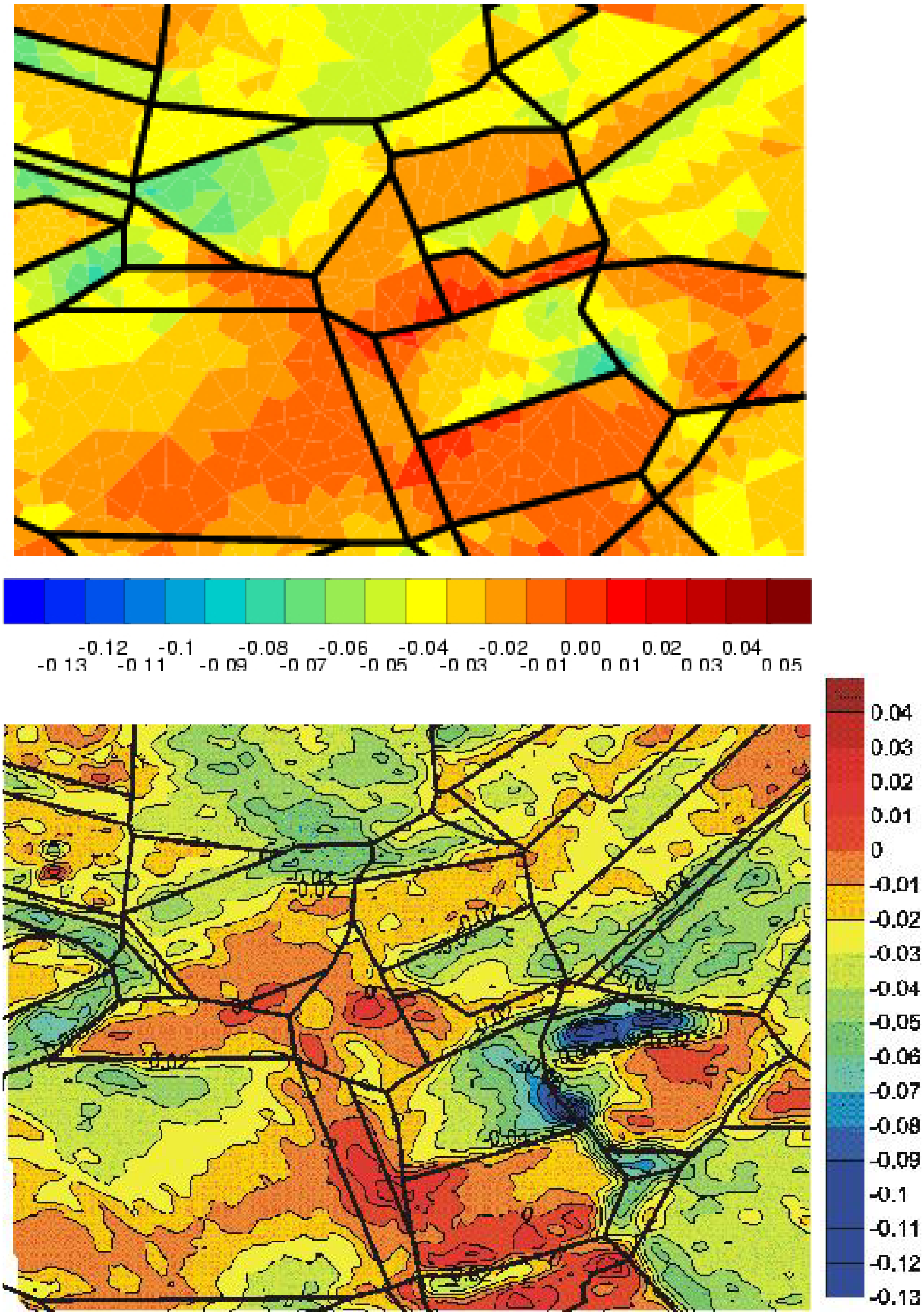

Figure VI.15 : Comparison for ϵ_{22} at 5% macrostrain ("small" mesh and experiment)

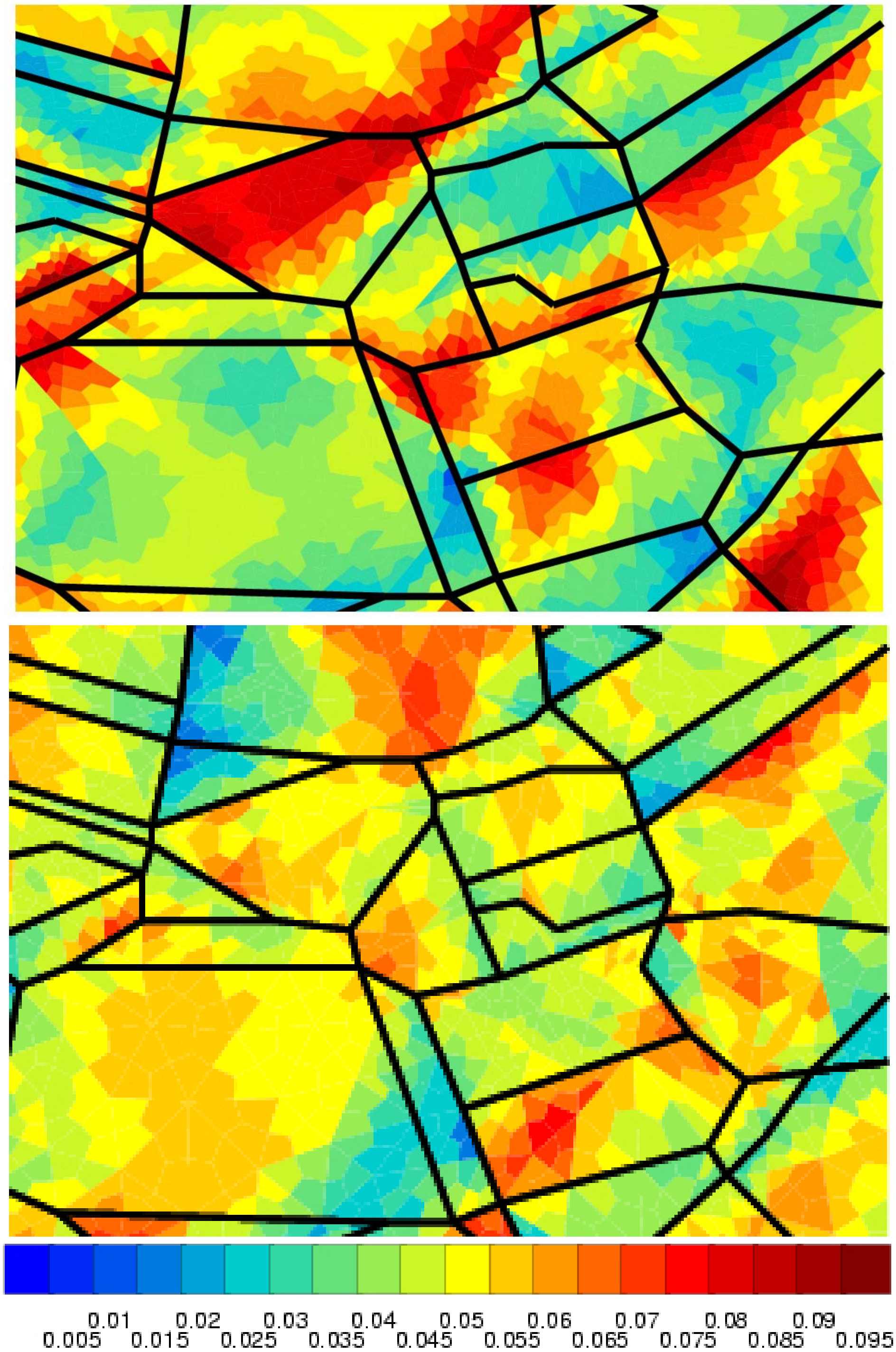

Figure VI.16 : Comparison for ϵ_{11} at 5% macrostrain ("2D extended small" and "3D small" mesh)

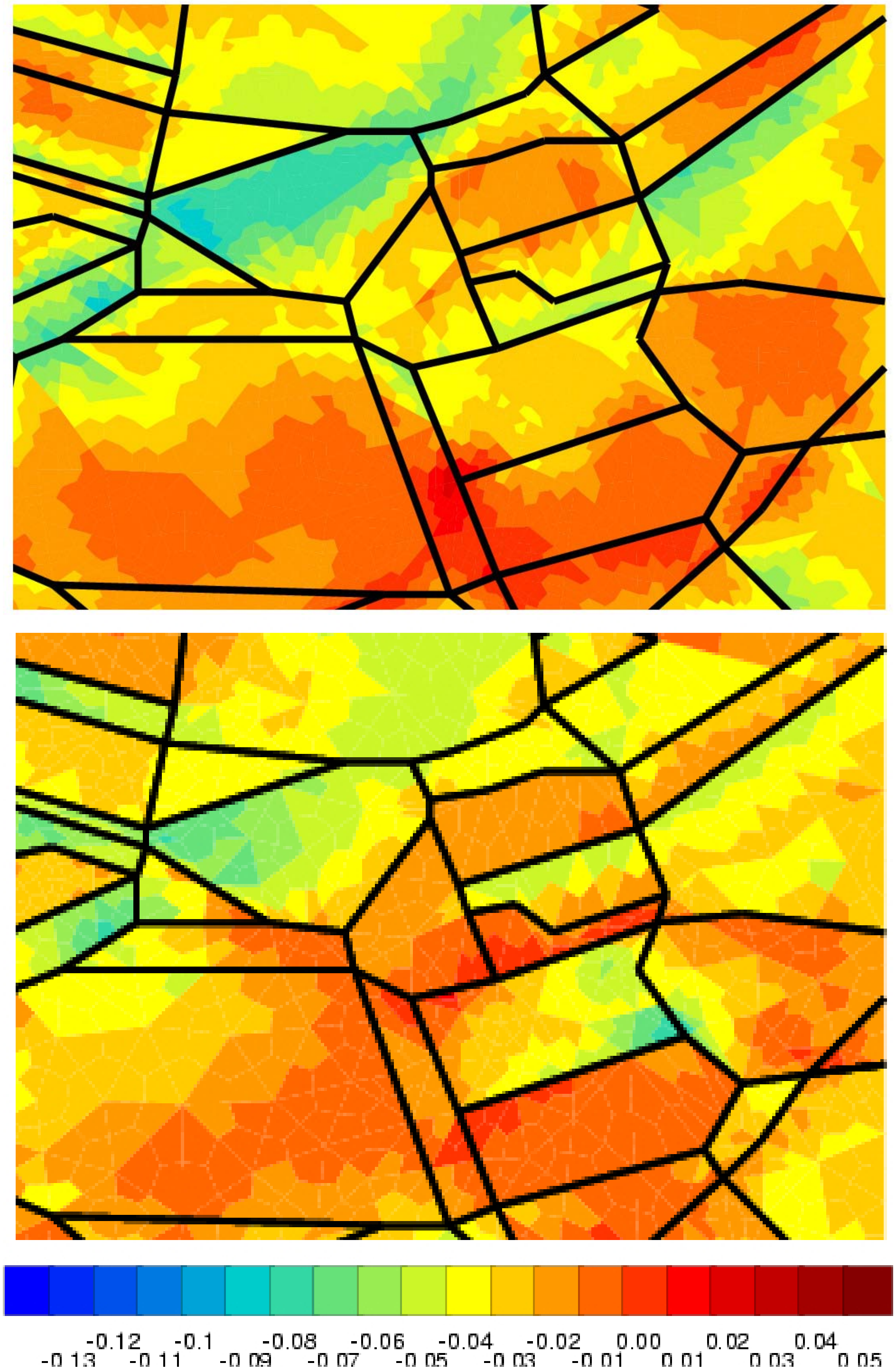

Figure VI.17 : Comparison for ϵ_{22} at 5% macrostrain ("2D extended small" and "3D small" mesh)

Chapter -VII-

Zircaloy computations

Contents

VII.1 Introduction **89**

VII.2 Damaged grain boundaries versus perfect interface **90**

VII.2.1 Crystal parameters and texture 90

VII.2.2 GB material parameters 90

VII.2.3 Boundary conditions 94

VII.2.4 Results and discussion 94

VII.2.5 Local fields 96

VII.2.6 Conclusion 96

VII.3 Uncoupled intergranular fracture **97**

VII.4 Iodine influenced intergranular fracture **98**

VII.4.1 Diffusion-damage coupling parameters 98

VII.4.2 Quasi-2D computational results 99

VII.4.3 3D computational results 100

VII.4.4 Crack propagation rate 100

VII.5 Iodine-influenced inter-transgranular fracture **100**

VII.6 Conclusions **101**

VII.1 Introduction

Preliminary results for iodine-induced intergranular cracking were obtained in (Diard, 2001). It was done for quasi-2D case, for quite a few number of grains (10 grains).

The present study represent a step forward in the solution of this problem, since its purpose is to:

- perform simulations for a larger number of grains,
- perform simulations in 3D case,
- simulate a mixed inter-transgranular fracture mode.

The chapter is organized as follows. A series of computations with non-damaged grain boundaries are shown first. Different possibilities for grain boundary behavior were tested (weak or strong elastic, J_2 elasto-plastic). The comparison of these results with a classical aggregate computation with perfect grain interfaces shows the necessity to represent grain boundaries with no damage as two layers, having the material properties of the two neighboring grains.

An example of intergranular fracture for a quasi-2D aggregate is then presented. It shows crack initiation for all the grain boundaries normal to tension direction. Finally, only some of them form two main cracks. Similar results can be found in recent papers of (Clayton and McDowell, 2004)(Clayton, 2005)(Wei and Anand, 2004).

Iodine influenced intergranular cracking is then presented for quasi-2D and 3D cases. Crack initiation now happens on the iodine affected surface of the aggregate, then one main crack propagates into the depth of the aggregate.

Finally, mixed inter-transgranular corrosion-affected cracking is presented. Two computations are shown. In both of them intergranular material behavior was environment dependent. For transgranular material behavior, two possibilities were studied: either uncoupled, or coupled with corrosion. The second one, fully iodine coupled formulation is shown to give an intergranular crack propagation, immediately followed by transgranular one.

VII.2 Damaged grain boundaries versus perfect interface

Let us assume that the grain boundaries are not damaged yet. Let us have two computations in hand:

- *without GB*, a reference computation for a finite element mesh like 100gr2dext (see tab.IV.3.2), with a crystal material model for the grains, and a given texture,
- *with GB*, computation for the same mesh with added GB - 100gr2dextGB - the same material model and texture for the grains, and some unknown behavior for GB

The question of this chapter is: **What is the material behavior for the GB to make the two results similar to each other ?**

VII.2.1 Crystal parameters and texture

The parameters for the single crystal model proposed in (Cailletaud, 1991) were already identified by O.Diard in the case of Zircaloy (Diard, 2001). Namely, the proposed parameters are presented in table VII.1.

For the present work, only the most active prismatic slip systems will be taken into account, with kinematic hardening only, and without recovery effect (M and m parameters are supposed to be zero).

Numerically generated random orientations were taken for 115 grains of the aggregate.

VII.2.2 GB material parameters

a) Anisotropic elasticity with high stiffness

A special orthotropic elasticity is chosen, for the grain boundaries, as follows:

Slip system	Prismatic	Pyramidal $\pi_1 < a >$	Basal	Pyramidal $\pi_1 < c + a >$
τ_0(MPa)	20.	107.	132.	195.
K(MPa$\cdot s^{1/n}$)	198.	500	90.	55.
n	9.5	7.5	5.5	11.3
d	170.			170.
c(MPa)	22100.			6120.
M(MPa$\cdot s^{1/m}$)	500.			55.
m	9.5			9.5

Table VII.1 : Material parameters for Zircaloy

```
**elasticity orthotropic
    y3333 1.  y2222 1.  y1122 0. y2233 0.  y3311 0.  y2323 1.
    y1111 100000000.
    y1212 100000000.
    y3131 100000000.
```

The direction 1 was supposed to be normal to the GB plane. One can see quite elevated values of Y_{1111} and Y_{1212}, Y_{3131}, that means high resistance of the GB material to the normal tension and in-plane shear. The aim of this first computation is to be totally invisible in the aggregate.

b) Average elasticity - Voigt-Reuss-Hill estimation

A lot of approaches are developed up to now, to estimate the properties of a polycrystal, starting from the single crystal properties.

Let us suppose, that the polycristal is elastically isotropic. If so, only two moduli, K – the bulk modulus–, and G –the shear modulus–, characterize the mechanical response. The most simple (but quite effective) approach is known under the names of Voigt-Reuss-Hill. It is based on a number of postulates.

1. *Voigt postulate*: all the grains have the same deformation, the stresses can be discontinuous
2. *Reuss postulate*: all the grains have the same stresses, deformations can be discontinuous
3. *Hill postulate*: geometrical average of the Voigt and Reuss estimations is used:

$$K_H = \frac{1}{2}(K_R + K_V)$$

$$G_H = \frac{1}{2}(G_R + G_V)$$

For some particular crystal symmetries, analytical formulae for the Voigt and Reuss estimations are available. Namely, for the case of HCP material, these formulae are as follows.

$$K_V = \frac{1}{9}(2(C_{11} + C_{12}) + C_{33} + 4C_{13})$$

$$G_V = \frac{1}{30}(M + 12C_{44} + 12C_{66})$$

$$M = C_{11} + C_{12} + 2C_{33} - 4C_{13}$$

$$C_{66} = \frac{1}{2}(C_{11} - C_{12})$$

$$K_R = \frac{c^2}{M}$$

$$G_R = \frac{5}{2} \cdot \frac{c^2 C_{44} C_{66}}{3K_V C_{44} C_{66} + c^2 (C_{44} + C_{66})}$$

$$c^2 = (C_{11} + C_{12})C_{33} - 2C_{13}^2$$

One can easily check, that for isotropic elasticity with a stiffness tensor like

$$\underset{\approx}{\mathbf{\Lambda}} = 2\mu \underset{\approx}{\mathbf{I}} + (K - \frac{2}{3}\mu) \underset{\sim}{\mathbf{I}} \otimes \underset{\sim}{\mathbf{I}}$$

$$\underset{\approx}{\mathbf{\Lambda}} = \begin{pmatrix} C_{11} & C_{12} & C_{13} & 0 & 0 & 0 \\ & C_{11} & C_{13} & 0 & 0 & 0 \\ & & C_{33} & 0 & 0 & 0 \\ & & & C_{44} = \frac{1}{2}(C_{11} - C_{12}) & 0 & 0 \\ & symm & & & C_{66} & 0 \\ & & & & & C_{66} \end{pmatrix} = \begin{pmatrix} K + \frac{4}{3}\mu & K - \frac{2}{3}\mu & K - \frac{2}{3}\mu & 0 & 0 & 0 \\ & K + \frac{4}{3}\mu & K - \frac{2}{3}\mu & 0 & 0 & 0 \\ & & K + \frac{4}{3}\mu & 0 & 0 & 0 \\ & & & \mu & 0 & 0 \\ & symm & & & \mu & 0 \\ & & & & & \mu \end{pmatrix} \tag{VII.1}$$

both Voigt and Reuss estimations are equivalent:

$$K_V = K_R = K$$

$$G_V = G_R = \mu$$

As a first estimation for the GB elasticity one can then propose the isotropic elasticity, calculated by means of the Hill approach, starting from the crystal parameters for Zircaloy:

$$\begin{pmatrix} 103210. & 51605. & 46590. & 0 & 0 & 0 \\ & 103210. & 46590. & 0 & 0 & 0 \\ & & 118260. & 0 & 0 & 0 \\ & & & 25800. & 0 & 0 \\ & symm & & & 23010. & 0 \\ & & & & & 23010. \end{pmatrix} \tag{VII.2}$$

Using the formulae above, the elasticity estimations are: $K_V = 68250MPa$ $K_R = 68140MPa$, $K_H = 68195.4MPa$, $G_V = 26357.5MPa$, $G_R = 25806.5MPa$, $G_H = 26082.0MPa$.

Young modulus E and Poisson ratio ν connected with the volume modulus K and shear modulus G as follows :

$$E = \frac{9KG}{3K + G}$$

$$\nu = \frac{3K - 2G}{6K + 2G}$$

The values calculated on the basis of Hill estimation are: $E_{Hill} = 69398.7MPa$, $\nu_{Hill} = 0.33$

The values of $E = 70000MPa$, $\nu = 0.33$ were taken for the computations. These values give $K = \frac{E}{3(1-2\nu)} = 68627MPa$, which is formally outside the Voigt-Reuss bounds. But, $\frac{K-K_H}{K_H}$ does not exceed 1%, which is acceptable for our qualitative computations.

c) Weak elasticity

Isotropic elasticity was taken here, with $E = 700MPa$, $\nu = 0.33$

d) High stiffness isotropic elasticity

Isotropic elasticity was taken here, with $E = 700000MPa$ –which is ten times the average Zircaloy value– and $\nu = 0.33$.

e) Average elastoplasticity

An elasto-plastic model with isotropic hardening was taken. Isotropic elasticity was taken as $E = 70000MPa$, $\nu = 0.33$, the plastic parameters are defined by means of ZeBuLoN's optimization procedure, so that the model response follows the results of the computation without GB (see fig.VII.1). The parameters were identified as follows:

```
***behavior gen_evp
**elasticity isotropic
young 70000. poisson 0.33
**potential gen_evp ep
  *flow norton
  K 200.
  n 9.
  *isotropic nonlinear
 R0 278.
 Q  498.
 b  107.
***return
```

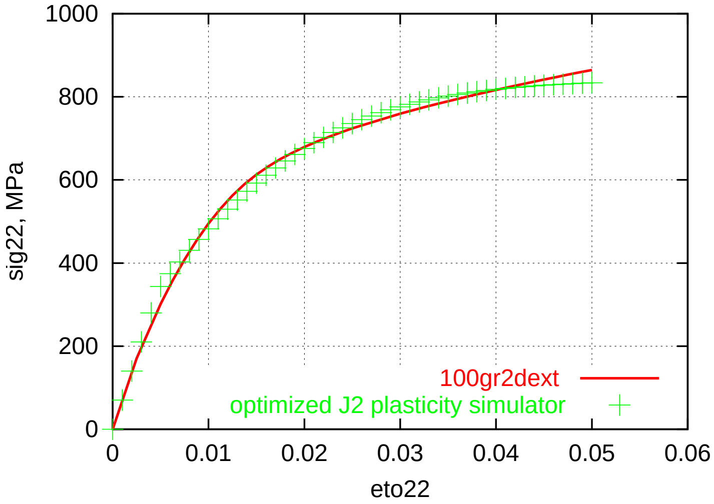

Figure VII.1 : Stress–strain curve for optimized J_2 theory parameters

f) Attached grain properties

In order to have such a possibility, the finite element mesh procedure was specially adopted. A two-layer GB mesh was made, as shown in fig.IV.8. Attached crystal properties (with appropriate orientation) was taken for each layer of grain boundary, so that two layers of GB have two different material properties.

VII.2.3 Boundary conditions

An uniaxial tension (in the direction Y) till 5% strain was performed. Some node sets (nsets) were defined, as shown in the fig. VII.2

Displacements were then imposed as follows:

- x=0: free
- xmax: Ux = 0
- y=0: Uy = 0
- ymax: Uy = (0..0.05)·*meshsize* in 1000s
- z=0: Uz = 0

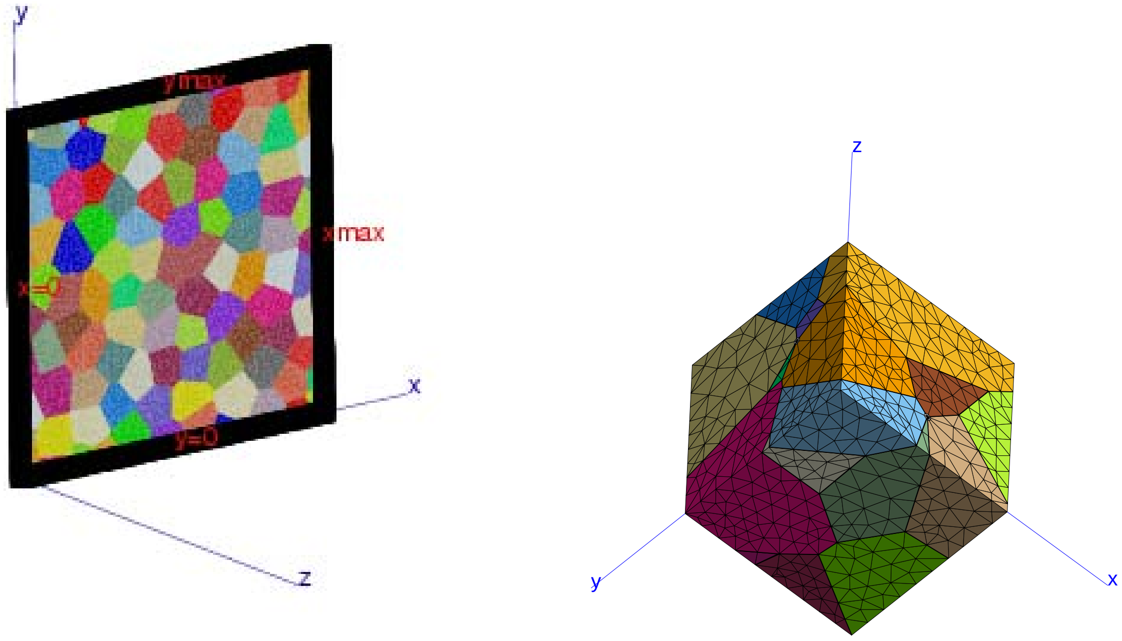

(a) (b)

Figure VII.2 : Mesh coordinate systems to illustrate boundary conditions: (a) 100gr2dext; (b) 20gr3d

VII.2.4 Results and discussion

a) Average stress-strain curve

In the fig.VII.3 the average stress versus average strain for entire aggregate are plotted for all the computations of the table VII.2.3. The tension direction (”y” or 22 in our case) is presented.

Several points could be noted:

Table VII.2 : List of FE computations

Notation	Mesh	crystal material	GB material	CPU time, s
100gr2dext	100gr2dext[a]	VII.2.1	-	-
100gr2dextGB-rigid	100gr2dextGB	VII.2.1	section a)	-
100gr2dextGB-iso	100gr2dextGB	VII.2.1	section b)	-
100gr2dextGB-faible	100gr2dextGB	VII.2.1	section c)	6200.
100gr2dextGB-dur	100gr2dextGB	VII.2.1	section d)	-
100gr2dextGB-plast	100gr2dextGB	VII.2.1	section e)	11070.
100gr2dextGB2ele-crystal	100gr2dextGB2ele	VII.2.1	section f)	9230.

---

[a] see tab.IV.3.2

- Curve 100gr2dextGB2ele-crystal is close to, but below the curve 100gr2dext. It is consistent with a well-known fact, that finite element mesh refinement causes a softer response of the polycrystalline aggregate.

- 100gr2dextGB-faible is much softer, and 100gr2dextGB-dur is much more rigid, then the others. It is natural, because of weak (or rigid) GB elasticity. Nevertheless, one can note similar $d\sigma/d\varepsilon$ for 100gr2dextGB-faible and 100gr2dext for quite developped plastic strains (say, at 2..5% of macrostrain). That is not the case for 100gr2dextGB-dur.

- 100gr2dextGB-iso represents the highest average stresses. It seems normal, compared to 100gr2dextGB2ele-crystal, 100gr2dextGB-faible and 100gr2dextGB-plast.

- One would expect 100gr2dextGB-plast to be closer to 100gr2dext. Apparently, the response is surprisingly soft, compared to 100gr2dext.

- 100gr2dextGB-rigid is quite close to 100gr2dext. It is not an evident result. One could expect to have something different from 100gr2dext, because of the anisotropic GB elasticity.

b) Average normal stress in GB, versus GB angle to tension direction

In this section, stress component in GB, normal to GB plane is calculated first. Then, the average value is found for corresponding GB elset (set of finite elements). Finally this average stress is plotted as a function of GB plane angle with the tension direction (”y” axe in our case). It was done twice, for second and 30th computation increments (see figs. VII.4, VII.5), that corresponds to negligibly small, or quite developed plastic deformation.

One can note the following:

- the dependence (in both map2 and map30) for 100gr2dextGB-rigid is quite complex, and not monotonous.

- 100gr2dextGB-iso, 100gr2dextGB-plast, 100gr2dextGB-faible and 100gr2dextGB2ele-crystal represent a quite linear angle dependence, specially for map2.

- for map30 the resulting points have a larger scatter about average line than for map2 (100gr2dextGB-iso, 100gr2dextGB-plast, 100gr2dextGB-faible, 100gr2dextGB2ele-crystal).

- It seems that the scatter for 100gr2dextGB-faible –at map 30– is less than for the others.
- For map 2, the scatter is quite similar for 100gr2dextGB-iso, 100gr2dextGB-plast, 100gr2dextGB-faible, 100gr2dextGB2ele-crystal, 100gr2dext.

c) Local stress state

For the local stress study, the easily accessible line $y = 0$ is taken –see fig.VII.2–. Stress component σ_{22} (sig22, corresponding to the tension direction) is then plotted *versus* y-coordinate at 1% of applied strain (fig.VII.6).

One can note the following:

- 100gr2dextGB-rigid is quite perturbed, in comparison with the reference solution 100gr2dext,
- 100gr2dextGB-iso, 100gr2dextGB-plast and 100gr2dextGB2ele-crystal, are in rather good agreement with 100gr2dext,
- 100gr2dextGB-faible is approximatively two times lower than 100gr2dext. 100gr2dextGB-faible is not always similar to 100gr2dext, one can find some grains with opposite signs for sig22(y).

VII.2.5 Local fields

Local stress and strain fields are presented below. Namely, cumulated plastic strain (fig.VII.8) and von Mises stress (fig. VII.7) are presented. One can note that the fields for 100gr2dextGB-iso, 100gr2dextGB-plast and 100gr2dextGB2ele-crystal are similar to 100gr2dext. The stress and plastic strain values for 100gr2dextGB-faible are lower. The stresses for 100gr2dextGB-rigid form more explicit maximum and minimum zones. One can also mention that the stress "bands" (zones of relatively high stress) are oriented rather in vertical direction, while plastic strain bands make rather 45°angle with tension direction.

VII.2.6 Conclusion

1. The question of this chapter was: What is the GB material behavior, to get similar results with and without GB ? One can conclude, that the best results are obtained with the GB as attached grains (100gr2dextGB2ele-crystal computation). Average elasto-plasticity, or even average elasticity (for the entire aggregate) seems to give quite acceptable results as well. It seems that weak or strong isotropic behavior, as well as strongly anisotropic behavior are not good candidates for the basis of GB model.

2. Under relatively small plastic strains, the normal stress in GB versus GB angle to the tension direction (for some of investigated GB properties) can be approximated by a linear function. The maximum appears for the GB, normal to the tension direction. But for quite developed plastic strains the dispersion of normal stresses is higher.

   So, if the failure of GB is supposed to be stress-driven, one can expect the GB, normal to the tension direction, to be the less resistive. And, this fact does not depend on the isotropic behavior of GB. But, it can only be expected for relatively small plastic strains. Even at 5% of global tensile strain, this effect seems to be much less significant.

The conclusions above were made after extended 2d computations. Because of the time limits, 3d validation was not done for this particular part of the study. Nevertheless, this study was a motivation to chose the strategy of grain boundary modeling, as explained in chap.II.2.

VII.3 Uncoupled intergranular fracture

Let us have a test with intergranular fracture possibility only, without iodine influence. The same extended 2D aggregate of 115 grains was used. The basic crystal model was used for the grain core, with parameters from table VII.1. Parameters for the grain boundary material, corresponding to damage, are given in table VII.3. Node sets used for boundary conditions are shown in the fig. VII.2 Displacements were imposed as follows:

- x=0: free
- xmax: Ux = 0
- y=0: Uy = 0
- ymax: Uy = (0..0.05)·*meshsize* in 250
- z=0: Uz = 0

R_n	K_n	n_n	R_t	K_t	n_t	A	k	r	β
900.	200.	8.	900.	200.	8.	2000.	3.	4.	0.01

Table VII.3 : Damage parameters for DOS only test

R_n	K_n	n_n	R_t	K_t	n_t	A	k	r	β
10.	750.	8.	10.	750.	8.	5000.	3.	2.	0.01

Table VII.4 : Damage parameters for DOS only test –alternative set–

In fig. VII.9 one can see the consequence of Mises stress and damage distributions. One can note that grain boundaries normal to the tension direction are damaged first, then they link together in longer cracks, and finally one has two big cracks able to separate the aggregate into two parts. A progressive stress drop is produced by the opening of the crack.

One of the "bad" results is also presented here. In fig.VII.11 one can see damage and inelastic opening fields from two computations, with grain boundary parameters from (tab.VII.3 and tab.VII.4 respectively). They are called then "wanted" and "unwanted" results. For the "unwanted" map one can see all the grain boundaries, normal to tension direction, to be damaged in the same manner. Hence in "wanted" result a preferential crack path can be remarked. The DOS model responses for both "wanted" and "unwanted" parameter sets were presented above – see figs.II.18, II.19–. From these results one can establish a principle : if you want the deformation to be localized in one crack, the GB material should damage first, and then get inelastic opening.

VII.4 Iodine influenced intergranular fracture

VII.4.1 Diffusion-damage coupling parameters

Notations: Both damage and diffusion coefficient are usually denoted as D. We need to distinguish them here. That is why the diffusion coefficient will be written in bold.

D – damage
D – diffusion coefficient

Non-damaged state: Diffusion of iodine in the non-damaged Zircaloy-4 is known to be non-significant. In (Fregonese, 1997), the difference between the iodine profiles was found to be about 100nm after 16 hours of the experiment. An appropriate diffusion coefficient was then estimated as

$$\mathbf{D} < 2 \cdot 10^{-19} m^2 s^{-1} = 2 \cdot 10^{-13} mm^2 s^{-1}$$

The inter-transgranular fracture, studied here, happens in about 10 min in the Zircaloy tube wall of 600 mm width, with 0.1 μm/s rate for intergranular crack, and 1 to 20 μm/s rate for transgranular crack.

It means that, for our process, pure diffusion does not happen at all. One can take any small value for the grains as well as the grain boundaries diffusion coefficient **D** (even if grain boundaries are usually known to have higher **D**, than the grain core –see (Mishin and Herzig, 1999)–). The chosen value in absence of damage will then be

$$\mathbf{D}_{nd} = 2 \cdot 10^{-13} mm^2 s^{-1}$$

If there is no iodine, damage should not happen during the computation time. Let us repeat the damage law:

$$\dot{D} = \left(\frac{\sigma_d}{A}\right)^r (1 - D)^{-k}$$

One could want to have $D = 10^{-5}$ after 1000s of computation. With $r = 4$ it approximately gives:

$$\frac{\Delta D}{1000s} \approx \left(\frac{\sigma_d}{A}\right)^4$$
$$\left(\frac{\sigma_d}{A}\right) \approx 10^{-2}$$
$$A \approx 100 \cdot \sigma_d$$

A typical average stress in tension test for Zircaloy-4 is 500 MPa. The local maximum eigenstress, obtained from the aggregate computations, is higher – the reached level is about 1000 MPa. So, in a non-damaged state, one can take

$$A_{nd} = 100 \cdot 1000 MPa = 10^5 MPa$$

Damaged state: In a damaged grain boundary, the "diffusion" is believed to happen faster. Here we will make **D** dependent on the material damage, and the damage parameter - A - dependent on the iodine concentration. This coupling can be regulated in order to have given intergranular crack propagation rate (0.1μm/s).

As mentioned in (Adda and Philibert, 1977), the penetration of a given concentration value is time-dependent, following the relation

$$y \approx K \sqrt{D_{gb}} (t^{1/4})$$

A value of $\mathbf{D}_{gb} = 10^{-4} m^2 s^{-1}$ was found enough for the diffusion to traverse the mesh of 100 μm in 1000 s. The computation in 4000 s and $(0.5 \cdot \mathbf{D}_{gb})$ gives approximately the same result. This demonstrates that the kinetics really depends on $t^{1/4}$.

Now a law has to be chosen to raise the diffusion coefficient from its initial value of 10^{-13} (damage = 0) till effective value $\mathbf{D}_{eff}$ (damage = 1). The following function was found convenient:

$$\mathbf{D} = \mathbf{D}_{eff} \cdot (1 - e^{-b_1 \cdot D}) + 10^{-13}$$

Since the problem is fully coupled, the damage evolution will depend on iodine concentration C:

$$A = A_{eff} + 10^5 \cdot e^{-b_2 \cdot C}$$

The parameters D_{eff}, A_{eff}, b_1 and b_2 will define the crack propagation rate. As a final choice, two sets were defined, as shown below:

$$\mathbf{D} = 10^{-13} + 10^{-4} \cdot (1 - e^{-12 \cdot D})$$

$$A = 1000 + 10^5 \cdot e^{-12 \cdot C}$$

R_n	K_n	n_n	R_t	K_t	n_t	A	k	r	β
900.	200.	8.	900.	200.	8.	$1000 + 10^5 \cdot e^{-12. \cdot C}$	3.	4.	0.01

Table VII.5 : Damage parameters for coupled IG test

R_n	K_n	n_n	R_t	K_t	n_t	A	k	r	β
-	-	-	-	-	-	$1000 + 10^5 \cdot e^{-10. \cdot C}$	3.	2.	0.0

Table VII.6 : Damage parameters for coupled IG test - alternative set

VII.4.2 Quasi-2D computational results

The material parameters for the grain boundary material presented in table VII.5 are used here. The finite element mesh 100gr2dextGB2eleLin – see tab.IV.3.2 and fig. IV.6 – was used. Displacements were prescribed in order to have a tensile strain rate of $2 \cdot 10^{-4} 1/s$. Node sets (nsets) used for boundary conditions are shown in the fig. VII.2 Displacements were imposed as follows:

- x=0: free
- xmax: Ux = 0
- y=0: Uy = 0
- ymax: Uy = (0..0.20)$\cdot$*meshsize* in 1000s
- z=0: Uz = 0

As a result, one can see progressive crack propagation from the left side (fig. VII.12, which is influenced by iodine. There is a stress drop, due the presence of the crack. The iodine "diffusion" map is in accordance with the crack path, as seen in fig.VII.13.

On the other hand, the choice of the model itself does not guarantee the results. In fig.VII.13, the example of an "unwanted" result is presented, with GB parameters from table VII.6. Damage happens in all the GB touched by diffusion, without any preferential path.

VII.4.3 3D computational results

The material parameters are still taken from table VII.5. The finite element mesh 20gr3dGB2ele was used – see tab.IV.3.2 and fig. IV.15 – . The coordinate axes for the mesh are shown in the fig. VII.2. Displacements were imposed as follows:

- x=0: free
- xmax: Ux = 0
- y=0: Uy = 0
- z=0: Uz = 0
- ymax: Uy = (0..0.20)·*meshsize* in 1000s

The Iodine was applied on the face x=0.

In fig. VII.14, the von Mises stress and the damage fields are shown for three stages of intergranular crack propagation. One can note that crack appears at the grain boundary, which is the most perpendicular to the tensile axis. As a crack appears, a local unloading is observed. Damage on the grain boundary structure is shown in fig. VII.15.

VII.4.4 Crack propagation rate

In fig. VII.21, the crack projection length as a function of time is presented, for the three iodine influenced intergranular fracture computations. In fact, for all the computations the iodine influenced area corresponds to the aggregate surface x=0. Thus the crack length was found as a maximum x-coordinate of all the integration points, having damage value higher, then a given threshold (0.9 was taken here). The results for 2d –2d IG slow– and 3d computations (with parameters from table VII.5, and diffusion coefficient $\mathbf{D} = 10^{-13} + 4 \cdot 10^{-6} \cdot (1 - e^{-12 \cdot D}))$ are presented. One can mention, that 2d and 3d results are quite close to each other. On the other hand, these results are in agreement with the typical experimental crack propagation rate of 0.1 μm/s . In order to illustrate the model capabilities, one more 2d computation result is presented –2d IG fast–. Parameters corresponding to diffusion are different here ($\mathbf{D} = 10^{-13} + 10^{-4} \cdot (1 - e^{-12 \cdot D})$)

VII.5 Iodine-influenced inter-transgranular fracture

In addition to the intergranular damage mechanism, transgranular type of fracture is added here. As explained in Chapter 1, it is modelled by a deformation normal to the basal plane (with a $\underline{\mathbf{n}} \otimes \underline{\mathbf{n}}$ tensor) to represent the opening due to cleavage. This cleavage strain is supposed to appear only if the resolved stress on the cleavage plane becomes higher then a given threshold. For this threshold, two approaches were used here.

- uncoupled. The threshold was concstant during the computation ($R_{cleav} = 1000MPa$).
- corrosion–coupled. The threshold was given as a function of the iodine concentration ($R_{cleav} = 1000 + 10^5 \cdot e^{-20 \cdot C}$MPa). The presence of iodine will then promote the possibility of cleavage.

The extended 2d mesh of 100 grains and the boundary conditions were the same as for the purely intergranular test.

A general view of the results is presented in fig. VII.16. The first intergranular stage of fracture is similar for both approaches. On the other hand, a critical difference is observed for the transgranular initiation. With the uncoupled approach, the transgranular crack starts independently from the intergranular crack, as shown by fig. VII.17. On the other hand, the fully coupled approach gives a continuous passage from intergranular to transgranular crack propagation as shown in fig. VII.18. Analysis of the plastic strain field near the crack tip at the moment of transgranular crack initiation is shown in figs.VII.19, VII.20. Here the grain (gr59) - the upper one on the computed map is better oriented for prismatic or basal slip. It can be seen on the colored map or on the average slip curve. The other grain (gr53) has significantly less prismatic + basal slip. To follow the deformation of the neighboring grain, it represent more pyramidal slip. But, it is not enough, and another mode of "deformation" is needed – transgranular crack in basal plane.

VII.6 Conclusions

The main results obtained in this chapter are the following:

1. Quasi-2D inter-transgranular computations for a relatively high number of grains (100 grains), become rather standard and relatively fast (2 to 3 days for a reasonable mesh). It opens possibilities to get the ideas about material parameter choice.
2. A simulation of 3D corrosion-driven intergranular damage was performed. With the available algorithm, the CPU time is still huge (about one month), so that the computation is unique. It can be done only for validation purposes, once material parameters are chosen.
3. In our numerical simulation, it was possible to reproduce the switch from inter to transgranular fracture mode which is observed experimentally. An analysis of the interaction between crack and plastic strain can provide interesting information and prove the consistence of chosen material parameters.

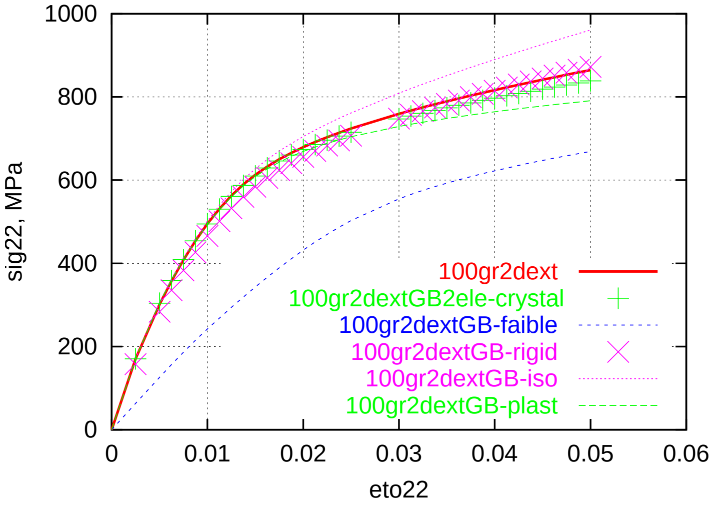

(a)

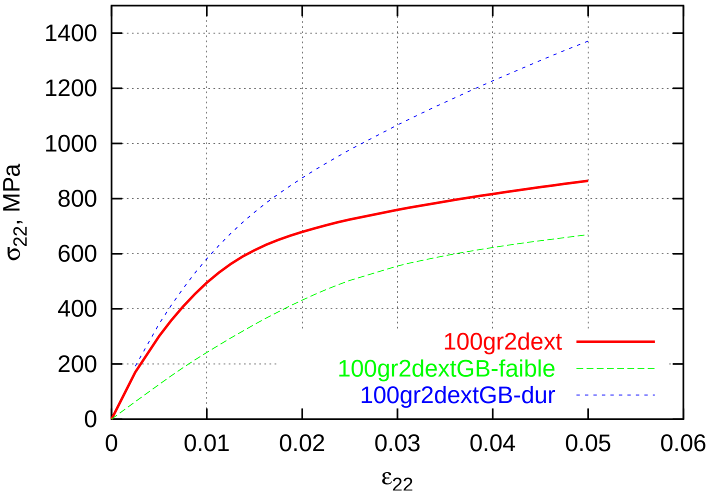

(b)

Figure VII.3 : Global average stress-strain curves

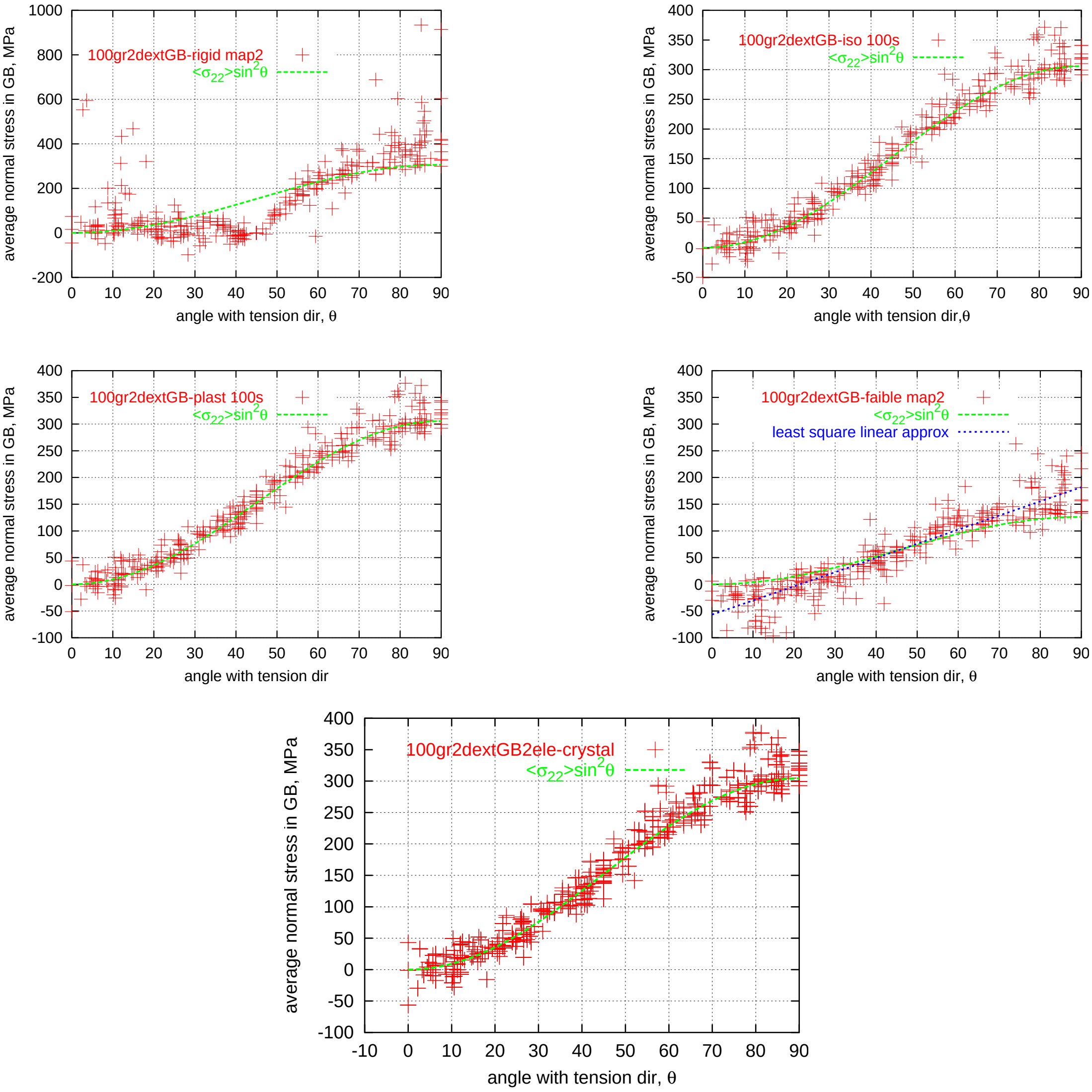

Figure VII.4 : Average normal stress in GB versus GB angle to tension direction. Relatively small plastic strains

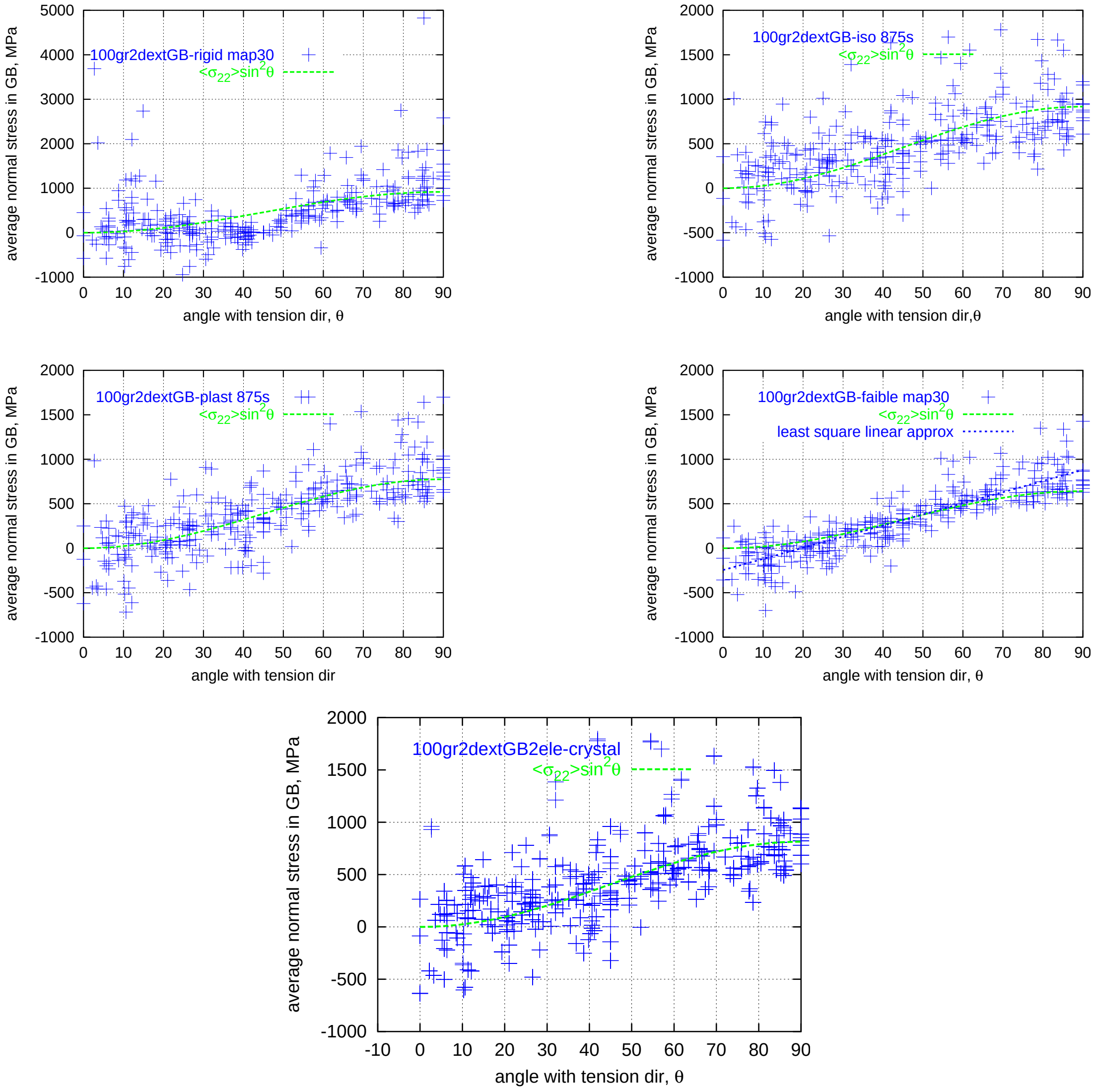

Figure VII.5 : Average normal stress in GB versus GB angle to tension direction. Developed plastic strains

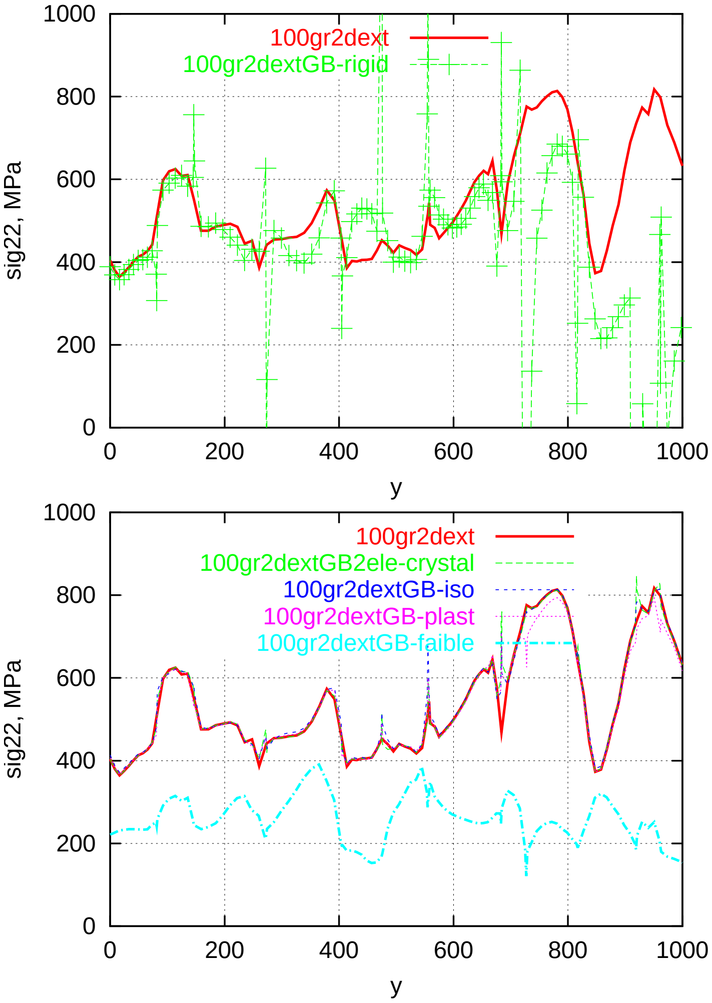

Figure VII.6 : sig22 dependence on Y coordinate for Y=0 line

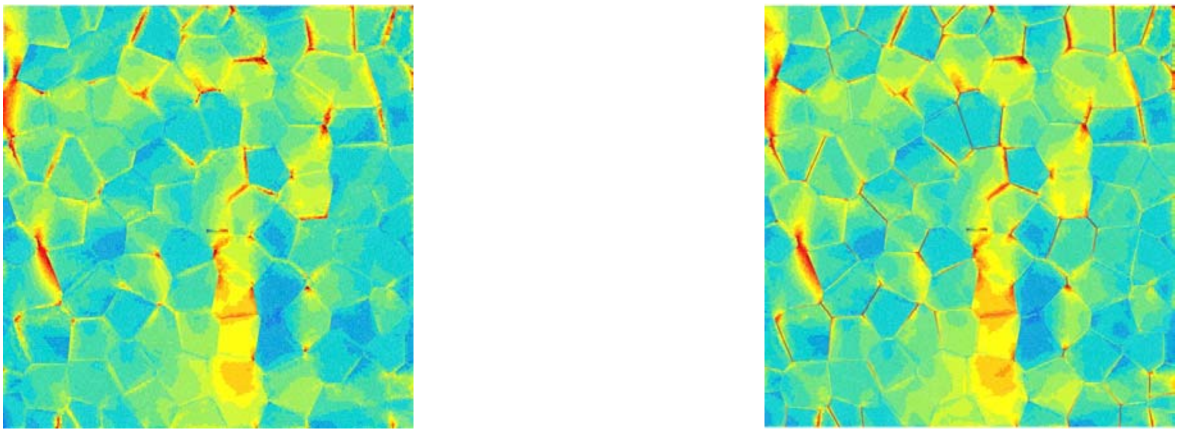

(a) 100gr2dext (b) 100gr2dextGBiso

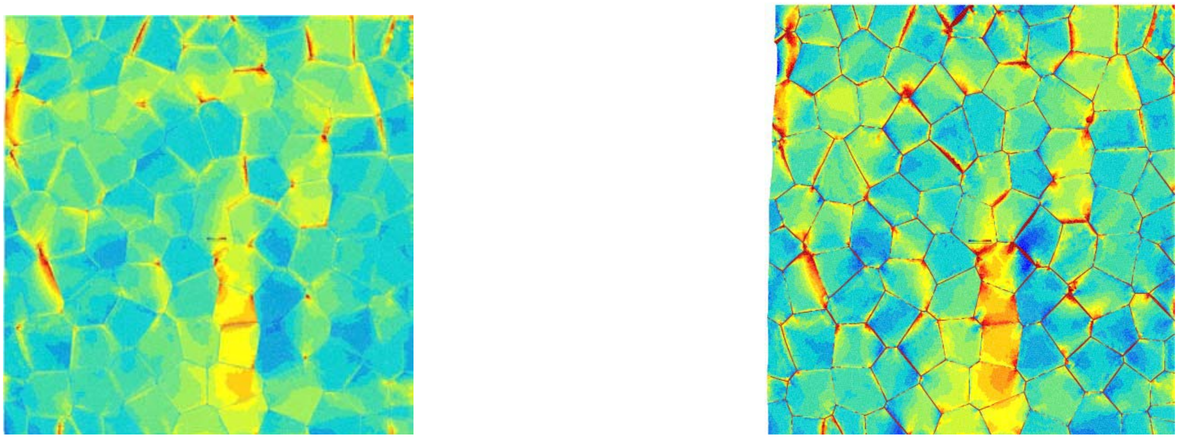

(c) 100gr2dextGBplast (d) 100gr2dextGBrigid

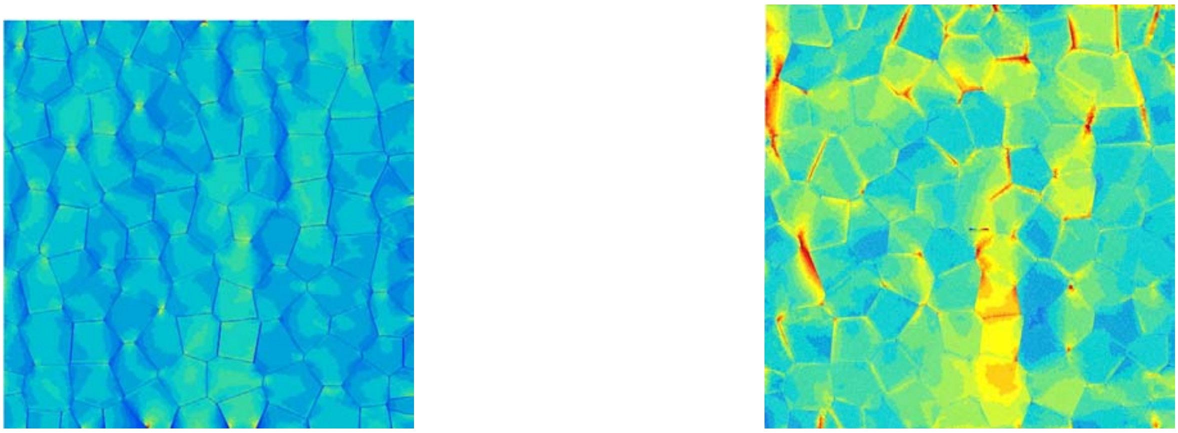

(e) 100gr2dextGBfaible (f) 100gr2dextGB2ele-crystal

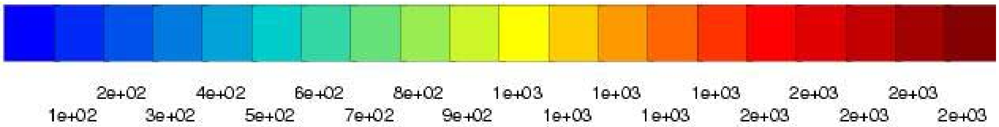

Figure VII.7 : Von Mises stress fields at 2% macrostrain

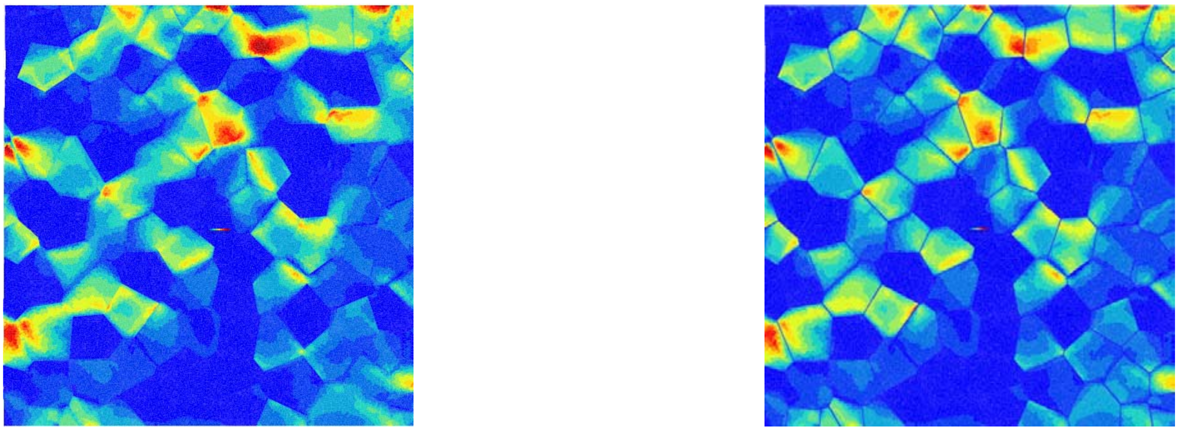

(a) 100gr2dext (b) 100gr2dextGBiso

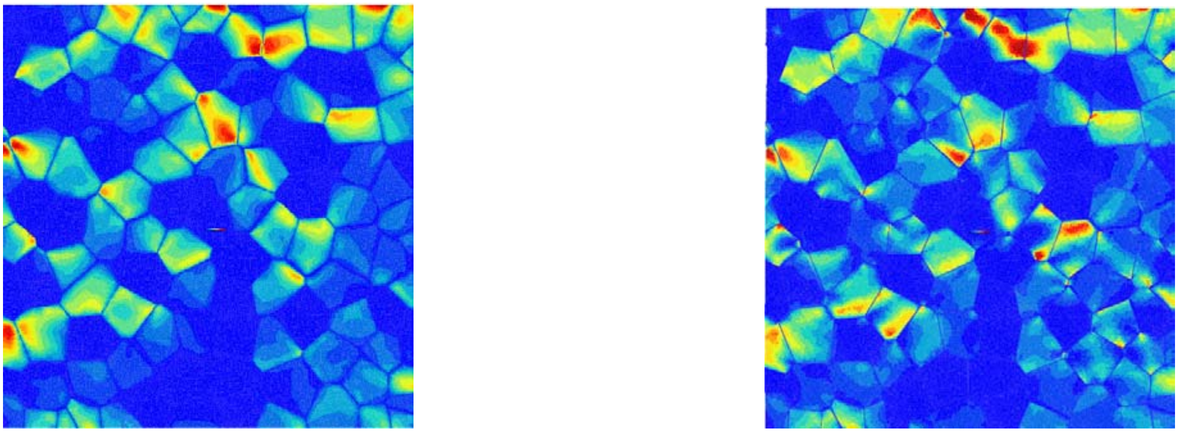

(c) 100gr2dextGBplast (d) 100gr2dextGBrigid

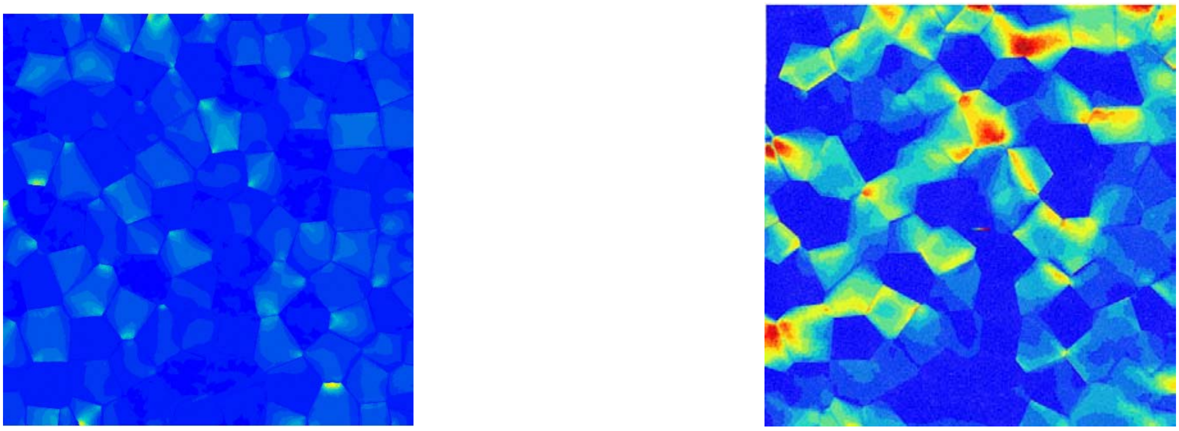

(e) 100gr2dextGBfaible (f) 100gr2dextGB2ele-crystal

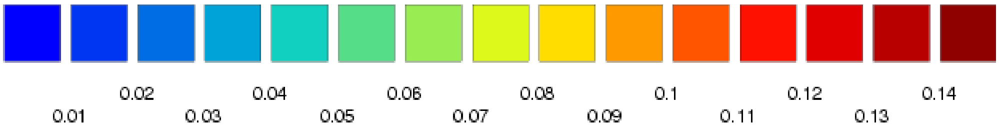

Figure VII.8 : Cumulated plastic strain fields at 2% macrostrain

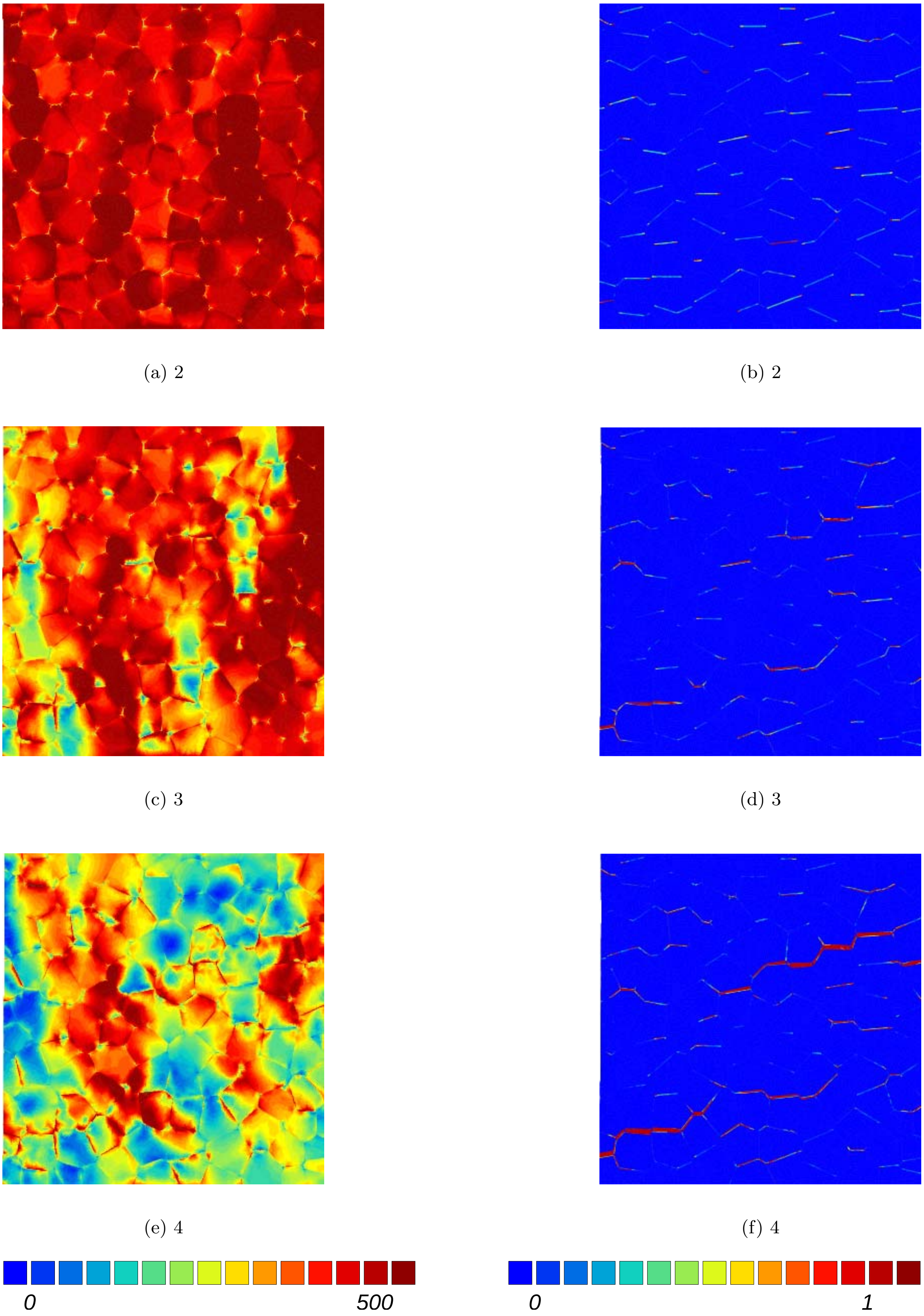

(a) 2

(b) 2

(c) 3

(d) 3

(e) 4

(f) 4

Figure VII.9 : Von Mises stress and damage fields evolution for non-coupled test

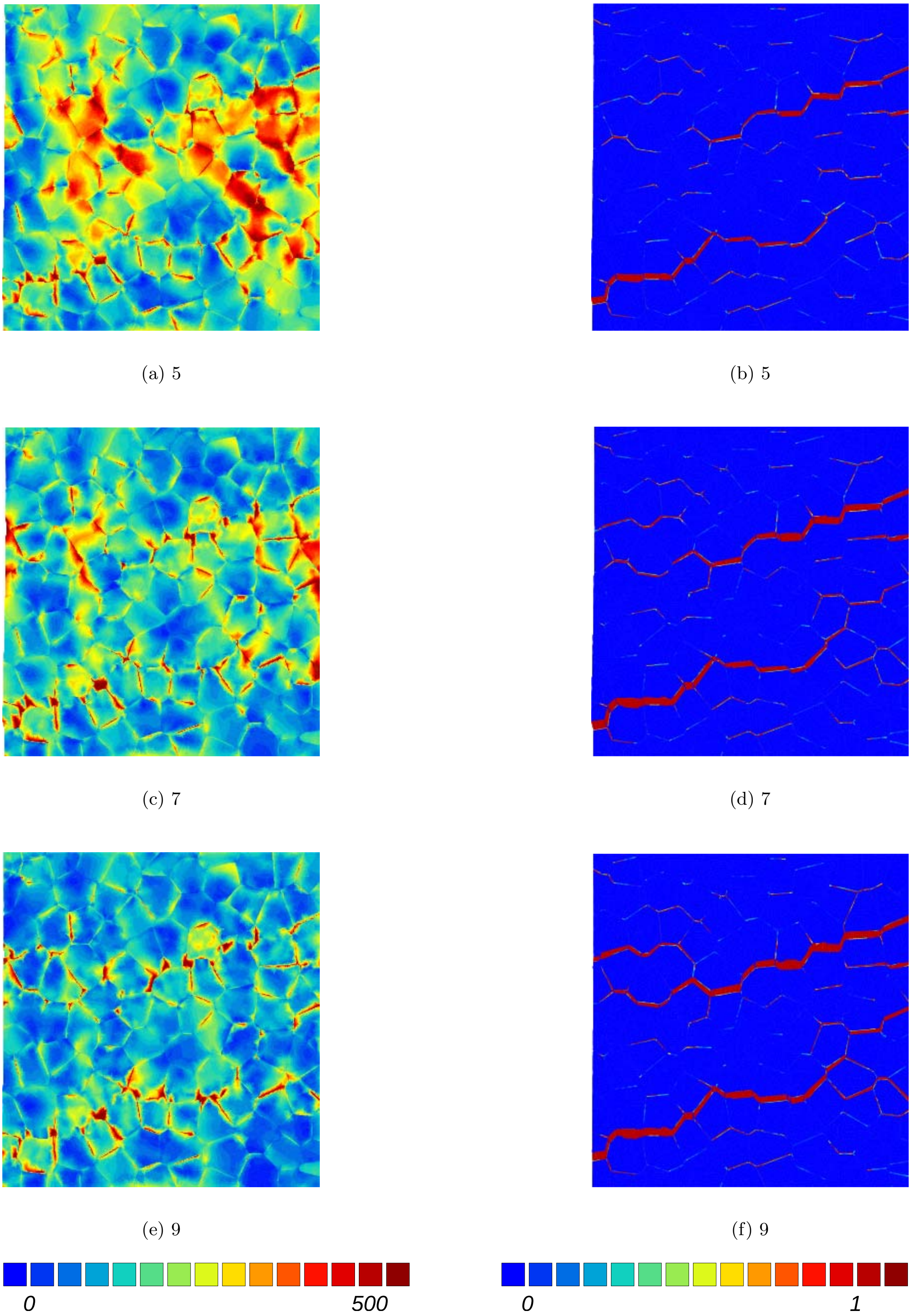

(a) 5

(b) 5

(c) 7

(d) 7

(e) 9

(f) 9

Figure VII.10 : Von Mises stress and damage fields evolution for non-coupled test - end

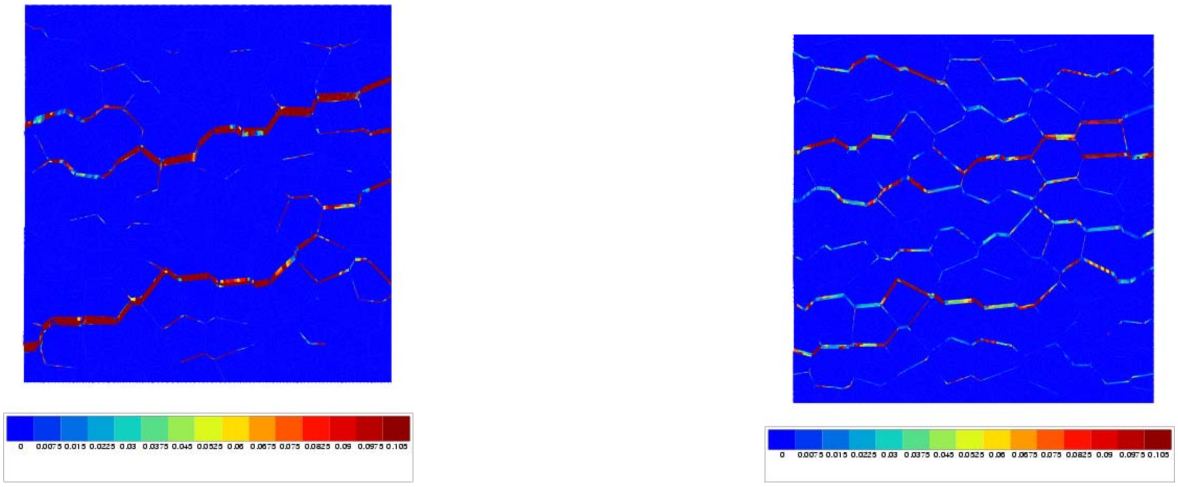

(a) wanted opening

(b) unwanted opening

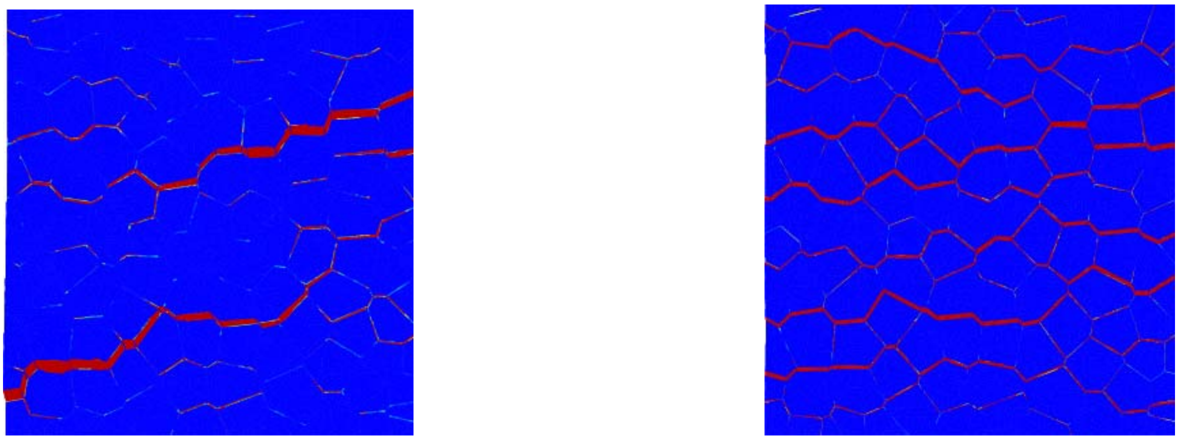

(c) wanted damage

(d) unwanted damage

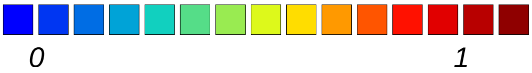

Figure VII.11 : Two parameter sets - wanted and unwanted damage and inelastic opening strain (δ) distributions

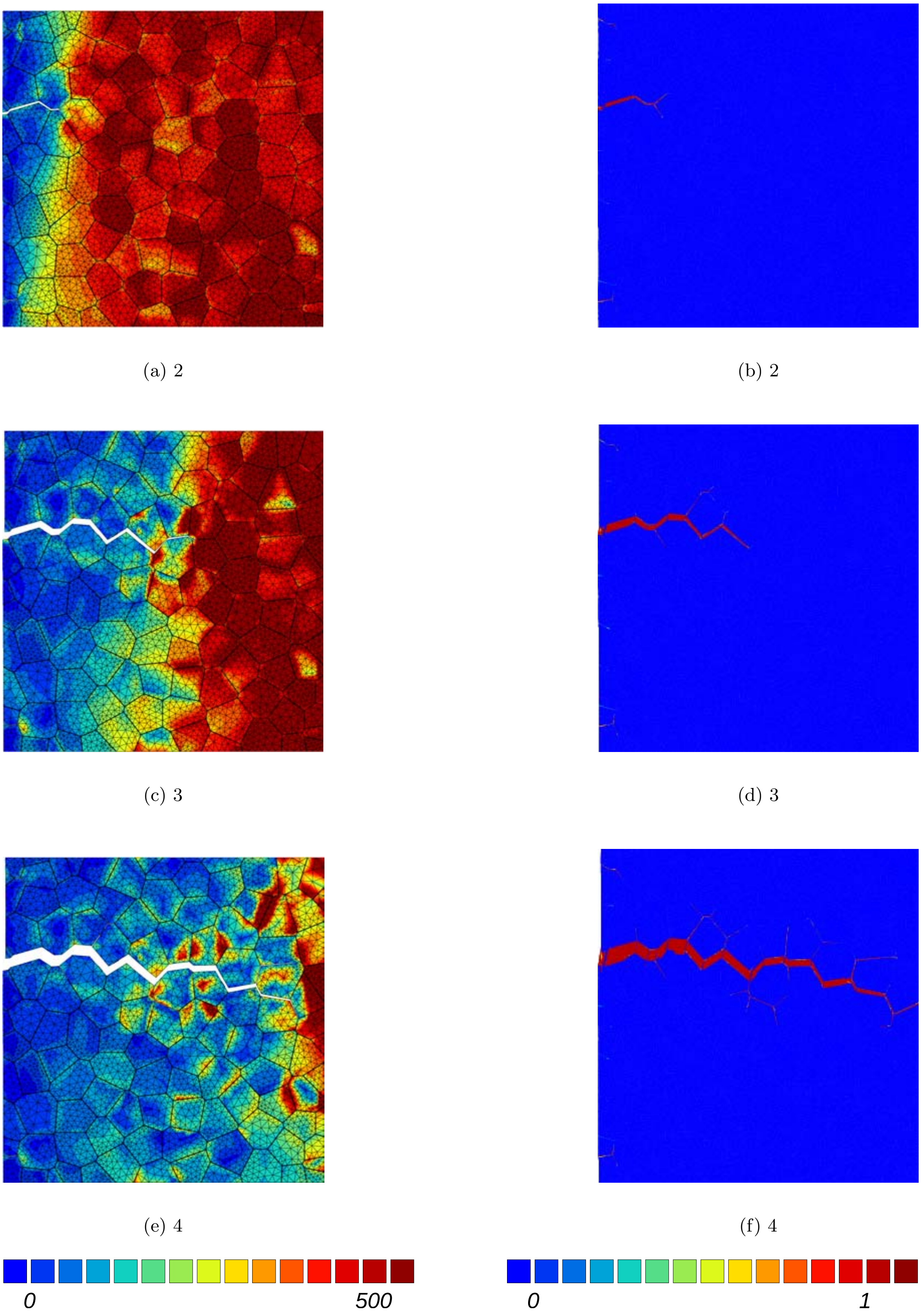
(a) 2

(b) 2

(c) 3

(d) 3

(e) 4

(f) 4

Figure VII.12 : Von Mises stress and damage fields evolution for coupled test

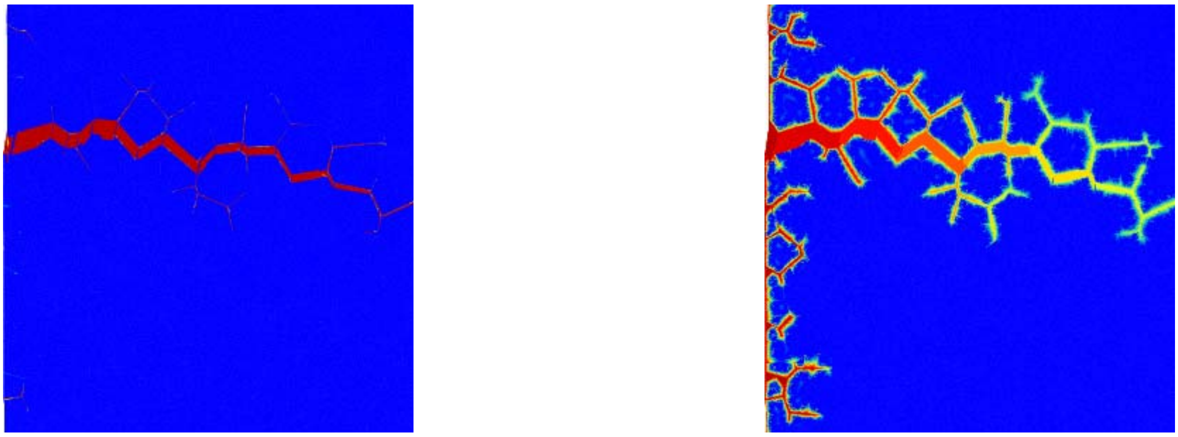

(a) wanted damage (b) wanted concentration

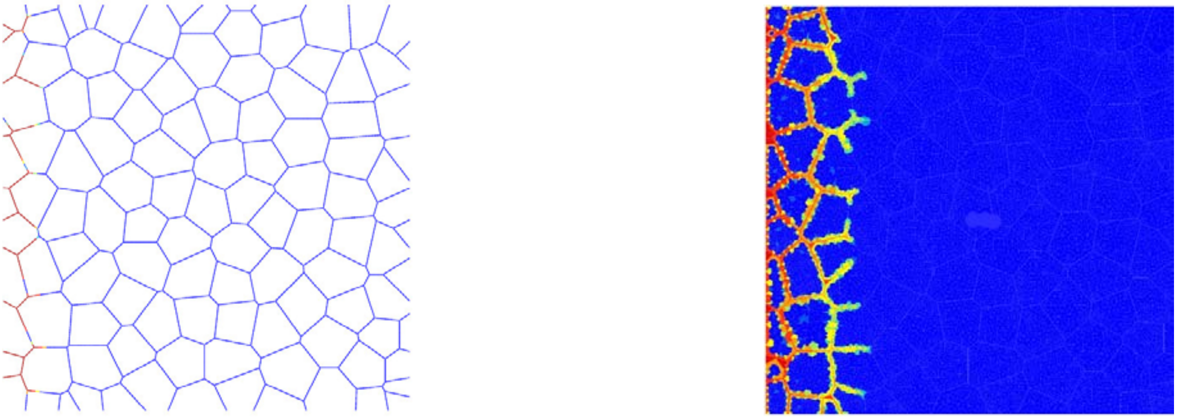

(c) unwanted damage (d) unwanted concentration

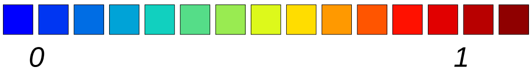

Figure VII.13 : Two parameter sets - wanted and unwanted iodine profile and damage field

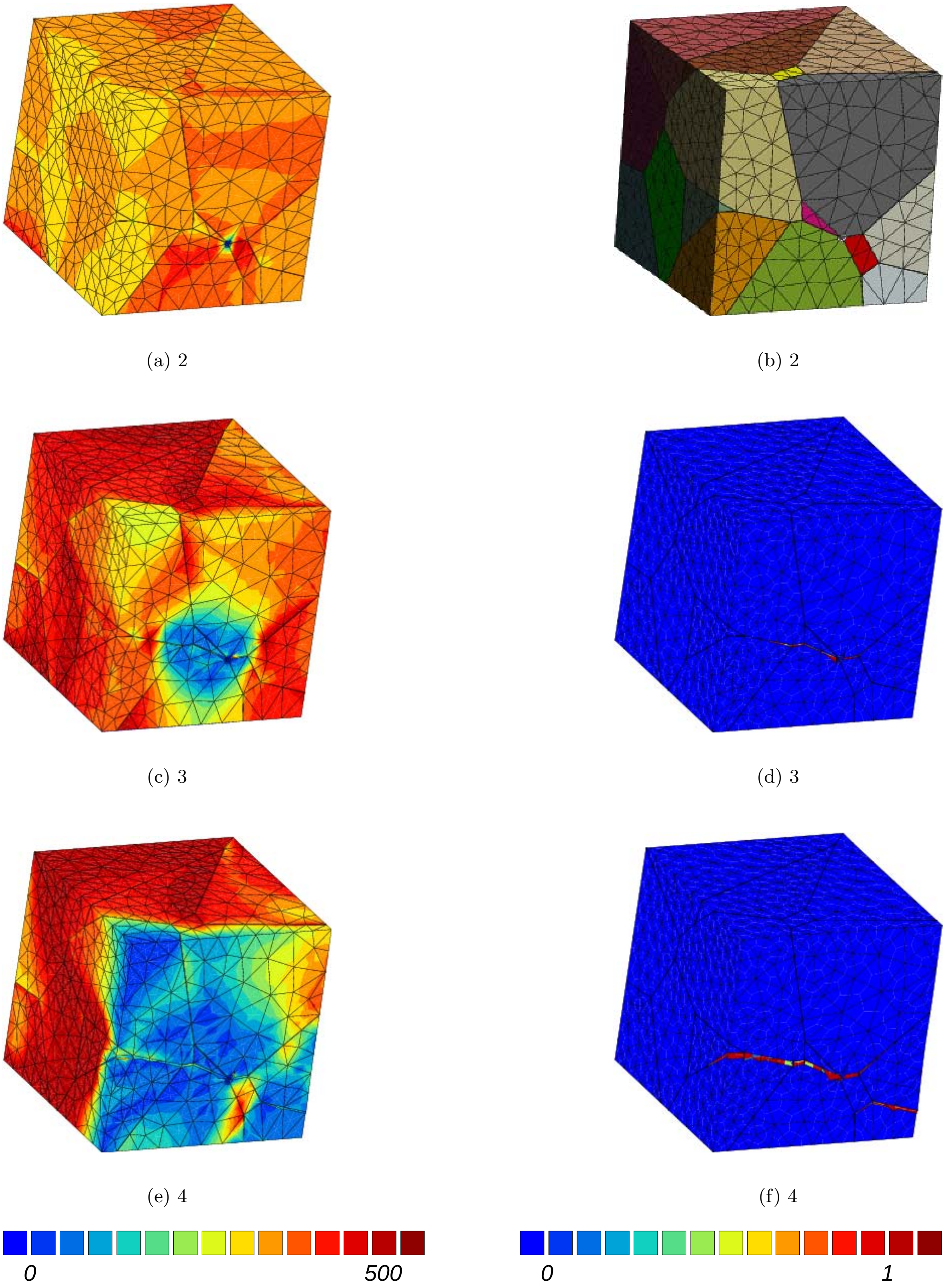
(a) 2

(b) 2

(c) 3

(d) 3

(e) 4

(f) 4

Figure VII.14 : Von Mises stress and damage fields evolution for coupled test - 3d

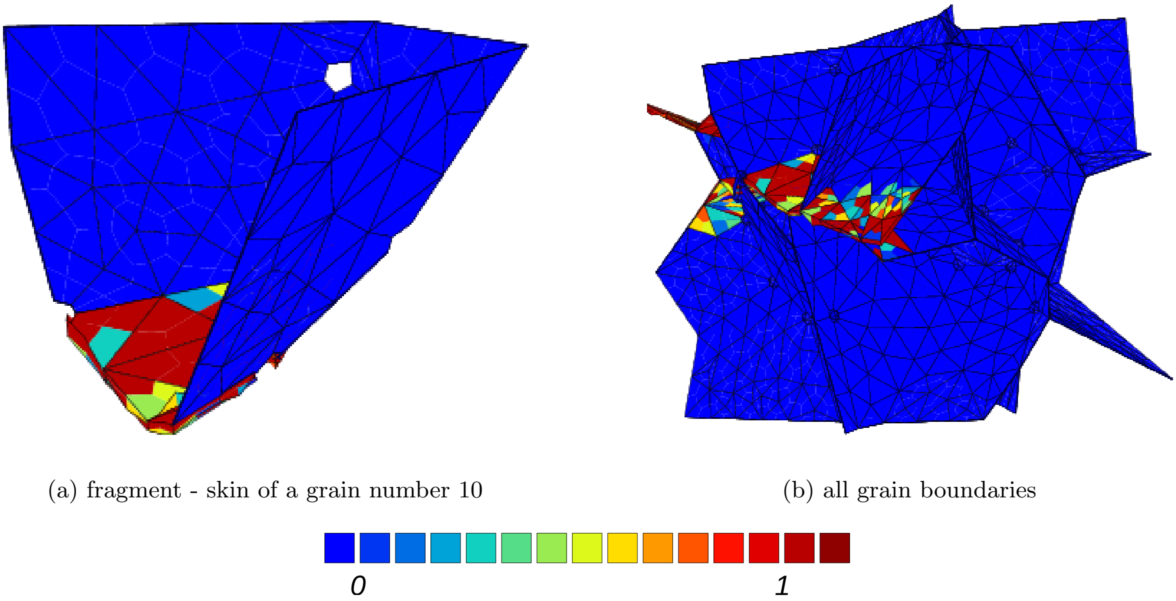

(a) fragment - skin of a grain number 10

(b) all grain boundaries

Figure VII.15 : Damage fields on grain boundary structure - 3d

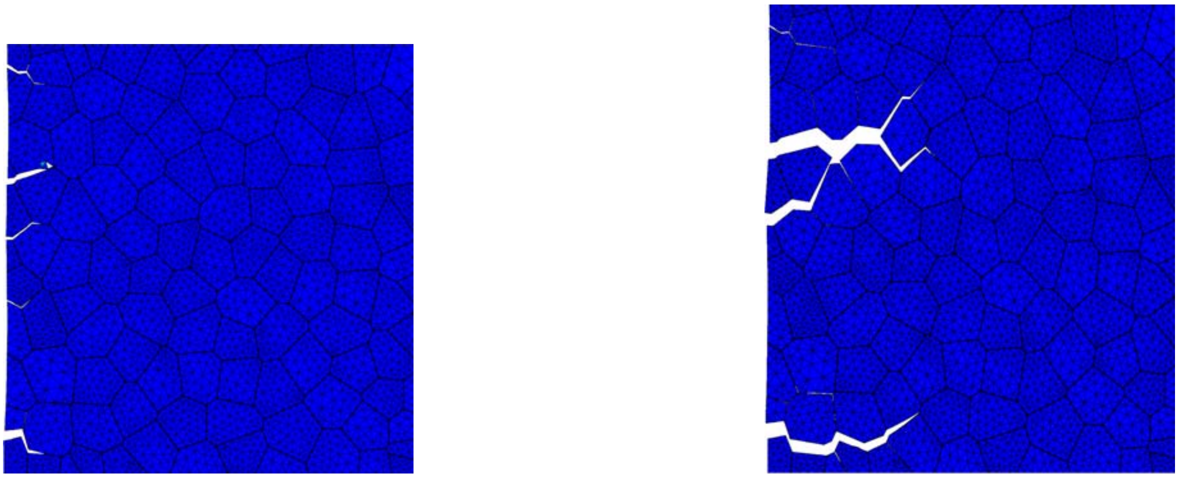

(a) intergranular (b) intergranular

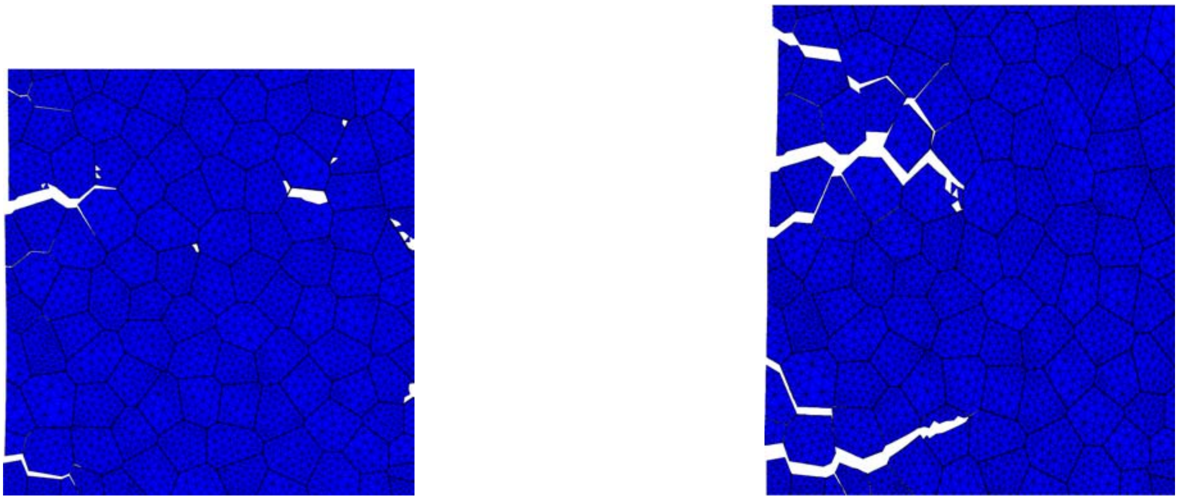

(c) transgranular initiation (d) transgranular initiation

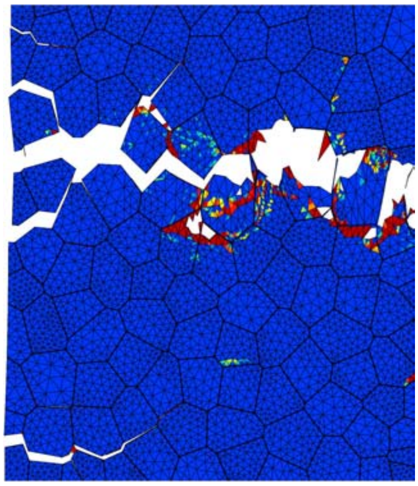

(e) rupture

Figure VII.16 : Inter-transgranular fracture transition

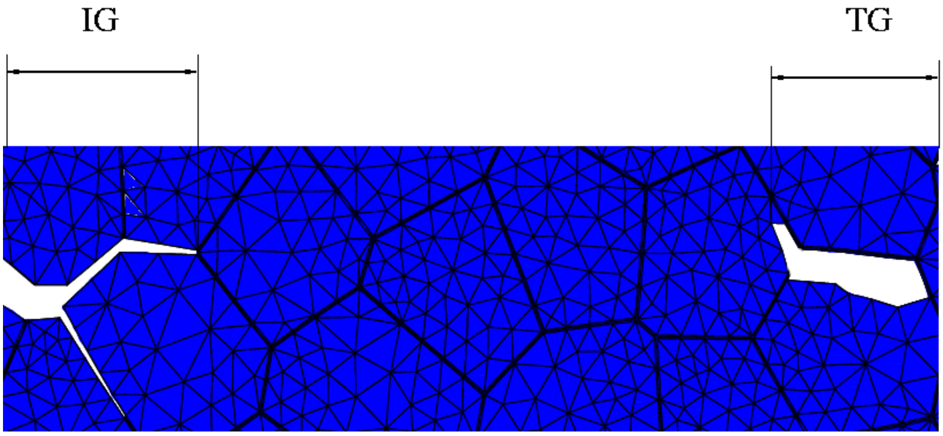

Figure VII.17 : Aggregate fragment, iodine coupled intergranular and uncoupled transgranular material behavior. One can see iodine coupled intergranular crack - on the left (IG), and transgranular crack initiation near the grain boundary, which then enters a neighboor grain - on the right (TG)

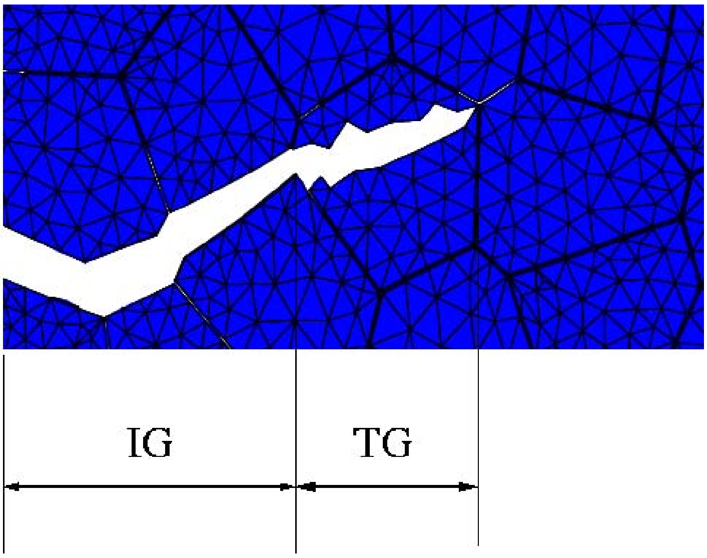

Figure VII.18 : Aggregate fragment, iodine-coupled intergranular and transgranular material behavior. One can see intergranular (IG) crack, followed by transgranular (TG) one

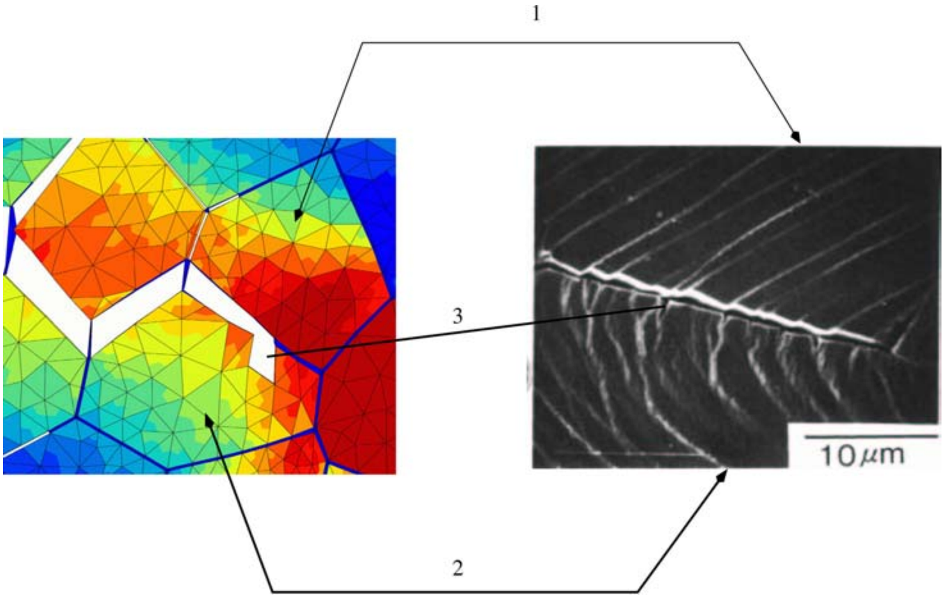

Figure VII.19 : Transgranular crack initiation, qualitative comparison of typical computation result and known literature image; computation field of cumulated prismatic+basal slip versus experimental micrograph from (Kubo et al., 1985). Here : 1 - grain, preferably oriented for prismatic or basal slip, gr59 in the computation ; 2 - grain with less prismatic+basal, but more pyramidal slip, gr53 in the computation; 3 - transgranular crack initiation

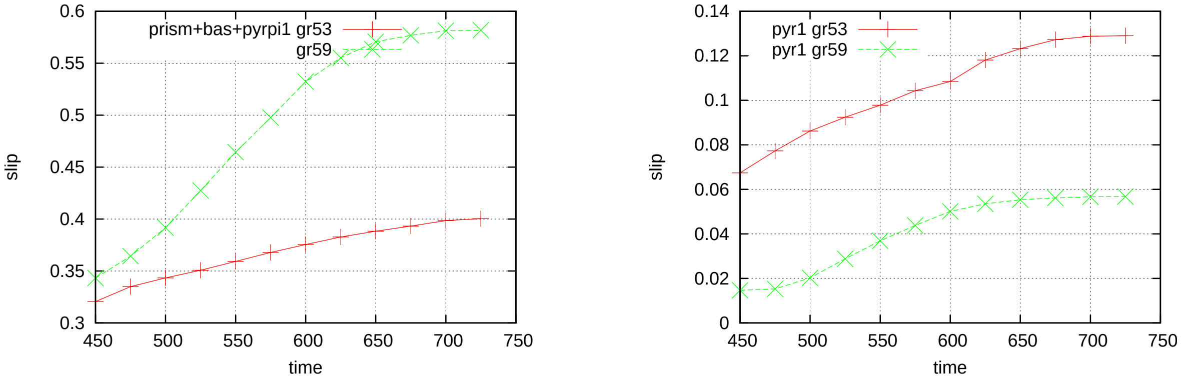

(a)

(b)

Figure VII.20 : Average slips for 2 grains near transgranular crack initiation

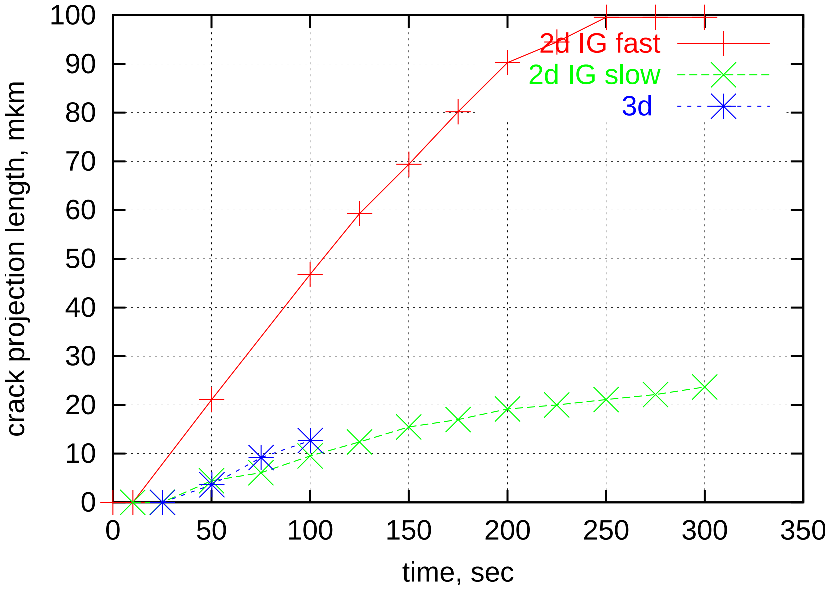

Figure VII.21 : Crack projection length as a function of time for iodine coupled intergranular fracture.

Chapter -VIII-

Conclusions and perspectives

The main purpose of this thesis was to contribute to the development of improved crystal plasticity algorithms, in order to allow for the large deformations and damage in finite element computations, and to present 2D and 3D calculations with crack propagation in intergranular and transgranular regime.

A series of results have been obtained concerning the algorithm development. The results obtained are perfectly clear for the case of elasticity and classical plasticity. Concerning the implementation of single crystal models, a review of the literature has shown that the discussion on the better algorithm is still open, specially for the problem related to the choice of the active slip systems. Several strategies have been tested. They allow us in some cases to present an improved performance, if compared with the preexisting algorithm in ZéBuLoN.

A copper specimen has been computed. A 3D mesh representing the real 3D grain microstructure was available. The code was then able to correctly simulate the high degree of heterogeneity present in the grains.

Crack propagation has been simulated using a new concept for the description of the grain boundary, which is now made of two elements. This type of approach allows us to propose a flexible modeling of any kind of interaction between mechanics and environment. In order to achieve this simulations, an automatic mesh generation procedure has been developed. The grain boundary elements can then be introduced in any real-like 2D or 3D polycrystalline aggregate.

After this work, 2D crack propagation becomes rather easy, even if it remains time consuming. 2D simulations with a relatively large number of grains (100) have been performed. Mechanics and environment are coupled, and the results are quite realistic. On the other hand, it was possible to reproduce the experimentally known transition from integranular to transgranular failure.

3D simulations are also available. A first 3D case has been shown. It was limited to 20 grains, due to the lack of time, but can be run in parallel, in order to improve the CPU time.

Some results of the thesis were published in (Musienko et al., 2002)(Musienko et al., 2003). The results were presented at a number of french and international summits:

- Algorithmes implicites en grandes transformation pour des modeles de plasticite classique et cristalline. Colloq. MECAMAT - Aussois (France) 21-25 janvier 2002

- FE simulation of multicrystals at large strains. A. Musienko, K. Schmidegg, O. Kolednik, R. Pippan, G. Cailletaud. 1st French-Russian Symposium 'Physics and

Mechanics of large plastic strains', St-Petersburg, Russia, 4-7 June 2002, Organized by CRISM "Prometey" (Russia) and LPMTM/CNRS (France)

- Computational aspects of crystal plasticity. Seminar at Laboratoire des Proprietes Mecanique et Thermiques des Materiaux, Univ. Paris XIII (France), 9 July 2002
- Computational aspects of finite strain crystal plasticity. Seminar at LMR, INSA, Rouen (France), 23 January 2003
- Micromechanical approach for stress corrosion cracking in Zircaloy tubes: a volumetric description of damage, opening and sliding of grain boundaries. A.Musienko, G.Cailletaud, O.Diard, S.Leclercq, G.Rousselier. Int.Conf. "Plasticity 2003", Quebec City (Canada), July 7-11, 2003
- Transgranular failure model, A.Musienko, G.Cailletaud - 5th Int Conf. "Scientific-technical problems of safety and lifetime prediction and methods of their solution", Russia, St-Petersburg, St-Petersburg State Tech.Univ. 14-17 Oct. 2003

VIII.1 Perspectives

There are still improvements and open questions.

- One should continue the systematic approach to finite strain algorithms. An improved tangent matrix is highly desirable, and a more efficient procedure for choosing the active slip systems.
- The meshes created in the framework of this study are also available for other types of applications. One could for instance imagine to apply the procedure to superplasticity effect, 2-phase materials with one phase as thin layers between the grains of the other, etc...
- Two types of perspectives are possible for copper computations: the results could probably be improved by using finer meshes, adapted material parameters, different boundary conditions, effect of crystal rotation; the importance of choosing a realistic 3D shape for the grains could be better demonstrated by using other type of grain geometries in our simulations (we tried extended 2D computations, but random grain morphology reconstruction from the 2D surface image could be investigated too).
- Having in hand the numerical procedure for iodine-coupled inter-transgranular fracture analysis, we could easily generate a series of results with complex sequences of interaction, like applying load first, then the effect of environment (for tests with delayed iodine interaction), or sequences with action of environment only, followed by a mechanical loading... This would allow to have a stronger idea about the values of the material parameters.
- Possible scenarii of real tube fracture can be simulated.

Appendix -A-

Pre-existing algorithm of ZéBuLoN for single crystal model

A.1 Stress update algorithm

A.1.1 Possible numerical methods

Let us consider a problem to numerically resolve differential equation, as follows:

$$\dot{v} = f(v), v(t_0) = v_0$$

Let us look at one time step, from time t till $t + \Delta t$. The value of the variable at time t – i.e. v_t – supposed to be known. The value at the end of time step – $v_{t+\Delta t}$ – should be found. Two strategies are classically known.

1. Explicit methods. The most simple of them is called "Forward Euler scheme". The increment of the unknown variable Δv is calculated in the explicit manner, starting from the value at the beginnnig of time step v_t. The expression is as follows :

   $$\Delta v = f(v_t)\Delta t$$

2. Implicit methods. The most simple of them is called "Backward Euler scheme". The increment of the unknown variable Δv is now found as a solution of a nonlinear algebraic equation, as follows :

   $$\Delta v = f(v_{t+\Delta t})\Delta t$$

   In other words, the residual $\mathcal{R}$ should be made equal to zero.

   $$\mathcal{R} = \Delta v - f(v_{t+\Delta t})\Delta t$$

   This equation is solved by the Newton method. For this method, the Jacobian has to be calculated :

   $$J = \frac{\partial \mathcal{R}}{\partial \Delta v}$$

A.1.2 Implicit integration for the single crystal model

For the case of a single crystal model, the residuals are as follows.

$$\begin{aligned}
\mathcal{F}_e &= \Delta\underset{\sim}{\varepsilon} - \Delta\underset{\sim}{\varepsilon}^e - \sum \Delta v_s \cdot \operatorname{sign}\tau_s \underset{\sim}{\mathbf{m}}_s \\
\mathcal{F}_{v_s} &= \Delta v_s - \left\langle \frac{|\tau_s^{t+\Delta t} - x_s^{t+\Delta t}| - r_s^{t+\Delta t}}{K} \right\rangle^n \Delta t
\end{aligned}$$

$$\begin{aligned}
\Delta x_s &= C\Delta\alpha_s \\
\Delta\alpha_s &= \Delta v_s(\operatorname{sign}(\tau_s - x_s) - D(\alpha_s^t))/(1 + D\Delta v_s) \\
\Delta r_s &= Q\sum h_{rs}\Delta\rho_r \\
\Delta\rho_r &= \frac{(1 - b\rho_r^t)\Delta v_r}{1 + b\Delta v_r}
\end{aligned}$$

The Jacobian matrix is found as a derivative of all the residuals by all the unknowns. It comes:

$$\begin{aligned}
\frac{\partial\mathcal{F}_e}{\partial\Delta\underset{\sim}{\varepsilon}_e} &= \underset{\approx}{\mathbf{I}} \\
\frac{\partial\mathcal{F}_e}{\partial\Delta v_s} &= \begin{cases} -\operatorname{sign}\tau_s \underset{\sim}{\mathbf{m}}_s & \text{active} \\ 0 & \text{nonactive} \end{cases} \\
\frac{\partial\mathcal{F}_{v_s}}{\partial\Delta\underset{\sim}{\varepsilon}_e} &= \begin{cases} -\frac{n}{K}\Delta t \left\langle \frac{|\tau_s^{t+\Delta t} - x_s^{t+\Delta t}| - r_s^{t+\Delta t}}{K} \right\rangle^{n-1} \operatorname{sign}\tau_s \underset{\sim}{\mathbf{m}}_s : \underset{\approx}{\mathbf{L}} & \text{active} \\ 0 & \text{nonactive} \end{cases} \\
\frac{\partial\mathcal{F}_{v_s}}{\partial\Delta v_r} &= \delta_{rs} + \frac{n}{K}\left\langle \frac{|\tau_s^{t+\Delta t} - x_s^{t+\Delta t}| - r_s^{t+\Delta t}}{K} \right\rangle^{n-1} \cdot \left[\operatorname{sign}(\tau_s - x_s)\frac{\partial\Delta x_s}{\partial\Delta v_r} + \frac{\partial\Delta r_s}{\partial\Delta v_r}\right]\Delta t
\end{aligned}$$

A.2 Algorithmic elasto-plastic moduli

The developement for consistent elasto-plastic tangent moduli is presented here. Similar results can be found in (Miehe and Schröder, 2001).

It is known, that

$$\underset{\approx}{\mathbf{C}}^{ep} = \frac{\partial\Delta\underset{\sim}{\sigma}}{\partial\Delta\underset{\sim}{\varepsilon}}$$

Additive elasto plastic decomposition for crystalline model is as follows :

$$\Delta\underset{\sim}{\sigma} = \underset{\approx}{\mathbf{C}} : \Delta\underset{\sim}{\varepsilon} - \sum_s \Delta\gamma_s \underset{\approx}{\mathbf{C}} : \underset{\sim}{\mathbf{m}}_s$$

$$\Delta\tau_r = \underset{\sim}{\mathbf{m}}_r : \Delta\underset{\sim}{\sigma} = \underset{\sim}{\mathbf{m}}_r : \underset{\approx}{\mathbf{C}} : \Delta\underset{\sim}{\varepsilon} - \sum_s \Delta\gamma_s \underset{\sim}{\mathbf{m}}_r : \underset{\approx}{\mathbf{C}} : \underset{\sim}{\mathbf{m}}_s$$

On the other hand, for active slip systems

$$R_r = R_0 + Q \cdot \sum_p h_{rp} v_p$$

$$\Delta R_r = Q \cdot \sum_p h_{rp} \Delta v_p$$

$$|\tau_r| = R_r \quad \Rightarrow \quad \operatorname{sign}\tau_r \tau_r = R_r \quad \Rightarrow \quad \operatorname{sign}\tau_r \Delta\tau_r = \Delta R_r$$

We consider here, that sign does not change on the increment.
Putting the 2 expressions for $\Delta\tau_r$ together, one can get :

$$Q \cdot \sum_p h_{rp} \Delta v_p = \operatorname{sign}\tau_r \left[\underset{\sim}{\mathbf{m}}_r : \underset{\approx}{\mathbf{C}} : \Delta\underset{\sim}{\varepsilon} - \sum_s \Delta\gamma_s \underset{\sim}{\mathbf{m}}_r : \underset{\approx}{\mathbf{C}} : \underset{\sim}{\mathbf{m}}_s \right]$$

One can use p=s, so

$$\operatorname{sign}\tau_r (\underset{\sim}{\mathbf{m}}_r : \underset{\approx}{\mathbf{C}} : \Delta\underset{\sim}{\varepsilon}) = \sum_s \left[\operatorname{sign}\tau_r \Delta\gamma_s \underset{\sim}{\mathbf{m}}_r : \underset{\approx}{\mathbf{C}} : \underset{\sim}{\mathbf{m}}_s + Q \cdot h_{rs} \Delta v_s \right]$$

$$\operatorname{sign}\tau_r (\underset{\sim}{\mathbf{m}}_r : \underset{\approx}{\mathbf{C}} : \Delta\underset{\sim}{\varepsilon}) = \sum_s \left[(\operatorname{sign}\tau_s \operatorname{sign}\tau_r) \underset{\sim}{\mathbf{m}}_r : \underset{\approx}{\mathbf{C}} : \underset{\sim}{\mathbf{m}}_s + Q \cdot h_{rs} \right] \Delta v_s$$

One can see the last expression in matrix form, as

$$\begin{pmatrix} \operatorname{sign}\tau_{active1} (\underset{\sim}{\mathbf{m}}_{active1} : \underset{\approx}{\mathbf{C}} : \Delta\underset{\sim}{\varepsilon}) \\ \ldots \\ \operatorname{sign}\tau_{activeN} (\underset{\sim}{\mathbf{m}}_{activeN} : \underset{\approx}{\mathbf{C}} : \Delta\underset{\sim}{\varepsilon}) \end{pmatrix} = \begin{pmatrix} D_{11} & \ldots & D_{1N} \\ \ldots & \ldots & \ldots \\ D_{N1} & \ldots & D_{NN} \end{pmatrix} \cdot \begin{pmatrix} \Delta v_{active1} \\ \ldots \\ \Delta v_{activeN} \end{pmatrix}$$

Here

$$D_{ij} = (\operatorname{sign}\tau_{active_i} \operatorname{sign}\tau_{active_j}) \underset{\sim}{\mathbf{m}}_{active_i} : \underset{\approx}{\mathbf{C}} : \underset{\sim}{\mathbf{m}}_{active_j} + Q \cdot h_{active_i active_j}$$

Taking the inverse of D-matrix, one have :

$$\begin{pmatrix} \Delta v_{active1} \\ \ldots \\ \Delta v_{activeN} \end{pmatrix} = [\mathcal{D}]^{-1} \cdot \begin{pmatrix} \operatorname{sign}\tau_{active1} \underset{\sim}{\mathbf{m}}_{active1} : \underset{\approx}{\mathbf{C}} : \Delta\underset{\sim}{\varepsilon} \\ \ldots \\ \operatorname{sign}\tau_{activeN} \underset{\sim}{\mathbf{m}}_{activeN} : \underset{\approx}{\mathbf{C}} : \Delta\underset{\sim}{\varepsilon} \end{pmatrix}$$

In other words,

$$\Delta v_\alpha = \sum_\beta [\mathcal{D}]^{-1}_{\alpha\beta} \operatorname{sign}\tau_\beta \underset{\sim}{\mathbf{m}}_\beta : \underset{\approx}{\mathbf{C}} : \Delta\underset{\sim}{\varepsilon}$$

$$\frac{\partial \Delta v_\alpha}{\partial \Delta\underset{\sim}{\varepsilon}} = \sum_\beta [\mathcal{D}]^{-1}_{\alpha\beta} \operatorname{sign}\tau_\beta \underset{\sim}{\mathbf{m}}_\beta : \underset{\approx}{\mathbf{C}}$$

Algorithmic tangent will finally take form :

$$\frac{\partial \Delta\underset{\sim}{\sigma}}{\partial \Delta\underset{\sim}{\varepsilon}} = \underset{\approx}{\mathbf{C}} - \sum_\alpha \sum_\beta [\mathcal{D}]^{-1}_{\alpha\beta} \operatorname{sign}\tau_\alpha \operatorname{sign}\tau_\beta (\underset{\approx}{\mathbf{C}} : \underset{\sim}{\mathbf{m}}_\alpha) \otimes (\underset{\sim}{\mathbf{m}}_\beta : \underset{\approx}{\mathbf{C}})$$

And again, we consider, that signum τ does not change.
For the case of elastic isotropic material,

$$\underset{\approx}{\mathbf{C}} = 2\mu \underset{\approx}{\mathbf{I}} + (k - \frac{2}{3}\mu) \underset{\sim}{\mathbf{I}} \otimes \underset{\sim}{\mathbf{I}}$$

As $\operatorname{Tr} \underset{\sim}{\mathbf{m}}_s = 0$, one gets

$$\underset{\approx}{\mathbf{C}} : \underset{\sim}{\mathbf{m}}_s = 2\mu \underset{\sim}{\mathbf{m}}_s$$

$$\frac{\partial \Delta \underset{\sim}{\sigma}}{\partial \Delta \underset{\sim}{\varepsilon}} = \underset{\approx}{\mathbf{C}} - 4\mu^2 \cdot \sum_{\alpha} \sum_{\beta} [\mathcal{D}]^{-1}_{\alpha\beta} \operatorname{sign} \tau_\alpha \operatorname{sign} \tau_\beta \underset{\sim}{\mathbf{m}}_\alpha \otimes \underset{\sim}{\mathbf{m}}_\beta$$

For D-matrix one will have :

$$D_{ij} = 2\mu(\operatorname{sign} \tau_{active_i} \operatorname{sign} \tau_{active_j}) \underset{\sim}{\mathbf{m}}_{active_i} : \underset{\sim}{\mathbf{m}}_{active_j} + Q \cdot h_{active_i active_j}$$

With just 1 slip system, matrix would be a scalar, as

$$\mathcal{D} = 2\mu \underset{\sim}{\mathbf{m}}_\sharp : \underset{\sim}{\mathbf{m}}_\sharp + Q \approx \mu$$

$$\mathcal{D}^{-1} = 1/\mu$$

Then, tangent will be

$$\frac{\partial \Delta \underset{\sim}{\sigma}}{\partial \Delta \underset{\sim}{\varepsilon}} = \underset{\approx}{\mathbf{C}} - 4\mu (\underset{\sim}{\mathbf{m}}_\sharp \otimes \underset{\sim}{\mathbf{m}}_\sharp)$$

In particular, for active slip number 7,

$$4\mu(\underset{\sim}{\mathbf{m}}_7 \otimes \underset{\sim}{\mathbf{m}}_7) = \frac{4}{6}\mu \begin{pmatrix} 0 & 0.5 & -0.5 \\ & -1 & 0 \\ sym & & 1 \end{pmatrix} \otimes \begin{pmatrix} 0 & 0.5 & -0.5 \\ & -1 & 0 \\ sym & & 1 \end{pmatrix} =$$

$$= \frac{2}{3}\mu \begin{pmatrix} 0 & 0 & 0 & 0 & 0 & 0 \\ 0 & 1 & -1 & -0.707107 & 0 & 0.707107 \\ 0 & -1 & 1 & 0.707107 & 0 & -0.707107 \\ 0 & -0.707107 & 0.707107 & 0.5 & 0 & -0.5 \\ 0 & 0 & 0 & 0 & 0 & 0 \\ 0 & 0.707107 & -0.707107 & -0.5 & -0 & 0.5 \end{pmatrix}$$

A.3 Check the nature of matrix $\mathcal{D}$

Let us check the values of $\underset{\sim}{\mathbf{m}}_i : \underset{\sim}{\mathbf{m}}_j$.

$$\underset{\sim}{\mathbf{m}}_i : \underset{\sim}{\mathbf{m}}_i = \frac{1}{6} \cdot 3$$

$$\underset{\sim}{\mathbf{m}}_i : \underset{\sim}{\mathbf{m}}_j = \frac{1}{6} \cdot \begin{pmatrix} 3 & 1.5 & 1.5 & 1 & 0.5 & -0.5 & 0.5 & 1.5 & 2 & 0.5 & -2 & -1.5 \\ 1.5 & 3 & -1.5 & 0.5 & 2 & 1.5 & 1 & -0.5 & 0.5 & -0.5 & -1.5 & -2 \\ 1.5 & -1.5 & 3 & 0.5 & -1.5 & -2 & -0.5 & 2 & 1.5 & 1 & -0.5 & 0.5 \\ 1 & 0.5 & 0.5 & 3 & 1.5 & -1.5 & 1.5 & 0.5 & 2 & 1.5 & -2 & -0.5 \\ 0.5 & 2 & -1.5 & 1.5 & 3 & 1.5 & 2 & -0.5 & 1.5 & -0.5 & -0.5 & -1 \\ -0.5 & 1.5 & -2 & -1.5 & 1.5 & 3 & 0.5 & -1 & -0.5 & -2 & 1.5 & -0.5 \\ 0.5 & 1 & -0.5 & 1.5 & 2 & 0.5 & 3 & -1.5 & 1.5 & -1.5 & -0.5 & -2 \\ 1.5 & -0.5 & 2 & 0.5 & -0.5 & -1 & -1.5 & 3 & 1.5 & 2 & -0.5 & 1.5 \\ 2 & 0.5 & 1.5 & 2 & 1.5 & -0.5 & 1.5 & 1.5 & 3 & 0.5 & -1 & -0.5 \\ 0.5 & -0.5 & 1 & 1.5 & -0.5 & -2 & -1.5 & 2 & 0.5 & 3 & -1.5 & 1.5 \\ -2 & -1.5 & -0.5 & -2 & -0.5 & 1.5 & -0.5 & -0.5 & -1 & -1.5 & 3 & 1.5 \\ -1.5 & -2 & 0.5 & -0.5 & -1 & -0.5 & -2 & 1.5 & -0.5 & 1.5 & 1.5 & 3 \end{pmatrix}$$

$$= \begin{pmatrix} \mathbf{0.5} & 0.25 & 0.25 & 0.166 & 0.0833 & -0.0833 & 0.0833 & 0.25 & 0.333 & 0.0833 & -0.333 & -0.25 \\ 0.25 & \mathbf{0.5} & -0.25 & 0.0833 & 0.333 & 0.25 & 0.166 & -0.0833 & 0.0833 & -0.0833 & -0.25 & -0.333 \\ 0.25 & -0.25 & \mathbf{0.5} & 0.0833 & -0.25 & -0.333 & -0.0833 & 0.333 & 0.25 & 0.166 & -0.0833 & 0.0833 \\ 0.166 & 0.0833 & 0.0833 & \mathbf{0.5} & 0.25 & -0.25 & 0.25 & 0.0833 & 0.333 & 0.25 & -0.333 & -0.0833 \\ 0.0833 & 0.333 & -0.25 & 0.25 & \mathbf{0.5} & 0.25 & 0.333 & -0.0833 & 0.25 & -0.0833 & -0.0833 & -0.166 \\ -0.0833 & 0.25 & -0.333 & -0.25 & 0.25 & \mathbf{0.5} & 0.0833 & -0.166 & -0.0833 & -0.333 & 0.25 & -0.0833 \\ 0.0833 & 0.166 & -0.0833 & 0.25 & 0.333 & 0.0833 & \mathbf{0.5} & -0.25 & 0.25 & -0.25 & -0.0833 & -0.333 \\ 0.25 & -0.0833 & 0.333 & 0.0833 & -0.0833 & -0.166 & -0.25 & \mathbf{0.5} & 0.25 & 0.333 & -0.0833 & 0.25 \\ 0.333 & 0.0833 & 0.25 & 0.333 & 0.25 & -0.0833 & 0.25 & 0.25 & \mathbf{0.5} & 0.0833 & -0.166 & -0.0833 \\ 0.0833 & -0.0833 & 0.166 & 0.25 & -0.0833 & -0.333 & -0.25 & 0.333 & 0.0833 & \mathbf{0.5} & -0.25 & 0.25 \\ -0.333 & -0.25 & -0.0833 & -0.333 & -0.0833 & 0.25 & -0.0833 & -0.0833 & -0.166 & -0.25 & \mathbf{0.5} & 0.25 \\ -0.25 & -0.333 & 0.0833 & -0.0833 & -0.166 & -0.0833 & -0.333 & 0.25 & -0.0833 & 0.25 & 0.25 & \mathbf{0.5} \end{pmatrix}$$

Note, that a block of this matrix can have a determinant equal to zero. Example – top left 3 by 3 block.

Appendix -B-

Examples of the source code for integration procedures of material behavior models

B.1 Elasticity

```
// ============================================================================
//   NeoHookean compressible elasticity
// ============================================================================
@Class NEO_HOOKE : BASIC_NL_BEHAVIOR {
   @Name     neo_hooke1;
   @Grad     usz F;
   @Coefs mu, lam;
};

@StrainPart {

TENSOR2 one = TENSOR2::unity(tsz());
TENSOR2 Ft = transpose(F);
TENSOR2 b = syme(F*Ft);
double J = F.determin();

double ko = mu/J;
sig = ko * (b - kronecker);
double ko1 = lam/J*log(J);
sig += ko1 * one;

TENSOR4 spacial_elasticity = lam/J * (one ^ one);
double coef = 2./J * (mu - lam * log(J));
spacial_elasticity += coef * (TENSOR4::I(tsz()));
//--------- tg_matrix...
      m_tg_matrix = spacial_elasticity;
}
```

B.2 J2 plasticity

```
// ============================================================================
//             Finite strain J2 plasticity with implicit integration
// ============================================================================

#include <Elasticity.h>

@Class anand1 : BASIC_NL_BEHAVIOR {
   @Name anand1;
   @SubClass ELASTICITY           elasticity;
   @Coefs R0, Q;
   @Grad     usz F;
   @tVarInt  eel;
   @sVarInt  epcum;
   @uVarAux  Fp;
   @uVarUtil Fe, Fe_tr,R_tr;
   @tVarUtil U_tr,Ue, T_bar, T, U;
   @tVarUtil norm, eel_tr;
   SMATRIX   ds_deel;
   @Implicit
};

@PreStep {
  Fe_tr = F* inverse(Fp);
  Fe_tr.strain_partion(R_tr, U_tr);
  eel_tr = U_tr.log_tensor();
}

@StrainPart {
  double  Jac   = 1./F.determin();
  Ue     = eel.exp_tensor();
  Fe     = R_tr * Ue;
  Fp    = inverse(Fe)*F;
  T_bar = *elasticity*eel;
  T = rotate_tensor(T_bar,R_tr);
  sig = T*Jac;
      SMATRIX tmp(psz,f_grad,0,0);
      SMATRIX H = *elasticity*tmp;
      SMATRIX Cstar = expand_in(TENSOR4::Ml(to_5_9(sig)) + TENSOR4::Mr(to_5_9(sig)));
      m_tg_matrix =Jac*rotate_matrix(H, R_tr);
      m_tg_matrix -= Cstar;
}

@CalcGradF {
            sig         = *elasticity*eel;
  double    radius      = R0 + Q*epcum;
  TENSOR2   devT = deviator(sig);
  double   sigeff       = sqrt(1.5*(devT|devT));
  double    yld          = sigeff - radius;
            f_vec_eel   = eel - eel_tr;
            ds_deel = *elasticity;
  if ( (yld>(double)0.0 && depcum>=0) || (depcum>(double)0.0) ) {
     norm               = (1.5/sigeff)*devT;
  SMATRIX dn_ds = (1.5/sigeff)* TENSOR4::J(tsz());
  dn_ds -= (1./sigeff) * (norm^norm);
  SMATRIX dn_deel            = dn_ds*ds_deel;
```

```
    f_vec_eel         += norm*depcum;
    deel_deel         = TENSOR4::I(tsz()) + depcum*dn_deel;
    deel_depcum        = norm;

    f_vec_epcum    = 0.01*yld;
    depcum_depcum  = (-0.01)*Q;
    depcum_deel    = 0.01*(norm*ds_deel);
  }
}
// ============================================================================
```

B.3 Crystal plasticity

```
// ============================================================================
//                     Implicit integration of the single crystal
//                             with multiplicative decomposition
// ============================================================================
#include <Elasticity.h>

@Class FS_SS1 : BASIC_NL_BEHAVIOR {
   @Name     fs_ss1;
   @SubClass ELASTICITY elasticity;
   @SubClass CRYSTAL_ORIENTATION  orientation;
   @Coefs    Q, b, R0, K, n;
   @Grad     usz F;
   @tVarInt  eel;
   @sVarInt  v [num_systems(1)];
   @uVarAux  Fp;
   @uVarAux  Fe;
   @tVarUtil  Ce,Ctr, eel_tr;
   @sVarUtil  norm [num_systems(1)];
   @sVarUtil  v_ini [num_systems(1)];
   int num_systems(int);
   @Implicit
};

@PreStep {
  TENSOR2 Fe_tr    = F*inverse(Fp);
  TENSOR2 Ft = transpose(Fe_tr);
  eel_tr     = 0.5*(syme(Ft*Fe_tr) - TENSOR2::unity(tsz()));
  int i, Nsyst = num_systems(1);
  for(i=0;i<Nsyst;i++) v_ini[i] = v[i];
}
//----------------------------------------------------------
@StrainPart {
double  Jac   = (double)1./F.determin();
double dv;
int c=0;
int Nsyst = num_systems(1);
         MARRAY<TENSOR2>& uloc1 = orientation->give_u_loc();
         MARRAY<TENSOR2>& mloc1 = orientation->give_m_loc();
//-----------update Fp
TENSOR2 deltafp;
deltafp.resize(usz); deltafp=0.;
for (c=0;c<Nsyst;c++)
{
dv = v[c]-v_ini[c];
deltafp += dv * norm[c] * (uloc1[c]+to_5_9(mloc1[c]));
}
TENSOR2 exp_deltafp = deltafp.exp_tensor();
Fp = exp_deltafp * Fp;

//-----------check det Fp = 1
if (Fp.determin()<=(double)0.0) { Fp=(double)0.0; Fp[0]=Fp[1]=Fp[2]=(double)1.0; }
Fp *= (double)1.0/(pow(Fp.determin(),((double)1./(double)3.)));
//----------update Fe
 Fe = F * inverse(Fp);
 TENSOR2 Fet = transpose(Fe);
//------update Cauchy stress
  Ce = 2.*eel + TENSOR2::unity(tsz());
  TENSOR2 sigm = *elasticity * eel;
  sig = syme((Fe*to_5_9(sigm)*Fet))/Fe.determin();
//---------global tg_matrix, to be updated later...
      MATRIX tmp(psz, psz,f_grad,0,0);
      SMATRIX H = *elasticity*tmp;
      SMATRIX Cstar = expand_in(TENSOR4::Ml(to_5_9(sig)) + TENSOR4::Mr(to_5_9(sig)));
      m_tg_matrix = Jac*rotate_matrix(H, Fe)-Cstar;
}
//----------------------------------------------------------
@CalcGradF {
//---stress
  Ce = 2.*eel + TENSOR2::unity(tsz());
  Ctr = 2.*eel_tr + TENSOR2::unity(tsz());
  TENSOR2 sigm   = *elasticity*eel;
         f_vec_eel = eel - eel_tr;
         deel_deel = TENSOR4::I(tsz());
         int c=0;
         int ns1 = num_systems(1);
//---orientation tensors...
         MARRAY<TENSOR2>& mloc1 = orientation->give_m_loc();
         MARRAY<TENSOR2>& uloc1 = orientation->give_u_loc();
//-----------------------------------------------------------
for (c=0;c<ns1;c++) {
        TENSOR2 loc = uloc1[c]+to_5_9(mloc1[c]);
//---formulate f_vecs starts
        double tau = (to_5_9(sigm))|loc;
        norm[c] = sign (tau);

    double R   = R0 + Q*((double)1. - exp(-b*v[c]));
      double overstress = fabs(tau) - R;
 if (overstress>(double)0.0)
          {
       TENSOR2 epl_c = syme(loc*to_5_9(Ctr));
f_vec_eel += epl_c*(norm[c]*dv[c]);
double deriv = (n/K) * pow(overstress/K,n-(double)1.)*dt;
          f_vec_v[c] = dv[c]- dt*pow(overstress/K,n);
//---derivatives for local Jacobian

deel_dv[c] = epl_c*norm[c];
dv_deel[c] =  ((-1.)*deriv*norm[c])*syme(loc * expand_out(*elasticity));
dv_dv(c,c) = 1.0 + deriv * (Q * b * exp(-b*v[c]));
}}}

//----------------------------------------------------
int FS_SS1::num_systems(int n)
{  if (orientation.if_null())
      ERROR("One orientation MUST be given with **orientation");
   if (n==1) return orientation->num_systems();
   else return 0;
}
```

Bibliography

Adda Y. and Philibert J. (1977). *La diffusion dans les solides.* Presses universitaires de France.

Anand L. (1979). *On H. Hencky's approximate strain-energy function for moderate deformations.* ASME Journal of Applied Mechanics, vol. 46, pp 78–82.

Anand L. (1986). *Moderate deformations in extension-torsion of incompressible isotropic elastic materials.* Journal of the Mechanics and Physics of Solids, vol. 34 n° 3, pp 293–304.

Anand L. (2004). *Single-crystal elasto-viscoplasticity: application to texture evolution in polycrystalline metals at large strains.* Computer Methods in Applied Mechanics and Engineering, vol. 193 n° 48-51, pp 5359–5383.

Anand L. and Kothari M. (1996). *A computational procedure for rate-independent crystal plasticity.* J.Mech.Phys.Solids, vol. 44 n° 3, pp 525–558.

Asaro R.J. (1983). *Crystal Plasticity.* J. of Applied Mechanics, vol. 50, pp 921–934.

Asaro R.J. and Needleman A. (1985). *Texture development and strain hardening in rate dependent polycrystals.* Acta Metall., vol. 33, pp 923–953.

Attouch Hedy (1996). *Viscosity solutions of minimization problems.* SIAM J. Optimization, vol. 6 n° 3, pp 769–806.

Barbe Fabrice, Decker Luc, Jeulin Dominique, and Cailletaud Georges (2001a). *Intergranular and intragranular behavior of polycrystalline aggregates. Part 1: model.* International Journal of Plasticity, vol. 17 n° 4, pp 513–536.

Barbe Fabrice., Forest Samuel., and Cailletaud Georges. (2001b). *Intergranular and intragranular behavior of polycrystalline aggregates.Part 2: Results.* International Journal of Plasticity, vol. 17 n° 4, pp 537–563.

Bathe K.-J. (1996). *Finite element procedures.* Prentice Hall.

Becker R. and Panchanadeeswaran S. (1995). *Effects of grain interactions on deformation and local texture in polycrystals.* Acta Metallurgica et Materialia, vol. 43 n° 7, pp 2701–2719.

Belytschko T., Liu W. K., and Moran B. (2000). *Nonlinear Finite Elements for Continua and Structures.* J. Wiley and Sons.

Besson J., Cailletaud G., Chaboche J.-L., and Forest S. (2001). *Mécanique non linéaire des matériaux.* Hermes.

Bhattacharyya Abhishek, El-Danaf Ehab, Kalidindi Surya R., and Doherty Roger D. (2001). *Evolution of grain-scale microstructure during large strain simple compression of polycrystalline aluminum with quasi-columnar grains: measurements and numerical simulations.* International Journal of Plasticity, vol. 17 n° 6, pp 861–883.

Bishop J.F.W. and Hill R. (1951). *A Theoretical Derivation of the Plastic Properties of a Polycrystalline Face–Centered Metal.* Philosophical Magasine, vol. 42, pp 414–427.

Bonet J. and Wood R. D. (1997). *Nonlinear Continuum Mechanics for Finite Element Analysis.* Cambridge University Press.

Budai J., Gaudig W., and Slass S. L. (1979). *The mesurements of grain boundary thinkness using X-ray diffraction techniques.* Phylosophical Magazine A, vol. 40 n° 6, pp 757–767.

Budiansky B. and Wu T.T. (1962). *Theoretical prediction of plastic strains of polycrystals.* In : 4th US Nat. Cong. Appl. Mech., pp 1175–1185.

Cailletaud G. (1991). *A Micromechanical Approach to Inelastic Behaviour of Metals.* Int.J.Plast., vol. 8, pp 55–73.

Cailletaud G., Chaboche J.-L., Forest S., and Rémy L. (2003a). *On the design of single crystal blades.* La Revue de Métallurgie, vol. 2, pp 165–172.

Cailletaud G., Forest S., Jeulin D., Feyel F., Galliet I., Mounoury V., and Quilici S. (2003b). *Some elements of microstructural mechanics.* Computational Materials Science, vol. 27 n° 3, pp 351–374.

Chaboche J.-L., Feyel F., and Monerie Y. (2001). *Interface Debonding Models: a Viscous Regularization with a Limited Rate Dependency.* Int. J. Solids Structures, vol. 38, pp 3127–3160.

Chaboche J. L., Girard R., and Schaff A. (1997). *Numerical analysis of composite systems by using interphase/interface models.* Computational Mechanics, vol. 20 n° 1 - 2, pp 3–11.

Chin G.Y. and Mammel W.L. (1969). *Generalization and Equivalence of the Minimum Work (Taylor) and Maximum Work (Bishop–Hill) Principles for Crystal Plasticity.* Trans. of the Met. Soc. of AIME, vol. 245, pp 1211–1214.

Cizelj Leon and Riesch-Oppermann Heinz (2002). *Modelling the early development of secondary side stress corrosion cracks in steam generator tubes using incomplete random tessellation.* Nuclear Engineering and Design, vol. 212 n° 1-3, pp 21–29.

Clayton J. D. (2005). *Dynamic plasticity and fracture in high density polycrystals: constitutive modeling and numerical simulation.* Journal of the Mechanics and Physics of Solids, vol. 53 n° 2, pp 261–301.

Clayton J. D. and McDowell D. L. (2003). *Finite polycrystalline elastoplasticity and damage: multiscale kinematics.* International Journal of Solids and Structures, vol. 40 n° 21, pp 5669–5688.

Clayton J. D. and McDowell D. L. (2004). *Homogenized finite elastoplasticity and damage: theory and computations.* Mechanics of Materials, vol. 36, pp 799–824.

Cox B. (1990). *Pellet-clad interaction) failures of zirconium alloy fuel cladding – review.* Journal of Nuclear Materials, vol. 172 n° 3, pp 249–292.

Cox B., Surette B.A., and Wood J.C. *Pellet-clad interaction failures: stress corrosion cracking by iodine or metal vapour embrittlement by cesium/cadmium vapours.* In : Environmental Degradation of Engineering Materials in Aggressive Environements Proceedings of 2nd Int.Conf., pp 153–168, Blackburg,VA.

Cuitino A.M. and Ortiz M. (1992). *Computational modelling of single crystals.* Modelling Simul. Mater. Sci. Eng., vol. 1, pp 225–263.

Decker L. and Jeulin D. (2000). *Simulation 3D de materiaux aleatoires polycristallins.* La Revue de Metallurgie-CIT, vol. 96, pp 271–275.

Delaire F., Raphanel J.L., and Rey C. (2000). *Plastic heterogeneities of a copper multicrystal deformed in uniaxial tension: experimental study and finite element simulations.* Acta Mat., vol. 48, pp 1075–1087.

Diard Olivier (2001). *Un exemple de couplage, comportement-endommagement-evironnement, dans les polycristaux. Application a l'Interation Pastille-Gaine.* PhD thesis, Ecole des Mines de Paris.

Diard O., Leclercq S., Rousselier G., and Cailletaud G. (2002). *Distribution of normal stress at grain boundaries in multicrystals: application to an intergranular damage modeling.* Computational Materials Science, vol. 25 n° 1-2, pp 73–84.

Duffo G. S. and Farina S. B. (2005). *Diffusional control in the intergranular corrosion of some hcp metals in iodine alcoholic solutions.* Corrosion Science, vol. In Press, Corrected Proof.

Eberl F. (2000). *Second order heterogeneities in a Multicrystal : Experimental Developments using X-ray Diffraction and Comparison with a Finite Element Model.* PhD thesis, ENSAM.

Eliseev V. V. (1999). *Mekhanika uprugih tel (Mechanics of elastic bodies).* St-Petersbourg State Technical Univ.

Erieau Philippe and Rey Colette (2004). *Modeling of deformation and rotation bands and of deformation induced grain boundaries in steel aggregate during large plane strain compression.* International Journal of Plasticity, vol. 20 n° 10, pp 1763–1788.

Espinosa Horacio D. and Zavattieri Pablo D. (2003a). *Grain level model for the study of failure initiation and evolution in polycrystalline brittle materials. Part 1: Theory and numerical implementation.* Mechanics of Materials, vol. 35 n° 3-6, pp 333–364.

Espinosa Horacio D. and Zavattieri Pablo D. (2003b). *Grain level model for the study of failure initiation and evolution in polycrystalline brittle materials. Part 2: Numerical examples.* Mechanics of Materials, vol. 35 n° 3-6, pp 365–394.

Eterovic A. L. and Bathe K. J. (1990). *A hyperelastic-based large strain elasto-plastic constitutive formulation with combined isotropic-kinematic hardening using the logarithmic stress and strain mesures.* Int.J.Num.Meth.Eng., vol. 30, pp 1099–1114.

Evers L. P., Parks D. M., Brekelmans W. A. M., and Geers M. G. D. (2002). *Crystal plasticity model with enhanced hardening by geometrically necessary dislocation accumulation.* Journal of the Mechanics and Physics of Solids, vol. 50 n° 11, pp 2403–2424.

Farina S. B., Duffo G. S., and Galvele J. R. (2003). *Stress corrosion cracking of zirconium and Zircaloy-4 in halide aqueous solutions.* Corrosion Science, vol. 45 n° 11, pp 2497–2512.

Flanagan W. F., Bastias P., and Lichter B. D. (1991). *theory of transgranular stress-corrosion cracking.* Acta Metallurgica et Materialia, vol. 39 n° 4, pp 695–705.

Flewitt P.E.J. and R.K.Wild (2001). *Grain Boundaries.* Wiley, New York.

Foerch Ronald (1996). *Un environnement orienté objet pour la modélisation numérique des materiaux en calcul de structures.* PhD thesis, Ecole des Mines de Paris.

Franciosi P. (1985). *The Concepts of Latent Hardening and Strain Hardening in Metallic Single Crystals.* Acta Metall., vol. 33, pp 1601–1612.

Franciosi P., Berveiller M., and Zaoui A. (1980). *Latent hardening in copper and aluminium single crystals.* Acta Metallurgica, vol. 28 n° 3, pp 273–283.

Fregonese Marion (1997). *Mecanismes de corrosion sous contrainte par l'iode dans le Zirconium et le Zircaloy-4. Transposition aux conditions d'interaction pastille-gaine dans les reacteurs a l'eau pressurisee.* PhD thesis, Ecole des Mines de Saint-Etienne.

Geyer P. (1999). *Etude de modelisation du comportement elastoviscoplastique de tubes en Zircaloy par une approche polycristalline.* PhD thesis, Ecole des Mines de Paris.

Haddad R.E. and Dorado A.O. (1994). *Grain-by-grain study of the mechanisms of crack propagation during iodine stress corrosion cracking of Zircaloy-4.* In : Zirconium in the nuclear industry. Tenth Int. Symposium. ASTM STP 1245, pp 559–575, Philadelphia.

Hashimoto K. and Margolin H. (1983a). *The role of elastic interaction stresses on the onset of slip in pol ycrystalline alpha brass-I. Experimental determination of operating slip systems and qualitative analysis.* Acta Metallurgica, vol. 31 n° 5, pp 773–785.

Hashimoto K. and Margolin H. (1983b). *The role of elastic interaction stresses on the onset of slip in polycrystalline alpha brass-II. Rationalization of slip behavior.* Acta Metallurgica, vol. 31 n° 5, pp 787–800.

Hoc T., Crepin J., Gelebart L., and Zaoui A. (2003). *procedure for identifying the plastic behavior of single crystals from the local response of polycrystals.* Acta Materialia, vol. 51 n° 18, pp 5477–5488.

Hoger Anne (1987). *The stress conjugate to logarithmic strain.* International Journal of Solids and Structures, vol. 23 n° 12, pp 1645–1656.

HUTCHINSON J. W. (1964). *Plastic stress-strain relations of polycrystalline metals hardening according to Taylor's rule.* Journal of the Mechanics and Physics of Solids, vol. 12 n° 1, pp 11–24.

IDESMAN ALEXANDER V. (2003). *Comparison of different isotropic elastoplastic models at finite strains used in numerical analysis.* Computer Methods in Applied Mechanics and Engineering, vol. 192 n° 41-42, pp 4659–4674.

JACQUES P. (1994). *Contribution a l'etude de l'amorçage des fissures de corrosion sous contrainte dans le zirconium et le Zircaloy-4.* PhD thesis, Institut National Polytechnique de Grenoble.

JILLSON D. C. (1950). *Quantitative Stress-Strain Studies on Zinc Single Crystals in Tension.* Transaction AIME, Journal of Metals, vol. 188 n° Sep., pp 1129–1133.

JONES D.A. (1985). *A unified mechanism of stress corrosion and corrosion fatigue cracking.* Metallurgical transactions A, vol. 16A n° 6, pp 1133–1141.

JORDAN E.H. AND WALKER K.P. (1985). *Biaxial constitutive modelling and testing of a single crystal superalloy at elevated temperature.* In : Conf. on Multiaxial Fatigue, pp –, Sheffield.

KALIDINDI S.R. AND ANAND L. (1994). *Macroscopic shape change and evolution of crystallographic tecture in pre-textured FCC metals.* J.Mech.Phys.Solids, vol. 42 n° 3, pp 459–490.

KNORR D. B. AND PELLOUX R.M; (1982). *Effects of Texture and Microstructure on the Propagation of Iodine Stress Corrosion Cracks in Zircaloy.* Metallurgical Transactions of ASM, vol. 13A n° 1, pp 73–83.

KOCKS U. F. (1970). *The relation between polycrystal deformation and single-crystal deformation.* Metallurgical transactions, vol. 1 n° 5, pp 1121–1143.

KOCKS U. F. AND BROWN T. J. (1966). *Latent hardening in aluminum.* Acta Metallurgica, vol. 14 n° 2, pp 87–98.

KUBO T., WAKASHIMA Y., AMANO K., AND NAGAI M. (1985). *Effects of crystallographic orientation on plastic deformation and initiation of zirconium alloys.* Journal of Nuclear Materials, vol. 132 n° 1, pp 1–9.

KUDO H. AND MATSUBARA S. (1979). *Joint examination project of validity of various numerical methods for the analysis of metal forming processes.* In : Metal Forming Plasticity, éd. Lippmann H., pp 378–403. Springer.

LEBON F., RIZZONI R., AND RONEL-IDRISSI S. (2004). *Asymptotic analysis of some non-linear soft thin layers.* Computers & Structures, vol. 82 n° 23-26, pp 1929–1938.

LEMAITRE JEAN (1985). *A continuous damage mechanics model for ductile fracture.* Transactions of the ASME. Journal of Engineering Materials and Technology, vol. 107 n° 1, pp 83–89.

LEMAITRE J. (1996). *A Course of Damage Mechanics.* Springer Verlag.

LIPPMANN N., STEINKOPFF TH., SCHMAUDER S., AND GUMBSCH P. (1997). *3D-finite-element-modelling of microstructures with the method of multiphase elements.* Computational Materials Science, vol. 9 n° 1-2, pp 28–35.

LURIE A. I. (1990). *Non-Linear Theory of Elasticity.* North-Holland.

LYNCH S. P. (1988). *Environmentally assisted cracking: Overview of evidence for an adsorption-induced localised-slip process.* Acta Metallurgica, vol. 36 n° 10, pp 2639–2661.

LYNCH S. P. (1989). *Metallographic contributions to Understanding of Mechanisms of Environementally Assisted Cracking.* Metallography, vol. 23, pp 147–171.

MADEC RONAN (2001). *Des intersections entre dislocations a la plasticite du monocristal CFC; etude par dynamique des dislocations.* PhD thesis, Universite Paris XI Orsay.

MAGNIN T., CHIERAGATTI R., AND OLTRA R. (1990). *Mechanism of brittle fracture in a ductile 316 alloy during stress corrosion.* Acta Metallurgica et Materialia, vol. 38 n° 7, pp 1313–1319.

MANDEL J. (1973). *Equations constitutives et directeurs dans les milieux plastiques et viscoplastiques.* Int. J. Solids Structures, vol. 9, pp 725–740.

Marsden J. E. and Hughes J. R. (1983). *Mathematical Foundations of Elasticity.* Dover Publications, New York.

Meric L., Cailletaud G., and Gasperini M. (1994). *Finite element calculations of copper bicrystal specimens submitted to tension-compression tests.* Acta metall. Mat., vol. 42, pp 921–935.

Meric L., Poubanne P., and Cailletaud G. (1991). *Single crystal modeling for structural calculations, Part 1 and 2.* J. of Eng. Mat. Tech., vol. 113, pp 162–182.

Michel Jean-Claude, Suquet Pierre, and Thebaud Frederic (1994). *Ine modélisation du role des interfaces dans le comportement des composites à matrice métallique.* Revue européenne des éléments finis, vol. 3 n° 4, pp 573–595.

Miehe C. (1996a). *Exponential map algorithm for stress updates in anisotropic multiplicative elastoplasticity for single crystals.* International Journal for Numerical Methods in Engineering, vol. 39, pp 3367–3390.

Miehe C. (1996b). *Multisurface thermoplasticity for single crystals at large strains in terms of eulerian vector updates.* International Journal of Solids and Structures, vol. 33 n° 20-22, pp 3103–3130.

Miehe C., Apel N., and Lambrecht M. (2002). *Anisotropic additive plasticity in the logarithmic strain space: modular kinematic formulation and implementation based on incremental minimization principles for standard materials.* Computer Methods in Applied Mechanics and Engineering, vol. 191 n° 47-48, pp 5383–5425.

Miehe Christian and Lambrecht Matthias (2001). *Algorithms for computation of stresses and elasticity moduli in terms of Sth-Hill's family of generalized strain tensors.* Communications in Numerical Methods in Engineering, vol. 17 n° 5, pp 337–353.

Miehe C. and Schröder J. (2001). *A comparative study of stress update algorithms for rate-independent and rate-dependent crystal plasticity.* International Journal for Numerical Methods in Engineering, vol. 50, pp 273–298.

Mishin Y. and Herzig Chr. (1999). *Grain boundary diffusion: recent progress and future research.* Materials Science and Engineering A, vol. 260 n° 1-2, pp 55–71.

Mishuris G. and Ochsner A. (2004). *Transmission conditions for a soft elasto-plastic interphase between two elastic materials.* Archives of Mechanics, vol. in press.

Miura H., Sakai T., Otsuka T., Monzen R., and Onaka S. (2000). *Sliding of copper [001]-twist grain boundaries detected by shear deformation of liquid B2O3 particles on the grain boundaries.* Acta Materialia, vol. 48 n° 8, pp 1959–1966.

Moran B., Ortiz M., and Shih C.F. (1990). *Formulation of Implicit Finite-Element Methods for Multiplicative Finite Deformation Plasticity.* Int. J. Num. Meth. Eng., vol. 29 n° 3, pp 483–514.

Mori G., Scherer D., Schwentenwein S., and Warbichler P. (2005). *Intergranular stress corrosion cracking of copper in nitrite solutions.* Corrosion Science, vol. In Press, Corrected Proof.

Mounoury V. (2002). *private communication.*

Musienko A., Cailletaud G., and Diard O. (2002). *Damage, opening and sliding of grain boundaries.* In : Multiscale Modeling and Characterization of Elastic-Inelastic Behavior of Engineering Materials, pp –, Marrakech.

Musienko A., Schmidegg K., Kolednik O., Pippan R., and Cailletaud G. (2003). *FE simulation of multicrystals at large strains.* Problems of Material Science, vol. 33 n° 1, pp 357–364.

Nedjar B. (2002a). *Frameworks for finite strain viscoelastic-plasticity based on multiplicative decompositions. Part 1: Continuum formulations.* Computer Methods in Applied Mechanics and Engineering, vol. 191 n° 15-16, pp 1541–1562.

Nedjar B. (2002b). *Frameworks for finite strain viscoelastic-plasticity based on multiplicative decompositions. Part 2: Computational aspects.* Computer Methods in Applied Mechanics and Engineering, vol. 191 n° 15-16, pp 1563–1593.

Needleman A. (1987). *A Continuum Model for Void Nucleation by Inclusion Debonding.* J. of Applied Mechanics, vol. 54, pp 525–531.

Onck Patrick and van der Giessen Eric (1997). *Microstructurally-based modelling of intergranular creep fracture using grain elements.* Mech. of Materials, vol. 26, pp 109–126.

Papadopoulos Panayiotis and Lu Jia (1998). *General framework for the numerical solution of problems in finite elasto-plasticity.* Computer Methods in Applied Mechanics and Engineering, vol. 159 n° 1-2, pp 1–18.

Papadopoulos Panayiotis and Lu Jia (2001). *On the formulation and numerical solution of problems in anisotropic finite plasticity.* Computer Methods in Applied Mechanics and Engineering, vol. 190 n° 37-38, pp 4889–4910.

Parker J. D. and Wilshire B. (1977). *surface measurement study of grain-boundary sliding during creep of a two-phase, copper-cobalt alloy.* Materials Science and Engineering, vol. 29 n° 3, pp 219–225.

Roberts A. P. and Garboczi E. J. (2001). *Elastic moduli of model random three-dimensional closed-cell cellular solids.* Acta Materialia, vol. 49 n° 2, pp 189–197.

Sachtleber M., Zhao Z., and Raabe D. (2002). *Experimental investigation of plastic grain interaction.* Materials Science and Engineering A, vol. 336 n° 1-2, pp 81–87.

Schmid E. and Boas W. (1935). *Kristallplastizität.* Springer, Berlin.

Schmidegg Klaus (2000). *Finite element simulation of local defromations in polycrystals and comparison to experimental results.* Master's thesis, Leoben University.

Schmidt-Baldassari Martin (2003). *Numerical concepts for rate-independent single crystal plasticity.* Computer Methods in Applied Mechanics and Engineering, vol. 192 n° 11-12, pp 1261–1280.

Schroeter Brian M. and McDowell David L. (2003). *Measurement of deformation fields in polycrystalline copper.* International Journal of Plasticity, vol. 19 n° 9, pp 1355–1376.

Semenov A. S., Melnikov B. E., and Ju. Gorokhov M. (2003). *Cyclic instability in the calculations of large elasto-plastic strains.* Nauchno-tehnicheskie vedomosti SPbGTU, vol. 33 n° 3, pp 129–138.

Shtremel M. A. (1997). *Procnost splavov (Strength of alloys - in Russian).* MISIS, Moscow.

Sidky P. S. (1998). *Iodine stress corrosion cracking of Zircaloy reactor cladding: iodine chemistry (a review).* Journal of Nuclear Materials, vol. 256 n° 1, pp 1–17.

Simo J.C. and Hughes T.J.R. (1997). *Computational Inelasticity.* Springer.

Suquet P.M. (1987). *Discontinuities and Plasticity.* In : Nonsmooth mechanics and applications, éds. Moreau J.J. and Panagiotopoulos P.D., pp 280–340, Springer,Berlin.

Tatschl Arnold (2000). *Neue experimentelle Methoden zur Charakterisierung von Verformungsvorgangen.* PhD thesis, Leoben University.

Tatschl A. and Kolednik O. (2002a). *A new tool for the experimental characteriazation of microplasticity.* Materials Science and Engineering A, vol. in press, pp 1–16.

Tatschl A. and Kolednik O. (2002b). *On the experimental characterization of crystal plasticity in polycrystals.* Materials Science and Engineering A, vol. in press, pp 1–17.

Taylor L. M. and Becker E. B. (1983). *Some computational aspects of large deformation, rate-dependent plasticity problems.* Computer Methods in Applied Mechanics and Engineering, vol. 41 n° 3, pp 251–277.

Teodosiu C., Raphanel J.L., and Tabourot L. (1993). *Finite element simulation of the large elastoplastic deformation of multicrystals.* In : Large plastic deformations. Fundamental aspects and applications to metal forming. Proceedings of the International Seminar MECAMAT-91, éds. Teodosiu C., Raphanel J.L., and Sidoroff F., pp 153–168.

Tome C. and Kocks U. F. (1985). *The yield surface of h.c.p. crystals.* Acta Metallurgica, vol. 33 n° 4, pp 603–621.

Truesdell C. (1972). *A first curse in rational continuum mechanics.* The Johns Hopkins University, Baltimore, Maryland.

Tvergaard V. (1984). *On the creep constrained diffusive cavitation of grain boundary facets.* J. Mech. Phys. Sol., vol. 32 n° 5, pp 373–393.

Tvergaard V. (1990). *Effect of Fiber Debonding in a Whisker-Reinforced Metal.* Material Science and Engineering, vol. 125, pp 203–213.

Voyiadjis George Z. and Deliktas Babur (2000). *coupled anisotropic damage model for the inelastic response of composite materials.* Computer Methods in Applied Mechanics and Engineering, vol. 183 n° 3-4, pp 159–199.

Watanabe T. (1983). *Grain boundary sliding and stress concentration during creep.* Metallurgical transactions A, vol. 14A n° 4, pp 531–545.

Weber Gustavo and Anand Lallit (1990). *Finite deformation constitutive equations and a time integration procedure for isotropic, hyperelastic-viscoplastic solids.* Computer Methods in Applied Mechanics and Engineering, vol. 79 n° 2, pp 173–202.

Wei Y. J. and Anand L. (2004). *Grain-boundary sliding and separation in polycrystalline metals: application to nanocrystalline fcc metals.* Journal of the Mechanics and Physics of Solids, vol. 52 n° 11, pp 2587–2616.

Weyer Stefan, Frohlich Andreas, Riesch-Oppermann Heinz, Cizelj Leon, and Kovac Marko (2002). *Automatic finite element meshing of planar Voronoi tessellations.* Engineering Fracture Mechanics, vol. 69 n° 8, pp 945–958.

Woo Seog Ryu, Young Hwan Kang, and Jai-Young Lee (1988). *Effects of iodine concentration on iodine-induced stress corrosion cracking of zircaloy-4 tube.* Journal of Nuclear Materials, vol. 152 n° 2-3, pp 194–203.

Xiao H., Bruhns O. T., and Meyers A. (2000). *Consistent finite elastoplasticity theory combining additive and multiplicative decomposition of the stretching and the deformation gradient.* International Journal of Plasticity, vol. 16 n° 2, pp 143–177.

Yoshida Hidehiro, Yokoyama Kenji, Shibata Naoya, Ikuhara Yuichi, and Sakuma Taketo (2004). *High-temperature grain boundary sliding behavior and grain boundary energy in cubic zirconia bicrystals.* Acta Materialia, vol. 52 n° 8, pp 2349–2357.

Zeghadi A., Forest S., and Gourgues A.F. (2005). *Effets des gradients de déformation induits par la microstructure sur le comportement mécanique.* Technical Report 20/9/02, Centre des Materiaux, Ecole des Mines de Paris, Evry, France.

Zhang D., Wu M. S., and Feng R. (2004). *Micromechanical investigation of heterogeneous microplasticity in ceramics deformed under high confining stresses.* Mechanics of Materials, vol. In Press, Corrected Proof.

Zhang Nian and Tong Wei (2004). *An experimental study on grain deformation and interactions in an Al-0.5Mg multicrystal.* International Journal of Plasticity, vol. 20 n° 3, pp 523–542.